FIELD, KINETIC, AND THERMODYNAMIC STUDIES OF MAGMATIC ASSIMILATION IN THE NORTHERN CORDILLERAN VOLCANIC PROVINCE, NORTHWESTERN BRITISH COLUMBIA

By

BENJAMIN RALPH EDWARDS

B.A., Carleton College, Northfield, Mn., U.S.A., 1989
M.Sc., University of Wyoming, Laramie, Wy., U.S.A., 1993

A THESIS SUBMITTED IN PARTIAL FULFILLMENT OF THE REQUIREMENTS
FOR THE DEGREE OF DOCTOR OF PHILOSOPHY

in

THE FACULTY OF GRADUATE STUDIES
GEOLOGICAL SCIENCE DIVISION
DEPARTMENT OF EARTH AND OCEAN SCIENCES

We accept this thesis as conforming to the required standard

THE UNIVERSITY OF BRITISH COLUMBIA

July, 1997

©Benjamin Ralph Edwards, 1997

In presenting this thesis in partial fulfilment of the requirements for an advanced degree at the University of British Columbia, I agree that the Library shall make it freely available for reference and study. I further agree that permission for extensive copying of this thesis for scholarly purposes may be granted by the head of my department or by his or her representatives. It is understood that copying or publication of this thesis for financial gain shall not be allowed without my written permission.

Department of Earth & Ocean Sciences

The University of British Columbia
Vancouver, Canada

Date 01 Aug 97

PLATE 1A. GEOLOGY OF THE QUATERNARY HOODOO MOUNTAIN VOLCANIC COMPLEX

PARTS OF HOODOO MOUNTAIN (NTS 104B/14), AND CRAIG RIVER (104B/11) MAP AREAS BRITISH COLUMBIA

Scale 1:20 000

500 0 1000 2000 3000
Metres Metres

Universal Transverse Mercator Projection
North American Datum – NAD83
UTM coordinates, Zone 9

Geology by: B.R. Edwards (1993, 1994)

Assistance by: R.G. Anderson (map production), G. Edwards (1994 field season), N. Hastings (digital cartography and fieldlog database management), J.K. Russell (1993 field season) and M.V. Stasiuk (1993 field season)

The following names have not been approved by the Canadian Permanent Committee on Geographical Names: Lake Hoodoo, Little Bear Mountain, Long Valley, North Fork Upper Hoodoo River, Northwest Flow, Pointer Ridge, Pumice Point, Horn Ridge, Ship Rock, Slide Canyon, South Fork Upper Hoodoo River, The Bluff, The Bowl, The Hook, The Horn, The Monument, The Wall,

AWS-B7
1998-250059
(PhD
Fall 1997]

AWS B7 1997-250059
Edwards, Benjamin
Ph.D, Fall 1997
Sheet 1 of 3 (Appendix)
(Plate IA)

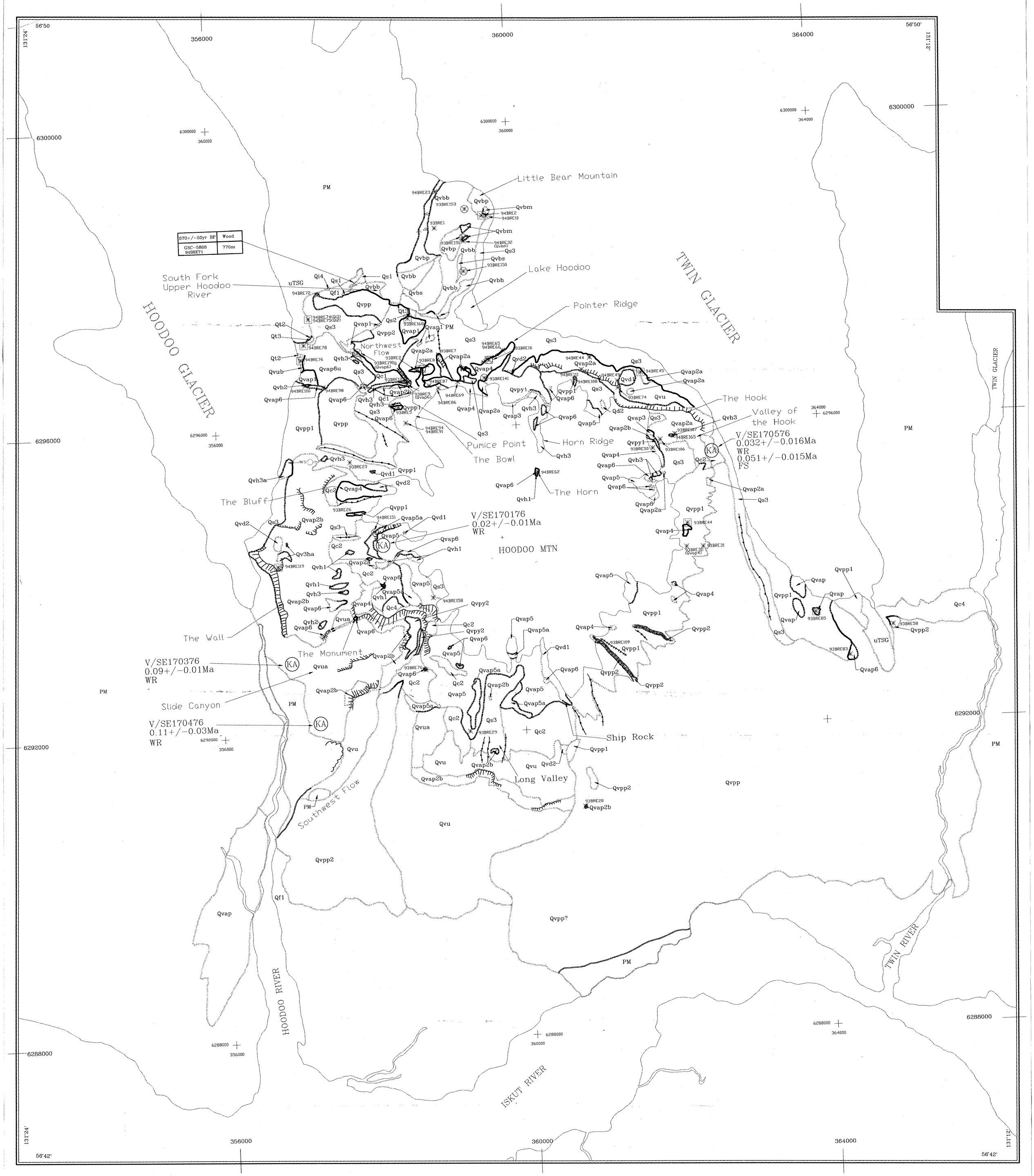
56°50'
131°24'
356000
360000
364000
131°12'
6300000
6296000
6292000
6288000
6296000 360000
6300000 360000
6300000 364000
364000 6296000
356000 6296000
356000 6292000
356000 6288000
360000 6288000
364000 6288000
56°42'
131°24'
131°12'
PM
Qvpp1
Qvpp
Qvpp2
Qvpp?
Qvap
Qvu
Qvua
Qvh1
Qvh2
Qvh3
Qvh3a
Qv3ha
Qvap1
Qvap2a
Qvap2b
Qvap4
Qvap5
Qvap5a
Qvap6
Qvpy1
Qvpy2
Qvd1
Qvd2
Qvub
Qvap6u
Qf1
Qi4
Qs1
Qs2
Qs3
Qc1
Qc2
Qc4
Qt2
Qt3
Qvbb
Qvbp
Qvbm
Qvbs
Qvbh
Qs3
Qvap1 PM
Qvap2a
Qvap4
Qvap2b
Qvap5
Qvap5a
Qvap6
Qvpp1
Qvpp2
Qvpy1
Qvpy2
Qvd1
Qvd2
Qvu
Qvua
Qvap
Qf1
Qvpp?
Qvpp2
Qvap2b
Qvu
Qvpp
Qvpp1
Qvpp2
Qvap
Qvap4
Qvap5
Qvap6
Qc4
Qvap6
Qvap2b
Qvap5
Qvap5a
Qvd1
Qvap6
Qvpp1
Qvpp2
Qvap2b
Qvu
Qvd2
Qvap2b
Qvpp2
Qvpp
Qvap2b
Qvpp1
Qvpp2
Qvap2a
Qvap4
Qvap5

AWS 87 1997-250059

Edwards, Benjamin
Ph. D., Fall 1997
Sheet 2 of 3 (appendix)

(Plate 18)

PLATE 1C. GEOLOGY OF THE QUATERNARY HOODOO MOUNTAIN VOLCANIC COMPLEX

LEGEND

STRATIFIED ROCKS

Quaternary

SURFICIAL DEPOSITS

Qc4 — soil, marsh and snow (above 1500 m)

COLLUVIAL DEPOSITS

Qc3 — unstratified colluvium including glacial till, outwash, and talus

Qc2 — talus derived from local exposures

Qc1 — colluvium comprising black, glassy clasts and lava fragments; found on the northwest corner of Hoodoo Mountain

FLUVIAL AND GLACIOFLUVIAL DEPOSITS

Qf1 — stream gravel and associated fluvial deposits

GLACIAL DEPOSITS

Qs3 — unconsolidated glacial till and moraine deposits

GLACIOLACUSTRINE DEPOSITS

Qs2 — black, tan, light green to variegated, thinly-laminated glaciolacustrine sediments consisting of sand and clay; clay laminae are less than 1 mm thick; along south fork of upper Hoodoo River

Qs1 — black, tan to variegated, thin-bedded fluvial to glaciolacustrine sediments comprising sand, clay and minor gravel beds; at the confluence of the north and south forks of upper Hoodoo River. Unit is unconsolidated, more drab and more clay-rich than Qs3. ^{14}C age = 670 +/- 50 yr BP (radiocarbon age determination GSC-5868)

Pleistocene and Holocene

Boundary Ranges volcanic region

HOODOO MOUNTAIN VOLCANIC COMPLEX

Qvpp$_{(1,2)}$ — undivided porphyritic phonolite lavas covered by talus or forest; probably equivalent to Qvpp1. Elsewhere, the unit is subdivided in two subunits:

Qvpp2 — unglaciated, alkali feldspar-phyric phonolite lava flows with preserved aa flow surface and/or lava channel levees; on the northwestern, southwestern and southeastern sides of Hoodoo Mountain

Qvpp1 — alkali feldspar-phyric phonolite lava flows whose flow surfaces have been partly removed by glaciation; lava channels still preserved (sample 93BRE9 and 93BRE44 submitted for $^{40}Ar/^{39}Ar$ dating)

Qvap$_{(1-6)}$ — undivided aphanitic phonolite lavas or those of poorly-constrained stratigraphic position; includes three lava domes at the terminus of Twin Glacier with characteristics similar to several other Qvap units; unit is overlain by Qvpp1; also includes a lava flow / avanlanche deposit of angular blocks of black, aphanitic lava on the west side of lower Hoodoo River, near the confluence with the Iskut River; K-Ar dates for this unit from Souther and Armstrong (unpubl. data, see Souther, 1990a) range from 0.11 +/- 0.03 Ma to 0.02 +/- 0.01 Ma (sample 93BRE65 submitted for $^{40}Ar/^{39}Ar$ dating). Elsewhere the unit is subdivided into six subunits:

Qvap6, Qvap6u — aphanitic phonolite subglacial lava flows and spines; green to grey-green; highly vesicular with irregularly shaped vesicles and local analcite-lined vesicles and amygdules

Qvap6u: undivided aphanitic phonolite subglacial lava flow deposits; on the northwest corner of Hoodoo Mountain, bordering the southwestern side of large exposures of Qvpp2; it includes isolated occurrences of Qvh2 and Qvh3, as well as some lava flow breccia (sample 94BRE78 submitted for $^{40}Ar/^{39}Ar$ dating)

Qvap5, Qvap5a — structurally highest aphanitic phonolite lava flows interbedded with flow breccia and hyaloclasite; on the northeast, southeast, south and west sides of Hoodoo Mountain; common irregular to radial columnar jointing

Qvap5a: domes and thick lava flows within or at the base of flow breccia; south and southwestern sides of Hoodoo Mountain

Qvap4 — stratigraphically medial aphanitic to slightly porphyritic phonolite lava flows, generally black on fresh surfaces but weathering to rusty brown; often with coarse (>0.5 m in diameter) columnar joints and varying between 1 and 10 m in thickness (sample 93BRE16 submitted for $^{40}Ar/^{39}Ar$ dating)

Qvap3 — aphanitic phonolite lava flow(?) with abundant fresh and devitrified glass and heterolithic clasts; on the north side of Hoodoo Mountain capping the large deposit of Qvpy1 and as an isolated occurrence on the northeast corner of Hoodoo Mountain

Qvap2$_{(a,b)}$ — stratigraphically medial aphanitic phonolite lava flows and domes; on northern and western sides of Hoodoo Mountain directly overlain by Qvap4 and Qvpy1

a: commonly with narrow (<0.5 m in diameter) columnar joints, locally radially oriented, and with distinctive flow banding; on the north and northeast sides of Hoodoo Mountain, (sample 94BRE45 submitted for $^{40}Ar/^{39}Ar$ dating)

b: undivided medial aphanitic phonolite lava flows and flow breccia; mainly on west side of Hoodoo Mountain, (sample 94BRE119 submitted for $^{40}Ar/^{39}Ar$ dating)

Qvap1 — stratigraphically lowest aphanitic phonolite lava flows and domes, with closely-spaced columnar joints and platy jointing oriented parallel to the columns (sample 94BRE168 submitted for $^{40}Ar/^{39}Ar$ dating)

Qvu$_{(a-b)}$ — undivided volcanic rocks including lava flows and volcanic breccias; commonly weather to form hoodoos and/or occur below treeline; not directly sampled or identified; elsewhere the undivided volcanic rocks are distinguished:

Qvua — yellow to brown volcanic rocks that form hoodoos in the steep canyons on the southwest sides of Hoodoo Mountain

Qvub — pinkish brown Holocene(?) volcanic rocks exposed at the eastern edge of Hoodoo Glacier; feldspar phyric with columnar joints and resembling Qi3; overlain by Qt1 and Qt2 (sample 94BRE76 submitted for $^{40}Ar/^{39}Ar$ dating)

INTRUSIVE ROCKS

Dykes

Quaternary
Pleistocene and Holocene

Qi — undivided Holocene(?) dykes that crosscut Mesozoic basement rocks and occur within or crosscut some of the lower units in Hoodoo Mountain and Little Bear mountain volcanic complexes. Elsewhere the unit is subdivided into four types:

Qi1 — basalt dykes which contain white granitic xenoliths characterized by disseminated patches of black glass; intrude Qvbb on northern Little Bear mountain near the summit

Qi2 — purple-brown, tephrite dykes: intrude Mesozoic rocks west of Little Bear mountain and east of Hoodoo Glacier (sample 94BRE75 submitted for $^{40}Ar/^{39}Ar$ dating)

Qi3 — Pink-brown, trachyandesite dykes: intrude Mesozoic rocks and crosscut Qvd2 immediately east of Hoodoo Glacier (sample 94BRE74 submitted for $^{40}Ar/^{39}Ar$ dating)

Qi4 — Grey-green, phonolitic (?) dykes: intrude Mesozoic rocks on the north side of upper Hoodoo River near the confluence and both Qvap2b and Qvap5 on the west side of Hoodoo Mountain

PALEOZOIC AND MESOZOIC BASEMENT ROCKS

PM — undivided basement rocks comprising Carboniferous or Permian and Triassic limestone, and volcanic flow, volcaniclastic, metasedimentary, and meta-volcanic rocks of Stikine assemblage and Stuhini Group; undivided Late Triassic to Middle Jurassic plutonic rocks of mafic, intermediate, felsic and alkaline composition

Qt3 — tan-grey till characterized by flaggy jointing and alignmed oblong fragments; clasts include green quartzite(?) cobbles and black, vitric sand; conformably overlies Qvbb on the south fork of the upper Hoodoo River and overlies Qvh2 directly east of Hoodoo Glacier and is overlain by Qvpp1. Locally Qt3 overlies thin hyaloclastite and Qt2 units.

Qt2 — massive brown till characterized by basalt and metavolcanic cobbles; in stream bed of upper Hoodoo River directly east of Hoodoo Glacier; overlain by Qt3

Qvd$_{(1-2)}$ — matrix- or clast-supported diamictite, consisting of black, angular clasts of Qvap and other units in orange-brown to red matrix; also local minor interbedded stratified deposits. Subdivided into two subunits:

Qvd2 diamictite with subangular to subrounded heterolithic clasts of Qvap lava and Qt(?); several of the fragments are boulders up to 3 m in size; on the northeastern, northern and western sides of Hoodoo Mountain; interpreted as debris flow deposits

Qvd1 diamictite with yellow, tuffaceous matrix and clasts of Qvap, angular vitric fragments, and subrounded siliceous metavolcanic rock clasts; on west side of Hoodoo Mountain deposits occur beneath Qvpp and interbedded with Qvap5; minor interbedded and well-sorted layers of both sand- and cobble-sized clasts; may be water-transported, reworked pyroclastic deposit

Qt1 — grey till; less resistant than Qt2; underlies Qt2 east of Hoodoo Glacier; equivalent(?) to till underlying oldest Hoodoo lava flows described by Kerr (1948)

Qvh$_{(1-3)}$ — hyaloclastite, consisting of black to brown, vitric lapilli-size fragments in a yellow or green matrix of palagonite(?); commonly found in small outcrops associated with Qvap6. Subdivided into three subunits:

Qvh3 hyaloclastite with fresh, non-altered vitric lapilli in yellow matrix
Qvh3a yellow hyaloclastite interbedded with green mudstone

Qvh2 hyaloclastite with fresh, non-altered vitric lapilli in greenish grey matrix

Qvh1 hyaloclasite with devitrified vitric lapilli in yellow to red matrix

Qvpy — coeval deposition of flanking units to main phonolite edifice inferred from stratigraphic relationships

Qvpy$_{(1-2)}$ — yellow to green pyroclastic rocks consisting of lapilli to ash-size fragments of pumice, crystals and accidental lithic fragments; unwelded to strongly welded layers; yellow portions form distinctively recessive units

Qvpy1 on north-central side of Hoodoo Mountain adjacent to Pointer ridge and at the Hook

Qvpy2 on the west-central and southwest sides of Hoodoo, exposed in inaccessible cliffs; correlated with Qvpy1 based on stratigraphic position, recessive character and yellow colour

Qvb — LITTLE BEAR MOUNTAIN VOLCANIC COMPLEX

Qvbs — orange to reddish orange basaltic volcanic sandstone and lithic crystal lapilli tuff; mainly on south end of Little Bear mountain

Qvbb — orange to mottled black and orange, basaltic breccia with bomb-sized fragments of basalt in a glass matrix but no recognizable pillow basalt fragments

Qvbh — grey basaltic hyaloclastite; lapilli to ash-size glass fragments with scattered fragments of plagioclase, olivine, clinopyroxene and basalt

Qvbm | Qvpb — black to grey, massive basalt flows; mainly on north end of Little Bear mountain (sample 94BRE2 submitted for $^{40}Ar/^{39}Ar$ dating); Qvpb: black to grey, basaltic pillow breccia and/or hyaloclastite; mainly on central northwestern sides of Little Bear mountain

SYMBOLS

- limits of map area
- geological contact: defined, approximate, assumed
- lava channel
- morainal ridge
- cliff formed by ice-damming
- pillow basalt
- landslide scar
- warm spring
- in Qv: bedding known, dip estimated (g = gentle (0-15° dip), m = moderate (15-30° dip); s = steep (>30° dip); in Mesozoic basement rocks: bedding, inclined, vertical
- flow foliation
- apparent bedding orientation: inclined, subhorizontal
- Qi1 — dyke trend
- fresh, post-kinematic dyke orientation: inclined, vetical
- 670+/-50yr BP | Wood | GSC-5868 | 770m — radiocarbon-dated sample; ^{14}C age = 670 +/- 50 yr BP (box gives date, material dated, elevation of sample 94BRE-71 in meters and radiocarbon age determination number GSC-5868)
- V/SE170476 | Q 1.1+/-0.03Ma | WR — whole rock K-Ar sample, location poorly known and compiled from 1:250,000 scale field map; age in Ma (Souther, 1990a; R.L. Armstrong, unpublished data); FS=feldspar, WR=Whole Rock
- 94BRE72 — chemically-analyzed whole rock sample
- 94BRE76 — whole rock sample collected for $^{40}Ar/^{39}Ar$ dating
- 93BRE190 — sample analyzed for Sr and Nd isotopic compositions

AWS 87 1997-250059

Edwards, Benjamin
PhD, Fall 1994

Sheet 3 of 3 (appendix)

Abstract

This thesis investigates the process of magmatic assimilation. Field observations, kinetic considerations, and thermodynamic calculations are used together to form a calculational model for assimilation processes in mafic magmas. Field and petrographic constraints derive from lavas within the newly defined Northern Cordilleran Volcanic Province (NCVP) of northwestern British Columbia and the Yukon Territories (Chapter One). Petrographic and geochemical evidence for assimilation is common throughout the NCVP and is especially important at the Hoodoo Mountain volcanic complex (HMVC), a pair of previously unstudied alkaline to peralkaline volcanoes within the Stikine subprovince of the NCVP, in northwestern British Columbia. Chapter Two presents the geology, stratigraphy, geochronology, petrography, and geochemistry of the HMVC and discusses its chemical and physical evolution. Subglacial volcanism and magmatic assimilation are shown to be important processes in the physical and chemical evolution of the HMVC.

Chapter Three reviews kinetic constraints on magmatic assimilation and the available experimental data for rates of mineral dissolution in mafic silicate melts. Published mineral dissolution experiments in basaltic melts are

consistent with a time-independent dissolution mechanism. The most extensive experimental dataset (Donaldson 1985) is used to develop a model for predicting rates of mineral dissolution in basaltic silicate melts. It is shown that rates of dissolution can be simply predicted by calculating the thermodynamic driving force for the dissolution reactions (the Affinity), using the thermodynamic database of Ghiorso and Sack (1995).

An existing model based soley on equilibrium thermodynamics (MELTS; Ghiorso and Sack 1995) demonstrates that crystal growth and compositional zoning are sensitive recorders of specific assimilation paths (Chapter Four). The thermodynamic database for the MELTS model is combined with the kinetic model for predicting mineral dissolution rates to produce a new model for magmatic assimilation (Chapter Five). The new model is different from pre-existing models because it predicts cooling and crystallization rates implied by kinetically-controlled magmatic assimilation. Results from the new model demonstrate that magmatic assimilation processes that are controlled by kinetics operate on the time-scale of days to weeks. Given the time-scale of magma transport and volcanism, magmatic assimilation is shown to be a temporally, as well as geochemically, viable process during transport of mantle derived magmas and in the evolution of Hoodoo Mountain volcanic complex (~240 Ka).

Table of Contents

Abstract.....ii

Table of Contents.....iv

List of Figures.....vii

List of Tables.....xvi

Acknowledgements.....xix

Preface.....xxi

1. The Northern Cordilleran Volcanic Province **1**

1.1. INTRODUCTION.....1

1.2. DEFINITION OF THE NORTHERN CORDILLERA VOLCANIC PROVINCE...2

1.3. VOLCANOLOGY.....7

1.4. GEOCHRONOMETRY.....16

1.5. PETROLOGY.....18

1.6. PETROGENETIC PROCESSES.....30

1.7. SUMMARY.....37

2. Geology, Stratigraphy, and Geochemistry of the Hoodoo Mountain Volcanic Complex.....**39**

2.1. INTRODUCTION.....39

2.2. GEOLOGY AND STRATIGRAPHY.....41

2.3. DESCRIPTIVE PETROGRAPHY AND PETROCHEMISTRY.....81

2.4. ORIGINS OF THE HMVC.....123

2.5. SUMMARY.....136

3. Thermodynamic and Kinetic Controls on Magmatic Assimilation.....138

3.1. INTRODUCTION.....138

3.2. THERMODYNAMIC CONSTRAINTS.....139

3.3. KINETIC CONSTRAINTS.....143

3.4. SUMMARY.....170

4. Equilibrium Modeling of Magmatic Assimilation.....172

4.1. INTRODUCTION.....172

4.2. MODEL PATHS OF ASSIMILATION.....173

4.3. ASSIMILATION AND MINERAL ZONING.....183

4.4. DISCUSSION OF MELTS MODELING.....192

4.5. SUMMARY OF EQUILIBRIUM THERMODYNAMIC MODELING.....198

5. A New Model for Assimilation-Fractional Crystallization (AFC) 200

5.1. INTRODUCTION.....200

5.2. DEVELOPMENT OF A FORWARD MODEL FOR TIME-DEPENDENT AFC 201

5.3. EFFECTS OF VARYING P, T_a, AND ASSIMILANT COMPOSITION.....235

5.4. DISCUSSION....260

5.5. CONCLUSIONS....270

6. Summary....271

References....274

Appendix A2: Sample Information for the HMVC....307

Appendix A3: Error Propagation and Affinity Calculations....322

Plate 1A. Geology of the Quaternary Hoodoo Mountain Volcanic Complex

Plate 1B. Geology of the Quaternary Hoodoo Mountain Volcanic Complex

Plate 1C. Geology of the Quaternary Hoodoo Mountain Volcanic Complex

List of Figures

Figure 1.1 Neogene to Quaternary volcanism in the northern Cordillera of British Columbia and the Yukon Territory 3

Figure 1.2 Previous definitions of the Stikine Volcanic Belt and boundaries recommended in this work 5

Figure 1.3 Total alkalies versus SiO_2 (wt.%) rock classification diagram after LeBas et al. (1986) for: a) volcanic rocks within the Stikine volcanic belt, and b) all other volcanic rocks from the Northern Cordillera Volcanic Province (NCVP). 20

Figure 1.4 AFM diagram for: a) data for the SVB and, b) data for other NCVP centres. 22

Figure 1.5 Distribution of xenoliths in the NCVP 26

Figure 1.6 Distribution of xenoliths in the NCVP with respect to major terrane boundaries 27

Figure 1.7 Schematic lithospheric cross-sections through three terranes underlying NCVP volcanic centres. 35

Figure 2.1 Location of the Hoodoo Mountain volcanic complex and other Quaternary volcanic centres along the Iskut River (from Hauksdóttir 1994). Inset shows volcanic centres in the Northern Cordilleran Volcanic Province. 40

Figure 2.2 Aerial photograph of the Hoodoo Mountain volcanic complex. Scale is approximately 1:66 700 42

Figure 2.3 Photographs of Hoodoo Mountain volcano. Views are: a) from the southeast (Iskut River in foreground), from the southwest, c) from the east, d) cliffs of Qvap on the south side, and e) cliffs of Qvap on the west side 43

Figure 2.4 Geologic map of the Hoodoo Mountain Volcanic Complex 45

Figure 2.5 Photographs of unit Qvap. Views are: a) $Qvap_1$ overlying glacial till, b) irregular columnar jointing in $Qvap_5$ (person for scale), c) five stacked lava flows of $Qvap_4$, d) spine of $Qvap_6$ (the "Monument"), e) dome of $Qvap_5$, and f) spines and breccia of $Qvap_5$. 52

Figure 2.6 Photographs of units $Qvap_6$, Qvh_3, and Qt. Views are: a) dyke of $Qvap_6$ cutting $Qvap_5$, b) Horn Ridge, c) radial jointing in $Qvap_6$ at the Horn, d) $Qvap_6$ and Qvh_3 at the Horn (person for scale), e) $Qvap_6$ overlying Qvh_2 below Pumice Ridge (person for scale), and f) Qvh_2 between Qt_2 and Qt_3 53

Figure 2.7 Photograph of the north side of Hoodoo Mountain volcano. Boundaries for map units are shown by white lines (dotted) 55

Figure 2.8 Photographs of unit Qvpp. Views are: a) NW Flow (tents for scale), b) outcrop of trachytic Qvpp, c) nine stacked lava flow sheets, d) Qvpp above and below cliff of Qvap2, and e) preserved lava channel levées at NW Flow 57

Figure 2.9 Photographs of units $Qvpy_1$, Qvap, and Qvh_2. Views are: a) Pointer Ridge deposit, b) eutaxitic texture in $Qvpy_1$, c) Qvap breccia, d) block of "woody pumice" at Pumice Ridge, e) lapillus and bombs in Qvh_3. 60

Figure 2.10 Photographs of Little Bear Mountain. Views are: a) Little Bear Mountain, b) lense of Qvbb cutting Qvbh (person for scale), c) pillow of Qvb, d) basement overlain sequentially by Qvbb, Qt_3, and $Qvpp_2$ (person for scale) 66

Figure 2.11 Photographs of glacial deposits. Views are: a) finely laminated mudstones, b) interlayered sand and silt (person for scale), and c) well-indurated till (Qt_2) 72

Figure 2.12 Schematic stratigraphic column for Hoodoo Mountain and Little Bear Mountain volcanoes 75

Figure 2.13 Stratigraphic positions of samples dated by $^{40}Ar/^{39}Ar$ 79

Figure 2.14 Photomicrographs of lava samples from Hoodoo Mountain volcano. Views are: a) $Qvap_2$, b) $Qvap_5$, c) $Qvap_6$, and d) Qvpp. Field of view is approximately 2 by 3 cm 85

Figure 2.15 Photomicrograph and NDIC images of lava samples from Little Bear Mountain. Views are: a) sample 94BRE153a (Qvbm) with gabbroic inclusion (field of view approximately 2 by 3 cm) and b-e) NDIC images of plagioclase phenocrysts and xenocrysts in sample 94BRE2 89

Figure 2.16 Plots showing variations in major and minor element abundances for samples from the HMVC. Absissa are the Differentiation Index (DI) of Thorton and Tuttle (1960) and ordinates are: a) SiO2 (wt. %), b) FeO_{total} (wt. %), c) $FeO_{measured}$ (wt. %), d) Fe_2O_3 (wt. %), e) MgO (wt. %), f) MnO (wt. %) 96

Figure 2.17 Plots showing a) TAS classification for volcanic rocks and, b) variations in calculated ln a_{SiO2} versus calculated ln fO_2. 100

Figure 2.18 Plots showing a) projected compositions of Hoodoo Mountain, Mount Edziza, and Level Mountain evolved rocks in Ne-Qtz-Ks ternary and b) molar Al / (K + Na) versus molar K / Na for samples of trachytes from Hoodoo Mountain, Mount Edziza, and Level Mountain. 104

Figure 2.19 Minor and trace element patterns normalized to values for a tholeiitic mid ocean ridge basalt (Pearce 1983) for: a) subunits $Qvap_{1-2}$, b) subunits $Qvap_{4-5}$, c) volcanic glass from Qvh and $Qvap_6$, d) subunit $Qvap_6$, e) unit Qvpp, f) unit Qvb, g) unit Qi, and h) xenoliths from Little Bear Mountain volcano 107

Figure 2.20 Minor and trace element patterns normalized to values of volcanic glass from unit Qvh (94BRE98) for: a) subunits $Qvap_{1-2}$, b) subunits $Qvap_{4-5}$, c) volcanic glass from Qvh and $Qvap_6$, d) subunit $Qvap_6$, e) unit Qvpp, f) unit Qvb, g) unit Qi, and h) xenoliths from Little Bear Mountain volcano 108

Figure 2.21 Minor and trace element patterns normalized to values of the most Mg-rich Quaternary basalt in the Iskut area (SC-23; Hauksdóttir 1994) for: a) subunits $Qvap_{1-2}$, b) subunits $Qvap_{4-5}$, c) volcanic glass from Qvh and $Qvap_6$, d) subunit $Qvap_6$, e) unit Qvpp, f) unit Qvb, g) unit Qi, and h) xenoliths from Little Bear Mountain volcano 109

Figure 2.22 Rare earth element patterns normalized to values of average

chondritic meteorites (Boynton 1984) for: a) subunits $Qvap_{1-2}$, b) subunits $Qvap_{4-5}$, c) volcanic glass from Qvh and $Qvap_6$, d) subunit $Qvap_6$, e) unit Qvpp, f) unit Qvb, g) unit Qi, and h) xenoliths from Little Bear Mountain volcano.....113

Figure 2.23 Geometrical characteristics of chondrite normalized REE patterns: $(La / Yb)_N$ versus Yb_N, b) $(La / Sm)_N$ versus Sm_N, c) $(Gd / Yb)_N$ versus Yb_N, d) $(Eu / Eu^*)_N$ versus $(La / Sm)_N$ and e) $(Eu / Eu^*)_N$ versus $(La / Sm)_N$ for samples from Hoodoo Mountain only.....114

Figure 2.24 Rare earth element patterns normalized to values of volcanic glass from unit Qvh (94BRE98) for: a) subunits $Qvap_{1-2}$, b) subunits $Qvap_{4-5}$, c) volcanic glass from Qvh and $Qvap_6$, d) subunit $Qvap_6$, unit Qvpp, f) unit Qvb, g) unit Qi, and h) xenoliths from Little Bear Mountain volcano 115

Figure 2.25 Rare earth element patterns normalized to values of the most Mg-rich Quaternary basalt in the Iskut area (SC-23; Hauksdóttir 1994) for: a) subunits $Qvap_{1-2}$, b) subunits $Qvap_{4-5}$, c) volcanic glass from Qvh and $Qvap_6$, d) subunit $Qvap_6$, e) unit Qvpp, f) unit Qvb, g) unit Qi, and h) xenoliths from Little Bear Mountain volcano 116

Figure 2.26 Epsilon Nd versus measured $^{87}Sr/^{86}Sr$ for: a) samples from the HMVC and the Stikine Terrane (ST - after Sampson et al. 1989), and b) Quaternary volcanic rocks from the Northern Cordilleran Volcanic Province.....120

Figure 2.27 Element ratio plots for samples from: a) Kilauea, Hawaii, b) Lava Fork, and c) Little Bear Mountain.....133

Figure 2.28 Total alkalies ($Na_2O + K_2O$ in wt. %) versus SiO_2 (wt. %) diagram for samples from Little Bear Mountain (open circles) and Hoodoo Mountain (filled squares). 135

Figure 3.1 Experimental data from Donaldson (1985) for olivine ($FO_{88.5}$) at 1250°C plotted as time (seconds) versus change in radius (mm) 148

Figure 3.2 Mensuration formulas and volume derivatives for geometries of samples used in experiments.....150

Figure 3.3 Normalized experimentally-measured values of *v* (oxygen equivalent moles [o.e.m.] $cm^{-2}s^{-1}$) for olivine are plotted as in v versus 1000/T(K) 161

Figure 3.4 Diagram summarizing in *v* (measured) versus 1000 T/(K) relationships for a variety of minerals 163

Figure 3.5 Time (years) versus T (°C) for complete dissolution of 1 cm diameterspheres of olivine ($Fo_{88.5}$ and $Fo_{91.5}$), plagioclase ($An_{52.5}$ and $An_{29.5}$),and quartz in a basaltic melt of constant composition at $P=10^5$Pa 166

Figure 3.6 Summary of relationships leading to predictive models for mineral dissolution in silicate melts illustrated with the 10^5 Pa experiments of Donaldson (1985) 169

Figure 4.1 Six model simulations are represented as F (fraction of system crystallized) versus magmatic T (°C) 180

Figure 4.2 Ternary feldspar diagram showing distribution of model feldspar compositions derived from six model simulations (lines with arrows) 185

Figure 4.3 Model feldspar compositions plotted against T (°C) 186

Figure 4.4 Model pyroxene compositions plotted against T (°C) 190

Figure 4.5 Diagram of *v* (oxygen equivalent moles cm^2 s^{-1}) versus **A** (J * number of oxygen atoms $mole^{-1}$ of mineral) for Qtz, Pl, and Ol..195

Figure 5.1 Flow diagram for the fractional crystallization (FC) algorithm.....207

Figure 5.2 T(° C) versus predicted values of a) X_{an} and b) X_{fo} for a liquid of composition SH-44. Predicted values are from **Petros** (bold) and MELTS (light). 211

Figure 5.3 SiO_2 (wt. %) versus predicted values of a) T, b) TiO_2 (wt. %), c) FeO (wt. %), d) MgO (wt. %), e) K_2O (wt. %), f) Al_2O_3(wt. %), g) CaO (wt. %) and h) Na_2O (wt. %) for a liquid of composition SH-44. 212

Figure 5.4 T(° C) versus a) X_{Fo} and b) X_{An} for a liquid of composition SC-23.

Predicted values are from **Petros** (bold) and MELTS (light). 215

Figure 5.5 SiO_2 (wt. %) versus predicted values of a) T (° C), b) TiO_2 (wt. %), c) FeO (wt. %), d) MgO (wt. %), e) K_2O (wt. %), f) Al_2O_3(wt. %), g) CaO (wt. %) and h) Na_2O (wt. %) for a liquid of composition SC-23. Predicted values are from **Petros** (bold) and MELTS (light). 216

Figure 5.6. Algorithm for kinetically-driven AFC model 224

Figure 5.7 T(° C) versus a) X_{Fo} and b) X_{an} for a liquid of composition SC-23. Predicted values are from **Petros-AFC** (bold) and Petros (light). Pressure is equal to 10^{-4} GPa. 227

Figure 5.8 SiO_2 (wt. %) versus a) T (° C), b) TiO_2 (wt. %), c) FeO (wt. %), d) MgO (wt. %), e K_2O (wt. %), f) Al_2O_3(wt. %), g) CaO (wt. %) and h) Na_2O (wt. %) for a liquid of composition SC-23. Predicted values are from **Petros-AFC** (bold) and **Petros** (light). Pressure is equal to 10^{-4} GPa. 229

Figure 5.9 Time (hours) versus a) F (moles of melt), b) T (° C), and c) cooling rate (° C s^{-1}) for a liquid of composition SC-23. Predicted values are from **Petros-AFC** for scenario AFC1 (Table 5.7). Pressure is equal to 10^{-4} GPa.. 231

Figure 5.10 Time (hours) versus a) r (moles assimilated divided by moles crystallized), b) cumulative moles crystallized, and c) crystallization rates (moles s^{-1}) for a liquid of composition SC-23. Predicted values are from **Petros- AFC** for scenario AFC1 (Table 5.7). Pressure is equal to 10^{-4} GPa....232

Figure 5.11 Effects of P on AFC simulations for a liquid of composition SC-23: a) X_{An} versus T (° C), b) SiO_2 (wt. %) versus Al_2O_3 (wt. %), and c) SiO_2 (wt. %) versus MgO (wt. %). Predicted values are from **Petros-AFC** for P=10^{-4} GPa (bold), P=0.1 GPa (light), and P=0.3 (dashed). 237

Figure 5.12 Time (hours) versus a) F (moles of melt), b) T (° C), and c) cooling rate (° C s^{-1}). Predicted values are from **Petros-AFC** for a liquid of composition SC-23 and P=10^{-4} GPa (bold), P=0.1 GPa (light), and P=0.3 GPa (dashed). Open circles denote total moles crystallized (0.05 increments). 239

Figure 5.13 Time (hours) versus a) cumulative moles of Ol crystallized, b) cumulative moles of Pl crystallized, and c) total moles crystallized (Ol + Pl). Predicted values are from **Petros-AFC** for a liquid of composition SC-23 and P=10^{-4} GPa (bold), P=0.1 GPa (light), and P=0.3 GPa (dashed).....240

Figure 5.14 Time (hours) versus a) r (moles assimilated divided by moles crystallized), b) Ol crystallization rates (moles s^{-1}), and c) Ol crystallization rates (moles s^{-1}). Predicted values are from **Petros-AFC** for a liquid of composition SC-23 and P=10^{-4} GPa (bold), P=0.1 GPa (light), and P=0.5 GPa (dashed).....241

Figure 5.15 Effects of T_a on AFC simulations: a) X_{An} versus T (° C), b) SiO_2 (wt. %) versus Al_2O_3 (wt. %), and c) SiO_2 (wt. %) versus MgO (wt. %). Predicted values are from **Petros-AFC** for a liquid of composition SC-23 and T_a = 500 ° C (bold), T_a = 200 ° C (light), and T_a = 800 ° C (dashed).....243

Figure 5.16 Time (hours) versus a) F (moles of melt), b) T (° C), and c) cooling rate (° C s^{-1}). Predicted values are from **Petros-AFC** for a liquid of composition SC-23 and T_a = 500 ° C (bold), T_a = 200 ° C (light), and T_a = 800 ° C (dashed).....245

Figure 5.17 Time (hours) versus a) cumulative moles of Ol crystallized, b) cumulative moles of Pl crystallized, and .....c) total moles crystallized(Ol + Pl). Predicted values are from **Petros-AFC** for a liquid of composition SC-23 and T_a = 500 ° C (bold), T_a = 200 ° C (light), and T_a = 800 ° C (dashed). 246

Figure 5.18 Time (hours) versus a) r (moles assimilated divided by moles crystallized), b) Ol crystallization rates (moles s^{-1}), and c) Pl crystallization rates (moles s^{-1}). Predicted values are from **Petros-AFC** for a liquid of composition SC-23 and T_a = 500 ° C (bold), T_a = 200° C (light), and T_a = 800 ° C (dashed).. 248

Figure 5.19 T(° C) versus X_{Fo} for a liquid of composition SC-23 and three different xenolith compositions: a) $An_{25}Ab_{67}San_8$ (AFC1 - bold line), b) $An_{93}Ab_7San_{0.04}$ (AFC4 - light line), and c) $An_7Ab_{55}San_{38}$ (AFC5 – bold dashes). Predicted values are from **Petros-AFC** and **Petros** (light dashes). Pressure is equal to 10^5 Pa.....250

Figure 5.20 T(^{o} C) versus X_{An} for a liquid of composition SC-23 and three different xenolith compositions: a) $An_{25}Ab_{67}San_{8}$ (AFC1 - bold line), b) $An_{93}Ab_{7}San_{0.04}$ (AFC4 - light line), and c) $An_{7}Ab_{55}San_{38}$ (AFC5 – bold dashes). Predicted values are from **Petros-AFC** and **Petros** (light dashes). Pressure is equal to 10^{5} Pa.. 252

Figure 5.21 SiO_2 (wt. %) versus a) T (^{o} C), b) TiO_2 (wt. %), c) FeO (wt. %), d) MgO (wt. %), e) K_2O (wt. %), f) Al_2O_3(wt. %), g) CaO (wt. %) and h) Na_2O (wt. %). Results are from **Petros-AFC** for a liquid of composition SC-23 and three different xenolith compositions: $An_{25}Ab_{67}San_{8}$ (bold line), $An_{93}Ab_{7}San_{0.04}$ (light line), and $An_{7}Ab_{55}San_{38}$ (bold dashs). Predicted values from **Petros** (light dashs) are included for comparison. Pressure is equal to 10^{-4} GPa.....253

Figure 5.22 Time (hours) versus T (^{o} C) for three different xenolith compositions: a) $An_{25}Ab_{67}San_{8}$ (AFC1 - bold line), b) $An_{93}Ab_{7}San_{0.04}$ (AFC4 - light line), and c) $An_{7}Ab_{55}San_{38}$ (AFC5 - bold dashes). Labelled lines predicted values of T_{sat} for Ol, Pl, Cpx, and Opx using a liquid of composition SC-23. Pressure is equal to 10^{5} Pa. 256

Figure 5.23 Time (hours) versus a) F (moles of melt), b) T (^{o} C), and c) cooling rate (^{o} C s^{-1}). Plots show results from **Petros-AFC** for a liquid of composition SC-23 and three different xenolith compositions: $An_{25}Ab_{67}San_{8}$ (bold), $An_{93}Ab_{7}San_{0.04}$ (light), and $An_{7}Ab_{55}San_{38}$ (bold dashs). Pressure is equal to 10^{5} Pa. 257

Figure 5.24 Time (hours) versus a) cumulative moles of Ol crystallized, b) cumulative moles of Pl crystallized, and c) total moles crystallized (Ol + Pl). Plots show results from **Petros-AFC** for a liquid of composition SC-23 and three different xenolith compositions: $An_{25}Ab_{67}San_{8}$ (bold), $An_{93}Ab_{7}San_{0.04}$ (light), and $An_{7}Ab_{55}San_{38}$ (bold dashs).....259

Figure 5.25 Time (seconds) versus a) r (moles assimilated divided by moles crystallized), b) Ol crystallization rate (moles s^{-1}), and c) Pl crystallization rate (moles s^{-1}). Plots show results from **Petros-AFC** for a liquid of composition SC-23 and three different xenolith compositions: $An_{25}Ab_{67}San_{8}$ (bold), $An_{93}Ab_{7}San_{0.04}$ (light), and $An_{7}Ab_{55}San_{38}$ (bold dashs). Pressure is equal to 10^{5} Pa.....261

Figure 5.26 AFM (A = Na_2O + K_2O, F = FeO, M = MgO) diagram for AFC

scenarios 1 to 7 (labelled lines). Data for Cinder Mountain (squares), the other Iskut-Unuk centres (diamonds), the HMVC (filled circles), and SC-23 are shown for comparison.....266

Figure 5.27 Logarithm$_{10}$ of time (seconds) versus 1000/T(K) for scenarios AFC1-7 (dark grey box). Time-scales for a variety of igneous processes including pluton solidification, lava dome growth, experimental mineral dissolution rates, mafic lava flows, transport of kimberlitic and other mafic magmas, and volcanic eruptions are included for comparison. 268

List of Tables

Table 1.1 Summary of Neogene to Quaternary volcanic centres in the Northern Cordilleran Volcanic Province 8

Table 1.2 Summary of principle rock types in the Northern Cordilleran Volcanic Province 19

Table 1.3 Summary of xenolith-bearing magmatic centres in the Northern Cordilleran Volcanic Province 24

Table 2.1 Summary field descriptions of non-fragmental volcanic units at Hoodoo Mountain Volcano 48

Table 2.2 Summary field descriptions of fragmental volcanic units and non-volcanic units at Hoodoo Mountain Volcano 49

Table 2.3 Summary field descriptions of map units at Little Bear Mountain Volcano 64

Table 2.4 Summary of radiometric age constraints for volcanic rocks from the Hoodoo Mountain Volcano Complex (HMVC) 78

Table 2.5 Summary of petrography for non-fragmental volcanic rocks from the Hoodoo Mountain Volcano Complex (HMVC) 83

Table 2.6 Representative major, minor, trace, and rare earth element analyses for samples from the Hoodoo Mountain Volcanic Complex 94

Table 3.1a Detailed enthalpy budget for assimilation of alkali feldspar ($Or_{88}Ab_{12}$) in basaltic magma at P=0.5 GPa (data from Table 4 of Nicholls & Stout (1982), p. 336) 141

Table 3.1b Modal mineralogy (in mole %) of five rock types used to calculate apparent ΔH_{fus} (after Russell et al. 1995; mineral abbreviations after Kretz 1983) 141

Table 3.1.c Calculated apparent ΔH_{fus} (kJ mole $^{-1}$) for five rock types for several different ambient temperatures and a magmatic temperature of 1120°C (after Russell et al. 1995) 141

Table 3.2 Summary of Silicate mineral dissolution experiments using both natural and synthetic melts 145

Table 3.3 Composition of melts used in mineral dissolution experiments 146

Table 3.4 Summary of dissolution rates at 10^{-4} GPa extracted from experimental data of Donaldson (1985; 1990) 153

Table 3.5 Summary of dissolution rates extracted from experimental data of Brearley and Scarfe (1986) 155

Table 3.6 Summary of dissolution rates at 10^{-4} GPa extracted from experimental data of Thornber and Huebner (1985) 157

Table 3.7 Summary of dissolution rates extracted from experimental data of Zhang et al. (1989) 158

Table 3.8 Activation energies (kJ/oxygen equivalent moles) implied by fits to data shown in Figures 3.3 and 3.4 160

Table 4.1 Chemical and modal composition of alkali olivine basalt SH-44 from Lava Fork, northwestern British Columbia 176

Table 4.2 Summary of sequence of crystallization for each of the model scenarios 179

Table 4.3 Calculated values of **A** and *v* for minerals in granite at 1175°C and 10^{-4} GPa 197

Table 4.4 Model prediction of time required to incorporate granite by selective assimilation 197

Table 5.1 Variables required to define magma system containing three phases (silicate liquid, Ol, Pl) 203

Table 5.2 System of equations describing the equilibrium state of an Ol and Pl saturated melt 205

Table 5.3 Calculated chemical composition and saturation conditions of alkali olivine basalts SH-44 and SC-23, from northwestern British Columbia 209

Table 5.4 Comparison of results from Petros and MELTS for predicted liquid lines of descent for alkali olivine basalts SH-44 and SC-23 214

Table 5.5 Formulae for converting reaction rate (moles $cm^{-2}s^{-1}$) to moles for a spherical xenolith 219

Table 5.6 Enthalpy balance equation and first derivatives 222

Table 5.7 Summary of assimilation-fractional crystallization scenarios using SC-23 as the starting melt composition 226

Table 5.8 Summary of temperatures, cooling rates, crystallization rates, and r-values for AFC scenarios 262

Table A2.1 Sample information for samples analyzed for whole rock chemistry (including major, minor, and trace elements, and rare earth element), Sr and Nd isotopes and $^{40}Ar/^{39}Ar$ dating 310

Table A2.2 List of all major, minor, and trace element and rare earth element analyses for samples from Hoodoo Mountain volcano 311

Table A2.3 List of all major, minor, and trace element and rare earth element analyses for samples from Little Bear Mountain volcano 315

Table A2.4 Electron microprobe analyses for plagioclase from Little Bear Mountain (94BRE02) 316

Table A2.5 Isotopic data for samples from the Hoodoo Mountain Volcanic Complex 321

Acknowledgements

I gladly acknowledge B. Anderson, C. Ashe, C. Evenchick, D. Francis, T. Hamilton, C. Hickson, M. Mihalynuk, J. Mortensen, J. Nicholls, and D. Thorkelson for sharing their knowledge and views about the volcanism in the northern Cordillera and providing helpful information about locations and access to xenolith-bearing centres. The research presented in Chapter One has been mainly supported by University Graduate Fellowships (1994-96) and by NSERC LITHOPROBE through the 1995-1996 supporting geosciences grants program.

Financial and technical support for the research at Hoodoo Mountain was provided by the Geological Survey of Canada and by NSERC Research Grant OGP0820 to JKR. Digital cartography by Nicki Hastings made the geological map a reality. I especially acknowledge Bob Anderson for help and encourage in putting together the geological map of the HMVC and Kelly Russell for continuing to find ways to get me back to Hoodoo Mountain. I also thank Jim Nicholls and Super Twins for supporting the 1996 Hoodoo expedition, and Mati Raudsepp and Maya Kopylova for help with the EMP.

Financial support for the research presented in Chapter Three was funded in part by NSERC Research Grant OGP0820, an Industrial Partnership

Grant with Canamera Geological Ltd., and a University Graduate Fellowship from the University of British Columbia (to BRE). I am indebted to K.A. Felknor-Edwards for help with database editing and J. Nicholls, G. Dipple, and K.J. Kirkpatrick for helpful discussions on thermodynamic modeling, data normalization, and supplying unpublished data, respectively. Reviews by two anonymous reviewers, K. Arden and especially L. Stillings substantially improved the manuscript version of Chapter Three.

Financial support for the research presented in Chapter Four derives from a University Graduate Fellowship (UBC) to BRE, NSERC (OGP0820) to JKR, and NSERC LITHOPROBE grants to JKR. I thank G.M. Dipple, R.F. Martin, R. Mason, J. Nicholls, R. Nielsen and J.F.H. Thompson for critically reviewing the manuscript version of Chapter Four.

The thermodynamic modeling presented in Chapter Five would have been a much more difficult task without the help of discussions with Jim Nicholls.

I thank the Igneous Petrology crew for putting up with my domination of several computers at the same time and for creating a supporting atmosphere in the lab (Yao, Steina, Lori, Allison, Rob, Maya, Susannah). Finally, I thank Kelly, Teagan, and especially Kim for continuing to have confidence in me and for support in stressful times. May they never need to be so patient with me again!

Preface

The main purpose of this thesis is to develop new, quantitative insights into the process of magmatic assimilation. The thesis presents the first calculational model that combines kinetic and thermodynamic constraints on assimilation processes. The model is applied to volcanic rocks from the Northern Cordilleran Volcanic Province (NCVP), where the importance of magmatic assimilation is well documented.

The first chapter is an overview of the volcanology and petrology of the NCVP and it highlights the evidence for magmatic assimilation processes in many of the volcanic centres of the province. The second chapter describes the geology, stratigraphy, and petrology of the Hoodoo Mountain volcanic complex (HMVC), a previously unstudied, major volcanic centre in the NCVP. The detailed study of the HMCV demonstrates the style of magmatic assimilation. Furthermore, the field and petrographic observations from the HMVC and the NCVP provide data against which the subsequent models for magmatic assimilation are compared. The third chapter develops a model for predicting rates of mineral dissolution using the available experimental data and a pre-existing thermodynamic database for silicate melts and minerals (MELTS; Ghiorso & Sack 1995). The fourth chapter uses the MELTS model to investigate

equilibrium assimilation paths. Lastly, the fifth chapter develops an integrated kinetic and thermodynamic model for magmatic assimilation and applies the new calculational model to magmatic assimilation processes represented in the southern NCVP.

Specifically the thesis contributes to the study of magmatic assimilation in five ways:

1. assimilation is shown to be an important process throughout the Northern Cordilleran Volcanic Province,
2. assimilation is shown to be an important process in the development of the Hoodoo Mountain volcanic centre,
3. reaction rates governing assimilation are shown to be directly proportional to Affinity,
4. equilibrium assimilation paths are shown to affect mineral growth and zoning, and
5. the first time-dependent assimilation paths are calculated; these paths predict cooling and crystallization rates in magmas undergoing concomitant isenthalpic crystallization and assimilation.

Several sections of the thesis have been published as either extended abstracts, government reports, or in scientific journals. The following is a list of these publications for each of the thesis chapters:

Chapter 1:

Edwards, B.R., Hamilton, T.S., Nicholls, J., Stout, M.Z., Russell, J.K. and Simpson, K. 1996. Late Tertiary to Quaternary volcanism in the Atlin area, northwestern British Columbia; in *Current Research, Part A; Geological Survey of Canada, Paper 96-1A*, 29-36.

Edwards, B.R. and Russell, J.K. 1996. An overview of the nature, distribution and tectonic significance of xenoliths from the Stikine volcanic belt. in *Cook, F. and Erdmer, P. (compilers), Slave-Northern Cordillera Lithospheric Evolution (SNORCLE) Transect and Cordilleran Tectonics Workshop Meeting (March 1-3), University of Calgary, Lithoprobe Report No. 50*, 96-107.

Edwards, B.R., Kopylova, M.L., & Russell, J.K. 1997. Petrology of the Lithosphere beneath the Northern Cordillera. in *Cook, F. and Erdmer, P. (compilers), Slave-Northern Cordillera Lithospheric Evolution (SNORCLE) Transect and Cordilleran Tectonics Workshop Meeting (March 7-9), University of Calgary, Lithoprobe Report No. 56*, 129-142.

Edwards, B.R. & Russell, J.K. 1997. Definition of a New Volcanic Province in Northwestern Canada: The Northern Cordilleran Volcanic Province, *Geological Association of Canada-Mineralogical Association of Canada 1997 Annual Meeting Program with Abstracts, Ottawa, A44.*

Chapter 2:

Edwards, B.R., and Russell, J.K. 1994. Preliminary stratigraphy, petrography and melt compositions of volcanic rocks from Hoodoo Mountain, northwestern British Columbia, Canada. *GAC-MAC 1994 Annual Meeting Program with Abstracts, Waterloo*, A32.

Edwards, B.R., and Russell, J.K. 1994. Preliminary stratigraphy of Hoodoo Mountain volcanic centre, northwestern British Columbia; in *Current Research, Part A; Geological Survey of Canada, Paper 94-1A*, 69-76.

Edwards, B.R., Edwards, G. and Russell, J.K. 1995. Revised stratigraphy for the Hoodoo Mountain volcanic center, northwestern British Columbia; in *Current Research, Part A; Geological Survey of Canada, Paper 95-1A*, 105-115.

Edwards, B.R., Anderson, R.G. & Russell, J.K. 1996. Geology of the Quaternary Hoodoo Mountain Volcanic Complex and adjacent Paleozoic and Mesozoic basement rocks; parts of Hoodoo Mountain (NTS 104B/14) and Craig River (NTS 104B/11) map areas, northwestern British Columbia. *Geological Survey of Canada, Open File 3321.*

Edwards, B.R., Anderson, R.G. & Russell, J.K. 1997. Geology and Stratigraphy of the Hoodoo Mountain Volcanic Complex, Northwestern British Columbia, *Geological Association of Canada-Mineralogical Association of Canada 1997 Annual Meeting Program with Abstracts, Ottawa, A44.*

Chapter 3:

Edwards, B.R., and Russell, J.K. 1994. Compilation and evaluation of experimental dissolution rates of silicate minerals in natural melts with comparison to thermodynamic models. *EOS Transactions of the American Geophysical Union*, 704-705.

Russell, J.K., **Edwards, B.R.** and Snyder, L.D. 1995. Volatile production possibilities during magmatic assimilation: heat and mass-balance

constraints. in *Magmas, Fluids, and Ore Deposits, J.F.H. Thompson (ed.), Mineralogical Association of Canada Short Course Volume 23*, 1-24.

Edwards, B.R., and Russell, J.K. 1995. Summary of silicate mineral dissolution rates in silicate melts and implications of chemical affinity for reaction rates. *American Chemical Society Spring Meeting 1995, Anaheim, Ca*, 82.

Edwards, B.R. and Russell, J.K. 1996. A review and analysis of silicate mineral dissolution experiments in natural silicate melts. *Chemical Geology*, **130**, 233-245.

Chapter 4:

Edwards, B.R., and Russell, J.K. 1995. Implications of assimilation for mineral growth and zoning. *Geological Association of Canada-Mineralogical Association of Canada 1995 Annual Meeting Program with Abstracts, Victoria*, A28.

Edwards, B.R. and Russell, J.K. 1996. Implications of assimilation for mineral growth and zoning. *Canadian Mineralogist*, **34**, 1149-1162.

Edwards, B.R., and Russell, J.K. 1996. A predictive model for mineral dissolution rates in mafic silicate melts: application to the dynamics of chemical zoning in plagioclase. *Geological Association of Canada-Mineralogical Association of Canada 1996 Annual Meeting Program with Abstracts, Winnipeg*, A25.

CHAPTER 1

The Northern Cordilleran Volcanic Province of British Columbia and the Yukon Territory, Canada

1.1. INTRODUCTION

This chapter presents an overview of the Northern Cordilleran Volcanic Province (NCVP), which is a group of Neogene to Quaternary volcanic rocks in northern British Columbia, the Yukon Territory, and Alaska (Edwards & Russell 1997). The chapter establishes a regional framework in support of the detailed volcanological research and petrological modeling presented in subsequent chapters. Chapter One has five ancillary goals:

- to define the boundaries of the Northern Cordillera Volcanic Province,
- to define the boundaries of Stikine subprovince of the NCVP,
- to summarize the volcanology, geochronometry, and petrology of the NCVP,
- to review previous petrogenetic studies of volcanic centres in the NCVP, and
- to review and highlight the role of magmatic assimilation in the NCVP.

1.2. DEFINITION OF THE NORTHERN CORDILLERA VOLCANIC PROVINCE

I propose to group all of the alkaline to peralkaline, Neogene to Recent volcanic centres in north-central B.C., the Yukon, and easternmost Alaska into the Northern Cordillera Volcanic Province (NCVP). As such, the NCVP encompasses a broad area, 1200 km long and up to 400 km wide (Figure 1.1). The southern margin of the NCVP is defined by isolated volcanic vents and eroded lava remnants of the Aiyansh volcanic field, in west-central British Columbia, near Terrace. The northernmost centres are erosional remnants of lava flows in the West Dawson volcanic field, 50 km west of Dawson City, Yukon Territory. The westernmost centre is Prindle Volcano, in east-central Alaska, and the easternmost centres are in the McConnell Creek area and include a volcanic neck called "the Thumb" (Nicholls & Stout 1996; Souther 1991e). As will be demonstrated below, all of the volcanic centres in the NCVP fit the classic definitions for a volcanic province by being spatially, temporally, and petrographically related (Tyrrell 1948; Turner & Verhoogen 1960; Carmichael et al. 1974).

Previous Terminology

Souther (1977a & b) first recognized similarities between a number of volcanic centres in the Northern Cordillera. He used the term "Stikine lavas" to refer to older plateaus of basalt at Heart Peaks, Level Mountain, Mount Edziza, and in the Maitland area (Souther 1977a) and the terms "Stikine Volcanic Belt"

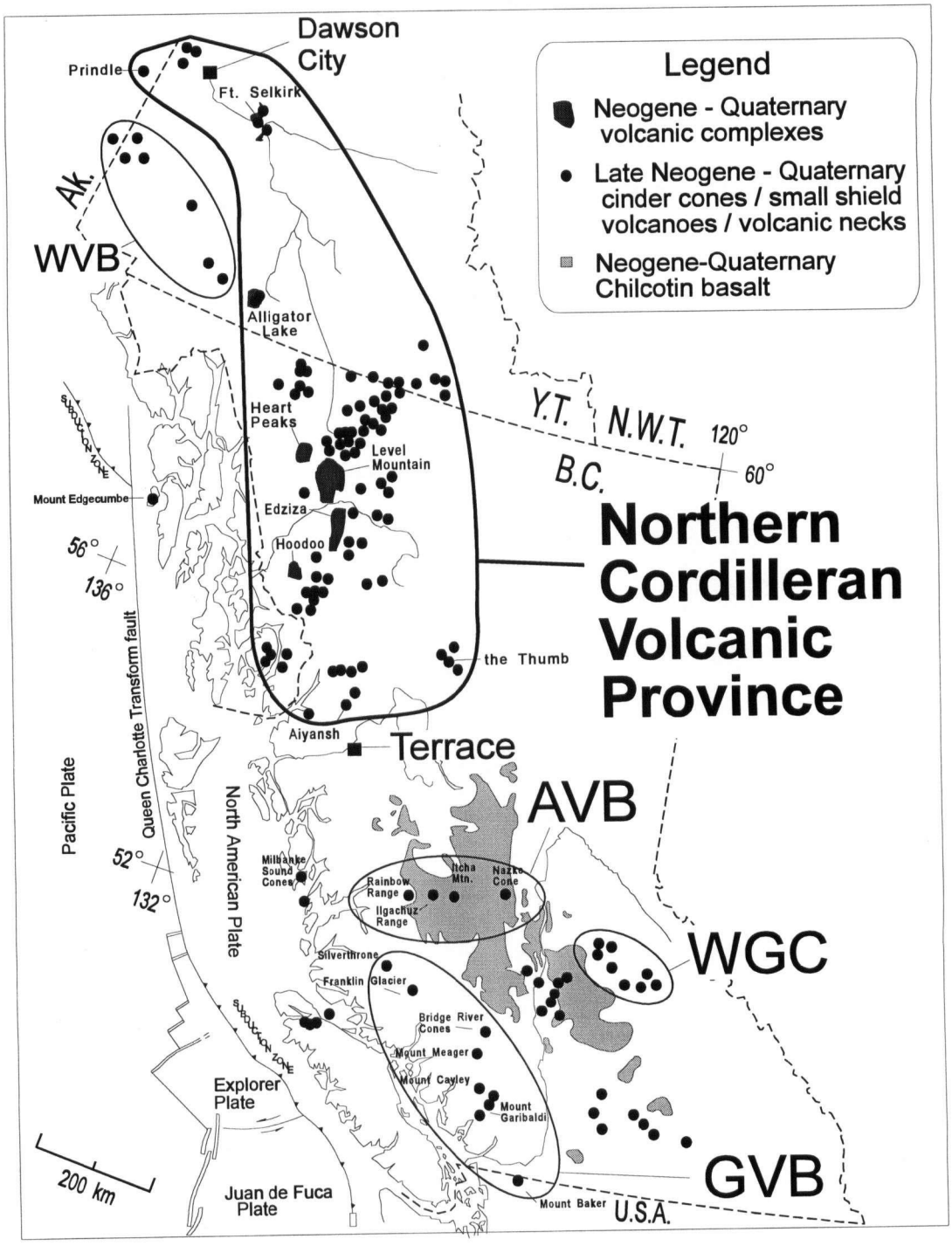

Figure 1.1. Neogene to Quaternary volcanism in the Northern Cordillera of British Columbia and the Yukon Territory (after Hickson 1991). Abbreviations for volcanic belts are: **WVB** - Wrangell volcanic belt, **AVB** - Anaheim volcanic belt, **WGC** - Wells Gray - Clearwater volcanic field, **GVB** - Garibaldi volcanic belt.

(SVB) or "Stikine Belt" (Souther 1977a & b) to refer to the Quaternary volcanic rocks in northern B.C. (Figure 1.2). Subsequent workers (Souther & Yorath 1991; Souther 1992) extended the boundaries of the SVB to include centres in the Atlin area, at Alligator Lake, and at Fort Selkirk. However, they also stated that "north of Mount Edziza the Stikine Belt is less clearly defined" (Souther & Yorath 1991, p. 391) and the extent and characteristics of the SVB remain poorly defined. Some workers extended the SVB from Level Mountain northeast to the Yukon border (Francis & Ludden 1995), whereas others also extended the boundaries of the SVB to the northwest to include Fort Selkirk in the central Yukon (Souther & Yorath 1991) (Figure 1.2).

The term "Stikine Volcanic Belt" has other disadvantages. Firstly, two other assemblages of rocks in the northern Cordillera share the Stikine designation: the Mesozoic Stikine Plutonic suite (Woodsworth et al. 1991) and the Paleozoic Stikine Assemblage (Monger 1977; Gunning 1996). Both of these stratigraphic assemblages are part of the Stikine tectonostratigraphic terrane (Woodsworth et al. 1991; Gunning 1996). However, the Neogene to Recent volcanic rocks that have previously been included in the SVB are not associated with either of those two stratigraphic packages nor are they confined to the Stikine Terrane (see Figure 1.6). Secondly, although three of the major volcanic centres, Level Mountain, Mount Edziza, and Hoodoo Mountain, are in the Stikine River region, the geographic distribution of related volcanism extends far

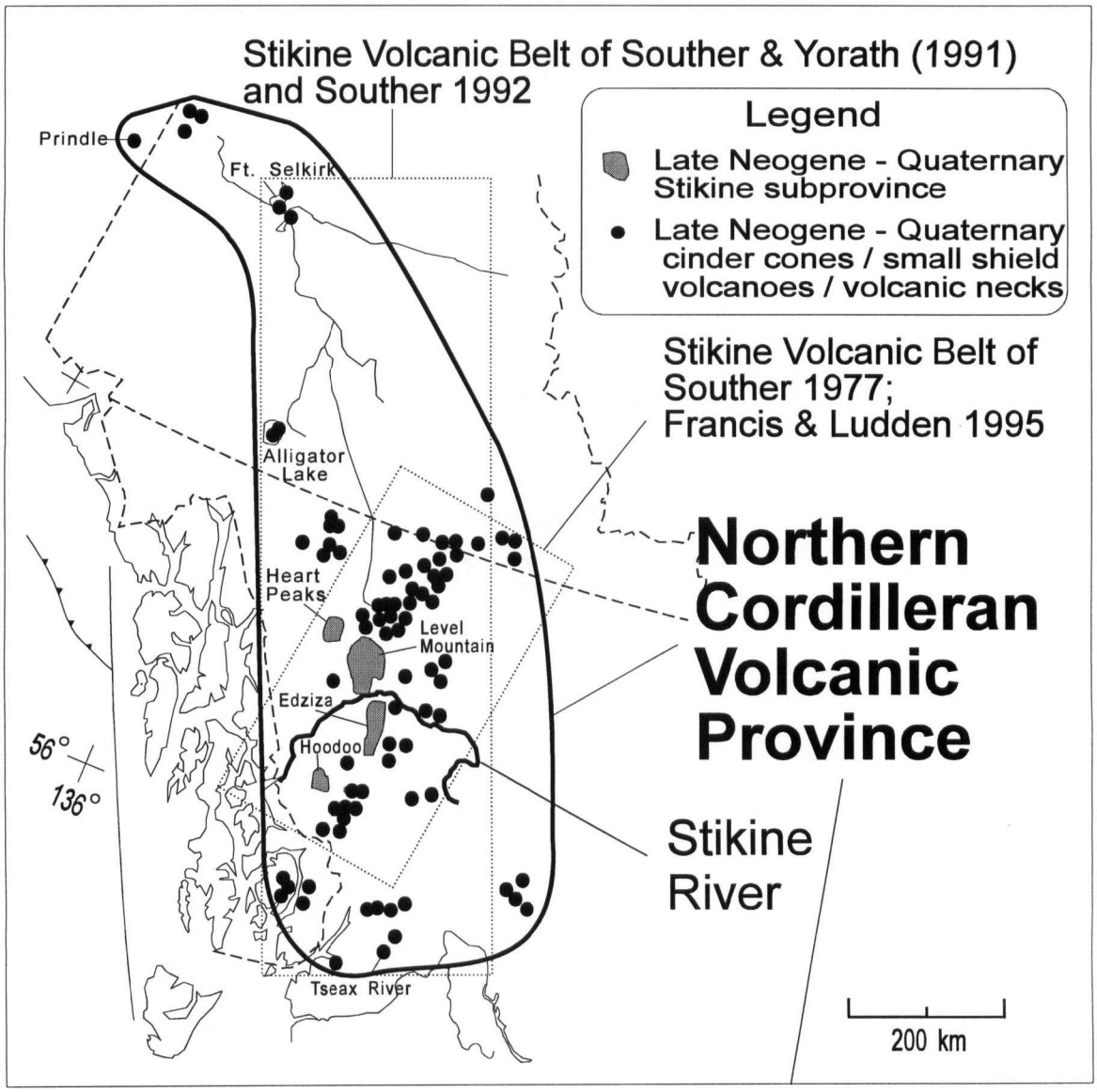

Figure 1.2. Previous definitions of the Stikine volcanic belt.

beyond the Stikine region. Finally, other volcanic belts in the Cordillera are well-defined, narrow, linear regions of volcanism (Figure 1.1) in contrast to the broad area previously referred to as the Stikine volcanic belt.

Stikine Subprovince

At least one volcanic subprovince is recognizable in the NCVP; it comprises Level Mountain, Heart Peaks, Mount Edziza, and Hoodoo Mountain. These centres formed the core of the original Stikine Volcanic Belt as defined by Souther (1977a & b). Recognition of the subprovince is based on three observations. Firstly, three of the four volcanic centres in the subprovince represent a unique style of magmatism within the NCVP and are volumetrically the largest in the NCVP (Heart Peaks, Level Mountain, Mount Edziza). Secondly, three of the four volcanic centres are the only centres within the NCVP that contain both mafic and intermediate to felsic volcanic rocks (Level Mountain, Mount Edziza, Hoodoo Mountain; see Table 1.2). All of the other centres in the NCVP comprise only mafic rocks. Thirdly, magmatism at two of the complexes (Level Mountain and Mt. Edziza) is much longer lived than for any of the other areas of volcanism in the NCVP; volcanism at Level Mountain spans 15 Ma (Hamilton 1981) and volcanism at Mt. Edziza spans 10 Ma (Souther & Yorath 1991; Souther 1992). Because all of the centres in this subprovince occur in the Stikine region, formed the core of the original Stikine Volcanic Belt, and formed

within the geological boundaries of the Stikine Terrane, I propose to name the subprovince the Stikine Subprovince.

1.3. VOLCANOLOGY

The volcanology of the NCVP is diverse, but three main types of volcanic centre dominate: i) areally-extensive, long-lived (> 5 Ma) volcanic plateaus with associated central domes and subvolcanic intrusions, ii) areally-restricted, polygenetic volcanic complexes, and iii) areally-restricted, monogenetic, short-lived stratovolcanoes, cinder cones, and isolated lava flows (Table 1.1). Volcanic deposits include lava flows, welded and non-welded pyroclastic deposits, hydroclastic deposits, and ice-contact volcanic deposits. The diversity of deposit types, in part, reflects the changes in eruption environments during the formation of the NCVP from dominantly subaerial to largely subglacial.

Broad plateaus of coalesced, basaltic shield volcanoes are the most voluminous volcanic deposits in the NCVP; however, they are only found in the central part of the province. They include Level Mountain, Mount Edziza, Heart Peaks, and volcanic deposits in the Maitland / Spatsizi area. At Level Mountain and Mount Edziza, the plateaus form a base for subsequent domes and flows of both mafic and felsic composition (Hamilton 1981; Souther 1992). Level Mountain is the largest of the volcanic plateaus and it comprises over 860 km^3 of flat-lying mafic lava flows, felsic lava flows, and felsic domes covering an

Table 1.1. Summary of locations, ages, volcanic features, and estimated volumes for Neogene to Quaternary volcanic centres within the Northern Cordilleran Volcanic Province.

Volcanic centre[1]	Location (Lat, Long)	Age[2]	Volcanic Feature	Estimated Volume (km^3)	References[3]
West Dawson volcanic field			5 isolated occurrences		
Prindle volcano	63.72 N, 141.62 W	3.57+/- 0.14 Ma, 6.26 +/- 0.15 Ma or younger(?)	cone and flow	~0.1	25, 69, 70, 76, 100
Sixty Mile	64.05 N, 140.74 W	17.2 +/- 0.3 Ma (Ar/Ar)	eroded conduit? / flow?	<<0.001(?)	68
Clinton Creek	64.40 N, 140.63 W	3.05 +/- 0.22 Ma	flow?	<<0.001(?)	67, 68
Forty Mile	64.38 N, 140.50 W	19.9 +/- 0.5 Ma (Ar/Ar)	flow? / neck?	<<0.001(?)	68
Moose Creek	64.16 N, 140.91 W	Tertiary / Quaternary (?)	boulders	<<0.001(?)	68
Fort Selkirk volcanic complex (Selkirk Group of Bostock (1936))			6 isolated occurrences		
Volcano Mountain	62.94 N, 137.32 W	Holocene (<0.0075 Ma)	cone and 3 flows	~0.04	7, 28, 30, 51, 53, 54, 90, 91
Wootton's Cone / Ne Ch'e Ddhäwa	62.74 N, 137.24 W	> 0.038 Ma	cone, flows; subglacial	~0.5	7, 30, 52, 55, 56, 68, 69
Fork Selkirk	62.78 N, 137.36 W	1.08 +/- 0.05 Ma	remnant cone, flows	(?)	7, 30, 55, 56, 71
Pelly Formation	62.8 N, 137.5 W	1.28 +/- 0.03 Ma, 1.6 to 0.89 Ma	valley-filling flows	~15	7, 30, 53
Wolverine Formation	62.7 N, 137.4 W	Pleistocene / Quaternary (?) 1.6 to 0.89 Ma	valley-filling flows	~23	7, 30
Whitehorse volcanic field (Miles Canyon Group of Wheeler (1961))			25 isolated occurrences		
Alligator Lake volcanic complex	60.42 N, 135.42 W	Quaternary / Holocene (?)	2 cones and 5 flow units	~0.5	9, 10, 19, 20-22, 27, 99
Ibex Mountain	60.51 N, 135.50 W	Tertiary / Quaternary (?) / glacially-modified	small cone		19, 99
Miles Canyon	60.6 N, 135.0 W	Tertiary / Quaternary (?)	remnants of lava flows	<1	19, 99

Table 1.1. (continued)

Watson Lake volcanic field (including Little Rancheria lava flows)	60.0 N, 129.0 W	4.3 +/- 0.3 Ma 0.765 +/- 0.049 Ma 0.604 +/- 0.039 Ma 0.545 +/- 0.046 Ma 0.232 +/- 0.021 Ma	4(?) isolated occurrences; flows & cones(?)	(?)	45, 58, 61
Atlin volcanic field			11 isolated occurrences		
Anderson / Moose Bay	59.30 N, 133.75 W	27.5 +/- 4.3 to 16.2 +/- 2 Ma	flows	<0.1 (?)	6, 8
Chikoida Mountain	59.20 N, 133.04 W	Tertiary / Quaternary (?)	4 eroded conduits	<0.001	17
Cracker Creek	59.70 N, 133.29 W	Late Quaternary	cone	0.003	1, 17
Hirschfeld Creek/Line Lake	59.53 N, 132.92 W	Tertiary / Quaternary (?)	neck	<0.1	1, 9, 31
Llangorse Mountain (north)	59.37 N, 132.78 W	Tertiary / Quaternary	neck / flow?	<0.1	1, 9, 17, 31, 74
(west)	59.32 N, 132.90 W	(?)	flow(?)	<0.001	
(south)	59.30 N, 132.78 W		flow(?)	<0.001	
Mount Sanford	59.42 N, 132.75 W	Tertiary / Quaternary (?)	5 intrusions / dykes(?)	<0.001	51
Ruby Mountain	59.70 N, 133.38 W	0.54 +/- 0.2 Ma	stratocone and flows	~1	1, 17, 59, 73, 75
Volcanic Creek	59.77 N, 133.40 W	Late Quaternary	cone(s) and flows	0.02	1, 17
Tuya-Teslin volcanic field			> 50 isolated occurrences		
Ash Mountain	59.28 N, 130.50 W	Pleistocene / Quaternary (?) (intraglacial)	flows, dykes, pillows, hyaloclastite; partly subglacial	3.2	2, 3, 33, 63, 65, 96, 97
Kawdy Mountain	58.87 N, 131.25 W	Pleistocene / Quaternary (?) (intraglacial)	cone?	~14	32, 50
Mathew's tuya	59.20 N, 130.43 W	Pleistocene / Quaternary (?) (intraglacial)	flows, hyaloclastite, pillows; subglacial; tuya	~1	3, 33, 65, 77
Metah Mountain / Isspah Butte	59.10 N, 131.32 W	Pleistocene / Quaternary (?) (intraglacial)	flows; subglacial	~5	3, 32, 50
Mount Josephine	59.08 N, 130.71 W	Pleistocene / Quaternary (?) (intraglacial)	flows?	~3	32, 50
South tuya	59.20 N, 130.50 W	Pleistocene / Quaternary (?) (intraglacial)	flows, dykes, pillows, hyaloclastite; subglacial	1.6	3, 65

Table 1.1. (continued)

Tanzilla butte	59.20 N, 130.43 W	Pleistocene / Quaternary (?) (intraglacial)	flows? / cone?	~3	32, 50
3 Caribou tuya	59.23 N, 130.57 W	Pleistocene / Quaternary (?) (intraglacial)	dykes, hyaloclastite; subglacial; tindar(?)	~0.5	3, 33, 65
Tuya Butte	59.13 N, 130.57 W	Pleistocene / Quaternary (?) (intraglacial)	flows, pillows, hyaloclastite; subglacial; tuya	2.6	2, 3, 33, 63, 65, 96
Heart Peaks volcanic complex	58.6 N, 131.9 W	Neogene to Recent(?)	valley-filling flows, minor palagonite tuff	<160	11, 12, 32, 87
Level Mountain volcanic complex	58.5 N, 131.3 W	14.9 Ma to Recent(?)	valley-filling flows, domes, cones, palagonite tuff	~860 (total)	32, 38-44, 87
Cry Lake volcanic field	58.3 N, 129.3 W	5.07 +/- 0.39 Ma, 0.73 +/- 0.03 Ma	24 isolated occurrences flows, breccia, tuff, cones(?)		4, 34, 35
Castle Rock volcanic field	57.8 N, 130.2 W	Pleistocene / Quaternary (?) (intraglacial)	6-7 isolated occurrences; eroded cones, fissures, pillow lavas		60, 75, 79
Mount Edziza volcanic complex				~665 (total)	
Raspberry Formation	57.5 N, 130.6 W	7.4 Ma	3 overlapping shield volcanoes	119	79, 80, 85, 86, 87, 88
Little Iskut Formation	57.5 N, 130.6 W	7.2 Ma	flows, dykes, subaerial / subaqueous deposits	14.6	79, 80, 85, 86, 87, 88
Armadillo Formation	57.5 N, 130.6 W	6.3 Ma	caldera, flows, domes, dykes, pyroclastic deposits	159 (50,109)	79, 80, 85, 86, 87, 88
Nido Formation	57.5 N, 130.6 W	4.4 Ma	7 vents, flows, dykes, necks, subvolcanic intrusions, subaqueous / subglacial deposits	127	79, 80, 85, 86, 87, 88
Spectrum Formation	57.5 N, 130.6 W	3.1 Ma	caldera(?), flows, subvolcanic intrusions, welded pyroclastic deposits	118	79, 80, 85, 86, 87, 88
Pyramid Formation	57.5 N, 130.6 W	1.1 Ma	3 vents, flows, domes, pyroclastic deposits	11.4	79, 80, 85, 86, 87, 88
Ice Peak Formation	57.5 N, 130.6 W	~1 Ma	flows, subglacial deposits, dykes, sills, subvolcanic intrusions, necks	76.7	79, 80, 85, 86, 87, 88

Table 1.1. (continued)

Pillow Ridge Formation	57.5 N, 130.6 W	0.9 Ma	2 remnant subglacial fissures (tindars)	2.9	79, 80, 85, 86, 87, 88
Edziza Formation	57.5 N, 130.6 W	0.9 Ma	caldera / crater, flows, domes, subvolcanic intrusions, pyroclastic deposits	18	79, 80, 85, 86, 87, 88
Arctic Lake Formation	57.5 N, 130.6 W	0.71 Ma	flows, subglacial deposits	2.0	79, 80, 85, 86, 87, 88
Klastline Formation	57.5 N, 130.6 W	0.62 Ma	3 vents, flows	5.4	79, 80, 85, 86, 87, 88
Kakiddi Formation	57.5 N, 130.6 W	0.3 Ma	flows, subglacial deposits, remnant subglacial fissure (tindar)	8.3	79, 80, 85, 86, 87, 88
Big Raven Formation	57.5 N, 130.6 W	0.002 Ma	> 30 isolated vents with flows, pillows, sideromelane breccia	1.7	79, 80, 85, 86, 87, 88
Maitland volcanic field			> 30 isolated occurrences		
Griffith Creek	57.5 N, 128.5 W	1.32 +/- 0.03 Ma	necks/plugs	<0.001	92, 93
Maitland Creek	57.4 N, 129.7 W	4-5 Ma	>14 necks and associated lava flows remnants	<0.	23, 24, 84
Tumeka Lake	57.2 N, 129.5 W	Tertiary / Quaternary (?)	vent(?)	<0.001	23, 24
Konigus Creek	57.0 N, 129.3 W	Tertiary / Quaternary (?)	vent(?)	<0.001	23, 24
Nass River	57.1 N, 129.0 W	Pleistocene / Quaternary (?) (intraglacial)	cone(?); pillows, hyaloclastite, subglacial	<0.1	23, 24
Iskut volcanic field			8 isolated occurrences		
Cinder Mountain	56.58 N, 130.63 W	0.033 +/- 0.0024 Ma	1 vent	<0.08	5, 13, 37, 46-48, 57, 83, 89
Cone Glacier	56.57 N, 130.67 W	Recent	2 vents with flows	<0.09	5, 13, 37, 46-48, 57, 83, 89
Iskut River	56.73 N, 130.62 W	0.07 +/- 0.03 Ma to 2555 +/- 60 y.b.p.	3 vents with flows	<8.6	5, 13, 37, 46-48, 57, 74, 83, 89
King Creek	56.48 N, 130.67 W	Recent	1 vent	<0.07	5, 13, 37, 46-48, 57, 83, 89
Lava Fork	56.42 N, 130.87 W	360 +/- 60 y.b.p. to ~150 y.b.p.	2 vents with flows	<0.22	5, 13, 37, 46-48, 57, 83, 89

Table 1.1. (continued)

Second Canyon	56.40 N, 130.71 W	Recent	2 vents with flows	<0.13	5, 13, 37, 46-48, 57, 83, 89
Snippaker Creek	56.63 N, 130.82 W	Recent	1vent (?) with flows	<0.15	5, 13, 37, 46-48, 57, 83, 89
Tom Mackay Creek	56.71 N, 130.55 W	Recent	1 vent with flow	<0.012	5, 13, 37, 46-48, 57, 83, 89
Hoodoo Mountain volcanic complex					
Hoodoo Mountain volcano	56.77 N, 131.29 W	0.11 to 0.02 Ma; 0.085 to 0.009 Ma (Ar/Ar)	stratovolcano; flows, domes, hyaloclastite, welded pyroclastic breccia, subglacial	17.3	5, 14-16, 18
Little Bear mountain volcano	56.82 N, 131.31 W	0.235 Ma (Ar/Ar)	eroded vent; pillows, hyaloclastite, dykes, subglacial	1.8	14-16, 18
Aiyansh volcanic field			14 isolated occurrences		
Bowser Basin	56.9 N, 129.3 W	1.6 Ma, Quaternary	4 isolated cones	(?)	37, 49
Widdzech Mountain	55.45 N, 129.33 W	Pleistocene/Quaternary (?)	7 isolated occurrences, flows, breccia	(?)	23, 37
Hoan Creek	55.34 N, 129.28 W	0.175 +/- 0.05 Ma	lava flow (?)	(?)	23, 64
Aiyansh/Tseax River	55.1 N, 128.9 W	250+/-130 y.b.p. 625+/-70 y.b.p.	2 cones and associated flows	(?)	37, 49, 73, 90, 91, 100
McConnell Creek volcanic field			10 isolated occurrences		
The Thumb	56.16 N, 126.70 W	Quaternary(?)	eroded neck, hyaloclastite	(?)	62, 73, 74

[1] - Volcanic field designations are informal designations
[2] - All radiometric ages are K-Ar unless otherwise noted
[3] - Key to numbered references is on the following page

Table 1.1. (continued)

Key to numbered references:

1- Aitken (1959)
2- Allen (1991)
3- Allen et al. (1982)
4- Anderson (GSC 92-16) in Hunt & Roddick (1992)
5- BC Hydro (1985)
6- Bloodgood & Bellefontaine (1990)
7- Bostock (1936)
8- Bultman (1979)
9- Carignan et al. (1994)
10- Carignan et al. (1995)
11- Casey (1980)
12- Casey & Scarfe (1980)
13- Cousens & Bevier (1995)
14- Edwards & Russell (1994a)
15- Edwards & Russell (1994b)
16- Edwards et al. (1995)
17- Edwards et al. (1996)
18- Edwards et al. (1997)
19- Eiché (1986)
20- Eiché et al. (1985a)
21- Eiché et al. (1985b)
22- Eiché et al. (1987)
23- Evenchick (per. comm., 1995)
24- Evenchick & Thorkelson (1993)
25- Foster et al. (1966)
26- Francis et al. (1996)
27- Francis (1987)
28- Francis (1991a)
29- Francis (1991b)
30- Francis & Ludden (1990)
31- Francis & Ludden (1995)
32- Gabrielse (1968)
33- Gabrielse (1969)
34- Gabrielse (1978)
35- Gabrielse (GSC 92-24) in Hunt & Roddick (1992)
36- Gabrielse & Tipper (1984)
37- Grove (1986)
38- Hamilton (1981)
39- Hamilton (1991)
40- Hamilton & Evans (1983)
41- Hamilton & Muehlenbachs (1977)
42- Hamilton & Scarfe (1976)
43- Hamilton & Scarfe (1977)
44- Hamilton et al. (1978)
45- Hasik et al. (1993)
46- Hauksdóttir (1994)
47- Hauksdóttir et al. (1994)
48- Hauksdóttir & Russell (1994)
49- Hickson (1991)
50- Hickson (per. comm., 1995)
51- Higgins & Allen (1984)
52- Jackson (1989)
53- Jackson (GSC 92-43) in Hunt & Roddick 1992
54- Jackson & Stevens (1992)
55- Jackson et al. (1990)
56- Jackson et al. (1996)
57- Kerr (1948)
58- Klassen (1987)
59- Levson (1992)
60- Littlejohn & Greenwood (1974)
61- Lord (1944)
62- Lord (1948)
63- Mathews (1947)
64- V. McNicoll (unpublished, 1997)
65- Moore et al. (1995)
66- Mortensen (GSC 92-29) in Hunt & Roddick (1992)
67- Mortensen (GSC 92-50) in Hunt & Roddick (1992)
68- Mortensen & Roddick (1989)
69- Mortensen & Wirth (GSC 92-97) in Hunt & Roddick (1992)
70- Mortensen & Wirth (GSC 92-98) in Hunt & Roddick (1992)
71- Naeser et al. (1982)
72- Nelson (GSC 92-25) in Hunt & Roddick (1992)
73- Nicholls & Stout (1996)
74- Nicholls & Stout (1997)
75- Nicholls et al. (1982)
76- Prescott (1983)
77- Ross (1983)
78- Simpson (1996)
79- Sinclair et al. (1978)
80- Souther (1972)
81- Souther (1991a)
82- Souther (1991b)
83- Souther (1991c)
84- Souther (1991d)
85- Souther (1991e)
86- Souther (1992)
87- Souther & Hickson (1984)
88- Souther & Yorath (1991)
89- Souther et al. (1984)
90- Stasiuk & Russell (1989)
91- Sutherland Brown (1969)
92- Symons (1975)
93- Thorkelson (GSC 92-23) in Hunt & Roddick (1992)
94- Thorkelson (1992)
95- Trupia (1992)
96- Trupia & Nicholls (1996)
97- Watson & Mathews (1944)
98- Watson & Mathews (1948)
99- Wheeler (1961)
100-Wirth (1991)
101-Wuorinen (1978)

area of ~1800 km^2 (Hamilton 1981). The Mount Edziza Volcanic Complex is the second largest centre in the NCVP and it is one of the best studied volcanic complexes in the NCVP. It comprises five "magmatic cycles" with large variations in eruption style and lava compositions within each cycle (Souther 1992). The total volume of volcanic rocks erupted at Mount Edziza is estimated to be 665 km^3 and the total surface area covered is ~1000 km^2 (Souther 1992). Heart Peaks is the third largest centre in the NCVP and is immediately west of Level Mountain. It comprises solely mafic lava flows whose composite thickness ranges up to 430 m and covers an area of ~275 km^2 (Souther & Yorath 1991). The other large shield volcano is in the Maitland area, 50 km east of Mount Edziza (Figure 1.1). The Maitland shield volcano is estimated to have originally covered over 900 km^2 but comprises only scattered remnants of flat lying lava flows and a cluster of volcanic necks (Souther 1991e).

The Fort Selkirk, Alligator Lake, and Hoodoo Mountain volcanic complexes are intermediate in size between the larger centres and the smaller, monogenetic centres. Fort Selkirk, in the north-central Yukon Territory, comprises two sequences of valley-filling basaltic lava flows (Pelly River and Wolverine Formations, Francis & Ludden 1990) and three basaltic to nephelinitic volcanic centres (Fort Selkirk, Ne Ché Dhawa / Wooten's Cone, Volcano Mountain; Jackson 1989; Francis & Ludden 1990; Trupia & Nicholls 1995). The Alligator Lake volcanic complex, in the south-central Yukon Territory,

comprises remnants of 5 different sequences of basaltic lava flows and two younger cinder cones (Eiché et al. 1987). The Hoodoo Mountain volcanic complex, in west-central British Columbia, comprises a small basaltic volcano and an overlapping, larger phonolitic / trachytic volcano. Although the complex is similar in size to Fort Selkirk and Alligator Lake, it is also petrologically similar to Level Mountain and Mount Edziza because it is the only other centre in the NCVP that comprises both basaltic and trachytic volcanic rocks.

Smaller, valley-filling lava flows and cinder cones are numerous and have been identified by regional scale geologic mapping throughout the NCVP (e.g., Gabrielse & Souther 1962; Gabrielse 1968; Evenchick & Thorkelson 1993). Locally the lava flows issued from small cinder cones which are still preserved (e.g., Aiyansh - Sutherland Brown 1969; Iskut River - Hauksdóttir 1994; Prindle volcano- Foster 1991). However, in the northern half of the NCVP many of the lava flows have been heavily eroded and commonly their associated vents are unknown (e.g., West Dawson - Mortensen & Roddick 1989).

Volumetrically minor subvolcanic intrusions have been exposed in areas of extensive erosion. Volcanic necks or plugs are documented in the Atlin and the Maitland volcanic fields, and at Mount Edziza, Level Mountain, Hoodoo Mountain, Castle Rock, and the Thumb (Francis & Ludden 1995; Souther 1992; Hamilton 1981; Edwards et al. 1995, 1996; Prescott 1982; Souther 1971, 1991f;

Lord 1948). Many of the isolated necks in the Atlin and Maitland areas are olivine nephelinite or basanite in composition (e.g., Francis & Ludden 1995; Thorkelson 1992). Small granitic and gabbroic plugs that are spatially and temporally associated with volcanic deposits are described from both Mount Edziza and Level Mountain (Souther 1992; Hamilton 1981).

The NCVP also has abundant deposits of subglacial and/or subaqueous volcanic debris (Table 1.1 and references therein); probably the NCVP is second only to Iceland and possibly Antarctica in its numbers of documented subglacial volcanic deposits. The type locality for "tuyas" (flat-topped volcanoes interpreted as the products of subglacial eruptions) is the Tuya-Teslin volcanic field, in the central part of the NCVP (Mathews 1947). The abundance of subglacial volcanic deposits results from the fact that the region was glaciated several times during the late Pliocene and Quaternary (Clague 1991).

1.4. GEOCHRONOMETRY

Volcanism in the NCVP ranges in age from Neogene to Quaternary (20 Ma to approximately 150 y.b.p.; Table 1.1). Early Neogene-age alkali-olivine basalt (> 15 Ma) is found mainly in the northern NCVP including at West Dawson and Atlin (Mortensen & Roddick 1989; Bultman 1979). Mid Neogene-age volcanic deposits (15 to 5 Ma) are found along the length of the NCVP and

include deposits at Mount Edziza (Raspberry Formation), Maitland, Level Mountain, Heart Peaks, Atlin Lake, and West Dawson (Table 1.1; Souther 1991, 1992; Hamilton 1981; Bultman 1979; Mortensen and Roddick 1989). The three largest volcanic centres in the NCVP (Heart Peaks, Level Mountain and Mount Edziza) have extended magmatic histories; these centres were intermittently active from the late Neogene to the Quaternary (Casey 1980; Hamilton 1981; Souther 1992; Souther & Yorath 1991). The next three largest volcanic centres (Fort Selkirk, Alligator Lake, Hoodoo Mountain) all are Quaternary in age (Francis & Ludden 1990; Trupia & Nicholls 1996; Eiché et al. 1987; Souther & Yorath 1991; Chapter 2). Smaller, and presumably shorter-lived volcanic centres, are distributed throughout the length of the NCVP and are predominantly Quaternary in age (Table 1.1). Many of these isolated volcanic centres occur in the central part of the NCVP and are indirectly dated as Pliocene / Pleistocene based on the presence of subglacial and/or intraglacial deposits (Table 1.1; Watson & Mathews 1944; Moore et al. 1995; C. Hickson, per. comm., 1995). Recent eruptions (< 5000 y.b.p.) have been reported from at least four different areas, including the youngest flows from Volcano Mountain (Trupia & Nicholls 1995), the Lava Fork volcanic centre (360+/-60 to 130 y.b.p., Elliott et al. 1981; BC Hydro 1985; Grove 1986), the Aiyansh volcanic field (250 +/- 130 y.b.p. and 625 +/- 70 y.b.p.; Sutherland Brown 1969; Symons 1975;

Wuorinen 1976) and a possible occurrence south of Atlin, B.C. (< 100 y.b.p.; Anonymous 1899).

1.5. PETROLOGY

The petrology of the Northern Cordilleran Volcanic Province has three important components: i) alkaline to mildly alkaline mafic rocks, ii) peralkaline Si-saturated and Si-undersaturated rocks, and iii) ultramafic to felsic xenoliths and magmatic inclusions.

Volcanic Rocks

The NCVP comprises predominantly alkaline volcanic rocks (Table 1.2; Figure 1.3). Alkali olivine basalt and hawaiite occur throughout the length of the NCVP and are volumetrically the most abundant rock types. Both basanite and olivine nephelinite are less common, and are most abundant in the northern half of the NCVP, from Atlin to the West Dawson area. However, isolated occurrences of both nephelinite and basanite occur throughout the NCVP. Locally tristanite, mugearite, picritic basalt, and ankaramite have also been reported (Hamilton 1981; Souther 1992). More evolved rock types such as phonolite, trachyte, and comendite, are limited in distribution to the southern half of the NCVP and are only associated with the large volcanic centres (e.g., Level Mountain - Hamilton, 1981; Mount Edziza - Souther, 1992; Hoodoo Mountain - Edwards & Russell, 1994b, Chapter 2). At Mount Edziza, comendite

Table 1.2. Summary of principle rock types within the Northern Cordilleran Volcanic Province.

Reported rock type	Occurrence	Phenocryst Phases[1,2]	Groundmass Phases	References[6]
Ankaramite	Level Mountain, Mt. Edziza	Ol ± Pl	Ti-Aug ± Pl ± Ti-Mag ± glass	38, 86
Olivine nephelinite	Volcano Mountain, Fort Selkirk, Mount Llangorse, Hirschfeld Creek, Griffiths Creek	Ol ± Ti-Di	Ol ± Ti-Di ± Usp-Mag ± Ne ± Na-Lct ± Lct ± glass ± Cc	29, 30, 31, 51, 94-96
Basanite	West Dawson, Fort Selkirk, Alligator Lake, Hirschfeld Creek, Ruby Mountain	Ol ± Cpx	Ol ± Cpx ± Pl ± Usp ± A-Fsp ± Lct(?)	19, 22, 25, 30, 31, 73, 75, 100
Alkali olivine basalt	Fort Selkirk, Alligator Lake, Heart Peaks, Level Mountain, Mount Edziza, Tuya-Teslin, Hoodoo, Iskut-Unuk rivers, Ayansh	Ol ± Pl ± Cpx	Ti-Aug ± Pl ± Mag ± A-Fsp ± glass	7, 11, 14, 18, 19, 22, 30, 31, 38, 46, 65, 73, 78, 86, 87, 91
Hy- to Qtz-norm basalt	Fort Selkirk, Alligator Lake, Level Mountain, Hirschfeld Creek, Ash Mountain, South Tuya, Tuya Buttes	Ol ± Pl ± Cpx	Ti-Aug ± Pl ± Mag ± A-Fsp ± glass	19, 30, 31, 38, 60, 65
Hawaiite	Level Mountain, Mount Edziza, Cinder Mountain	Ol ± Pl ± Cpx	Ti-Aug ± Pl ± Mag ± A-Fsp ± glass	38, 46, 86, 87
Phonolite/trachyte	Level Mountain, Mount Edziza, Hoodoo	A-Fsp[3] (Sa & Acl[4]) ± Fe-Hd ± Agt ± Mag ± Arf ± Aen[5]	A-Fsp ± Mag ± Arf ± Aen ± Ne ± Rt ± glass	14, 18, 38, 86,
Tristanite	Level Mountain, Mount Edziza	Agt ± Pl	Agt ± Pl ± Sa ± Mag	38, 86,
Comendite/pantellerite	Level Mountain, Mount Edziza	Agt ± A-Fsp ± Aen	Agt ± A-Fsp ± Aen ± Qtz ± Mag ± glass	38, 86,

[1] mineral abbreviations after Kretz (1983) where available
[2] includes microphenocrysts where identified
[3] alkali feldspar
[4] anorthoclase
[5] aenigmatite
[6] see Table 1 for reference numbers; note that only references with petrographic data are included

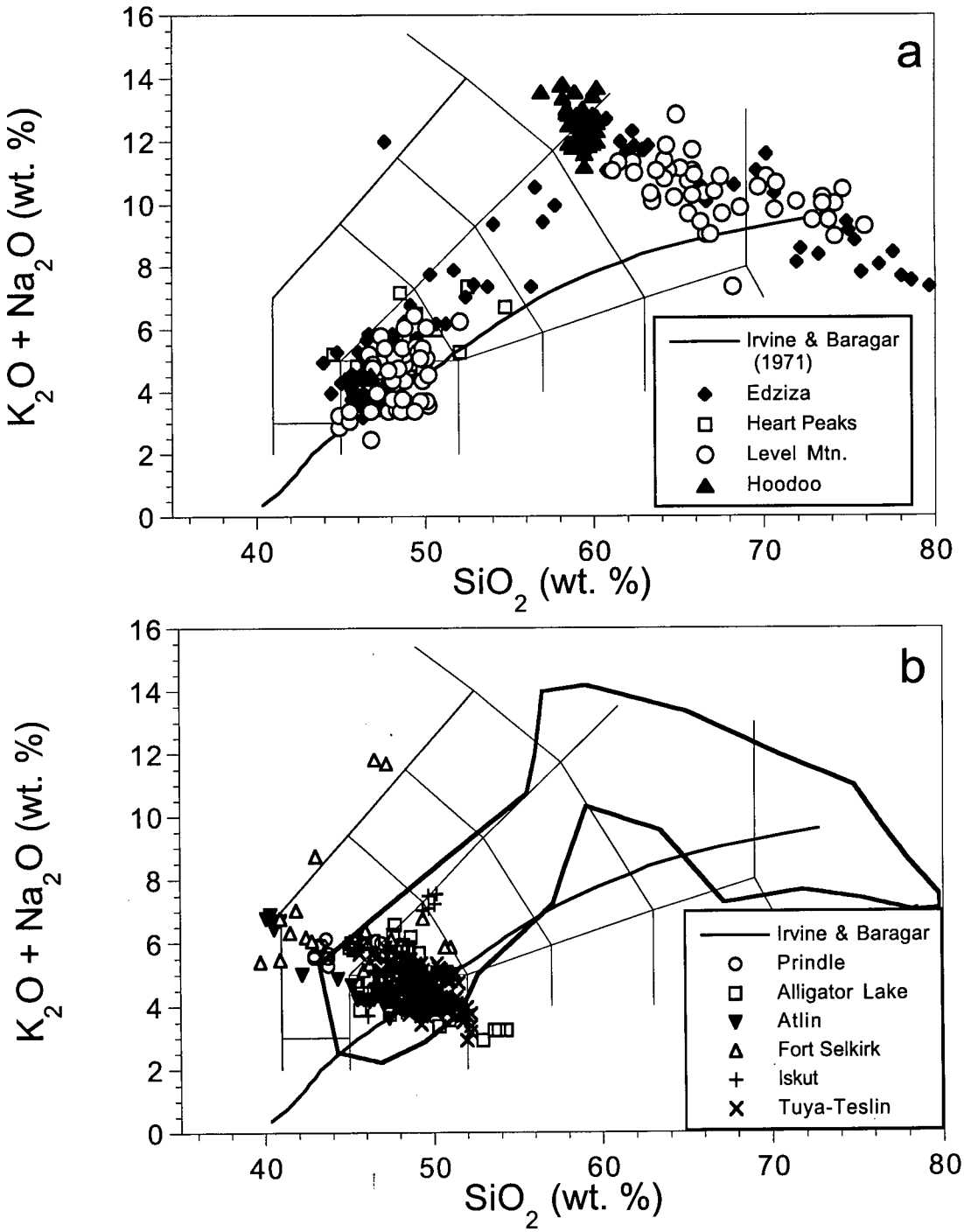

Figure 1.3. Total $Na_2O + K_2O$ (wt. %) versus SiO_2 (wt. %) rock classification diagram after Le Bas et al. (1986) for: a) volcanic rocks within the Stikine Subprovince, and b) other volcanic rocks within the Northern Cordilleran Volcanic Province. Field in b) (bold outline) is the data from a).

and pantellerite comprise ~50 % by volume of the complex (Souther 1992). At Hoodoo Mountain, phonolite and trachyte make up >90 % of the presently exposed volcanic pile.

The alkaline signature found throughout the NCVP is expressed both mineralogically and geochemically. Mafic rocks commonly have coexisting olivine and titanaugite in the groundmass and thus fit the mineralogical definition for alkali olivine basalts (McDonald & Katsura 1968). Whole rock compositions generally plot in the alkaline field (Irvine & Baragar 1971; Le Bas et al. 1986) (Figure 1.3). However, some exceptions occur, most notably at Whitehorse, Atlin, and the Tuya- Teslin volcanic fields (Eiché et al. 1987; Francis & Ludden 1995; Moore et al. 1995). Evolved rock types (SiO_2 > 56 wt. %) include both SiO_2-undersaturated nepheline-bearing phonolite and SiO_2-saturated, peralkaline (molar Na + K > Al), aegirine-augite-, arfvedsonite- and aenigmatite-bearing trachyte, comendite, and pantellerite (Table 1.2).

Rocks of the NCVP are relatively Fe-rich (Figure 1.4). Many of the basaltic rocks have > 10 wt. % $FeO_{(Total)}$, and the suite as a whole shows a progressive Fe-enrichment trend (cf. Thingmuli data; Figure 1.4) in contrast to a typical calc-alkaline, subduction-related suite from the Cascade volcanic province.

Detailed petrological studies of NCVP volcanic centres are not numerous. However, a relatively large body of published literature and / or unpublished graduate theses is available including work on the Fort Selkirk

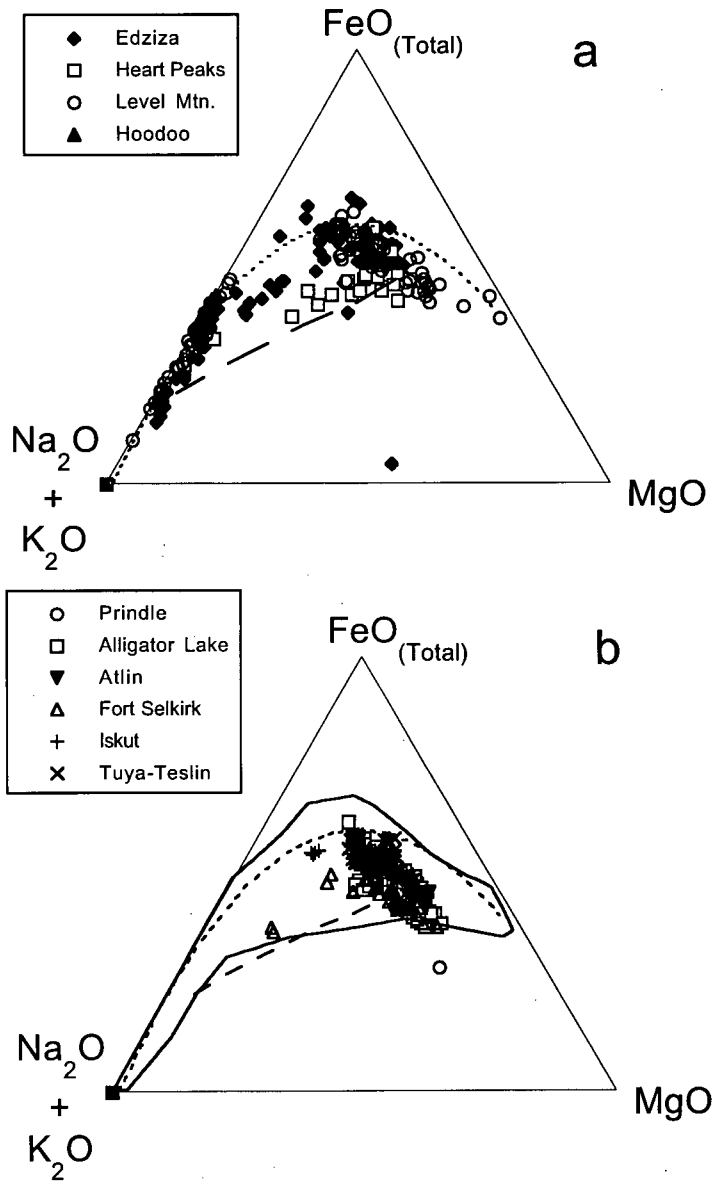

Figure 1.4. AFM diagram (in wt. %) for: a) data from the Stikine Subprovince, and b) data for other NCVP volcanic rocks. Trends for Thingmuli (short dashes) and the Cascade volcanic province (long dashes) are from Carmichael (1964) and are shown for comparison. Field in b) (bold outline) is data from a).

volcanic complex (Prescott 1983; Francis & Ludden 1990; Trupia & Nicholls 1996), Alligator Lake (Eiché 1987; Eiché et al. 1987), Level Mountain (Hamilton 1981), Tuya Buttes (Mathews 1947; Watson & Mathews 1948; Allen et al. 1981; Moore et al. 1995; Simpson 1996), Mount Edziza (Souther 1992), Iskut-Unuk rivers areas (Grove 1986; Stasiuk & Russell 1989; Hauksdóttir 1994; Hauksdóttir & Russell 1994; Cousens & Bevier 1995), and the Hoodoo Mountain volcanic complex (Edwards & Russell 1994a, 1994b, Edwards et al. 1995, Edwards et al. 1997, Chapter 2).

Xenoliths and Magmatic Inclusions

Xenoliths and magmatic inclusions are found in volcanic centres throughout the NCVP (Table 1.3) and range in composition from spinel peridotite to granite. The xenoliths can be grouped into three broad categories: 1) ultramafic xenoliths, 2) felsic igneous xenoliths, and 3) metamorphic xenoliths. Ultramafic xenoliths have been described in detail for a limited number of locations including Fort Selkirk (Sinclair et al. 1978; Prescott 1983; Ross 1983; Francis & Ludden 1990), Alligator Lake (Francis 1987), Atlin (Ruby Mountain, Nicholls et al. 1982) and Castle Rock (Littlejohn & Greenwood 1974; Prescott 1983; Ross 1983). Felsic igneous xenoliths have been described in detail only from Ash Mountain (Watson & Mathews 1948) and from the Iskut-Unuk rivers centres (Hauksdóttir 1994). Magmatic inclusions are also found at many of the centres and range in composition from gabbro to syenite.

Table 1.3. Summary of xenolith-bearing magmatic centres within the Northern Cordilleran Volcanic Province.

Volcanic centre	Terrane	Types of xenoliths/inclusions	References[1]
West Dawson (including Prindle, 60 Mile, Clinton Creek, 40 Mile)	Yukon-Tanana	spinel lherzolite, spinel harzburgite, spinel wehrlite, granulite, sedimentary rocks, granite, clinopyroxene xenocrysts	25, 68, 76, 100
Fort Selkirk (including Volcano Mountain, Wootton's Cone/Ne Che Dhwaha, Fork Selkirk, Pelly Formation, Wolverine Formation)	Yukon-Tanana / northern Stikinia	spinel lherzolite, websterite, dunite, granitoids, schist, xenocrysts (quartz, feldspar, olivine, spinel, Cr-diopside, enstatite)	27, 30, 76, 77, 79, 95, 96
Alligator Lake	northern Coast Plutonic Complex	spinel lherzolite, spinel harzburgite, granite	9, 10, 19, 22
Atlin (Ruby Mountain, Cracker Creek, Volcano Creek, Chikoida Mountain, Hirschfeld Creek/Line Lake, Llangorse Mountain)	northern Cache Creek	dunite, spinel lherzolite, spinel harzburgite, websterite, garnet pyroxenite, gabbro, granite, granodiorite, clinopyroxene/olivine/ spinel xenocrysts	9, 17, 75
Tuya-Teslin (Ash Mountain, 3 Caribou tuya, Mathew's tuya, South tuya, Kawdy Mountain)	Cache Creek/Cassiar	granite, granodiorite, troctolite	65, 98
Heart Peaks	northern Stikinia	possible xenocrysts	11
Level Mountain	northern Stikinia	spinel lherzolite, garnet wehrlite, gabbro, granitic gneiss, sedimentary rocks, clinopyroxene xenocrysts	39
Castle Rock	northern Stikinia	spinel lherzolite, granite, gneiss, gabbro, dunite, granulite	60, 76, 77
Mount Edziza	northern Stikinia	hornblende biotite granite, gabbro, peridotite(?)	86
Maitland (Maitland Creek, Kunigus Creek, Tumeka Lake and Griffith Creek)	northern Stikinia	peridotite, feldspathic xenoliths	23, 85
Hoodoo Mountain (Little Bear mountain)	northwestern Stikinia	granite and syenite; clinopyroxene xenocrysts	14-16
Iskut-Unuk rivers (Lava Fork, Iskut River, Snippaker Creek, King Creek, Cone Glacier)	northwestern Stikinia	gabbro, granulite, granitic gneiss and schist; plagioclase & clinopyroxene xenocrysts	46-48, 75, 90
The Thumb	eastern Stikinia	layered gabbro	73, 74

[1] see Table 1 for reference numbers; note that only references with data on xenoliths are included

Ultramafic Xenoliths

Ultramafic xenoliths have been documented at 15 different centres covering over two-thirds of the length of the NCVP (Figure 1.5; Table 1.3). Their distribution is skewed towards the northern half of the NCVP as well as the Yukon-Tanana and Cache Creek terranes (Figure 1.6). Ultramafic xenoliths are found in the majority of centres located in Yukon-Tanana, in approximately one-half of the centres in Cache Creek, and in some of the centres within the Stikine terrane. Ultramafic xenoliths have not been reported from any NCVP centres within the Cassiar terrane or to the east of the Cassiar terrane (D. Francis, pers. comm., 1996).

Ultramafic xenoliths from the NCVP range in composition and include dunite, lherzolite, harzburgite, websterite, wehrlite, and garnet pyroxenite (Foster et al. 1967; Littlejohn & Greenwood 1974; Sinclair et al. 1978; Hamilton 1981; Nicholls et al. 1982; Prescott 1983; Ross 1983; Higgens & Allen 1985; Francis 1987). Three geochemical studies found both depleted and undepleted ultramafic xenolith populations at Fort Selkirk (Prescott 1983; Ross 1983), Alligator Lake (Francis 1987) and Castle Rock (Prescott 1983; Ross 1983). At Alligator Lake, Francis (1987) reported that all peridotite xenoliths were Type I (Cr-rich clinopyroxene). These studies also reported the occurrence of both deformed and undeformed xenoliths.

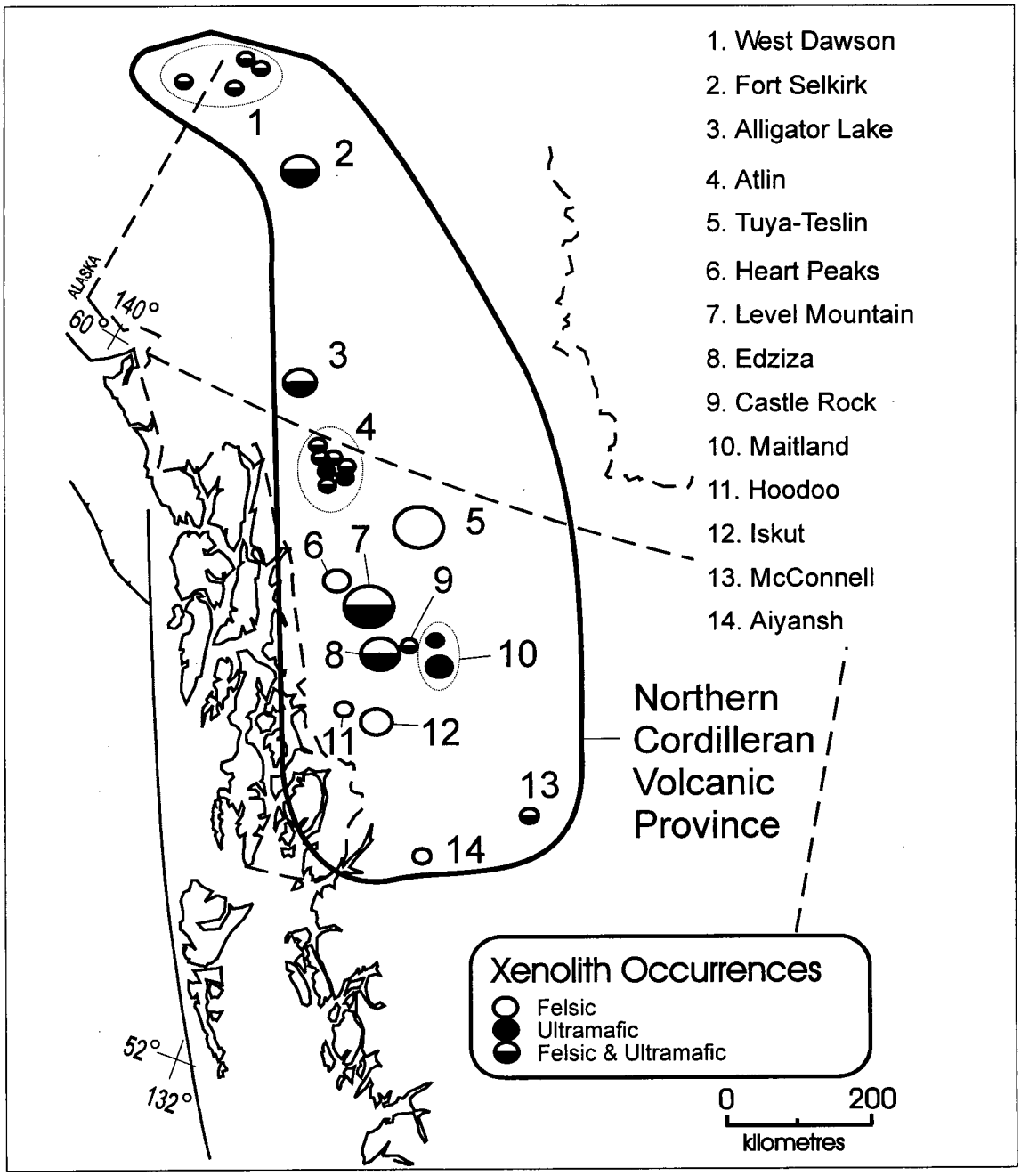

Figure 1.5. Distribution of xenoliths in the NCVP. Large symbols represent groups of volcanic centres.

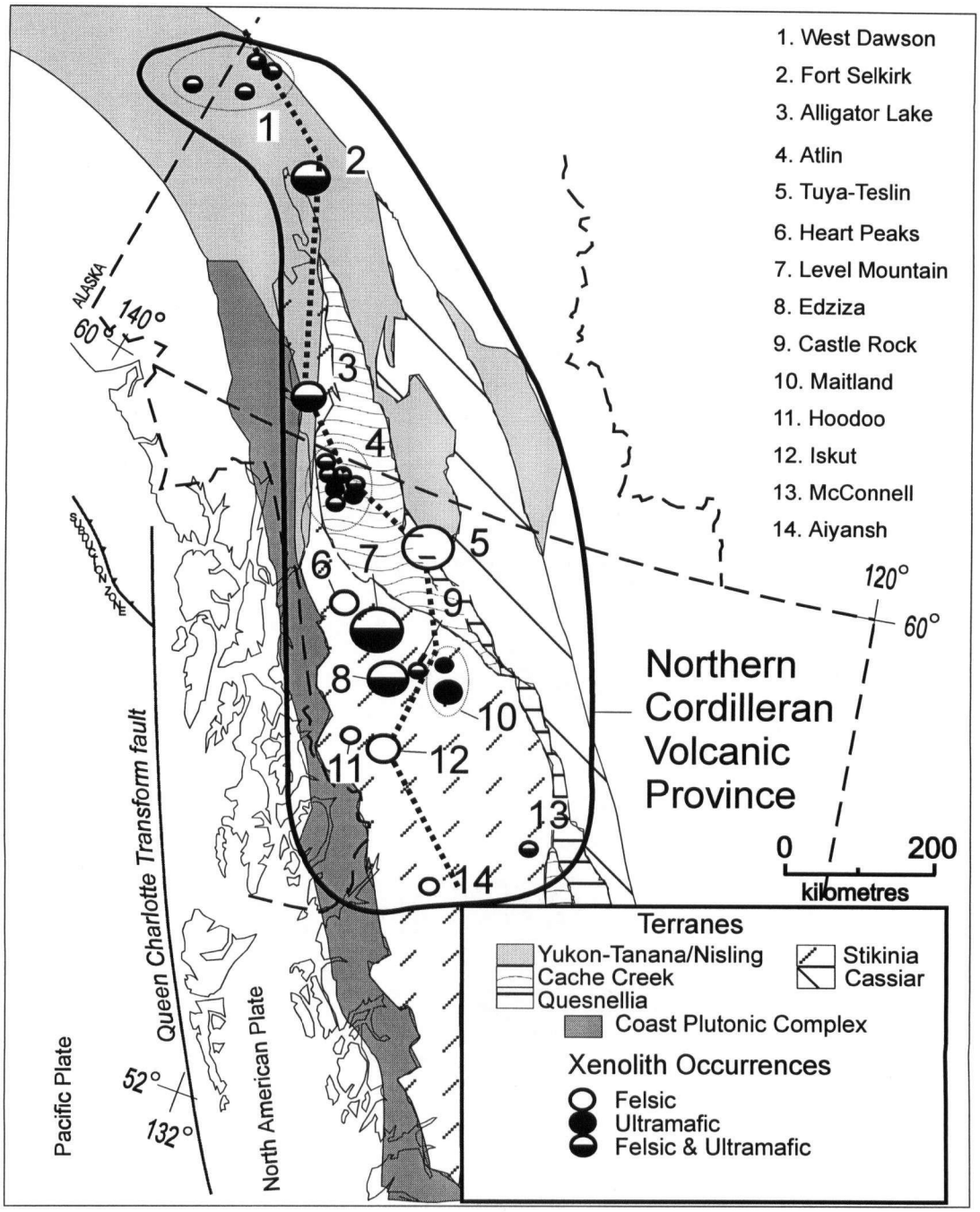

Figure 1.6. Distribution of xenoliths in the NCVP with respect to major terrane boundaries (after Wheeler & McFeely 1991). Line of section for Figure 1.7 (bold dashes) is shown for reference.

Felsic Igneous Xenoliths

The felsic igneous xenoliths have been found throughout the NCVP (Figure 1.5). The most common type is granitic in composition and locally derived. For example, Eiché et al. (1987) found granitic xenoliths at Alligator Lake that appeared to be derived from nearby intrusions of the Coast Belt. However, at both Castle Rock and Little Bear Mountain (informal name), igneous xenoliths are not derived from exposed basement rocks immediately adjacent to the volcanoes.

Many of the felsic igneous xenoliths exhibit reaction textures with the surrounding magma. Some have been partly melted and now contain glass (Watson & Mathews 1948; Eiché et al. 1987; Hauksdóttir 1994). Such fused xenoliths have been noted at Alligator Lake (Eiché et al. 1987; Carignan et al. 1994), Ruby Mountain (Edwards et al. 1996), Volcanic Creek (Edwards et al. 1996), Cracker Creek (Edwards et al. 1996), Chikoida Mountain (Edwards et al. 1996), Level Mountain (Hamilton 1981), Ash Mountain (De P. Watson & Mathews, 1948), South Tuya, Mathew's Tuya (Simpson 1996), Mount Edziza (Souther 1992), Hoodoo Mountain (Edwards & Russell 1994a; Edwards et al. 1995), and the Iskut-Unuk rivers centres (Stasiuk & Russell 1989; Hauksdóttir 1994; Hauksdóttir et al. 1994; Hauksdóttir & Russell 1994).

Metamorphic xenoliths

In contrast to the always present but numerically rare felsic igneous xenoliths, crustal xenoliths of metamorphic origin are found in only a few centres in the NCVP. The crustal metamorphic xenoliths are mainly high-grade, granulite-facies metamorphic rocks and are found only at Prindle (Foster et al., 1967; Prescott 1983), Fort Selkirk (Prescott 1983), Castle Rock (Prescott 1983), and Iskut River (Nicholls et al., 1982). Granulite facies basement rocks are not exposed adjacent to any of these centres.

Magmatic Inclusions

Magmatic inclusions include troctolite from Ash Mountain (Moore et al., 1995), a suite of plagioclase-dominated inclusions from Level Mountain (Hamilton, 1981), gabbroic inclusions from Little Bear mountain, the Iskut River and Mt. Edziza (Chapter 4; Nicholls et al. 1982; Souther, 1992), and syenitic inclusions from Hoodoo Mountain. With the exception of Ash Mountain, the magmatic inclusions are confined to the larger volcanic centres in the central and southern NCVP, which is within the Stikine terrane. However, Ash Mountain is near the boundary between the southern Yukon-Tanana and Cassiar terranes.

Megacrysts of uncertain origin are also included as magmatic inclusions and have been reported in most of the NCVP centres that are xenolith-bearing (Table 1.3). The megacrysts comprise three distinct groups with non-obvious

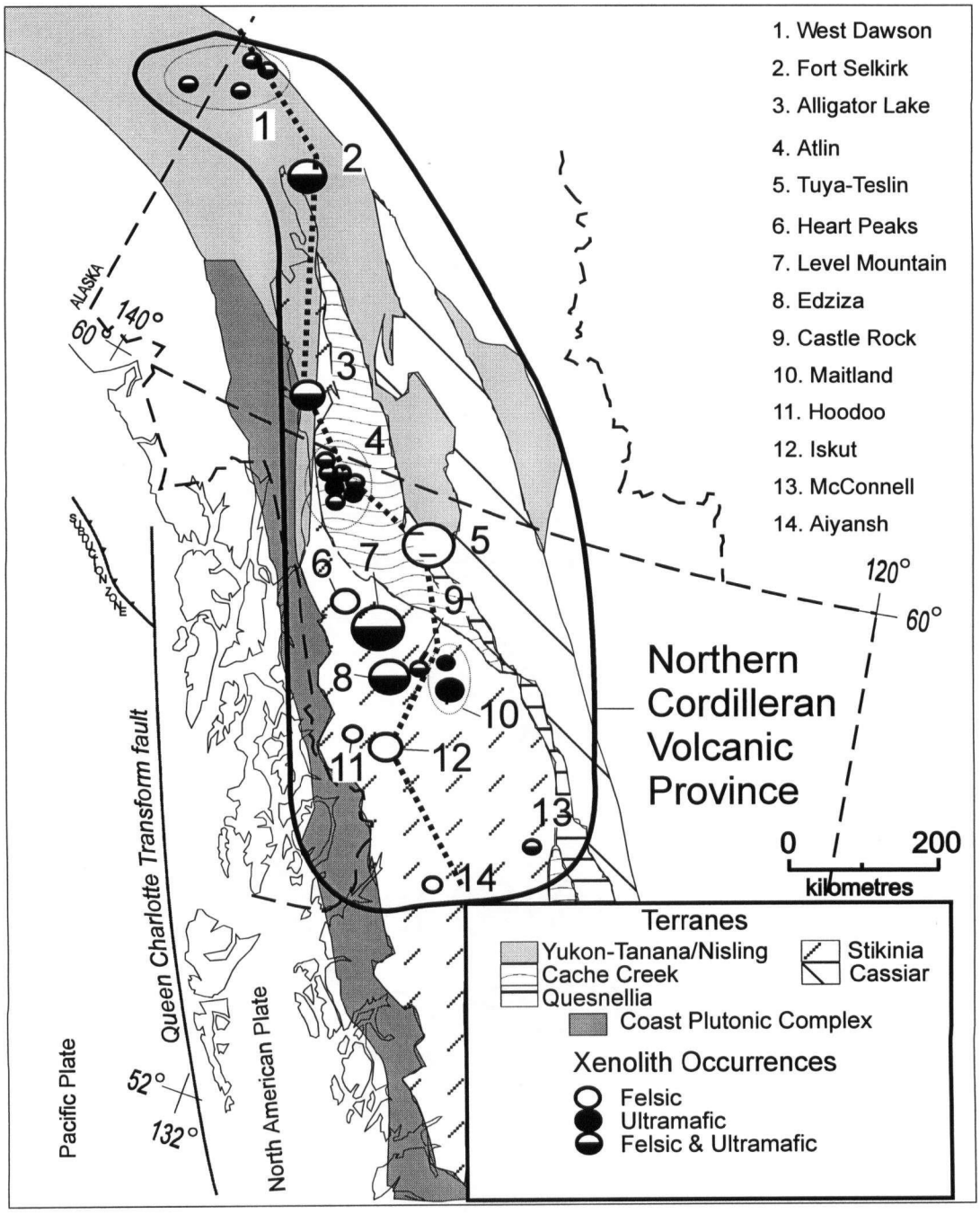

Figure 1.6. Distribution of xenoliths in the NCVP with respect to major terrane boundaries (after Wheeler & McFeely 1991). Line of section for Figure 1.7 (bold dashes) is shown for reference.

1994), and 3) the petrogenesis of lavas from individual volcanic centres (Hauksdóttir 1994; Cousens & Bevier 1995; Moore et al. 1995; Trupia & Nicholls 1996). Several studies have found evidence that the abundant partly-fused xenoliths found throughout the NCVP have chemically contaminated their host magmas (e.g., Hamilton 1981; Souther 1992; Hauksdóttir 1994).

Primary magmas and source regions

Most of the work on primary magmas has been done in the northern half of the NCVP. Francis and coworkers have postulated the existence of three different magma series represented in the Atlin and Fort Selkirk areas: olivine nephelinite (>15 wt % norm Ne; Ol-NEPH of Francis & Ludden, 1995), basanite (5< wt % norm Ne < 15; BASAN of Francis & Ludden, 1995), alkali olivine basalt and transitional basalt (wt % norm Ne < 5; AOB to HYP-NORM of Francis & Ludden, 1995). Each series is distinguished by trace element characteristics and by normative Ne content (Francis & Ludden 1990, 1995; Carignan et al. 1994). The three magmas series are interpreted as representing primary magmas that originated from differing degrees of partial melting of the same source (amphibole-bearing spinel lherzolite) in the lithosphere.

Based on radiogenic isotopic signatures, Carignan et al. (1994) suggested that at least 3 distinct mantle sources were present in the NCVP: a non-radiogenic source for olivine nephelinites at Fort Selkirk and Atlin; a somewhat more radiogenic source for alkali olivine basalts from Fort Selkirk;

and, a source with radiogenic Pb but non-radiogenic Sr for alkali olivine basalts from Mount Edziza. At the Tuya Buttes volcanic field, Moore et al. (1995) also hypothesized at least two different parental magmas to explain major element differences between hypersthene- and nepheline-normative basalts.

Relationships between mafic and felsic magmatism

Only one study has examined in detail the petrological relationships between contemporaneous mafic and felsic rocks in the NCVP. Souther and Hickson (1984) suggested that trachybasalts, trachytes, and comendites at Mount Edziza could be related by multistage fractional crystallization from an alkali olivine basalt parent based on mass balance modeling. The mass balance models required from 80 to 95 % crystallization of the parental basalt to produce the Si-enriched trachyte and comendite (Souther & Hickson 1984); however, the volumetric ratios of basalt to trachyte plus comendite at Mount Edziza are approximately 1 to 1 (Souther 1992).

Petrogenesis of individual centres

Several workers have investigated the petrogenesis of individual mafic volcanic centres (Hauksdóttir 1994; Cousens & Bevier 1995; Moore et al. 1995; Trupia & Nicholls 1996; Simpson 1996). The petrogenetic processes described include: i) fractional crystallization of single magma batches (e.g., Trupia & Nicholls 1996), ii) eruption of two separate magma types from the same vent (e.g., Moore et al. 1995), and iii) combined fractional crystallization

and magmatic assimilation (e.g., Hauksdóttir 1994). At Volcano Mountain in the northern NCVP, Trupia & Nicholls (1996) found that of the three sampled olivine nephelinite lava flows, the oldest two flows appeared to be derived from the same magma batch. However, the youngest flow could not be related to the other two by fractional crystallization. In the central NCVP, at Ash Mountain, Tuya Buttes, and South Tuya, Moore et al. (1995) postulated the existence of two separate magma types to explain the coexistence of hypersthene normative basalts and nepheline normative basalts in the same centres. In the southern NCVP, Hauksdóttir (1994) documented the petrographic and geochemical consequences of magmatic assimilation at four volcanic centres along the Iskut and Unuk rivers. A subsequent isotopic study of the same samples by Cousens and Bevier (1995) reached similar conclusions.

Evidence for magmatic assimilation

The abundance of fused xenoliths and xenocrysts in volcanic centres throughout the NCVP indicates that magmatic assimilation is an important petrogenetic process in the NCVP. In the northern NCVP, Francis and Ludden (1990) found quartz xenocrysts in both the basanite and olivine nephelinite units and sieve-textured feldspars in the basanite unit at Fort Selkirk. In the central NCVP, partly fused granitic xenoliths have been documented at Alligator Lake (Eiché et al. 1987), Ruby Mountain (Edwards et al. 1996), Ash Mountain (Watson & Mathews 1948), Level Mountain (Hamilton 1981), and Mount Edziza

(Souther 1992). In the southern NCVP, Hauksdóttir (1994) recorded both partly fused xenoliths and a diverse population of xenocrysts at the Iskut-Unuk rivers centres.

However, documentation of magmatic assimilation within the NCVP is complicated because the region is underlain by at least four major, distinct geological terranes (Figures 1.6 and 1.7). For example, at Alligator Lake Carignan et al. (1994) could not clearly identify the signature of magmatic assimilation in part because the potential contaminant was isotopically similar to the mantle source regions for the volcanic rocks. Clearly, because of the geological diversity of the Cordilleran lithosphere, the chemical characteristics of potential contaminants can vary significantly. The differences in Sr and Pb isotopic ratios documented at Fort Selkirk, Alligator Lake, Atlin, and Mount Edziza by Carignan et al. (1994) could reflect real source region differences or could result from contamination during transport of magmas through isotopically diverse lithosphere (Figure 1.7).

Studies of the two largest volcanic centres in the NCVP have reported extensive petrographic and geochemical evidence for assimilation. Hamilton (1981) called on magmatic assimilation as an important process at Level Mountain volcanic complex, which is the largest in the NCVP. He based his conclusions on the abundance of xenoliths in the mafic units and on elevated values of $\delta^{18}O$ and $^{87}Sr/^{86}Sr$ in the Si-enriched units (Hamilton 1981). Souther

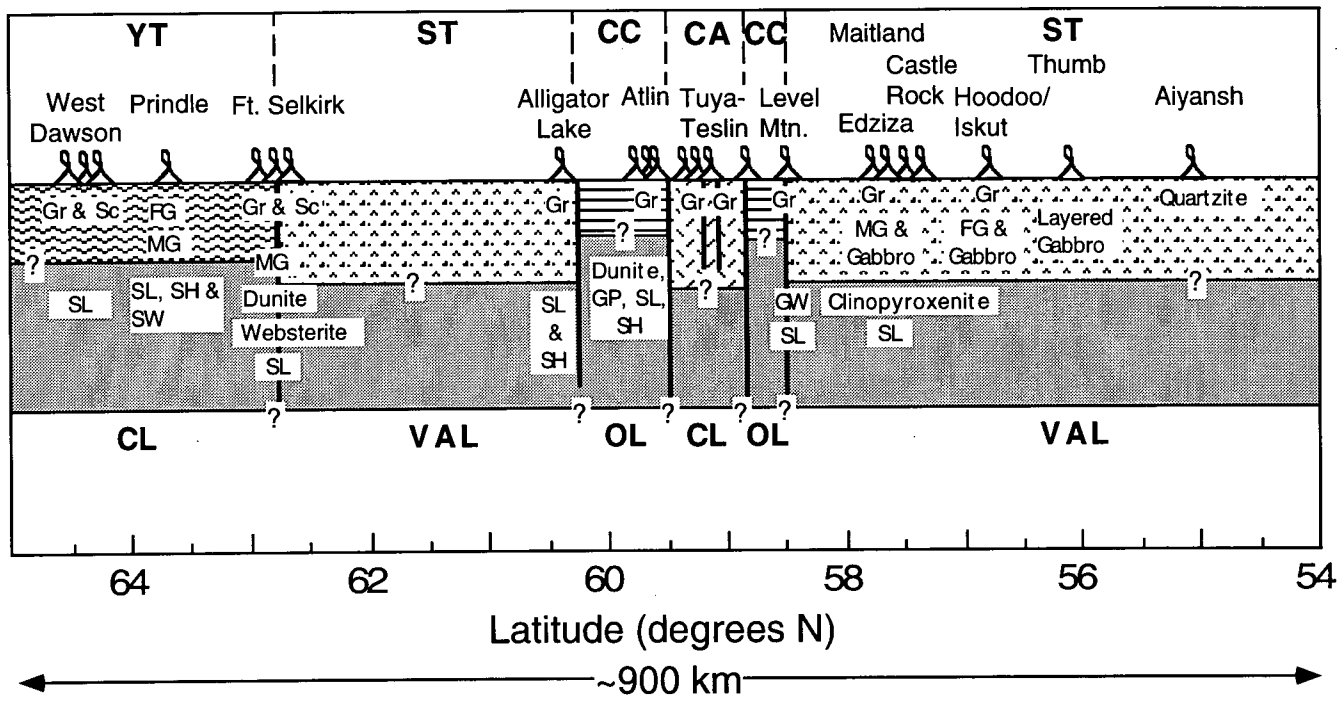

Figure 1.7. Schematic lithospheric cross-section through the Northern Cordillera Volcanic Province (see Figure 1.6 for line of section). Abbreviations are as follows: YT- Yukon-Tanana terrane, ST - Stikine terrane,CC - Cache Creek terrane, CA - Cassiar terrane, CL - continental lithosphere, VAL - volcanic arc lithosphere, OL - oceanic lithosphere, Gr - granite xenoliths, Sc - schistose xenoliths, FG - felsic granulite xenoliths, MG - mafic granulite xenoliths, SL - spinel lherzolite xenoliths, SH - spinel harzburgite xenoliths, SW - spinel wehrlite xenoliths, GP - garnet pyroxenite xenoliths, GW - garnet wehrlite xenoliths. Bold vertical lines are faults after Wheeler and McFeely (1991); fault orientations are assumed to be vertical.

(1992) documented evidence for complex mineral - melt reactions in 8 of the 13 units he described at Mount Edziza, which is the second largest volcanic centre in the NCVP. The reactions included disequilibrium phenocryst textures such as embayed feldspar and / or clinopyroxene (Raspberry, Nido, Spectrum, and Big Raven formations), fritted rims on feldspars (Nido and Big Raven formations), and partly reacted xenoliths (Pillow Ridge and Edziza formations). Souther (1992) postulated that the assimilation of crustal rocks was an important process in the petrogenesis of the Ice Peak Formation and that assimilation might also have been important in the development of several other formations that are enriched in radiogenic Sr (e.g., the Raspberry Formation).

However, only one detailed study has fully documented the effects of assimilation in volcanic centres from the NCVP. Hauksdóttir (1994) used detailed petrographic and chemical studies to identify contamination in four basaltic centres in the southern NCVP. Hauksdóttir (1994) showed conclusively that lavas from individual centres in the Iskut River volcanic field could not be related by closed system differentiation. In addition she found partly melted xenoliths at several of the centres and documented texturally and compositionally distinct plagioclase populations. Taken together the evidence from Hauksdóttir (1994) overwhelmingly supports the hypothesis that crustal contamination played an important role in the differentiation history of this

volcanic field. Subsequent work by Cousens and Bevier (1995) also found isotopic and trace element evidence consistent with crustal or lithospheric contamination in the Iskut-Unuk volcanic field.

The detailed study by Hauksdóttir (1994), coupled with the more general results from Level Mountain (Hamilton 1981) and Mount Edziza (Souther 1992), demonstrates the importance of magmatic assimilation in the NCVP. The presence of xenoliths and xenocrysts throughout other centres within the NCVP is a strong indication that magmatic assimilation is an important petrogenetic process throughout the northern Cordillera.

1.7. SUMMARY

The Northern Cordilleran Volcanic Province represents a spatially- and temporally-related suite of alkaline volcanic rocks in the northern Canadian Cordillera. Shared volcanological, geochronometric, and petrological features serve to link this area of volcanism including:

- the occurrence of felsic domes and lava flows associated with long-lived complexes of overlapping basaltic shield volcanoes,
- subglacial volcanic deposits,
- age ranges from Neogene to late Quaternary distributed throughout the province,
- the alkaline nature of both mafic and felsic rock types, and

- the abundant petrographical and geochemical evidence for magmatic assimilation including widespread fused xenoliths and xenocrysts with disequilibrium textures.

Taken together, these features point to several volcanological and petrological problems that constitute many lifetimes worth of work. In the following chapters I will focus on one problem that is locally and regionally significant: *the nature and style of magmatic assimilation recorded in lavas from the southern NCVP*.

CHAPTER 2

Geology, Stratigraphy, and Geochemistry of the Hoodoo Mountain Volcanic Complex, northwestern British Columbia

2.1. INTRODUCTION

The Hoodoo Mountain volcanic complex (HMVC) is the southernmost of three large volcanic complexes that comprise the Stikine Subprovince of the Northern Cordilleran Volcanic Province (NCVP; Figure 2.1; Chapter 1). Unlike the two largest complexes in the subprovince, Level Mountain (Hamilton 1981) and Mount Edziza (Souther 1992), which were mapped and characterized chemically and petrographically, the HMVC was virtually unstudied prior to this work (Edwards & Russell 1994a & b; Edwards et al. 1995; Edwards et al. 1997a & b). Only brief, general descriptions of Hoodoo Mountain volcano existed (Kerr 1948; Souther & Yorath 1990; Souther 1991).

The purpose of this chapter is three-fold: i) to describe the geology and stratigraphy of the HMVC based on two summers of mapping (1993 and 1994), ii) to describe the petrology of the non-fragmental volcanic units in the complex, and iii) to discuss the origins of the volcanic rocks in the complex. The last topic has two main components: a) the role of volcano-glacial interaction in the

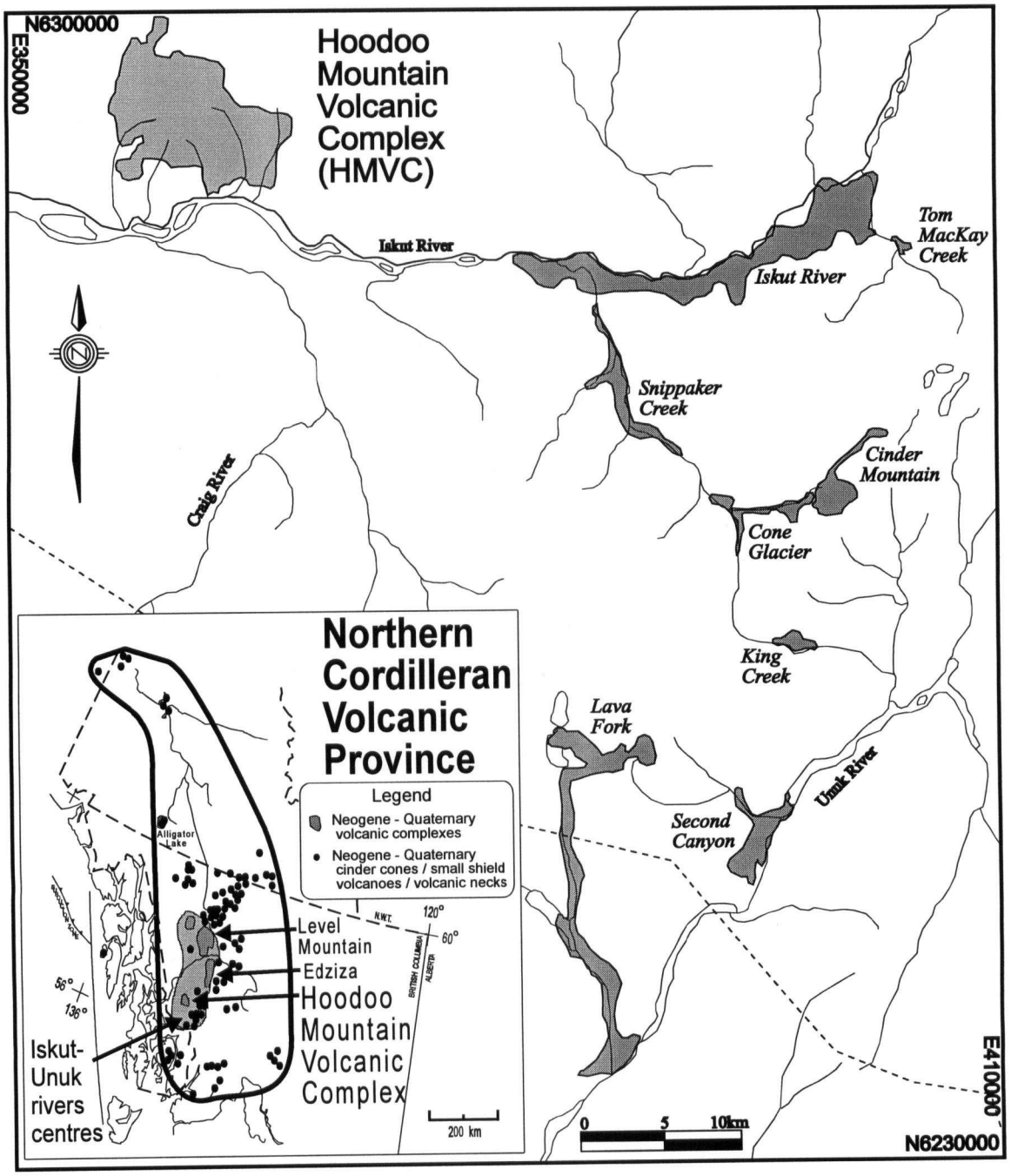

Figure 2.1. Location of the Hoodoo Mountain volcanic complex and other Quaternary volcanic centres along the Iskut River (from Hauksdóttir 1994). Inset shows volcanic centres in the Northern Cordilleran Volcanic Province.

physical development of the HMVC, and b) the role of magmatic assimilation in the chemical evolution of the HMVC. Detailed 1:20 000 scale geological and sample location maps, and an accompanying legend and stratigraphic relationships chart included as Plates 1, 2, and 3 were published as Edwards et al. (1997a). Throughout the text informal physiographic names are in *italics*.

2.2. GEOLOGY AND STRATIGRAPHY

Overview

A total of ten Quaternary volcanic centres occur along the Iskut and Unuk rivers in the Coast Mountains of northwestern British Columbia, Canada (Figure 2.1). The HMVC comprises two of the ten volcanic centres: Hoodoo Mountain and *Little Bear Mountain* volcanoes (Figure 2.2). The HMVC extends north from the Iskut River for 10 km, reaching up between two prominant valley glaciers, Hoodoo and Twin glaciers (Figures 2.1 and 2.2), and is centred at latitude 56° 46' N and longitude 131° 17' W (UTM centre 360000E and/or 6295000N). It is located 120 km NW of Stewart, B.C., 30 km east of the confluence of the Stikine and Iskut rivers, and is only accessible by helicopter.

Hoodoo Mountain volcano, which attains an elevation of 1850 m above sea level on its gently rounded summit, is the larger of the two centres at the HMVC (Figures 2.2, 2.3a,b, and c). In plan view the volcano is symmetrical and circular (Figure 2.2). Two sets of cliffs discontinuously circumscribe the volcano

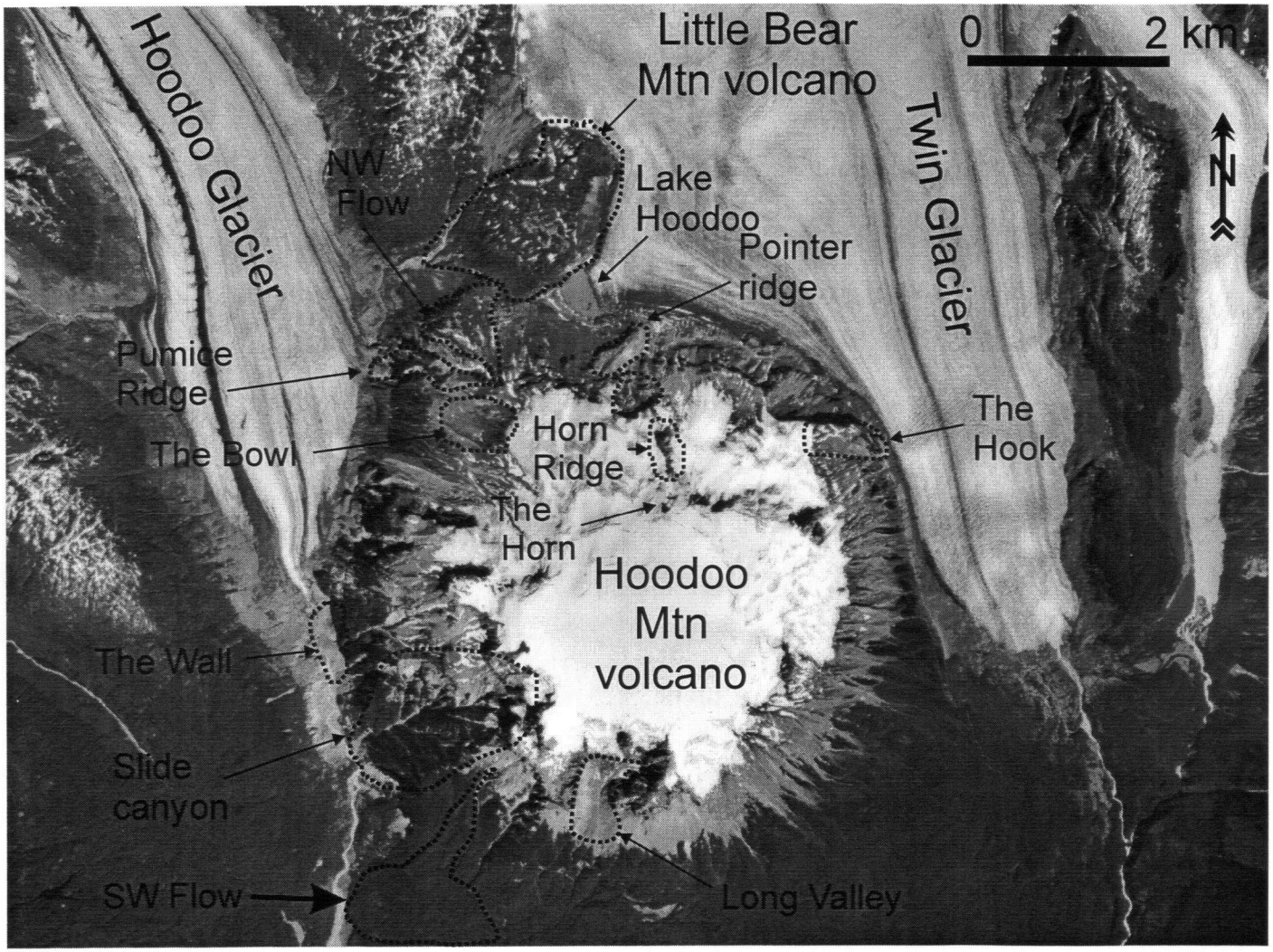

Figure 2.2. Aerial photograph of the Hoodoo Mountain volcanic complex (B.C. Airphoto BC82022).

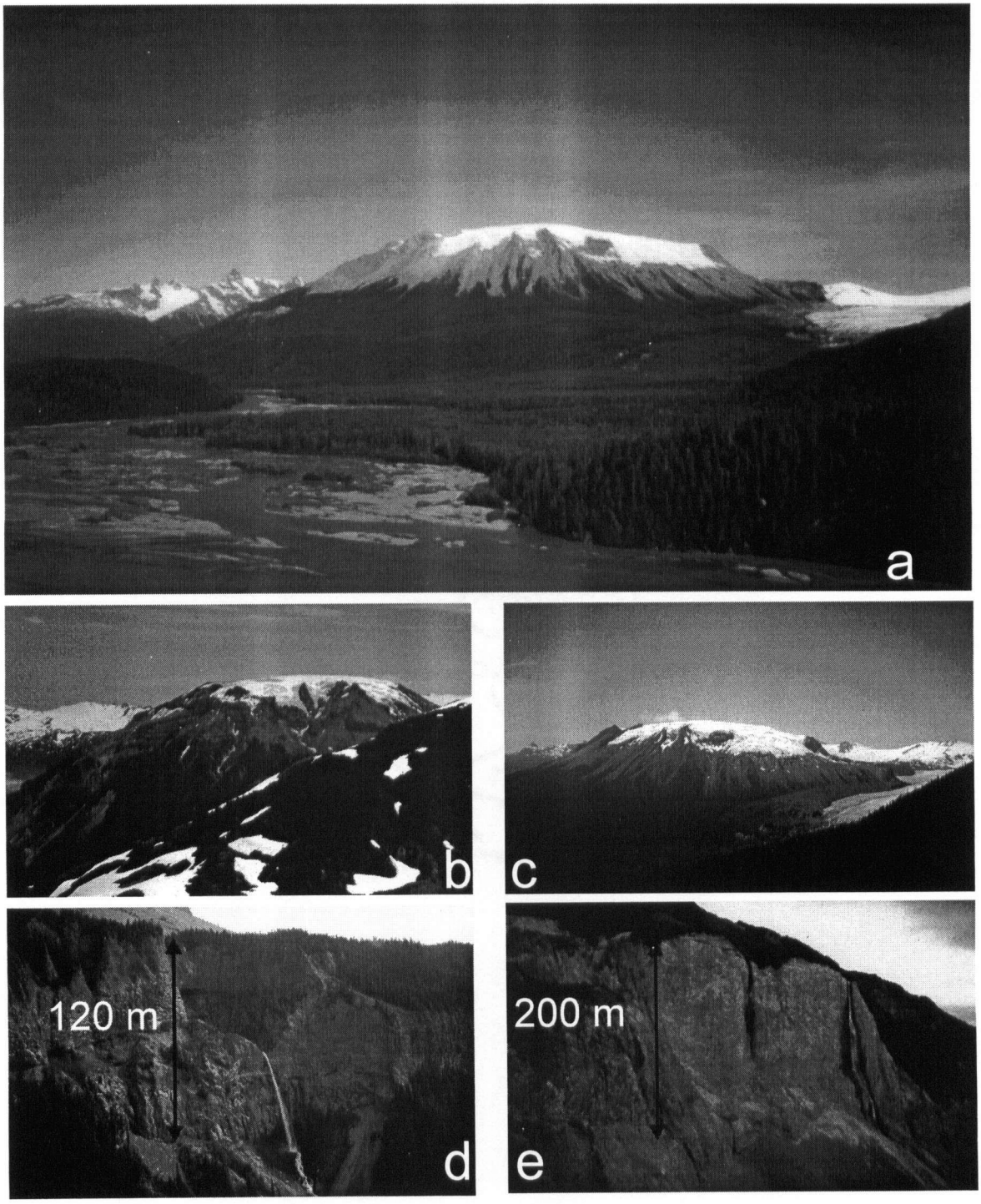

Figure 2.3. Photographs of Hoodoo Mountain volcano (the icecap on top of Hoodoo Mountain is approximately 3 km in diameter). Views are: a) from the southeast (Iskut River in foreground), b) from the southwest, c) from the east, d) cliffs of Qvap on the south side, and e) cliffs of Qvap on the west side.

(Figures 2.3d and e), with gentle slopes separating the cliffs. An icecap covers the summit. Of the ten centres in the Iskut area only Hoodoo Mountain volcano contains chemically evolved rock types (e.g., phonolites and trachytes).

The smaller edifice, informally named *Little Bear Mountain*, is 1230 m in elevation and is situated immediately north of Hoodoo Mountain (Figures 2.2, 2.4, and 2.9a). *Little Bear Mountain* is bounded to the east by Twin glacier, and is elongate northeast-southwest (Figures 2.2 and 2.4). The extreme north end of the mountain is a domical, narrow summit which slopes southward to a broad, central plateau (Figure 2.9a).

The HMVC comprises both fragmental and non-fragmental volcanic rocks. The non-fragmental units comprise predominantly fine- to medium-grained subglacial and subaerial lava flows, domes, spines, and dykes. Fragmental units are less abundant and comprise minor pyroclastic and mass flow deposits formed in both subglacial and intraglacial environments (Kerr 1948; Edwards & Russell 1994a; Edwards et al. 1995, Edwards et al. 1997). The rocks at *Little Bear Mountain* comprise alkali olivine basalt and are petrographically similar to the basalt centres described by Hauksdóttir (1994) in the Iskut area. The maximum total volume of volcanic material at the complex is 17.55 km^3 (17.3 km^3 at Hoodoo Mountain and 0.25 km^3 at *Little Bear Mountain*).

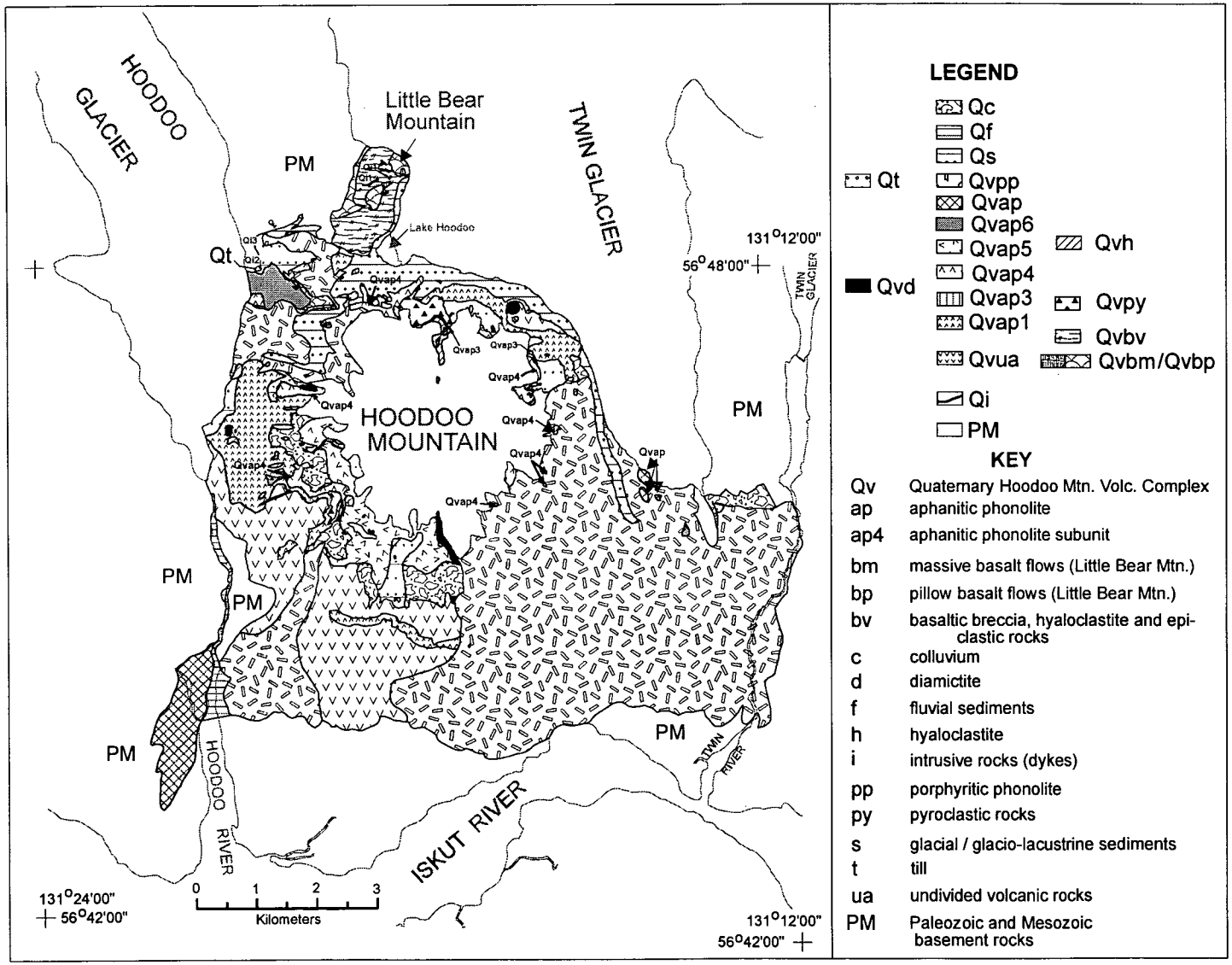

Figure 2.4. Geologic map of the Hoodoo Mountain volcanic complex.

The unit descriptions are separated into non-fragmental and fragmental volcanic units (summarized in Tables 2.1 to 2.3) for each of the volcanoes, followed by descriptions of dykes and selected sedimentary units that are important stratigraphic units in the HMVC. The section ends with a review of stratigraphic and isotopic age constraints for the HMVC. Plate 3 presents the details of the stratigraphic relationships amongst units for both volcanoes. The more detailed description of the basement and sedimentary units given in Edwards et al. (1997a) and Anderson (1993) is not repeated here.

Kerr (1948) first described the units and the stratigraphy of Hoodoo Mountain. He recognized three major episodes of volcanic activity: i) an early episode of subaerial eruption of aphanitic lava flows that were dammed by surrounding glaciers and formed steep cliffs, ii) a subsequent episode of subaerial eruption of porphyritic lava flows, found mainly on the south and east sides of the volcano, and iii) a late-stage subaerial eruption characterized by aa flows that form the top of the volcano. Kerr also recognized a basal grey till underlying the oldest lava series, and interflow pyroclastic deposits. A subsequent brief report by BC Hydro (1985) used Kerr's stratigraphy and descriptions, adding that tree ring counts on live trees growing on top of one of the most recent lava flows gave a minimum age for the flow of 180 years. However, the new results of this work, based on a more detailed stratigraphy derived from detailed mapping, indicates that the sequence of eruption for

Kerr's second and third phases is reversed (Edwards & Russell 1994a; Edwards et al. 1995; Edwards et al. 1997a & b).

Hoodoo Mountain volcano

The geology and stratigraphy of Hoodoo Mountain volcano is dominated by thick lava flows, domes, and volcanic breccia (Figure 2.4; Tables 2.1 and 2.2). More than 75% of the exposed rocks are part of unit Qvap, which comprises aphanitic trachyte and phonolite. Pyroclastic units (Qvpy and Qvh) are minor components and occur in the middle of the stratigraphic sequence; they are best exposed on the northern side of the volcano. The youngest lava flows (Qvpp) in the HMVC are volumetrically minor (<10%) but cover much of the northwest, south, and east sides of Hoodoo Mountain (Figure 2.4).

Non-fragmental Volcanic Rocks, Hoodoo Mountain volcano

Unit Qvu

Unit Qvu comprises the lowermost units at Hoodoo Mountain. It is poorly described because of poor accessibility in the field. In one location that is accessible, between the eastern edge of Hoodoo Glacier and the base of Pumice Ridge (Figure 2.2), Qvu outcrops as orange-red, columnar jointed, aphanitic lava. However, from the exposed area it is impossible to determine whether the unit is a dyke, a dome, or a lava flow. The unit is also mapped,

Table 2.1. Summary field descriptions of non-fragmental volcanic units at Hoodoo Mountain volcano.

Unit (map symbol)	Description (colour; texture; volcanic forms; distribution)
$Qvpp_{(1,2)}$	**colour**: dark to medium olive green, golden green, black (fresh surfaces) **textures**: trachytic, porphyritic (15-25 % clear to pale yellow, fractured, glassy feldspar phenocrysts up to 3 cm in length), massively jointed (columns > 1m in diameter), slightly vesicular (<10% in scoria) to non-vesicular (near base of flows) **volcanic forms**: channelized lava flows (1 to 5 m thick, reflecting local topography) with locally preserved lava flow levees and channel structures, aa flows, sheet lava flows, cinder cone **distribution**: dominantly on southeast and northwest quadrants of Hoodoo Mountain, with one large, composite flow and cinder cone on the southwest side (*Southwest flow*), and isolated single flows on the north and west sides **age**:28 ka, 9-10 ka, younger? (2 Ar-Ar dates); both glaciated and unglaciated surfaces occur locally
$Qvap_{6(a,u)}$	**colour**: light olive green with glassy sheen **textures**: aphanitic to sparsely porphyritic (<1 % phenocrysts), highly vesicular (>20%), locally amygdaloidal, locally heavily jointed (< 50 cm in diameter) **volcanic forms**: linear ridges, lava flows, dykes, bosses **distribution**: most abundant on northwest corner (*Pumice Ridge*), along *Horn Ridge*, as dykes on the northwest and west flanks, and an isolated boss on the lower east side, commonly spatially associated with Qvh **age**: 30-40 ka (Ar-Ar date)
$Qvap_{(1-5)}$	**colour**: dark green to black (fresh), orange to tan (weathered) **textures**: aphanitic to sparsely porphyritic (<5% phenocrysts), commonly jointed with either massive (>1 m) or fine (<0.5 m) columnar joints, locally with horizontal joints, commonly with mm thick weathering rinds **volcanic forms**: lava flows with partly preserved channels (5 to >50 m thick reflecting local topography), domes, glacially dammed (?) cliffs (> 200 m at *the Wall*) **distribution**: everywhere (most common unit) **age**: 85 ka ($Qvap_1$), 80 ($Qvap_2$), 54 ka ($Qvap_4$) (Ar-Ar dates)

Table 2.2. Summary field descriptions of fragmental volcanic units and non-volcanic units at Hoodoo Mountain volcano.

Unit (map symbol)	Description (colour; texture; volcanic forms; distribution)
$Qvh_{(1-3)}$	**colour**: yellow to tan, grey-green to black **textures**: clast-supported, poorly sorted to well sorted **clasts**: aphanitic Qvap, vitric lapilli, ash, blocks, bombs, pumiceous to slightly vesicular (<5%) **distribution**: mainly on the north and western sides, especially abundant at *Pumice Ridge, Horn ridge,* and *the Hook* **age**: 30-40 Ka (based on stratigraphic association with $Qvap_6$)
$Qvpy_{(1-2)}$	**colour**: yellow to red and black or green and black **textures**: eutaxitic, angular, hyalohyaline, aphanitic **clasts**: Qvap, granite, ash, lapilli, blocks, bombs **distribution**: between *Pointer Ridge* and *Horn ridge*, and *the Hook* **age**: >54 Ka, < 80 Ka (based on stratigraphic interpretation)
$Qd_{(1,2)}$	**colour**: tan to orange to red with black clasts **textures**: poorly sorted, dominantly clast supported, with angular clasts, clasts range from sand to boulder-size, **clast types**: Qvap, Qt(?) **distribution**: at the base of *Pointer Ridge* , north of *the Hook*, and isolated occurrences on the west side of Hoodoo Mountain **age**: >54 Ka at *Pointer Ridge*, generally poorly constrained (based on stratigraphy)
$Qt_{(1-3)}$	**colour**: tan-grey, brown with varying clast colours **textures**: poorly sorted, matrix-supported with angular and rounded clasts, clasts locally bullet-shaped and foliated **clast types**: olivine plagioclase phyric basalt, quartzite, metavolcanic rocks **distribution**: between Hoodoo Glacier and the lower west flanks of Hoodoo Mountain **age**:>9 Ka, <30-40 Ka (Qt_3), >30-40 Ka (Qt_2), >85 Ka (Qt_1)
$Qs_{(1,2)}$	**colour**: yellow to tan to green, variegated **textures**: well laminated, well sorted **clast types**: clay to gravelly sand, some volcanogenic clasts **distribution**: immediately east of *Northwest Flow* (Qs_2), at the confluence of north and south forks of upper Hoodoo River (Qs_1) **age**: 670 +/- 50 ybp (^{14}C; GSC 5868)

based on aerial recognizance, in the lower sections of *Slide Canyon*, which comprise highly jointed lava flows, domes, and breccia.

At the base of Pumice Ridge, Qvu is directly overlain by two tills ($Qt_{1,2}$) and a lava flow of $Qvap_6$. In *Slide Canyon*, Qvu is not distinguishable from $Qvap_1$ and both units are overlain by $Qvap_{2,4,5}$ and intruded by a dyke of $Qvap_6$.

Unit Qvap

Unit Qvap is volumetrically dominant at Hoodoo Mountain. It is subdivided into six subunits, based on field characteristics and relative stratigraphic position: i) basal (subunit $Qvap_1$), ii-v) medial (subunits $Qvap_{2-5}$), and vi) upper (subunit $Qvap_6$). The unit comprises mainly non-fragmental rocks but also includes monolithologic breccia that are comprised solely of clasts of Qvap; the Qvap breccia are described in the section on fragmental volcanic units. Subunits $Qvap_{1,2,4,5}$ are similar in appearance; they weather rusty brown to tan-yellow and are black on fresh surfaces. These subunits are non-vesicular and locally show flow banding. Subunit $Qvap_3$ varies from black to green and is locally vitrophyric. It typically contains a diverse suite of locally-derived xenoliths and/or autoliths. Subunit $Qvap_6$ is light green to grey-green in handsample, often has a distinctive sheen (similar to the luster of phyllitic metamorphic rocks), and is commonly vesicular. Subunits $Qvap_{1,2,4,6}$ are mainly aphyric (1 to 3 volume % visible feldspar phenocrysts). Locally $Qvap_5$ is distinctly more porphyritic (5-7 % phenocrysts). All subunits save $Qvap_3$ are

highly jointed and radial or curved columnar joints are common (Figures 2.5b and 2.6c).

Unit Qvap comprises lava flows, spires, domes, and dykes (Figures 2.5c, 2.5d, 2.5e, and 2.6a respectively). Subunit $Qvap_2$ comprises thick lava flows which form cliffs up to 200 m high (Figures 2.3d and e) and discontinuously circumscribe Hoodoo Mountain. The cliffs are shown on Plate 1B as hatchered lines and are visible on the Figure 2.2; they help to give Hoodoo Mountain its distinctive, rounded shape. Subunit $Qvap_3$ is very limited in extent. It forms 5 m thick lava flows(?) at the base of Horn Ridge and near the western end of the Hook. Subunit $Qvap_4$ comprises successions of lava flows, each from five to ten metres thick, with only flow breccia separating successive lava flows (Figure 2.5c). This subunit is most prominent in upper *Slide Canyon* and on the western half of the north side of Hoodoo Mountain. Subunit $Qvap_5$ comprises highly jointed lavas, many of which were either emplaced into pre-existing breccia or have thick carapaces of flowtop breccia surrounding them (Figure 2.5b). In Long Valley and upper *Slide Canyon* the subunit included domes with adjacent spines (Figures 2.5e and f).

Subunit $Qvap_6$ is represented by dykes (subunit Qi_4 on Plates 1-3), narrow dyke-like ridges, lava flows, domes, and spines. The dykes intrude older aphanitic phonolite flows and breccia (Figure 2.6a). Spines of $Qvap_6$, which may represent small volcanic necks, form large hoodoos on the western

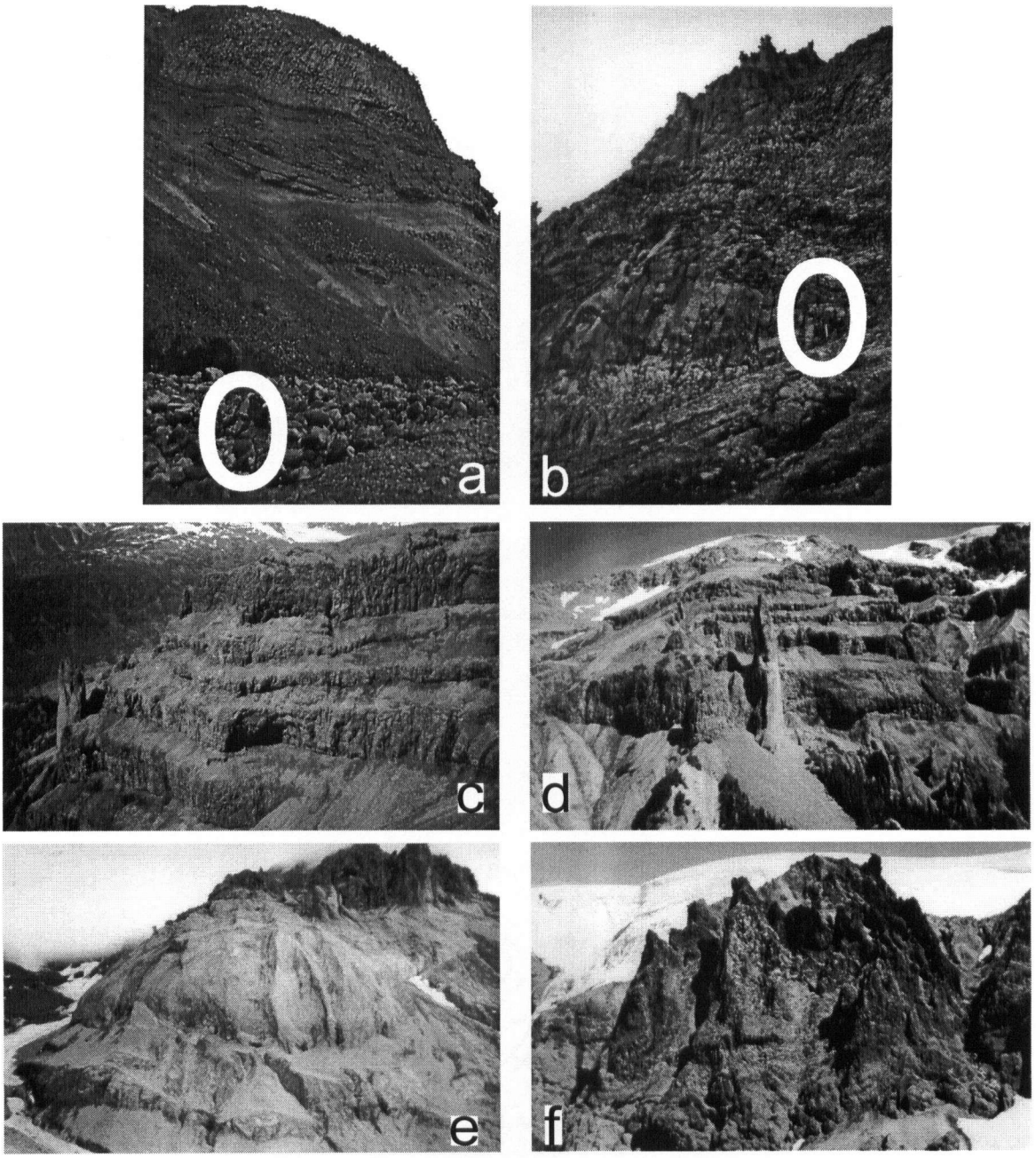

Figure 2.5. Physiographic and stratigraphic expression of the aphanitic phonolites (Qvap). Views are: a) $Qvap_1$ overlying glacial till, southwest Hoodoo Mountain (person for scale), b) irregular columnar jointing in $Qvap_5$ on south Hoodoo Mountain (person for scale), c) five stacked lava flows of $Qvap_4$ in upper *Slide Canyon* (spine in lower left is ~100 m in height), d) spine of $Qvap_6$ (the "Monument"), e) dome of $Qvap_5$ on south Hoodoo (~100 m in height) and f) spines and breccia of $Qvap_5$ in upper *Slide Canyon* (~200 m in height).

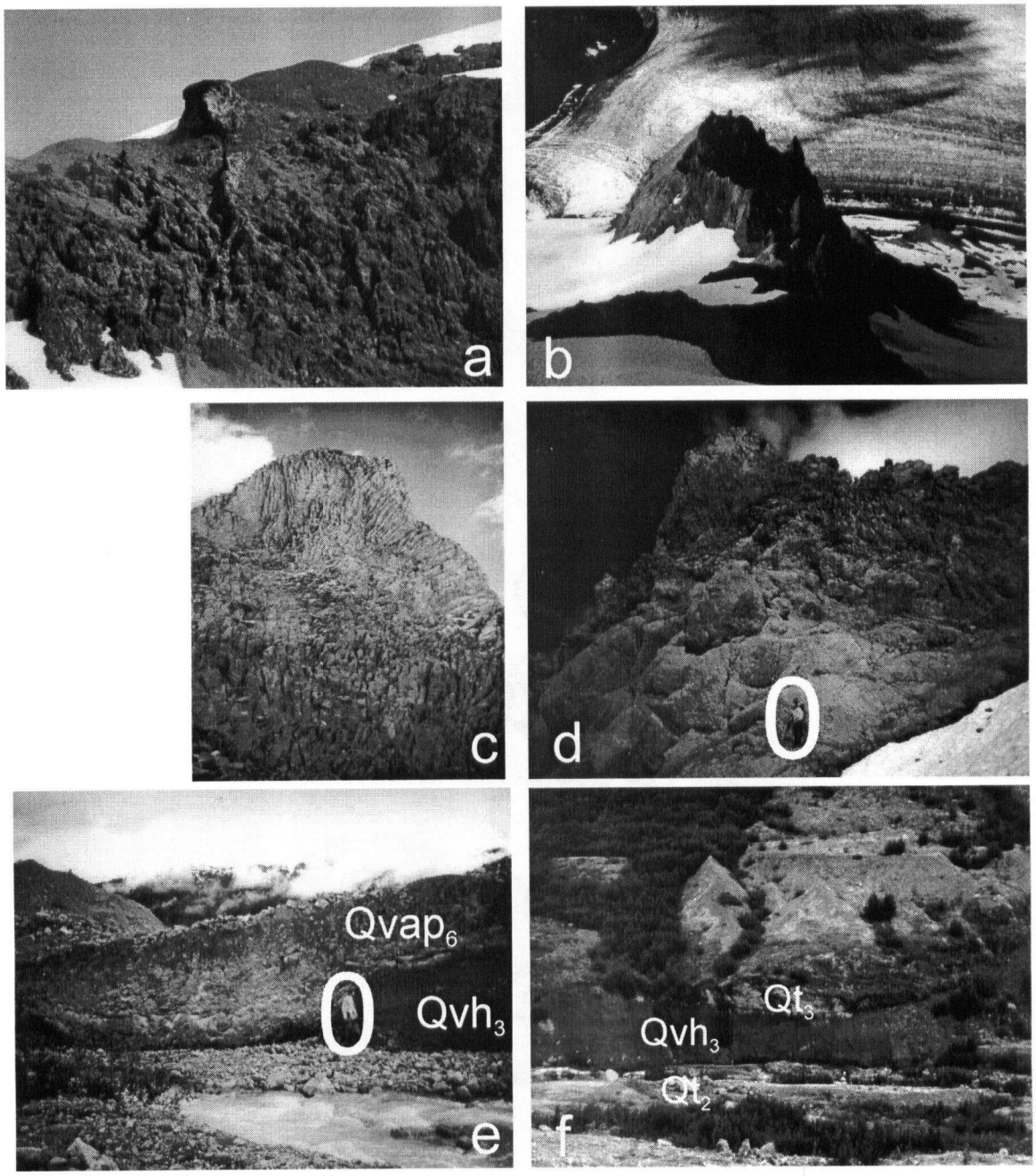

Figure 2.6. Physiographic and stratigraphic expression of units $Qvap_6$, Qvh_3, and Qt. Views are: a) dyke of $Qvap_6$ cutting $Qvap_5$ on southwest Hoodoo Mountain (dyke is ~2 m wide), b) *Horn Ridge* on north side Hoodoo Mountain (ridge ~20 m in height), c) radial jointing in $Qvap_6$ at *The Horn* (joints are ~ 1m wide), d) $Qvap_6$ and Qvh_3 at *The Horn* (person for scale), e) $Qvap_6$ overlying Qvh_2 below *Pumice Ridge* (person for scale), and f) Qvh_2 (~5 m thick) between Qt_2 and Qt_3 at northwestern base of Hoodoo Mountain.

and southern sides of Hoodoo Mountain and include "The Monument" (Kerr, 1948; Figure 2.5d). The Monument has horizontal columnar jointing and appears to be connected to a west-trending dyke (shown as unit $Qvap_6$ on Plate 1). Subunit $Qvap_6$ is commonly spatially associated with yellow deposits rich in glassy, vesicular lapillus (Qvh_3) (Figure 2.9e). The deposits of Qvh_3 overlie and appear to form a carapace around domes, dykes, and lava flows of $Qvap_6$. On the west bank of the upper Hoodoo River, $Qvap_6$ intrudes basement rock and contains a variety of locally derived xenoliths.

The stratigraphic relationships for most of the Qvap subunits are well exposed on the north and west sides of Hoodoo Mountain (Figure 2.7). In Figure 2.7 contacts between units (dotted lines) are irregular and partly obscured by ice and talus; however, $Qvap_{3,4}$, $Qvpy_1$, and $Qvpp_1$ clearly overlie $Qvap_2$. At the western end of the north side of the mountain, $Qvap_1$ is the lowest exposed unit and is directly overlain by $Qvpp_2$ (right hand side of Figure 2.7). At *Slide Canyon*, on the southwestern corner of the volcano (Figure 2.2), $Qvap_1$ and/or Qvu is directly overlain by $Qvap_{2,4,5}$ and $Qvpy_2$. It is also intruded by a spine ("the Monument") and a dyke, both presumed to be $Qvap_6$. Immediately north of *Slide Canyon* along the Hoodoo River a lava flow of $Qvap_1$ directly overlies a glacial till (Figure 2.5a).

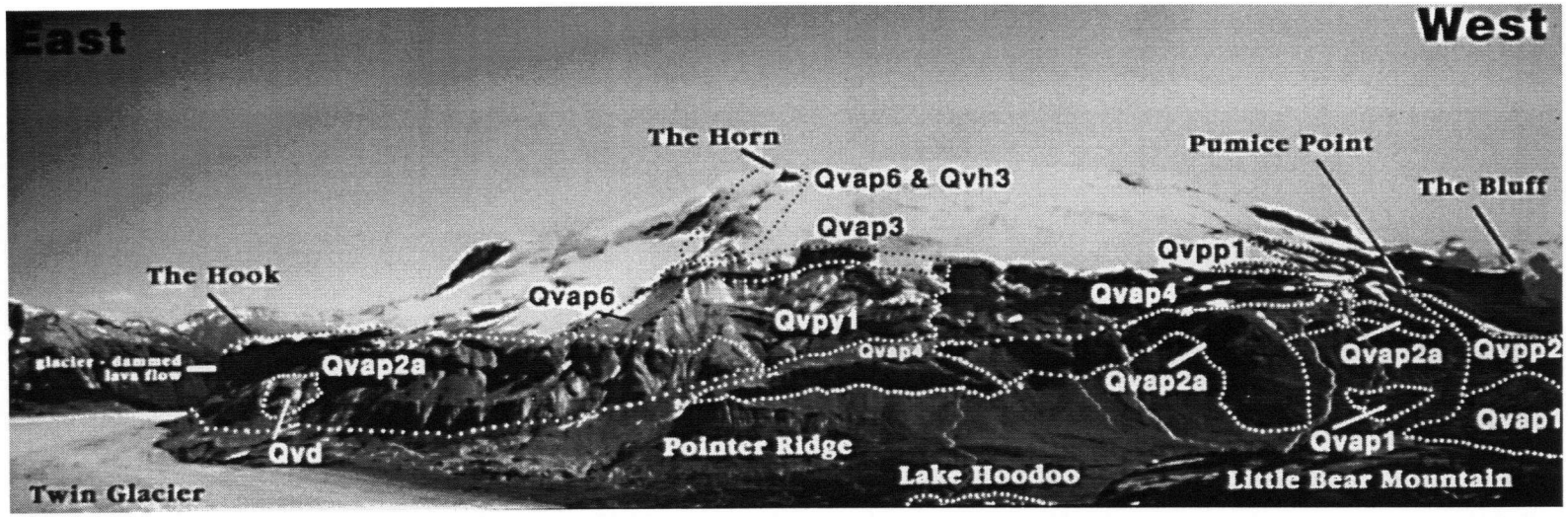

Figure 2.7. View of the north side of Hoodoo Mountain volcano from the summit of *Little Bear Mountain* volcano. The glacier-dammed lava flow (left side of figure) is ~200 m in height and the field of view (from the left edge of Twin Glacier to $Qvap_1$ at the extreme right) is ~5 km. See Figure 2.4 for unit abbreviations.

Unit Qvpp

Unit Qvpp comprises highly porphyritic lavas and two subunits are distinguished as either glacially scoured ($Qvpp_1$) or unglaciated ($Qvpp_2$). The unit comprises gold- to green-grey-weathering phonolite and/or trachyte distinguished from unit Qvap by a much greater abundance of large, clear, fractured alkali feldspar phenocrysts, commonly greater than 2.5 cm long (Figure 2.8b). The feldspars are strongly aligned with flow directions down the slope of the volcano. Phenocrysts of pyroxene and magnetite make up less than 10% of Qvpp and locally the unit contains autoliths and xenoliths of troctolite and gabbro.

Unit Qvpp forms 1-5 m thick lava flows, most of which originated from vents currently beneath the Hoodoo icecap. The upper portions of the lava flows are commonly vesicular and unglaciated flows have aa surfaces (Figure 2.8a). The flows show joint surfaces oriented perpendicular and parallel to flow. The flows are thinner on slopes up to 30°. Some of the flows appear to be sheet flows (i.e. flows not contained within identifiable channels); others are channelized (Figure 2.8e). Lava channels with well-preserved levées (such as the Northwest Flow - Figure 2.8a and e) are common but sheet flows predominate. Up to 11 separate lava pulses used the same channel (Figure 2.8c). Morphological lava flow features include: 1) basal flow breccia, 2) flow margin breccia, 3) flow levées, 4) sidewall and lava channel extension gashes

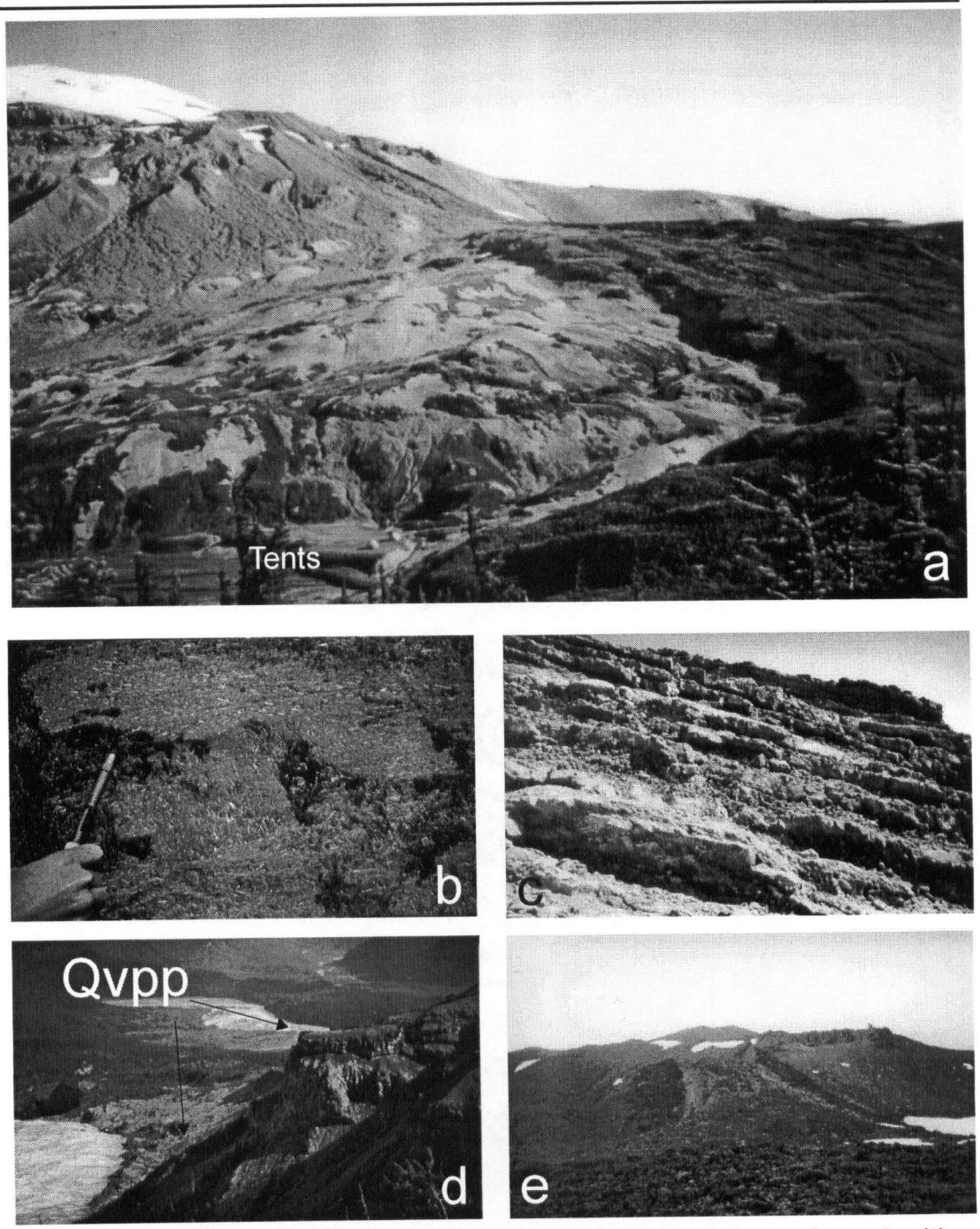

Figure 2.8. Physiographic, textural, and stratigraphic expressions of porphyritic phonolite (Qvpp). Views are: a) *Northwest Flow* (tents for scale are ~1.5 m in height), b) outcrop of trachytic texture (pencil is ~10 cm long), c) sequence of nine lava flows on south Hoodoo Mountain (each flow is ~1 m thick), d) flow of Qvpp over cliff of $Qvap_2$ on the east side of Hoodoo Mountain (cliff is ~50 m in height), and e) lava channel at *Northwest Flow* (channel is ~20 m wide).

(Reidel shears cf. Naranjo et al. 1992), 5) autholiths (Figure 2.8b), and 6) central channel domes (also refered to as Armadillo structures by Naranjo et al. 1992). Several lava channels were recognized on the south and east sides of Hoodoo Mountain and are shown on Plate 2. *Southwest Flow*, on the southwest flank of the volcano (Figure 2.2), appears to have issued from a poorly formed cinder cone (J. Nicholls, per. comm., 1996).

Unit Qvpp directly overlies $Qvap_1$ and $Qvap_4$ on the northern side of Hoodoo Mountain (Figures 2.8a and 2.7, respectively). It also directly overlies $Qvap_2$ on the eastern side of the mountain (Figure 2.8d). At *Pumice Point*, Qvpp of the *Northwest Flow* directly overlies Qvh_3 near the top of the preserved lava channel levées. In *The Bowl*, flows of Qvpp were deflected around a dome of $Qvap_6$, implying that the dome was a pre-existing feature. Below *The Bowl*, almost at the elevation of Hoodoo Glacier, Qvpp overlies $Qvap_6$ and $Qvh_{2,3}$. At the base of *Northwest Flow*, Qvpp overlies a till (Qt_3) and a basaltic breccia (Qvbb) from *Little Bear Mountain* (see Figure 2.10d). Unit Qvpp also underlies parts of both Twin and Hoodoo glaciers. At the terminus of Twin Glacier, Qvpp rests directly on top of Mesozoic basement rocks.

Fragmental Volcanic Rocks, Hoodoo Mountain volcano

Unit Qvap

In addition to lava flows and domes, unit Qvap comprises monolithologic volcanic breccia. The breccia are included in unit Qvap because they are

intimately intermixed with lava flows and domes of Qvap (Figures 2.5e and f) and because they consist almost entirely of clasts of Qvap (Figure 2.9c). The breccia are orange-tan to red-orange weathering, monolithologic, angular to subangular, and both clast- and matrix-supported (Figure 2.9c). The clasts range in size from less than 0.5 cm to greater than 20 cm and are black on freshly broken surfaces. They are cemented by both silica and iron-rich cements, and the surfaces of some clasts have hematite coatings. The breccia clasts commonly have yellow rims several millimetres thick implying that the clasts have been pervasively altered. A crude layering is present in some areas, particularly on the south central side of the volcano immediately east of Long Valley. Outcrops of Qvap breccia weather to form irregular pillars or hoodoos which are characteristic of Hoodoo Mountain. The breccia is most obvious at the top of the volcano where it is complexly intermingled with $Qvap_5$. It also occurs locally with $Qvap_1$ and $Qvap_2$ on the west and north sides of the volcano. Within *Slide Canyon* and immediately to the north, the breccia is intruded by dykes of $Qvap_6$.

Unit Qvpy

Unit Qvpy is mapped as two subunits that are stratigraphically equivalent but not physically contiguous. Subunit $Qvpy_1$ varies from yellow to grey-green and comprises well-indurated ash (juvenile volcanic material <2mm in diameter; Fisher & Schminke 1984) to lapilli (2mm-64mm in diameter; Fisher &

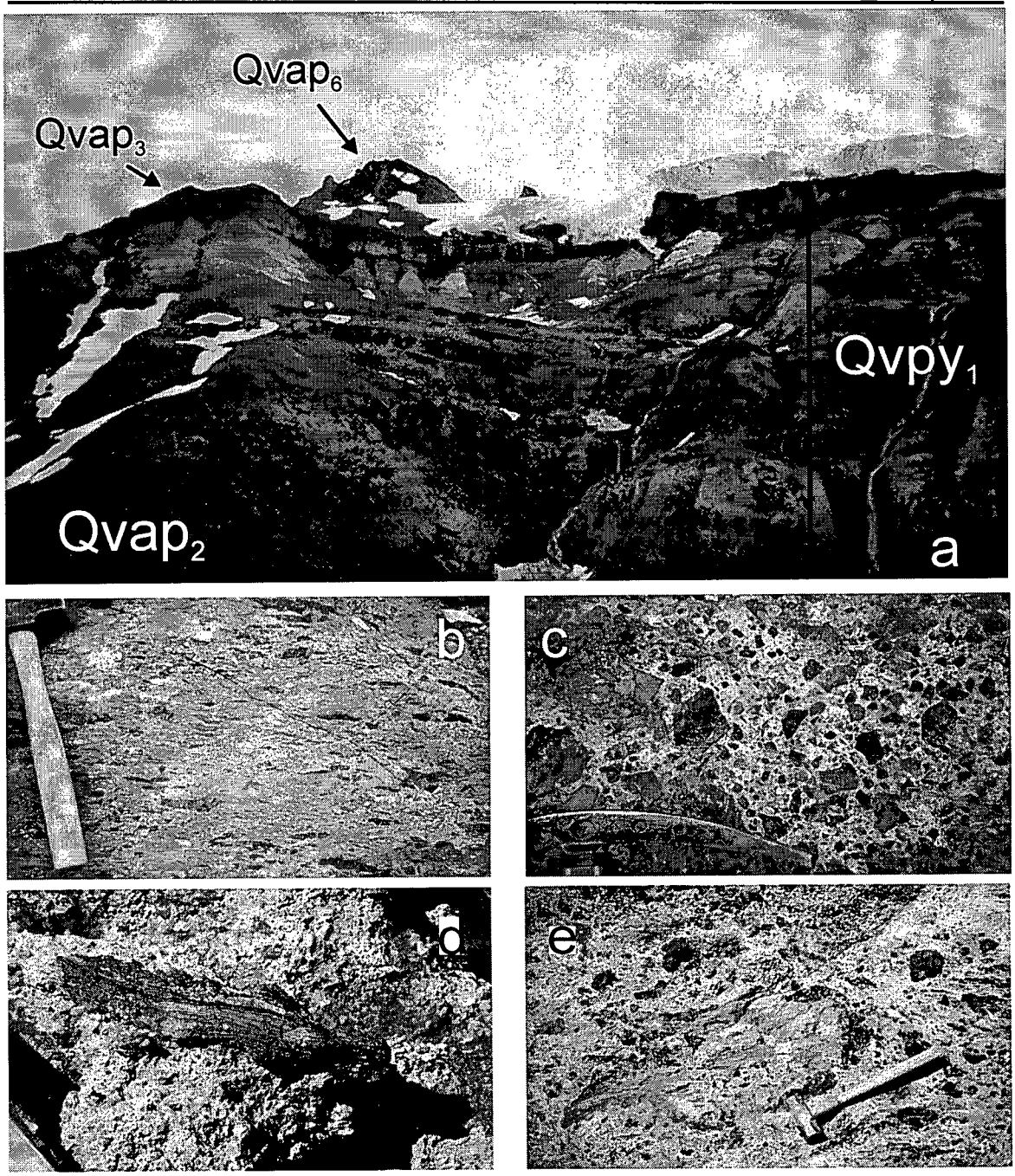

Figure 2.9. Physiographic and textural expressions of pyroclastic rocks ($Qvpy_1$, Qvap, and Qvh_2). Views are: a) *Pointer Ridge* deposit on the north side of Hoodoo Mountain, b) eutaxitic texture in $Qvpy_1$ (hammer is ~30 cm long), c) Qvap breccia (ice axe blade is ~15 cm long), d) block of "woody pumice" approximately 15 cm long at *Pumice Ridge*, and (e) lapilli and bombs in Qvh_3 (hammer is ~30 cm long).

Schminke 1984) consisting of poorly-sorted highly vesicular lava, crystals, and accidental lithic fragments. It is poorly lithified and is recessive. Welding varies from non-existent to strong (Figure 2.9a); locally fiamme (Figure 2.9b) and vitrophyre layers are well developed. The subunit is best exposed on the north-central side of Hoodoo Mountain adjacent to *Pointer Ridge*, where it has a composite thickness of 200 m (Figure 2.9a). Small outcrops of $Qvpy_1$ also occur in the upper *Valley of the Hook* and on the west-central side of the volcano.

Subunit $Qvpy_2$ is also yellow and reccessive. It occurs in upper *Slide Canyon* and along the western side of the volcano. It has not been directly sampled because it is inaccessible. However, it is correlated with $Qvpy_1$ based on its colour, weathering characteristics, and stratigraphic position.

Both Qvpy subunits overlie $Qvap_2$ and are overlain by $Qvap_4$ (Figure 2.7). At *Pointer Ridge*, $Qvap_3$ also directly overlies $Qvpy_1$ (Figure 2.9a).

Unit Qvh

Unit Qvh is divided into three subunits that are found on the southwest, west, north, and northeast sides of the volcano. Subunit Qvh_3 is yellow and contains black, vitric, pumiceous lapillus (Figure 2.9d), grey, vesicular, glass-rimmed blocks and bombs (juvenile volcanic fragments > 64 mm; Fisher and Schminke 1984; Figure 2.9e), and grey to black, accidental clasts of Qvap. The subunit is matrix-supported and generally moderately well sorted, with the

exception of local concentrations of lapilli and blocks. Commonly the highly vesicular, lapilli to block-size fragments are elongate and form "woody pumice" (Figure 2.9d).

Subunit Qvh_2 comprises mainly black to green ash, lapilli, and blocks and/or bombs. It is moderately- to well-sorted and is found only at two locations on the lower slopes of the northwestern edge of the volcano, near Hoodoo Glacier. At both locations it is directly overlain by $Qvap_6$. The southern occurrence is immediately south of lower *Pumice Ridge*. Here Qvh_2 is well-sorted and shows both reverse and normal grading. Glass-rimmed blocks and/or bombs occur as distinct horizons in the deposit, which is a minumum of eight metres thick. The northern occurrence is immediately north of the lower end of *Pumice Ridge*. The deposit is better sorted than at the southern location and comprises mainly vitric lapilli. The northern deposit varies in thickness from three to six metres and appears to thin beneath the middle of a $Qvap_6$ lava flow and thicken on either side of the lava flow (Figure 2.6e).

Subunit Qvh_1 is very similar in appearance to Qvh_3, except it has a much higher concentration of non-vesicular lithic fragments and lacks elongate, highly vesicular lapilli. It also is not clearly associated with $Qvap_6$, although it is cut by a dyke of $Qvap_6$ at one location. This subunit is found only on the southwestern part of the volcano, to the north and south of upper *Slide Canyon*.

Subunits Qvh_2 and Qvh_3 are spatially associated with lava flows, dykes, or domes of $Qvap_6$, except for one deposit in the upper Valley of the Hook. At *Horn Ridge*, *The Bowl*, and *Pumice Point*, Qvh_3 forms a carapace surrounding and on top of $Qvap_6$ and contains blocks of $Qvap_6$ (Figure 2.6d). At the western end of *Pumice Ridge*, Qvh_2 is overlain by $Qvap_6$ (Figure 2.6e) and is both overlain and underlain by glacial tills (Qt_2 and Qt_3; Figure 2.6f). Subunit Qvh_3 also directly overlies $Qvap_4$ and $Qvap_3$ on the northeast and western slopes of Hoodoo Mountain. At two locations on north of *Slide Canyon*, Qvh_1 is interbedded with light green, fine-grained, matrix-supported diamictite sedimentary units (Qvd; Plates 1 and 3).

***Little Bear Mountain* volcano**

Little Bear Mountain volcano comprises predominantly fragmental volcanic rocks, with lesser amounts of massive to pillowed basalt. Mapped units include massive basalt (Qvbm), pillowed basalt (Qvbp), basaltic dykes (Qi_1), basaltic hyaloclastite (Qvbh), basaltic volcanic sandstone and lapilli tuff (Qvbs), and basaltic breccia (Qvbb) (Figure 2.4; Table 2.3). Units Qvbm, Qvbp, and Qvbb commonly contain white, partly melted xenoliths of fine- to medium-grained plutonic and metamorphic rocks.

Table 2.3. Summary field descriptions of map units at *Little Bear Mountain* volcano.

Unit (map symbol)	Description (colour; texture; volcanic forms; distribution)
Qvbb	**colour**: orange to mottled orange-black **textures**: fragmental, sand- to boulder-size clasts, matrix-supported to clast-supported, crude bedding, channel-filling flows **clast types**: porphyritic basalt, crystal fragments **distribution**: everywhere, including down the drainage of the *south fork of the upper Hoodoo River* to the confluence with the *north fork of the upper Hoodoo River*
Qvbs	**colour**: red to orange (weathered), dark brown to black (fresh) **textures**: fragmental, sand-sized clasts, crude to moderately developed bedding, locally abundantly jointed **clast types:** basalt, crystals, glass, granite/syenite **distribution**: mainly on the southernmost flanks of *Little Bear Mountain* volcano
Qvbh	**colour**: dark grey **textures**: fragmental, sand-sized clasts, matrix-supported **clast types:** basalt, crystals, glass **distribution**: mainly on the southeast corner adjacent to *Lake Hoodoo*
Qvbm	**colour**: light to dark grey to black **textures**: porphyritic (10-15 % phenocrysts of plagioclase, olivine, pyroxene), unjointed, slightly vesicular (<10%), with granite/syenite inclusions **volcanic forms**: dykes, lava flows(?), lava tubes(?) **distribution**: mainly on the northern half of *Little Bear Mountain* volcano
Qvbp	**colour**: light to dark grey to black to mottled orange and black **textures**: porphyritic (10-15 % phenocrysts of plagioclase, olivine, pyroxene), unjointed, slightly vesicular (<10%), with granite/syenite inclusions **volcanic forms**: pillowed lava flows **distribution**: on the southwest flank of the northern summit of *Little Bear Mountain* volcano **age**: ~240 Ka (Ar-Ar date)

Non-fragmental Volcanic rocks, Little Bear Mountain volcano

Unit Qvbm

Unit Qvbm underlies the summit of *Little Bear Mountain* and comprises grey to black olivine basalt as lava flows and filled lava tubes. It is most abundant on the lower, northeast side of the summit near Twin Glacier. Unit Qvbm is highly porphyritic (>15% phenocrysts), vesicular, and contains large phenocrysts of plagioclase (greater than 2 cm), olivine, and black, glassy pyroxene.

Unit Qvbp

Unit Qvbp comprises round to oval pillows of Qvbm and interstitial basaltic hyaloclastite. Individual pillows range in size from 45 by 48 cm to 1 by 3 m (Figure 2.10c). The pillows are radially jointed and locally contain white xenoliths oriented parallel to the pillow exterior surfaces.

Unit Qi_1

Unit Qi_1 comprises dykes of Qvbm. The dykes intrude Qvbb on the northeast, south, and west flanks of the summit of the mountain and generally trend east to west (54 to 72 °). Some of the dykes are nearly conformable to the layering in the breccia; however, the dykes crosscut the breccia on top of the summit. Dykes of similar appearance intrude the Mesozoic basement rock immediately west of the volcano.

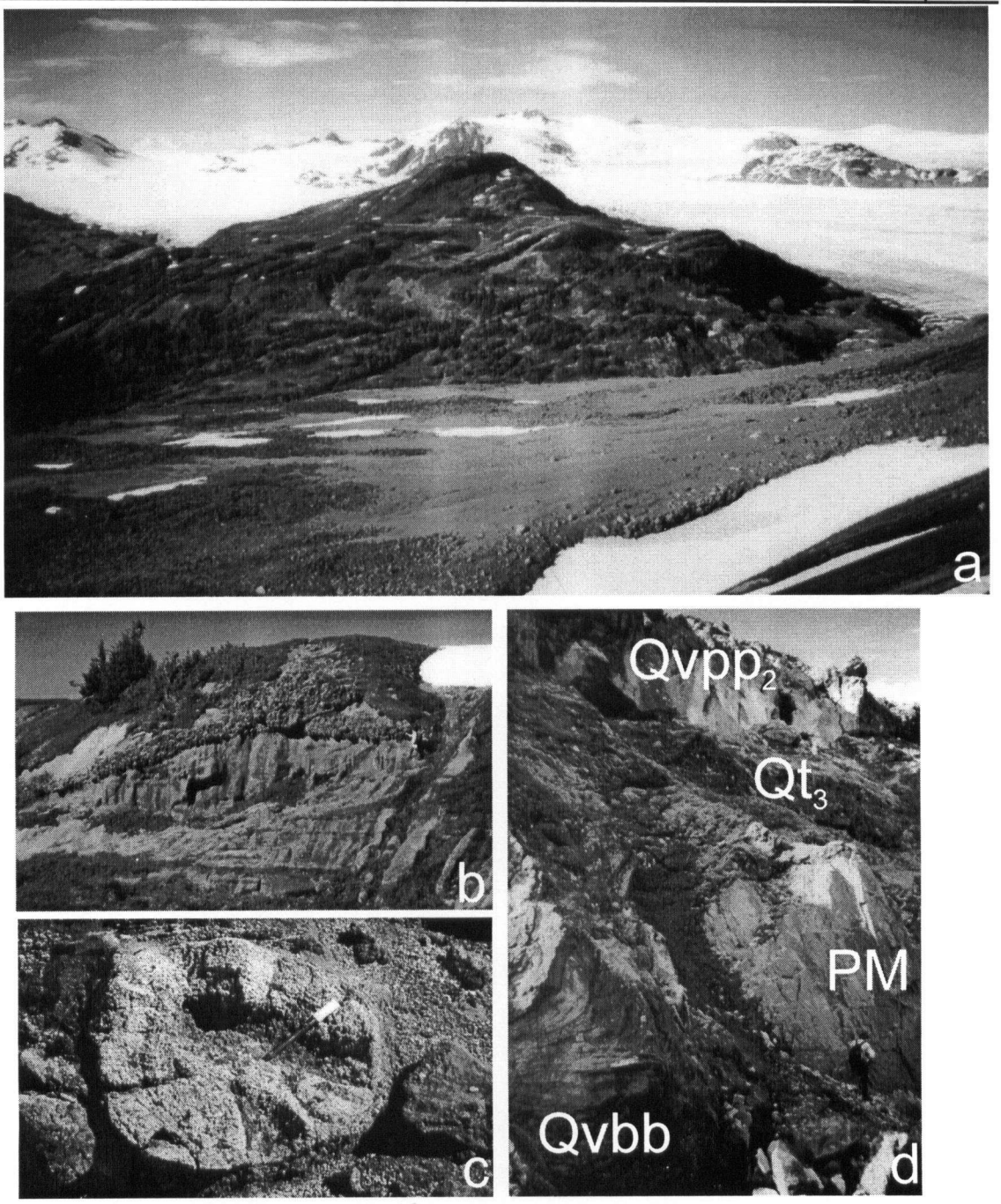

Figure 2.10. Physiographic and stratigraphic expression of units at *Little Bear Mountain*. Views are: a) summit and central plateau (~1.5 km wide) of *Little Bear Mountain* as viewed from Hoodoo Mountain, b) lens of basaltic breccia (Qvbb) cutting basaltic hyaloclastite (Qvbh) on southeast side of the volcano (person for scale), c) pillowed basalt (Qvb) (flare pen is ~15 cm long), d) basement overlain sequentially by Qvbb, till (Qt_3), and $Qvpp_2$ (person for scale).

Fragmental Volcanic Rocks, Little Bear Mountain volcano

Unit Qvbh

Unit Qvbh is volumetrically minor and comprises grey to orange-tan crystal lithic lapilli tuff on the southeastern side of *Little Bear Mountain*, near *Lake Hoodoo*. It comprises crystals of plagioclase, olivine, and pyroxene, all generally less than 0.5 cm long. Angular, equant fragments of basaltic glass with a continuous size range from 0.5 cm to less than 0.1 cm form the matrix. Unit Qvbh locally contains thin (<2 m) lenses of basaltic breccia (Figure 2.10b) as well as isolated cobbles of basalt and rounded metavolcanic rocks.

Unit Qvbs

Unit Qvbs is an orange to tan unit comprising ash-sized fragments of crystals, basalt, and volcanic glass. It is only abundant on the southern end of the volcano. The unit is poorly to moderately sorted but crude layering is present. The unit is characteristically cross-cut by conjugate sets of joints. The sorting and bedding are interpreted as indicating that this unit formed by local transport of juvenile volcanic material.

Unit Qvbb

Unit Qvbb is volumetrically the most abundant unit at *Little Bear Mountain* (Figure 2.4 and Plate 1). It is an orange-brown basaltic breccia containing vitrophyric, basalt clasts ranging from 1-20 cm in size. The matrix to the clasts comprises sand-sized vitric, lithic, and crystal grains. Matrix- and clast-

supported varieties exist and locally have abundant conjugate joint sets which have been filled with orange sand- sized matrix. On the northern half of the volcano, basalt clasts that are round to ovoid, contain heavily oxidized rims, and have vesicular interiors are interpreted as pillow lava fragments. In these areas the breccia is equivalent to para-pillow lava of Jones (1970). In several areas the basaltic breccia lava filled channels in underlying Qvbh (Figure 2.10b).

On the southernmost slopes of *Little Bear Mountain*, Qvbb is directly overlain by Qt_3 and $Qvpp_2$ (Figure 2.10d). It unconformably overlies Mesozoic basement rocks along both the southern and western parts of the volcano (Figure 2.10d). Immediately above the confluence of the north and south forks of upper Hoodoo River, the Qvbb is laminated and interbedded with reworked Qvbs. On the southeastern edge of *Little Bear Mountain* and the southern lip of the central plateau a southeastward plunging layer of Qvbb cuts Qvbh (Figure 2.10b).

Other Rock Types

Dykes

Intrusive rocks of unit Qi include dykes that cut both the HMVC stratigraphy and the surrounding Mesozoic country rocks. Qi_1 and Qi_4 were described above, as they are genetically related to *Little Bear Mountain* volcano or correlated to $Qvap_6$ respectively. The other two subunits, Qi_2 and Qi_3, cannot

be correlated with any other units based on field stratigraphic relationships alone.

Subunit Qi_2 comprises purple-brown, vesicular, basaltic dykes exposed in the bed of upper Hoodoo River, 200 m east of Hoodoo Glacier (Plate 1). The dykes trend 140°, vary in width from 0.3 to 1 m, and have horizontal columnar joints. One of the dykes has small, cm-sized granitic xenoliths.

Subunit Qi_3 comprises a pink-brown, vesicular, dacitic dyke. It occurs immediately west of upper Hoodoo River (Plate 1). The dyke is jointed and is 3 m wide. It is cut by vesicular dykelets of Qi_2.

Sedimentary Deposits

Sedimentary deposits of the HMVC include surficial colluvium (Qc), fluvial deposits (Qf), glacial deposits (Qs and Qt), and diamictites (Qd) (Figure 2.4, Table 2.2, Plates 1-3). The non-surficial glacial deposits that occur within the volcanic stratigraphy at Hoodoo Mountain volcano are described below in more detail. The diamictites and surficial sediments, including locally-derived talus (Qc), fluvial deposits (Qf), and one glacial till (Qt_4), are discussed elsewhere (Plate 3; Edwards et al. 1997).

Unit Qs

Rhythmically interbedded sand and silt of unit Qs weathers variegated tan, brown, green, and yellow. It is divided into two subunits, both of which

occur along the upper Hoodoo River. Subunit Qs_2 is an isolated occurrence 200 m west of *Lake Hoodoo*, on the northeastern edge of *Northwest Flow* (Figure 2.2 and Plate 1). Here, the well-laminated sequence comprises silt-rich mudstones at least 1 m thick and is underlain by a coarse, gravel-rich diamictite. The sequence is overlain by gravely black sand and brown to orange silt. Qs_2 has laminations that are less than 1 mm thick and are defined by variations in colour (brown to grey-green to yellow). The upper contact with the black sand is sharp and, locally, the upper part of the rhythmite has cm-scale, gravel-filled load structures. Micro-thrust faults disrupt some of the beds. Qs_2 appears to have been deposited in a small basin formed by blockage of the stream drainage by a lava flow of Qvpp from Hoodoo Mountain. Three different terrace levels are obvious at this location: two stratigraphically above Qs_2 and another at its base. On the west end of the paleobasin a levée of till dips steeply to the east, from the upper terrace down to a level below the exposed base of Qs_2.

Subunit Qs_1 is laterally more extensive than Qs_2 and comprises two adjacent deposits. It occurs immediately east of the confluence of two branches of the upper Hoodoo River (south fork and north fork), in a large basin topographically below *Northwest Flow* but above Hoodoo Glacier (Plate 1). At both the south fork and the north fork localities multiple sets of well-laminated,

alternating sand and silt layers occur within a thicker package of poorly sorted sand (Figures 2.11a and b).

On the south fork of upper Hoodoo River the laminated sediments are exposed in a 37 m high stream bank. The top of the upper rhythmite set is 31 m above the base and is 0.7 m thick. It is overlain by a dark, moist, gravely sand, which also occurs between the other two rhythmite sets. The individual layers are generally less than one centimetre thick and have been variably folded and faulted on a centimeter scale. The second deposit rises to a height of 25 m from the bottom of the stream bank of the north fork of upper Hoodoo River (Figure 2.11b), consists mainly of alternating light and dark sand size grains, and is 0.64 m thick. The top of the lowest set of well-laminated layers is 22 m from the bottom and 0.5 to 1 m thick. It consists of alternating dark layers of sand size grains and light layers of silt to clay size grains. The base of the bank comprises tan, matrix-supported, polymictic diamictite. Wood collected from near the base of the north fork deposit yielded a ^{14}C date of 670 +/- 50 years BP (radiocarbon age determination GSC 5868).

Unit Qt

Unit Qt comprises four subunits of polymictic diamictites that are interpreted as tills. Locally unit Qt is interbedded with units from *Little Bear Mountain* and Hoodoo Mountain volcanoes. Subunit Qt_4 comprises glacial till from the current period of glacial retreat and is not discussed further. Subunit

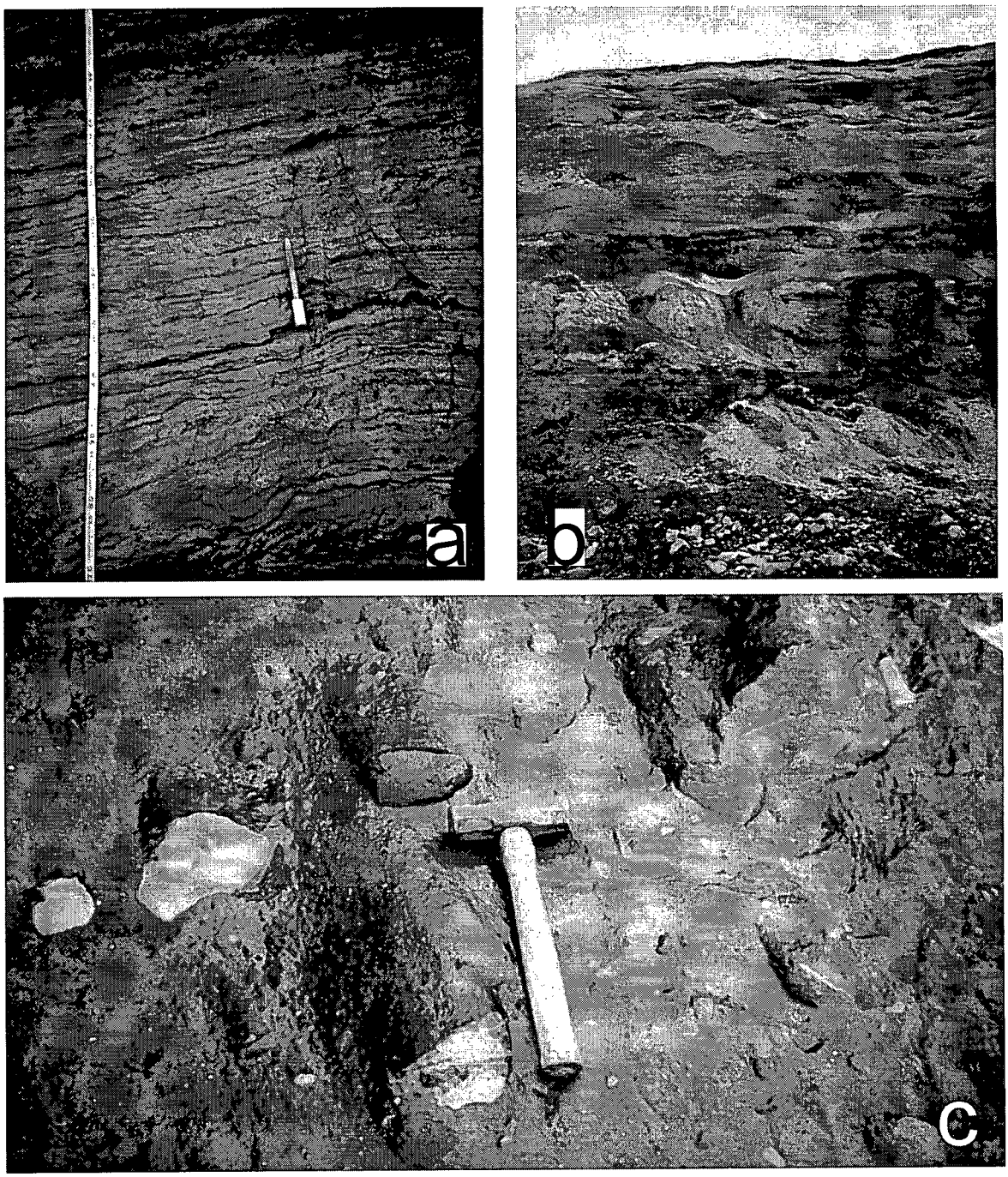

Figure 2.11. Stratigraphic and textural expressions of glacial deposits. Views are: a) finely lamenated mudstones along the south fork of upper Hoodoo River (flare pen is ~15 cm long), b) interlayered sand and silt along north fork of upper Hoodoo River (person for scale), and c) well-indurated till (Qt_2) northwest of Hoodoo Mountain.

Qt_1, the stratigraphically oldest till, is grey, polymictic, poorly lithified, approximately 5 m thick, and is directly on top of a pre-Hoodoo(?), jointed, rhyolitic to dacitic volcanic unit. Qt_1 is overlain by Qt_2, which is a brown, well-lithified till with rounded clasts of both fresh, vesicular, plagioclase-phyric basalt and of metamorphic basement rocks (Figure 2.11c). Subunit Qt_2 is approximately 5 m thick. The basalt clasts probably are derived from *Little Bear Mountain* volcano, as no other Recent basaltic volcanoes are known to occur immediately north of the HMVC.

Subunit Qt_3 is found along the south edge of *Little Bear Mountain* as well as overlying Qt_2 at the eastern edge of Hoodoo Glacier (Figure 2.6f). In both places Qt_3 is grayish tan and matrix-supported. Round clasts of green quartzite, metavolcanic rocks and vesicular basalt make up 15-20 % of the unit and occur in a fine sand to coarse silt matrix. Qt_3 also locally has irregular, flaggy horizontal joints and flattened clasts, which are oriented parallel to the jointing. This till ranges from only a few metres thick on most of *Little Bear Mountain* to 10 m thick on the south fork of upper Hoodoo River. Qt_3 is interpreted as a lodgment till based on: (1) the abundance of matrix over clasts, (2) subhorizontal jointing, (3) local clast imbrication, and (4) bullet-shaped clasts.

The lowest till directly overlies Qvu at the base of Pumice Ridge and appears to be overlain by lava flows of $Qvap_1$ at the base of *Slide Canyon*. However, because the tills have not been studied in detail, the correlation

between them is tenuous. Subunit Qt_2 is conformably overlain by Qvh_2, which is in turn overlain by Qt_3 at the base of Pumice Ridge. Further east, on the northeastern edge of *Northwest Flow*, Qt_3 overlies Qvbb and is overlain by $Qvpp_2$.

Summary of Relative and Absolute Stratigraphic Constraints

Relative Age Constraints

Although the stratigraphy and correlations for many of the units are well known (Figure 2.12 and Plate 1C), some of the units are not well-defined, as indicated by the long vertical bars on Plate 1C. For example, unit Qvu is overlain by three different tills (Qt_{1-3}) at the base of Pumice Ridge, but apparently rests on top of another till at the base of *Slide Canyon*. Thus, either a fourth till occurs in the stratigraphy, or unit Qvu was deposited over a time interval that included a period of glaciation, or unit Qvu has currently unrecognized subunits.

The maximum stratigraphic age of *Little Bear Mountain* volcano is also not well constrained by field relationships. Unit Qvbb from *Little Bear Mountain* rests directly and unconformably on Mesozoic country rocks along the west and south sides of the volcano (Figure 2.4). The south fork of the upper Hoodoo River exposes the contacts between the basement metamorphic rocks, Qvbb, Qt_3, and $Qvpp_2$ (Figure 2.10d). The stratigraphy in the exposures demonstrates that Qvbb is older than $Qvpp_2$ and Qt_3. Farther south, at the base of *Pumice*

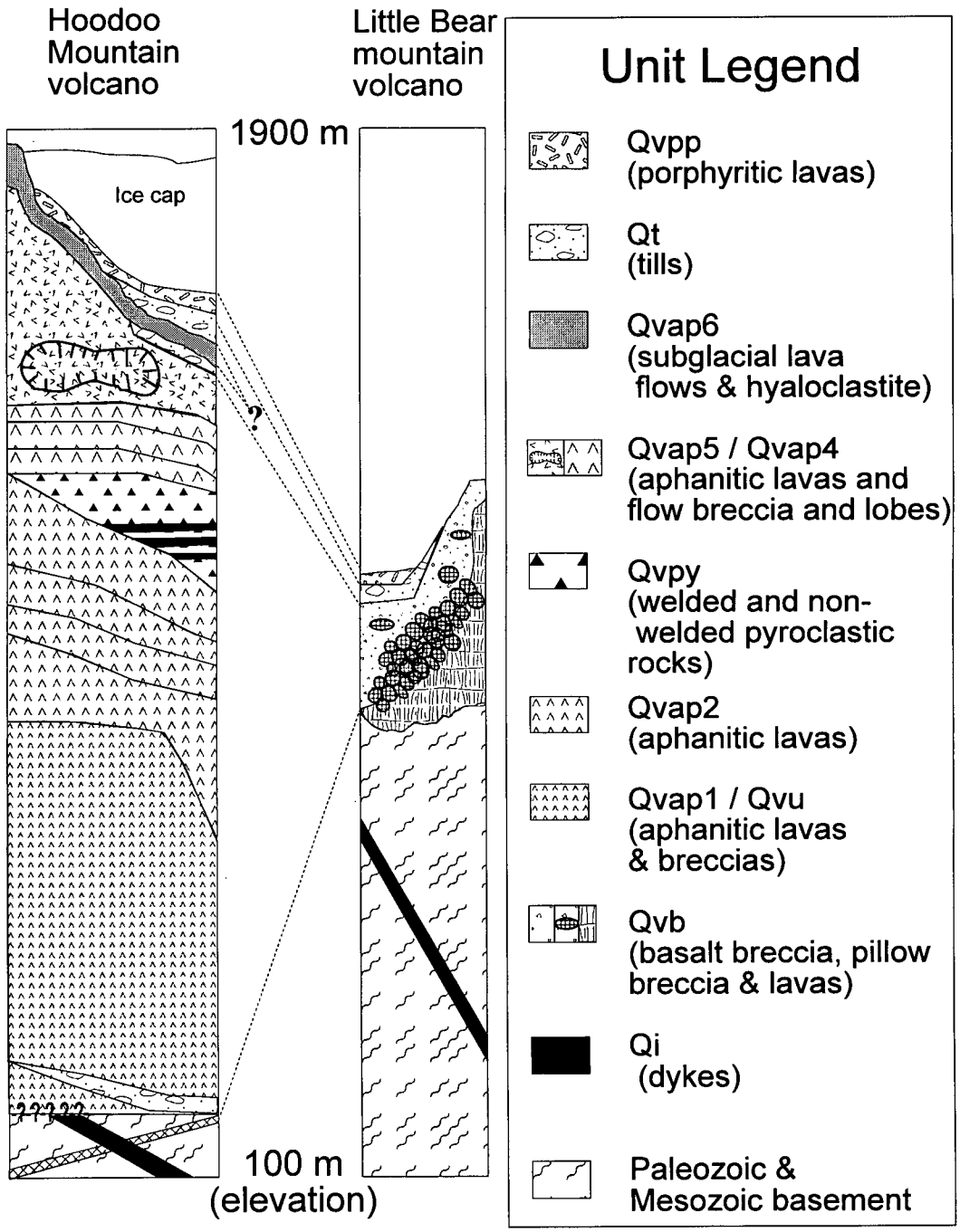

Figure 2.12. Composite stratigraphic section illustrates relationships, approximate thicknesses, and correlations of units of the Hoodoo Mountain and *Little Bear Mountain* volcanoes.

Ridge, Qt_2 has clasts of vesicular, plagioclase porphyritic basalt very similar to Qvbm. If the clasts are Qvbm, then *Little Bear Mountain* must be older than Qt_2 as well as $Qvap_6$, which is underlain by Qt_2. However, no other field relationships provide constraints on the maximum relative age of *Little Bear Mountain*.

Exposures on the north and west sides of Hoodoo Mountain provide stratigraphic constraints for Hoodoo Mountain volcano. Strata along the north side of Hoodoo Mountain (Figure 2.7) are the reference area for the stratigraphy presented in Figure 2.12. Unit $Qvap_1$ is exposed in two places in the west (lower right hand side of Figure 2.7). $Qvap_1$ is only directed overlain by $Qvpp_2$ from *Northwest Flow*. However, it is at a lower elevation than the cliffs that comprise $Qvap_2$, which extend from just west of *Pointer Ridge* to the Hook. At *Pointer Ridge*, $Qvpy_1$ was deposited on top of $Qvap_2$. Not as clear from this distance, however is the tongue of $Qvap_4$ that forms *Pointer Ridge* and overlies $Qvpy_1$. $Qvpp_1$ overlies $Qvap_4$ on the upper western side of Figure 2.7, and $Qvap_6$, forming *The Horn* and Horn Ridge, sits directly on top of $Qvap_3$. $Qvap_3$ is overlain by $Qvap_4$ at the western edge of the Hook.

As noted by Kerr (1948), the oldest units at Hoodoo Mountain have been heavily glaciated and may have experienced several episodes of glaciation.

Isotopic Age Dating

Isotopic age constraints for the HMVC include conventional unpublished K-Ar dates on five whole rock samples collected by J.G. Souther and R.L. Armstrong in 1976 (UBC geochronology laboratory unpublished data; Souther, 1990) and unpublished high precision ^{40}Ar-^{39}Ar dates for samples collected by the author during the new mapping and analyzed by M. Villeneuve (GSC Ottawa) (Table 2.4). The stratigraphic context described above for the samples dated by ^{40}Ar-^{39}Ar is shown in Figure 2.13. Because the new geochronometry is still underway the new ^{40}Ar-^{39}Ar dates reported here must be considered preliminary and no uncertainties are reported.

The K-Ar ages range from 110 +/- 30 Ka to 20 +/- 13 ka; however, the locations for the dated samples are plotted on large scale (1:250 000 scale) field maps and are not well known, due, in part, to the fact that no geological map for Hoodoo Mountain volcano existed prior to 1994. The dated samples appear to be from units Qvu and Qvap based on their petrographic character and poorly-known locations. The age range corroborates the protracted eruption of Qvap inferred from the field-based stratigraphy.

To better constrain the duration and sequence of eruption at the HMVC, ten samples were dated using specially developed ^{40}Ar-^{39}Ar techniques by M. Villeneuve (GSC Ottawa). The ^{40}Ar-^{39}Ar results generally corroborate the field-based stratigraphy and provide some additional stratigraphic constraints (Figure 2.13). The results for unit Qvpp show that it erupted over a period of at

Table 2.4. Summary of isotopic age constraints for volcanic rocks from the HMVC.

Sample No.	Map Unit	Age (Ka)	Dating method, material and comments
V/SE1701-76	$Qvap_2$[1]	20 +/- 13	K-Ar w.r.[3]; west Hoodoo
V/SE1703-76	Qvu[1]	90 +/- 10	K-Ar w.r.[3]; base of *Slide Canyon*
V/SE1704-76	Qvu[1]	110 +/- 30	K-Ar w.r.[3]; base of *Slide Canyon*, north of sample V/SE1703-76
V/SE1705-76	$Qvap_2$[1]	32 +/- 16	K-Ar w.r.[3]; near *the Hook*
V/SE1706-76	$Qvap_2$[1]	51 +/- 15	K-Ar Fsp[3]
93BRE8	$Qvpp_1$	9-10	^{40}Ar-^{39}Ar w.r.[2,3]; near *Northwest Flow*, northwest Hoodoo
93BRE44	$Qvpp_1$	28	^{40}Ar-^{39}Ar w.r.[2,3]; east Hoodoo
94BRE78	$Qvap_6$	30-40	^{40}Ar-^{39}Ar w.r.[2,3]; *Pumice Ridge*
93BRE16	$Qvap_4$	54	^{40}Ar-^{39}Ar w.r.[2,3]; north Hoodoo
94BRE119	$Qvap_2$	80	^{40}Ar-^{39}Ar w.r.[2,3]; west Hoodoo
93BRE168	$Qvap_1$	85	^{40}Ar-^{39}Ar w.r.[2,3]; northwest Hoodoo
94BRE2	Qvbm	235	^{40}Ar-^{39}Ar w.r.[2,3]; *Little Bear Mountain*
94BRE74	Qi_3	1800	^{40}Ar-^{39}Ar w.r.[2,3]; between upper Hoodoo River and Hoodoo Glacier

[1] Sample information from unpublished UBC geochronology files (Armstrong & Souther 1976; V = volcanic, SE1701-76 is the sample number and year of collection)
[2] M. Villeneuve (GSC unpublished data)
[3] w.r. = whole rock, Fsp = feldspar

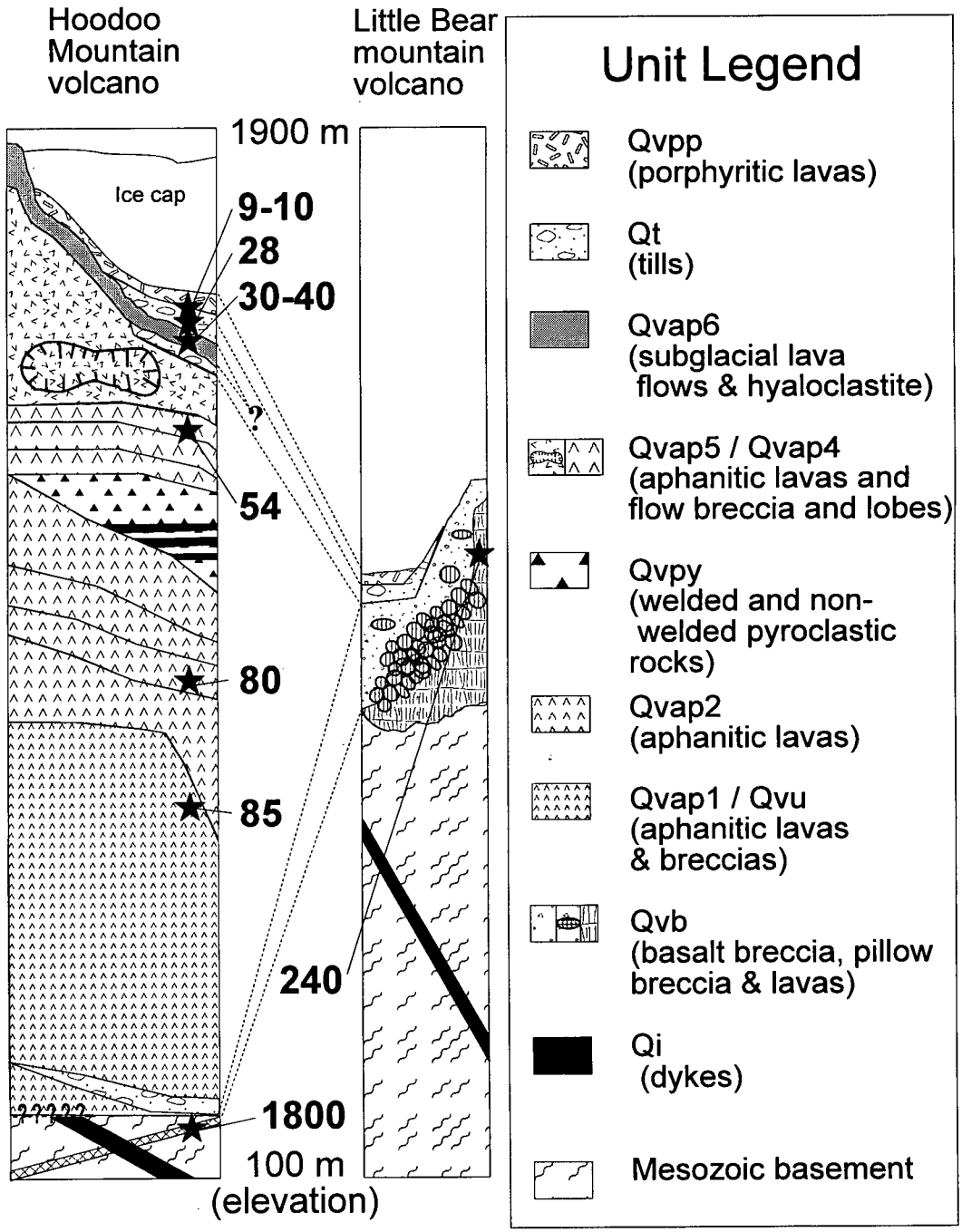

Figure 2.13. Stratigraphic positions of samples dated by $^{40}Ar/^{39}Ar$. Ages are from M. Villeneuve (GSC unpublished data), are given in units of Ka (in bold), and are also summarized in Table 2.4.

least 18 000 years, from 9-10 Ka to 28 Ka. The result of 30 to 40 Ka for unit $Qvap_6$ is significant because it gives a minimum age to till Qt_2 and a maximum age to Qt_3, thus constraining the ages for two different periods of glaciation. The results for subunits $Qvap_4$ and $Qvap_2$ of 54 Ka and 80 Ka respectively also constrain the timing for the deposition of interbedded unit $Qvpy_1$. The oldest ^{40}Ar-^{39}Ar age for Hoodoo Mountain is 85 Ka, from unit $Qvap_1$.

The ^{40}Ar-^{39}Ar results for *Little Bear Mountain* are very important for constraining the timing relationship between it and Hoodoo Mountain. The indicated age of 240 Ka demonstrates that *Little Bear Mountain* is older than all of the dated units at Hoodoo Mountain.

The importance of the ^{40}Ar-^{39}Ar results for Qi_3 is difficult to assess based on field observations because of the lack of stratigraphic constraints for this unit. However, if it is related to the HMVC, it extends the known period of magmatic activity at the complex to 1800 Ka.

Other absolute age constraints for units at the HMVC include a ^{14}C date on wood within a lacustrine rhythmite (Qs_2) of 670 +/- 50 yr BP (radiocarbon age determination GSC 5868) and age estimates from one of the youngest flows on southwest side of Hoodoo Mountain (*Southwest Flow*) of >180 years from tree ring estimates on living trees (BC Hydro, 1985). Sample 5868 is from a gravelly layer at the base of a sequence of rhythmically-layered sand and silt. The ^{14}C age places an upper limit on the depositional age of Qvbb from *Little*

Bear Mountain volcano. Both deposits of Qs_2 were probably deposited in a glacially-dammed lake when Hoodoo Glacier was at a much higher level than today - possibly during the Little Ice Age. If so, this age may provide an estimate for the age of the Little Ice Age in the Iskut Region.

The ^{40}Ar-^{39}Ar results and the new stratigraphic observations lead to a revision of the stratigraphy of the Hoodoo Mountain volcanic centre as follows: 1) magmatism at the HMVC may have begun as early at 1800 Ka with the intrusion of dykes; 2) for almost 1600 Ka no record is known until the formation of *Little Bear Mountain* at 240 ka; 3) in the last 100 Ka Hoodoo Mountain volcano has undergone at least five episodes of volcanic eruption producing lava flows and pyroclastic deposits.

2.3. DESCRIPTIVE PETROGRAPHY AND PETROCHEMISTRY

Samples of the non-fragmental volcanic rocks from all of the units in the HMVC were collected for petrographic and geochemical characterization. Sample locations, units, and rock types are given in Table A2.1 (see Appendix). The samples were examined petrographically using standard transmitted light techniques (Table 2.5). Plagioclase from one sample from *Little Bear Mountain* (94BRE2) was also examined using Nomarski Differential Interference Contrast imaging (NDIC) following the techniques given by Anderson (1984) and Pearce and Kolisnik (1992). Plagioclase from this sample was also

chemically analyzed using a Cameca SX-50 electron microprobe at U.B.C. under standard operating conditions (15 kV and 20 nA) (see Appendix A2.4 for results). A limited number of samples from Hoodoo Mountain volcano were also examined using a Scanning Electron Microscope at U.B.C. to identify groundmass phases.

A complete set of whole rock chemical analyses for major, minor, trace, and rare earth elements are given in the appendix (Tables A2.2 and A2.3 respectively). Representative chemical analyses for the major units are given in Table 2.6. All chemical analyses were done by the Geological Survey of Canada Analytical Laboratories; Hauksdóttir (1994) discussed in detail the precision and accuracy estimates for the GSC laboratory.

Petrography

The petrography of the non-fragmental volcanic units comprising the HMVC is summarized in Table 2.5; Figures 2.14 and 2.15 show typical textures of the units from Hoodoo Mountain and *Little Bear Mountain*. Based on mineralogy, all of the samples from Hoodoo Mountain are trachytes and/or phonolites, and all of the samples from *Little Bear Mountain* are plagioclase-phyric alkali olivine basalts.

Table 2.5. Summary of petrography for non-fragmental volcanic rocks from the HMVC.

Unit	Phenocryst Mineralogy[1,2]	Groundmass Mineralogy	Textures / Other
$Qvap_{(1-5)}$	alkali feldspar (5-10%, **p-mp**), clinopyroxene (1-5%, **p-mp**), magnetite[3] (1-5%, **p-mp**)	alkali feldspar, clinopyroxene, magnetite[3], nepheline[3], cancrinite[4]	holocrystalline, trachytic, with 5 different groundmass textures based on relationships among pyroxene, magnetite, and feldspar
Qvap6	alkali feldspar (1-5%, **mp**), clinopyroxene (1-5%, **p-mp**), magnetite[3] (1-5%, **mp**)	alkali feldspar, clinopyroxene, magnetite	holocrystalline to hyalocrystalline, sparsely porphyritic (<5% phenocrysts) to aphanitic, trachytic, vesicular
Qvpp	alkali feldspar (15-20%, **M-mp**), clinopyroxene (1-5%, **p-mp**), magnetite[3] (1-5%, **p-mp**)	alkali feldspar, clinopyroxene, magnetite[3], nepheline[3]	holocrystalline (<5% glass), trachytic, commonly glomeroporphyritic, vesicular, with rare troctolite inclusions
$Qvb_{(m,p)}$	plagioclase feldspar (10-15%, **M-mp**), olivine (5-10%, **M-mp**), clinopyroxene (1-5%, **M-mp**), magnetite[3] (1-5%, **p**), ilmenite[3] (1-5%, **p**)	plagioclase, olivine, titanaugite, opaques	holocrystalline to hyalocrystalline, porphyritic, tachylitic, glomeroporphyritic, xenocrystic with common inclusions of partly reacted coarse- and fine-grained granite and syenite and metarhyolite; at least three morphologically different populations of plagioclase phenocrysts and microphenocrysts; sieve-textured clinopyroxene; rounded apatite xenocrysts

[1] volume percent modes are visually estimated and in parentheses
[2] **M** = megacryst (>5mm), **p** = phenocryst (>0.5 mm, <5 mm), **mp** = microphenocryst (>0.05 mm, < 0.5mm)
[3] identified by scanning electron microscope
[4] qualitative SEM scan showed peaks for Na, Al, Si and Cl

Hoodoo Mountain

At Hoodoo Mountain volcano the non-fragmental volcanic units (Qvap and Qvpp) vary from aphanitic to porphyritic and comprise phenocrysts of alkali feldspar (Fsp), magnetite (Mt), and hedenbergitic clinopyroxene (Cpx) in a groundmass of similar mineralogy (Table 2.5); the groundmass also contains nepheline (Ne). Abundances of phenocrysts vary from one percent to greater than twenty percent (e.g., Figure 2.14). In general, samples from higher in the stratigraphy (e.g., unit Qvpp) have more phenocrysts. Samples are commonly holocrystalline, trachytic to pilotaxitic, and vary from intergranular to intersertal. Both nepheline and a Na-Al-Si-Cl bearing phase (cancrinite ?) were identified in the groundmass by qualitative EDS-SEM analysis. Aenigmatite is also present in the groundmass.

Magnetite rarely occurs as phenocrysts (2 to 5 volume %) but is common in the groundmass and in glomerocrysts with Fsp and Cpx. In unit Qvap phenocrysts of Mt are commonly subhedral and equant, but locally are embayed or skeletal. They attain a maximum size of 0.46 by 0.4 mm. In unit Qvpp phenocrysts of Mt attain a maximum size of 0.8 by 0.72 mm and are locally tabular. Groundmass Mt is generally equant and <0.04 mm in size.

Clinopyroxene is a more common phenocryst than Mt, but still is not abundant (<5% based on visual estimates). In units Qvap and Qvpp, Cpx commonly has green pleochroism and, based on qualitative SEM analysis, is

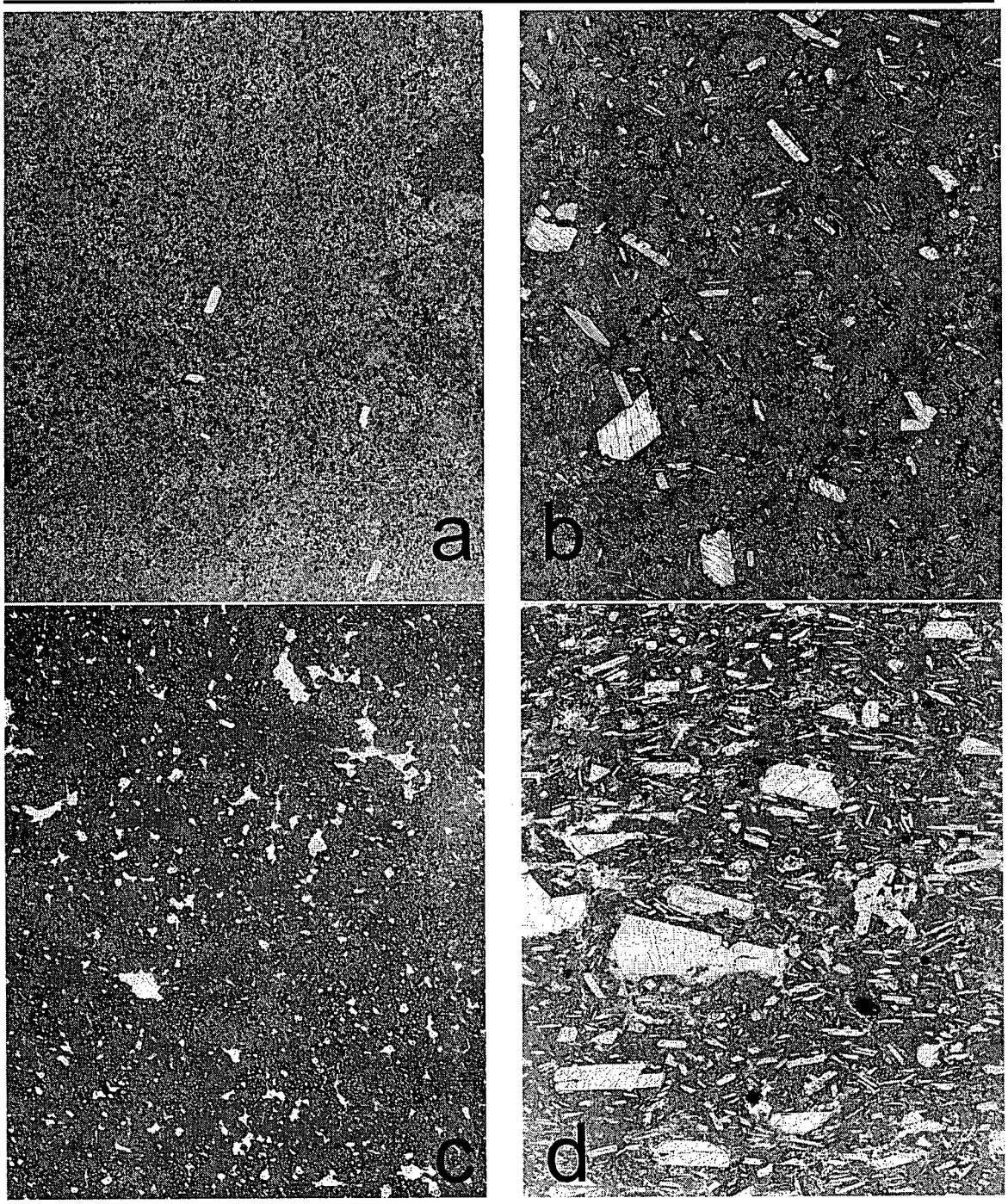

Figure 2.14. Textural expressions of lava samples from Hoodoo Mountain volcano. Views are: a) slightly porphyritic (<1%) $Qvap_2$, b) moderately porphyritic (~3-5 %) $Qvap_5$, c) vesicular and aphyric $Qvap_6$, and d) highly porphyritic (>15%) Qvpp. Field of view for all samples is approximately 2.5 by 3.5 cm but is slightly distorted.

Fe-rich (hedenbergitic) with Na-enriched rims. In unit Qvap, Cpx phenocrysts are commonly green from core to rim, attain a maximum size of 0.44 by 0.5 mm, are equant to lamellar, are locally embayed and skeletal, and commonly have inclusions of Mt and/or other opaques. In the groundmass Cpx is generally <0.02 mm in maximum dimension. In unit Qvpp, Cpx phenocrysts commonly have clear cores with green rims, attain a maximum size of 1.35 by 0.65 mm, are equant to tabular, are locally rounded, commonly have sector or oscillatory zoning, and are also frequently found with Mt. For example, in one sample 37 of 45 phenocrysts of Cpx contained Mt inclusions or were in glomerocrysts with Mt. Total estimated volumes for Cpx as phenocrysts and groundmass grains are between 5 and 10%.

Alkali feldspar is the dominant phenocryst and groundmass phase in both units Qvap and Qvpp, generally composing 85 to 90% of the samples. Both sanidine and anorthoclase are present in most samples. In unit Qvap Fsp phenocrysts attain a maximum size of 4.25 by 2.1 mm. They vary from euhedral to subhedral and from tabular to bladed. Alkali feldspar phenocrysts rarely show optical zoning and locally have inclusions of Mt and Cpx. In unit Qvpp Fsp phenocrysts attain a maximum size of 18 by 3 mm, vary from euhedral to subhedral, locally have both oscillatory zoning and distinct core and/or rim boundaries, and commonly have inclusions of Mt and Cpx. Groundmass Fsp are acicular, generally less than 0.26 by 0.02 mm in dimension, and often

aligned to form trachytic texture. Three different generations of Fsp exist. The earliest phase is represented by phenocrysts (exclusively Fsp). The second phase exists as laths in the groundmass, and last phase comprises irregular, void-fillings of Fsp and Ne.

All of the Qvap subunits are aphanitic to sparsely porphyritic (<5% phenocrysts; Figure 5.14a and b). Glomerocrysts are rare. All of the subunits, except for $Qvap_6$, are non-vesicular. Subunit $Qvap_6$ is vesicular (10-15%) and locally has amygdales of analcite. Phenocrysts are almost totally absent from $Qvap_6$ and where present are small (1.65 by 0.65 mm; Figure 5.14c).Other textural variations in unit Qvap relate to the spatial distribution of groundmass Fsp, Mt, and Cpx. In some samples these three minerals form clots, in others they are uniformly distributed in the groundmass.

Unit Qvpp is highly porphyritic (>15% phenocrysts; Figure 5.14d). It commonly contains glomerocrysts of Fsp, Mt, and Cpx. Unit Qvpp is locally vesicular, trachytic, glomerocrystic, xenocrystic, and holocrystalline. Rarely small patches of light green glass are preserved next to large phenocrysts. Centimetre-size troctolite xenoliths, olivine gabbro xenoliths, olivine xenocrysts, and plagioclase xenocrysts are rare.

The sequence of crystallization as inferred from inclusion relationships and glomerocryst assemblages is similar for all units. Alkali feldspar contains inclusions of both Cpx and Mt, and occurs in glomerocrysts with both Cpx and

Mt. Clinopyroxene contains inclusions of Mt, but Mt never contains inclusions of Cpx or Fsp. These observations are consistent with a sequence of crystallization of Mt followed by Mt + Cpx and finally Mt + Cpx + Fsp.

Little Bear Mountain

Samples of unit Qvbm and Qvbp from *Little Bear Mountain* are all porphyritic with phenocrysts of olivine (Ol), Cpx, Ti-magnetite, ilmenite (Ilm), and plagioclase (Pl) in a groundmass of Ol, Pl, titanaugite, and Mt (Figure 2.15a). However, abundant xenoliths, xenocrysts, and grains of uncertain origin complicate the petrography. Samples vary from massive to moderately vesicular (~ 10%). Generally the groundmass is tachylitic although sideromelane is locally present. Glomerocrysts are common and include Ol-Cpx, Ol-Pl, and Pl-Cpx-Mt. In addition to glomerocrysts some samples contain a variety of cognate and/or xenolithic fragments including a gabbroic inclusion of equant, granular Cpx-Pl-Mt. Feldspathic xenoliths including Cpx syenite, granite, and metavolcanic rocks are commonly partly melted.

Olivine phenocrysts are generally equant and euhedral, but locally individual grains are embayed. Optically they are weakly zoned, attain a maximum size of 0.75 to <0.1 mm, and occur both as isolated grains and as glomerocrysts with Cpx and/or Pl. Locally Ol has spinel inclusions.

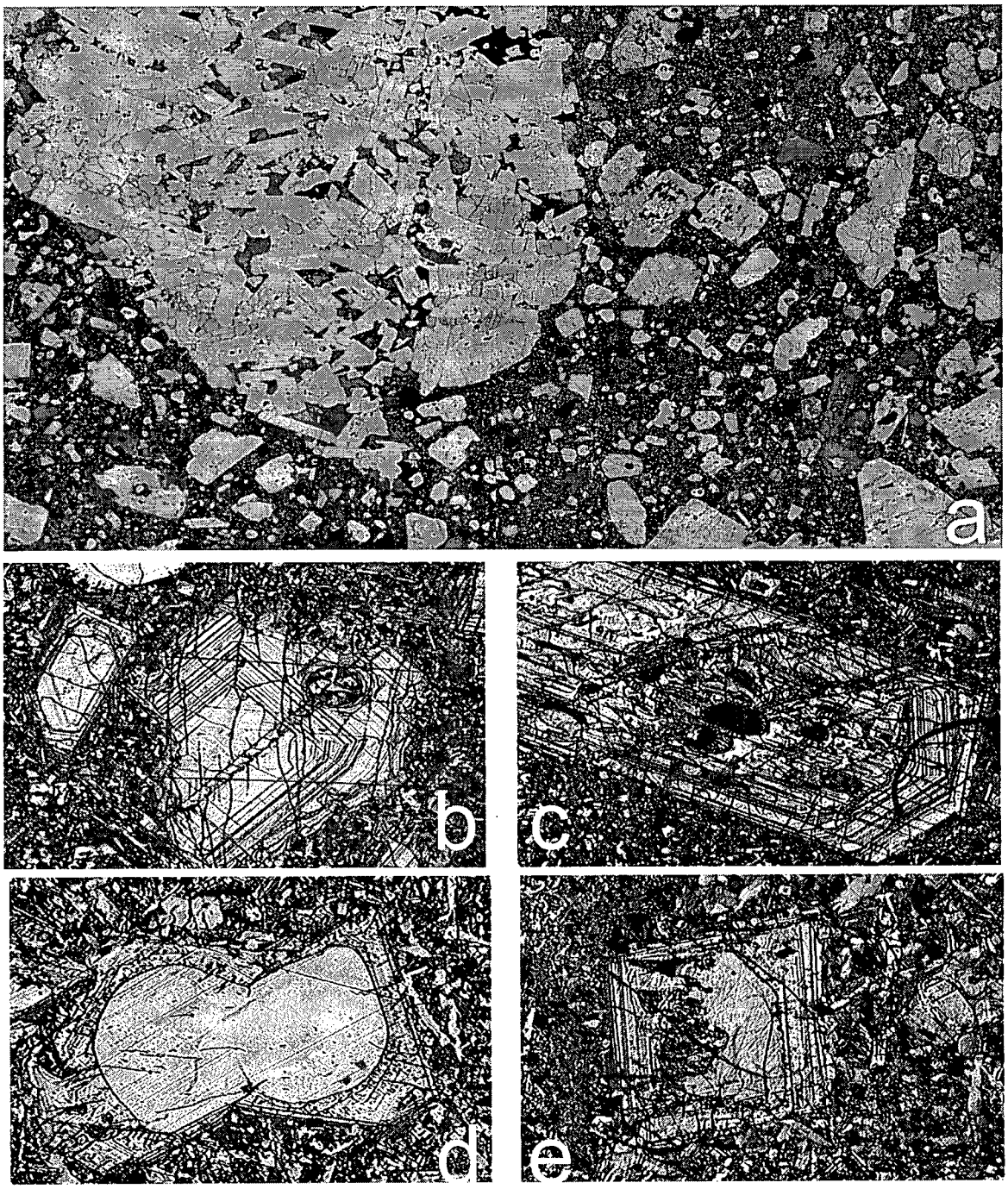

Figure 2.15. Photomicrograph and NDIC images of lava samples from *Little Bear Mountain* volcano. Views are: a) sample 94BRE153a (Qvbm) with gabbroic inclusion (field of view approximately 2 by 3.5 cm but is slightly distorted), and NDIC images of plagioclase phenocrysts (b & c) and xenocrysts (d & e) in sample 94BRE2 (field of view is ~1 by 2 mm but slightly distorted).

Clinopyroxene phenocrysts are less abundant than Ol or Pl. However, they are texturally and optically diverse and include at least three different populations. The first group is the most common type of Cpx phenocryst and comprises phenocrysts that are clear, equant, and often embayed with highly sieve-textured cores. This group locally has both opaque inclusions and brown spinel inclusions and ranges in size from 0.7 by 0.4 mm to 2.75 by 0.55 mm. The second group is second in abundance and it comprises grains that are also equant but have the distinctive brownish-purple colour of titanaugite. This group does not appear to be out of equilibrium with the surrounding groundmass. The third group is the least abundant and comprises Cpx phenocrysts that have lamellar shapes with a distinct, light green color in plane light. The third group typically has a fritted inner rim-outer rim boundary.

Plagioclase phenocrysts are also texturally diverse and similar to those described by Hauksdóttir (1994) from nearby basaltic centres. Nomarski DIC images show complex growth histories for many of the Pl phenocrysts and microphenocrysts (Figures 5.15b,c,d, and e). The Pl phenocrysts and microphenocrysts generally fall into one of three groups: 1) large, euhedral grains with or without visible zoning (Figures 5.15b and c), 2) smaller, euhedral to subhedral grains with euhedral rims overgrown on rounded and embayed cores (Figures 5.15d and e), and 3) anhedral grains with fritted rims and sieve-textured cores. Group 1 phenocrysts are generally tabular and attain a

maximum size of 15 by 8 mm. They locally have optically visible complex zoning including normal, reverse, and oscillatory types. They range in composition from An_{73} to An_{48}. Group 2 microphenocrysts are also tabular but have distinctly visible rounded cores. The cores have a small range in composition (An_{39-42}) and are compositionally distinct from the rims (An_{54-60}). Group 3 phenocrysts are anhedral, embayed, and have sieve-textured rims. They are reversely zoned with core compositions of An_{30-43}, and rim compositions of An_{55-61}.

The groundmass of all Qvbm samples is fine-grained and comprises Ol + Pl + Mt + titanaugite +/- Ilm +/- apatite +/- sideromelane. Olivine, Cpx and opaque grains are equant and Pl is tabular to lath-shaped.

The sequence of crystallization for samples of Qvbm is complicated by the presence of multiple populations of Pl and Cpx. However, Ol and Pl phenocrysts are the most abundant phenocrysts, the largest phenocrysts, and the only phases that consistently have equilibrium textures and also are present in the groundmass. Both Ol and opaque grains occur as inclusions in phenocrysts of Pl. Ol also contains inclusions of opaque grains. The most abundant large grains of Cpx do not have equilibrium textures except for smaller phenocrysts of titanaugite, which is also a groundmass phase. Grains interpreted as xenocrysts based on reaction textures and compositions (e.g., for Pl) commonly have overgrown rims; this is consistent with longer rather

than shorter residence times in the host magma. The inferred sequence of crystallization is minor Mt, then Ol, then Pl, followed by titanaugite.

All of the samples examined from *Little Bear Mountain* have crystals of Pl and Cpx that display disequilibrium textures (e.g., sieve-textures, embayments) that are commonly attributed to xenocrysts and are similar to xenocrysts from other basalts in the Iskut area (Hauksdóttir 1994). The fact that such textures are found in all examined samples is consistent with magmatic assimilation being a pervasive process at *Little Bear Mountain volcano*.

Dykes

Subunit Qi_2 is holocrystalline, amygdaloidal, porphyritic and comprises phenocrysts of Pl + Ol in a groundmass of Pl + Ol + opaques +/- titanaugite. Phenocrysts of Pl are columnar, euhedral to subhedral, and locally have oscillatory zoning and/or resorbed cores. Phenocrysts of Ol are equant, euhedral to subhedral, and locally are replaced with carbonate.

Subunit Qi_3 comprises phenocrysts of alkali feldspar in a groundmass of feldspar laths. The sample is very altered and has veinlets and amygdales of Qtz and carbonate.

Petrochemistry

Representative whole rock samples from all the non-fragmental rocks in the HMVC were analyzed for major elements, minor elements, trace elements,

and rare earth elements (REE). Whole rock samples were analyzed at the Ottawa GSC laboratory by a variety of techniques (XRF, ICP-MS, Wet chemistry; see Appendix A2 for references to analytical methods). Individual analyses are given in Tables A2.2 and A2.3. Representative analyses for each of the units are given in Table 2.6. Seven samples were also analyzed for Sr and Nd isotopes at the GSC laboratories by R. Theriault (Table A2.5). Results are discussed first for samples from Hooodoo Mountain, then for samples from *Little Bear Mountain*, and lastly for samples of the dykes and of xenoliths from *Little Bear Mountain*. Major element variations are shown on bivariate plots in Figure 2.16 as weight percent oxides plotted against the Differentiation Index (DI), which is calculated as the sum of normative Ne + Qtz + Ab + Or + Ks + Lct (Thornton & Tuttle 1960). The values of DI are used on the abscissa because of the small amount of variation in SiO_2 for the trachytes and phonolites. In Figures 2.16, 2.17, and 2.18 the symbols are the same and a key is given in Figure 2.16; symbols are larger than the estimated analytical precision on all figures. All samples from map unit Qvap (number = 24) are grouped together except for subunit $Qvap_6$ (n = 6). Other groups include volcanic glass from units Qvh and $Qvap_6$ (n = 4), samples of lava from Qvpp (n = 14), samples of lava from Qvb (n = 6), samples of $Qi_{2,3}$ (n = 2), and xenoliths from *Little Bear Mountain* (n = 2). Figures 2.19 to 2.25 show results for selected trace elements, REE, and isotopes.

Table 2.6. Representative major, minor, trace, and rare earth element analyses for samples from the Hoodoo Mountain Volcanic Complex.

Sample	93BRE29	94BRE76	94BRE62	94BRE165	94BRE108	94BRE2	94BRE75	94BRE74	93BRE153
Map Unit	Qvap	Qvap	Qvap6	Qvh	Qvpp	Qvb	Qi	Qi	xenolith
TAS name	phonolite	trachyte	phonolite	phonolite	phonolite	basalt	tephrite	trachyandesite	trachyte
Major and Minor Elements									
SiO_2	58.4	64.1	56.9	59.9	59.0	45.5	44.3	57.3	61.5
TiO_2	0.25	0.30	0.23	0.37	0.28	3.35	2.2	0.51	0.42
Al_2O_3	15.3	15.4	15.7	14.5	16.5	16.0	15.1	15.5	18.5
Fe_2O_3(total)	9.10	6.20	9.20	9.90	8.10	13.87	11.95	7.60	3.30
Fe_2O_3	4.50	3.20	5.30	2.80	4.50	4.17	3.25	1.30	0.90
FeO	4.10	2.70	3.50	6.40	3.20	8.70	7.8	5.70	2.20
MnO	0.21	0.15	0.21	0.24	0.19	0.19	0.18	0.18	0.06
MgO	b.d	0.06	b.d.	0.10	0.21	5.53	5.29	0.95	0.35
CaO	1.06	0.63	1.04	1.53	1.65	10.2	11.3	2.54	1.85
Na_2O	8.30	6.10	8.80	8.90	7.60	3.10	3	4.60	6.10
K_2O	4.61	5.13	4.77	4.59	4.94	1.35	0.75	4.56	5.17
P_2O_5	0.04	0.05	0.02	0.08	0.06	0.96	0.485	0.13	0.16
H_2O(total)	2.50	0.70	3.30	0.40	1.20	1.23	1.2	1.50	1.80
CO_2(total)	0.20	1.60	b.d.	b.d.	b.d.	b.d.	5.3	5.50	0.40
S(total)	0.03	0.02	0.03	0.05	b.d.	0.05	0.07	0.04	0.02
Total	100.00	100.44	100.10	100.10	99.60	100.30	101.13	100.40	99.80
Trace Elements									
Ag	1.0	0.5	0.1	0.1	b.d.	0.1	b.d.	b.d.	0.1
Ba	40	80	50	100	90	450	230	340	1600
Be	10	6	11	12	10	1	1.2	3	2.6
Co	b.d.	6	b.d.	7	6	35	37	b.d.	10
Cr	b.d.		b.d.	b.d.	b.d.	48	b.d.	b.d.	b.d.
Cs	1.5	0.52	2.4	3	2.6	0.17	0.49	0.41	0.14
Cu	b.d.		b.d.	b.d.	b.d.	22	b.d.	b.d.	b.d.
Ga	55	40	48	46	42	22	19	32	21
Hf	31	20	29	31	26	4.8	4.1	13	2.3
In	0.15	0.26	0.15	0.20	0.20	0.09	0.11	0.27	b.d.
La	130	100	130	150	120	31	17.5	70	17
Mo	14	100	5.7	16	9.0	2	1.7	6.7	1.6
Nb	170	4.4	170	190	150	36	b.d.	100	23
Ni	15	130	b.d.	b.d.	b.d.	30	b.d.	b.d.	
Pb	17	15	20	28	20	2	2	6	4
Rb	140	130	150	180	150	18	b.d.	100	55
Sc	b.d.	1	0.7	1.2	0.9	19	23	4	2.6
Sr	b.d.	9.1	b.d.	b.d.	b.d.	820	b.d.	77	230
Ta	12	14	14	16	10	3.0	1.3	7	1.3
Th	19	0.28	19	24	20	2.4	1.5	10	1.6
Tl	0.45	3.6	0.42	0.55	0.35	0.04	0.04	0	0.09
U	6.7	100	6.6	8.5	7.0	0.77	0.49	3.1	0.54
V	b.d.	94	b.d.	b.d.	b.d.	177	b.d.	b.d.	b.d.
Y	120	9.4	120	140	110	31	30.5	60	7.4
Yb	11.0	9	11.0	12.0	9.7	2.2	2.6	5.6	0.60
Zn	300	210	300	320	220	100	135	140	33
Zr	1700	1100	1700	1800	1500	223	195	650	95
Rare Earth Elements									
La	130	100	130	150	120	31	18	70	17
Ce	260	210	260	290	230	70	41	140	32
Pr	33	26	32	36	28	9.3	5.4	17	4.0
Nd	130	100	120	140	110	41	24	68	16
Sm	27	21	25	28	22	8.8	5.8	14	3.1
Eu	3.5	2.5	3.6	3	2.5	3.4	2.05	2.2	3.7
Gd	26	22	26	27	22	8.97	6.5	13	2.6
Tb	4.1	3.4	4.1	4.3	3.5	1.2	1.0	2.0	0.35
Dy	24	19	23	24	20	6.2	5.6	11	1.8
Ho	4.8	3.6	4.5	4.8	3.8	1.1	1.1	2.1	0.30
Er	13	9.4	12	13	10	2.6	2.8	5.5	0.74
Tm	1.9	1.6	1.9	2.1	1.7	0.40	0.44	0.91	0.10
Yb	11	9.4	11	12	9.7	2.2	2.6	5.6	0.60
Lu	1.5	1.5	1.6	1.6	1.5	0.34	0.40	0.90	0.10

Major Elements

Hoodoo Mountain volcano

The range in concentrations of major elements is small for samples from Hoodoo Mountain volcano. All samples contain between 56 and 64 weight % SiO_2 (Figure 2.16a). The total iron (as FeO) decreases as values of DI increase (Figure 2.16b). Samples of glass and some Qvap samples have the highest FeO_{total} (9 wt. %) and samples of Qvpp have the lowest FeO_{total} (6.5 wt. %). Measured FeO follows the same trend (Figure 2.16c), while values of Fe_2O_3 have exactly the opposite trend, with the samples of glass having the lowest values and samples of Qvpp, $Qvap_{1\text{-}5}$, and $Qvap_6$ having the highest values (Figure 2.16d). Values of FeO and Fe_2O_3 are not strongly correlated with DI. For 23 of the 34 samples of Qvap and glass, values of MgO are below the reported detection limit (0.04 wt. %; Figure 2.16e). Values of MgO for Qvpp are above detection limits (0.08 to 0.28), but are still quite low. Values of MnO vary from 0.15 to 0.28 and but do not vary systematically with increasing values of DI (Figure 2.16f); however, the samples of volcanic glass (DI = 76) are high (0.24) compared to the phenocryst-rich samples from unit Qvpp (DI = 82 to 88), which are uniformly low (0.18).

Values of CaO, Al_2O_3, and K_2O increase with increasing values of DI (Figures 2.16g, h, and j respectively), while values for Na_2O decrease with increasing DI (Figure 2.16i).

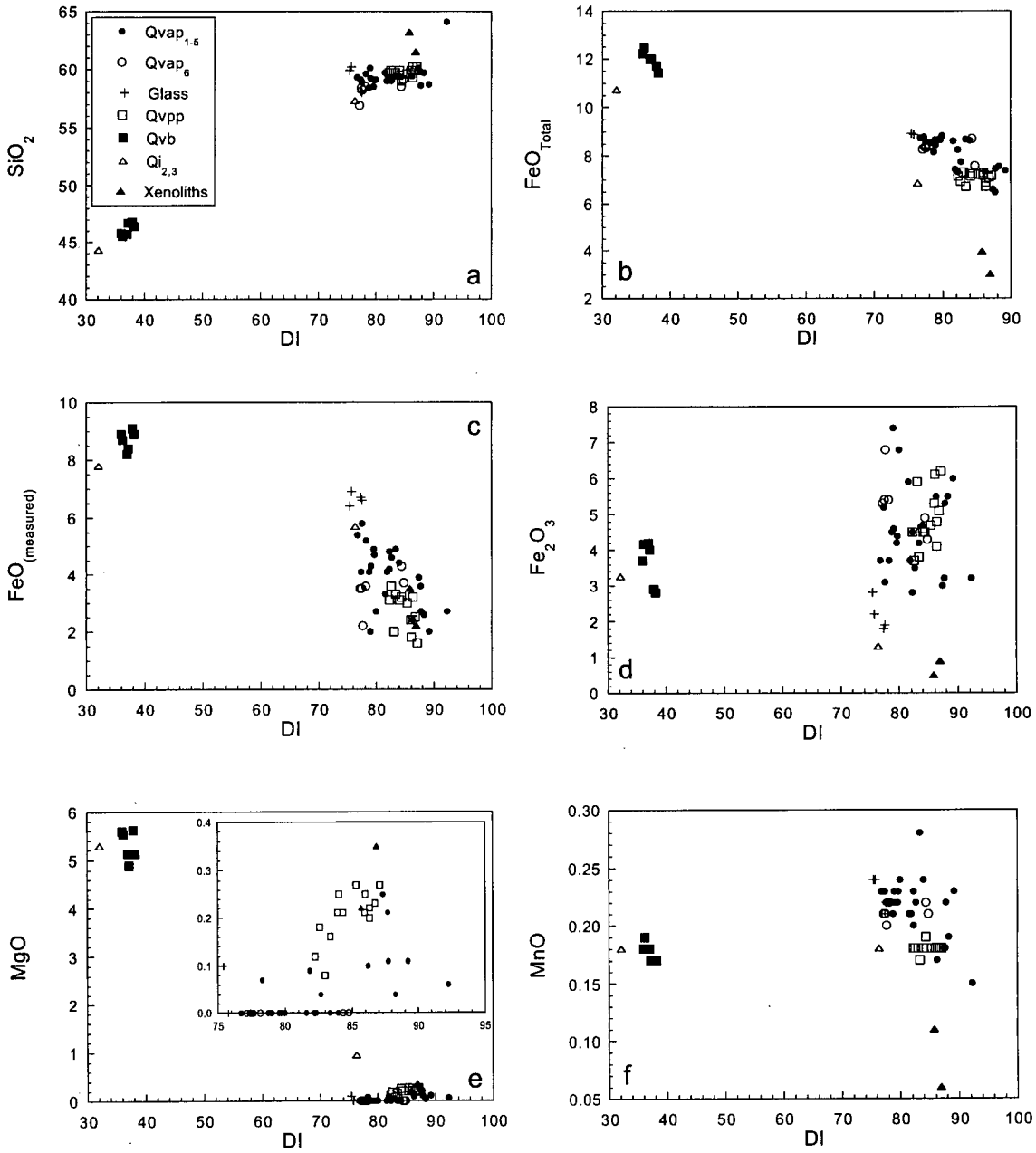

Figure 2.16. Plots showing weight percent variations in major and minor element abundances for samples from the HMVC. Abscissa are the Differentiation Index (DI) of Thorton and Tuttle (1960).

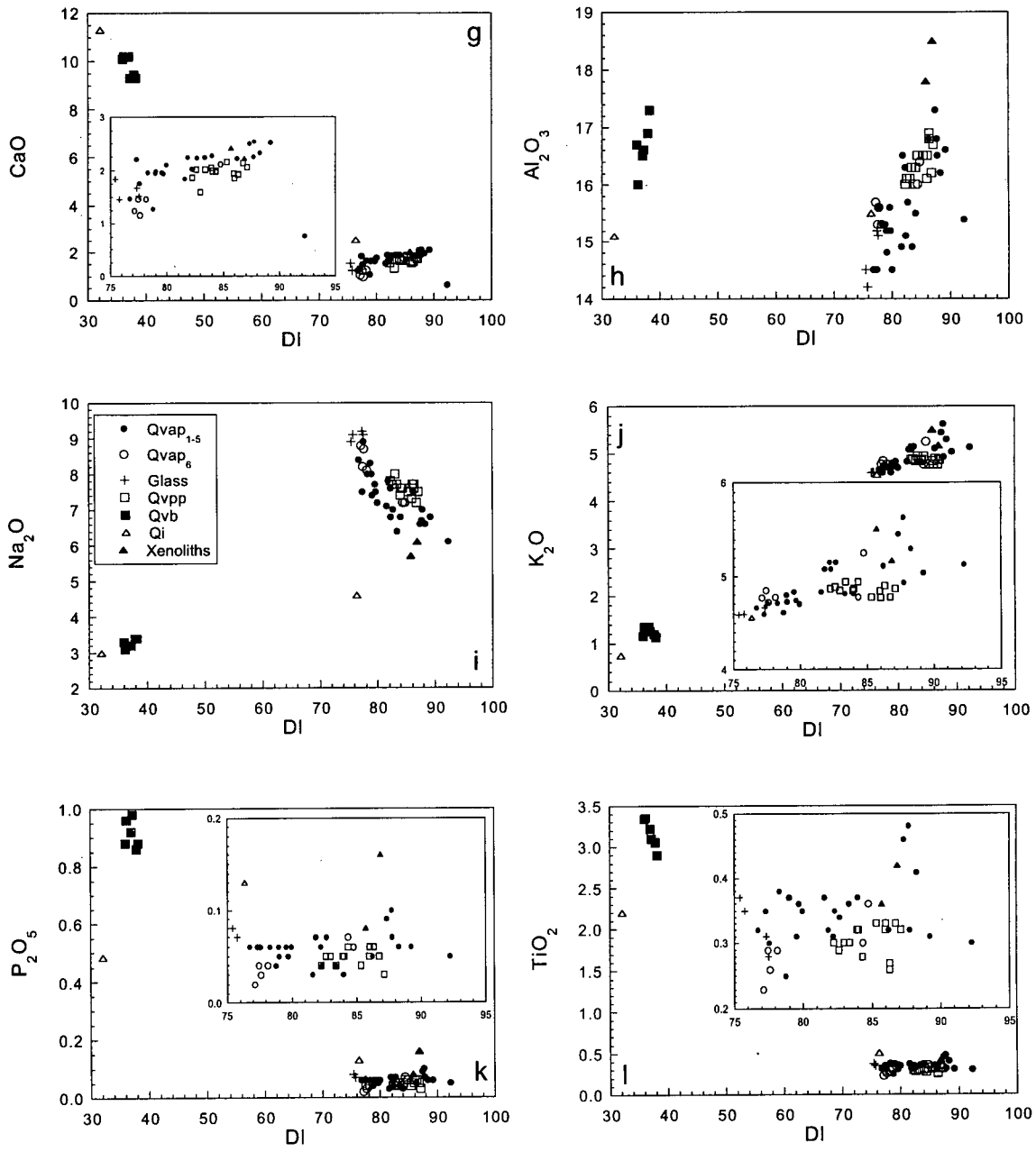

Figure 2.16. (continued) Plots showing weight percent variations in major and minor element abundances for samples from the HMVC. Abscissa are the Differentiation Index (DI) of Thorton and Tuttle (1960).

All four oxides have a broad range of values for unit Qvap (n = 30; CaO: 0.63 - 2.11; Al_2O_3: 14.5 - 17.3; Na_2O: 6.1 - 8.9; K_2O: 4.61 - 5.63), but a much smaller range for unit Qvpp (n = 14; CaO: 1.33 - 1.80; Al_2O_3: 16.0 - 16.9; Na_2O: 7.2 - 8.0; K_2O: 4.77 - 4.94).

Values for P_2O_5 and TiO_2 in Hoodoo Mountain samples are low and do not vary systematically as DI increases (Figures 2.16k and l, respectively).

Little Bear Mountain volcano

Variations in the oxide concentrations and values of DI for *Little Bear Mountain* basalts (Qvb) are generally small, except for Al_2O_3, which ranges from 16 to 17.4 wt. % (Figure 2.16h). Values for FeO_{total}, MgO, CaO, P_2O_5, and TiO_2 are higher for the Qvb samples than for samples from Hoodoo Mountain volcano, which is consistent with the Qvb samples having lower values of DI than the Hoodoo Mountain samples (Figures 2.16b, e, g, k, and l). Values for SiO_2, Na_2O, and K_2O are lower for the Qvb samples, which is again consistent with the low values of DI (Figures 2.16a, i, and j). Values of Fe_2O_3, MnO, and Al_2O_3 overlap for the *Little Bear Mountain* and Hoodoo Mountain samples (Figures 2.16d, f, and h).

Dykes

The chemical compositions of the two analyzed dyke samples (Qi) share similar traits with both *Little Bear Mountain* and Hoodoo Mountain samples. The sample from subunit Qi_2 (DI = 32) is similar to samples of Qvb, except it

has slightly lower values of SiO_2 (44.3 wt. %; Figure 2.16a), Al_2O_3 (15.1 wt. %; Figure 2.16h), P_2O_5 (0.5 wt. %; Figure 2.16k), and TiO_2 (2.2 wt. %; Figure 2.16l). However, it has a higher value of CaO (11.3 wt. %; Figure 2.16g). The sample from subunit Qi_3 (DI = 76) is compositionally similar to samples from Hoodoo Mountain volcano, except for distinctly higher MgO (0.95 wt. %; Figure 2.16e) and lower Na_2O (4.6 wt. %; Figure 2.16l).

Xenoliths

The two samples of xenoliths from *Little Bear Mountain* volcano (Qx) are also broadly similar in composition to Hoodoo Mountain samples. However, their concentrations of SiO_2 (61.5 and 63.2 wt. %) are higher than any of the Hoodoo Mountain samples except 94BRE76 (Figure 2.16a) and they have the highest values of Al_2O_3 of all the analyzed samples (17.8 and 18.5 wt. %; Figure 2.16h). The xenoliths also have distinctly lower values of FeO_{total} and MnO (Figures 2.16b and f).

Classification and Major Element Characteristics

The samples from Hoodoo Mountain all plot in the phonolite and trachyte fields of the total Na_2O plus K_2O versus SiO_2 classification of LeMaitre et al. (1989) (Figure 2.17a). Specifically, the glasses and four of the five samples of $Qvap_6$ are phonolites, while the samples of $Qvap_{1\text{-}5}$ are split between the trachyte and phonolite fields. Samples of Qvpp are all trachytes but plot near the phonolite - trachyte boundary. The samples of lava from *Little Bear*

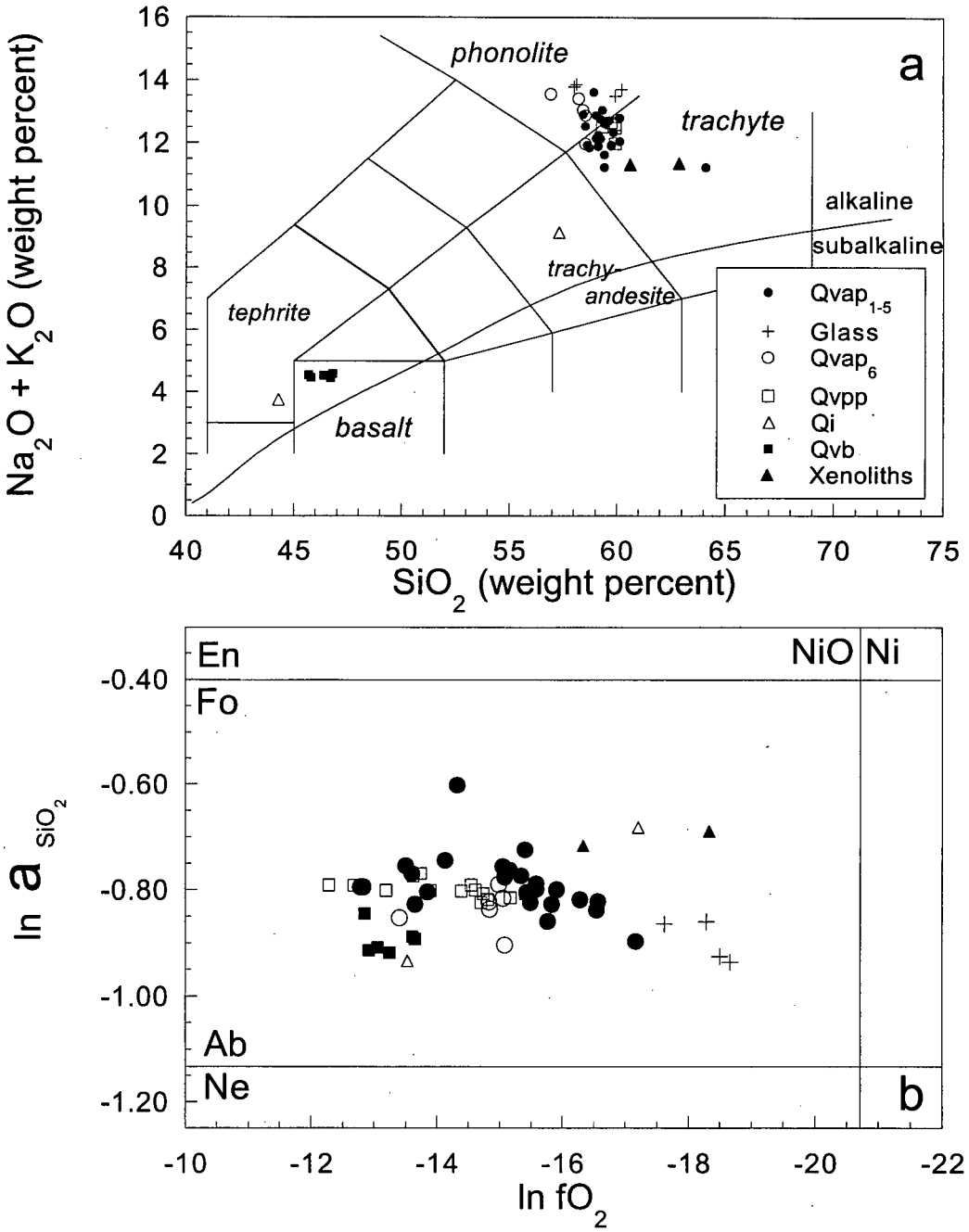

Figure 2.17. Plots showing a) LeMaitre et al. (1989) TAS classification for volcanic rocks and b) variations in calculated ln a_{SiO2} versus calculated ln fO_2. Alkaline and subalkaline fields in a) are from Irvine and Baragar (1971). Reference lines in b) are from Ghiorso and Carmichael (1987) (Ne-Ab and Fo-En) and Carmichael and Ghiorso (1990) (NiO-Ni).

Mountain all plot in the basalt field. The dyke sample from subunit Qi_2 is a tephrite and the dyke from subunit Qi_3 is a trachyandesite based on the LeMaitre et al. classification. All samples plot in the alkaline field of Irvine and Baragar (1971) in Figure 2.17a.

The activity of SiO_2 (a_{SiO_2}) and the oxygen fugacity (fO_2) are two important characteristics of natural silicate liquids; the a_{SiO_2} is a measure of the degree of silica saturation for a given liquid composition and the fO_2 reflects the oxidation state of the liquid (Carmichael et al. 1970; Ghiorso & Carmichael 1987; Carmichael & Ghiorso 1990). Values of a_{SiO_2} and fO_2 were calculated for all the samples from the HMVC using the thermodynamic database of Ghiorso and Sack (1995) for a_{SiO_2} and Kress and Carmichael (1992) for fO_2 (Figure 2.17b). Values of a_{SiO_2} and fO_2 for samples from the HMVC were calculated for temperatures of either 1100 ^{o} C (samples from Hoodoo Mountain; SiO_2 >55 wt. %) or 1200 ^{o} C (samples from *Little Bear Mountain*; SiO_2 < 47 wt. %). The temperatures used in the calculations were chosen to be near the low pressure liquidi for the two groups of rocks. Liquidus temperatures were used because the calculations are only valid for crystal-free silicate melts. Reaction boundaries for Ne + $SiO_2 \leftrightarrow$ Ab (Ghiorso & Carmichael 1987), Fo + $SiO_2 \leftrightarrow$ En (Ghiorso & Carmichael 1987), and Ni + $0.5O_2 \leftrightarrow$ NiO (Carmichael & Ghiorso 1990) are included in Figure 2.17b for reference; all boundaries are for a

temperature of 1100 ^{o} C and are for reactions between pure endmember phases.

The samples from the HMVC have values of ln a_{SiO_2} that plot between reaction boundaries for Ne-Ab and Fo-En (Figure 2.17b); this is the field defined for alkali olivine basalt magmas (Ghiorso & Carmichael 1987) and is consistent with the mineralogy of the basalts from *Little Bear Mountain*. It is also consistent with the mineralogy of the samples from Hoodoo Mountain, which are Si-undersaturated. All of the samples define a narrow range of ln a_{SiO_2}, with the Hoodoo Mountain glasses and the *Little Bear Mountain* basalts having the lowest values.

The values of ln fO_2 for the samples from Hoodoo Mountain range over six orders of magnitude. The samples of glass show the lowest values of fO_2 and the samples of Qvpp have the highest calculated values of fO_2. Samples of unit Qvap range between the two endmembers. The basalts from *Little Bear Mountain* also have high values of fO_2. Although all calculated values are within the range given for terrestrial magmas by Carmichael and Ghiorso (1987), high values for Qvpp and the basalts may indicate secondary oxidation of the samples.

Greater than 90% of the samples from the HMVC have normative Ne and only one sample, 94BRE76, has normative Qtz. When projected into the Ne-Qtz-Ks ternary system, the samples from Hoodoo Mountain all plot along the

Ab-Or join or below (Figure 2.18a). This is consistent with the samples containing nepheline in their normative mineral assemblages and in groundmass modes, and distinguishes the Hoodoo samples from samples of the evolved rocks from both Level Mountain and Mount Edziza. Both Level Mountain and Mount Edziza have Qtz-saturated rock types (peralkaline rhyolites; Hamilton 1981; Souther & Hickson 1984; Souther 1992) in addition to Qtz-free trachytes. However, Hoodoo Mountain has the most Qtz- undersaturated rock types in the Stikine Subprovince.

The lavas from Hoodoo Mountain also contain acmite in their norms and are chemically peralkaline (molar Al < molar Na + K; Figure 2.18b: symbols are the same as in Figures 2.16 and 2.17). The samples from Hoodoo Mountain form a coherent trend in Figure 2.18b with a positive slope. The samples of volcanic glass (+) have the lowest values for both ratios, the samples of Qvap have the greatest variance, and the samples of Qvpp plot slightly above the main trend with higher values of Al / (Na + K) for a given K / Na. Compared to trachytes from Level Mountain and Mount Edziza, the Hoodoo trachytes and phonolites have lower values of Al / (Na + K) and also lower values of K / Na. In Figure 2.18b the K to Na ratio for anorthoclase (0.59) is shown for reference as is a horizontal line at Al = Na + K. Greater than 90 % of the samples from all three volcanic centres have K / Na ratios greater than that for sanidine. However, while all of the Hoodoo lavas except one are peralkaline, only five out

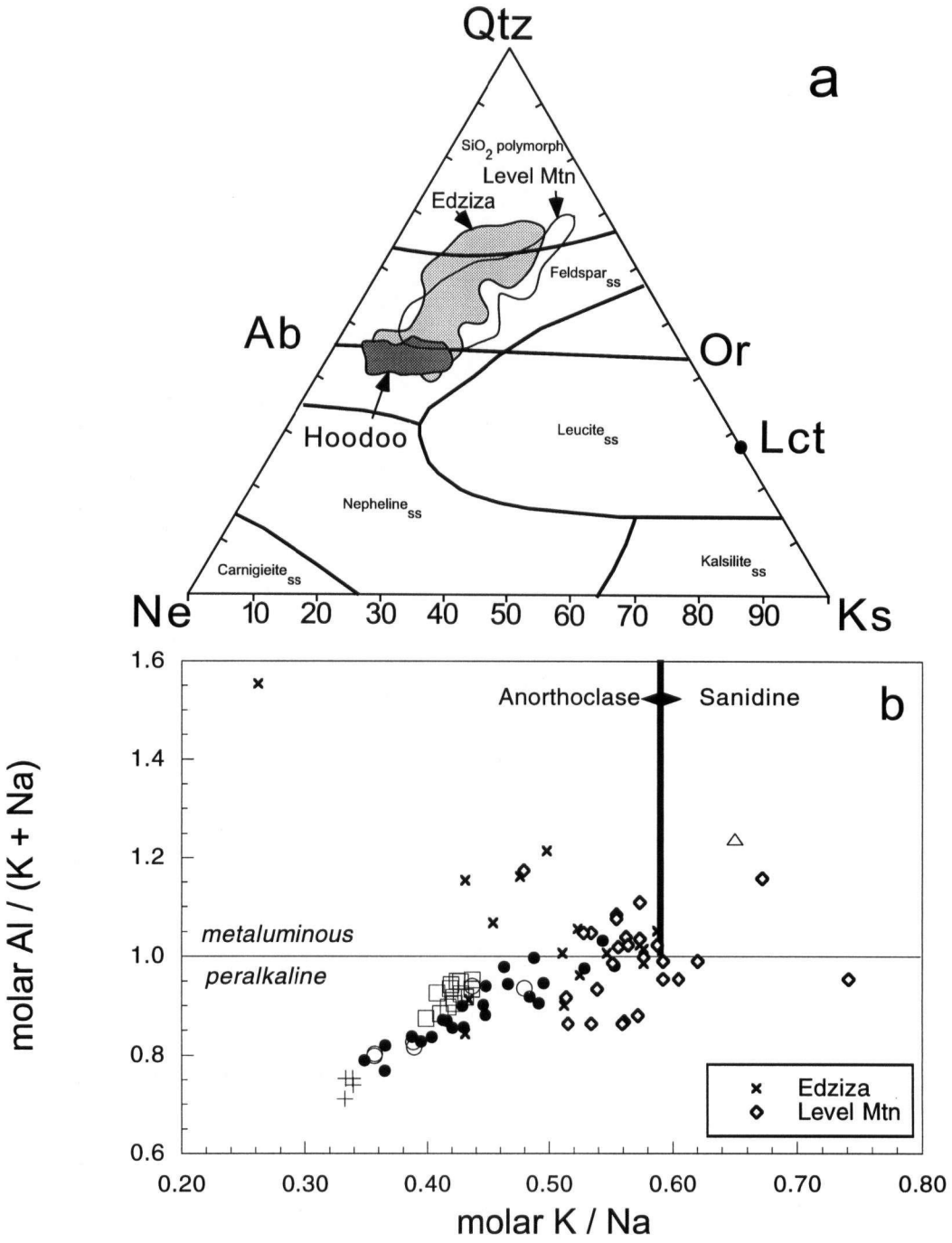

Figure 2.18. Projected compositions of Hoodoo Mountain, Mount Edziza, and Level Mountain phonolite, trachyte, comendite, and pantellerite in Nepheline-Quartz-Kalsilite ternary (Fudali 1963) and b) molar Al / (K + Na) versus molar K / Na for samples of phonolite and trachyte from Hoodoo Mountain, Mount Edziza, and Level Mountain. Symbols in b) are the same as in Figures 2.16 and 2.17.

of seventeen samples from Edziza are peralkaline, and slightly more than one half of the Level Mountain samples are peralkaline.

Trace Elements

A selected suite of major, minor, and trace elements is shown in figures 2.19, 2.20, and 2.21 as multi-element plots. In the figures the concentrations of the elements for each sample are normalized to a constant set of concentrations to facilitate comparison between samples. In general the ordering of the elements along the abscissa is for the elements to be increasingly compatible in mantle melts from left to right (Pearce 1983). Values that plot above one indicate enrichment in the sample relative to the normalizing values, and values that plot below one indicate relative depletion. Three different sets of normalization values were used: i) a tholeiitic mid-ocean ridge basalt (Pearce 1983), ii) a sample of volcanic glass from Hoodoo Mountain (94BRE98), and iii) the most Mg-rich basalt from the Iskut volcanic centres (SC-23; Hauksdóttir 1994; see Chapter 5, Table 5.3). The different normalizations were used to facilitate global, local, and regional comparisons respectively. Normalization to MORB concentrations helps to assess element concentrations relative to the depleted mantle (Pearce 1983). Normalization to the phonolite glass from Hoodoo Mountain volcano allows for easier within stratigraphy comparison of samples from Hoodoo Mountain and for

comparison between Hoodoo Mountain and *Little Bear Mountain* samples. Normalization to SC-23 facilitates comparison between the samples from the HMVC and contemporaneous volcanism from the Iskut-Unuk rivers volcanic centres. Sample SC-23 has the highest MgO wt. % of all Quaternary rocks from the Iskut area and is the best candidate for a primitive mantle melt. The sample is also used as a starting composition for assimilation modeling presented in Chapter 5.

Hoodoo Mountain volcano

The patterns for all of the samples from Hoodoo Mountain volcano are very similar (Figures 2.19a-e, 2.20a-e, and 2.21a-e). In general the MORB-normalized patterns have negative slopes (Figures 2.19a to e) indicating that they are more enriched in incompatible elements than compatible elements. All of the MORB-normalized element concentrations are enriched except for values of P and Ti, which are depleted. The patterns are enriched up to 100 times for highly incompatible elements (Th and Ta) but are only enriched two to four times for more compatible elements (Y and Yb). Patterns normalized to the sample 94BRE98 emphasize the similarities between all Hoodoo Mountain samples (Figures 2.20a to e). The patterns are relatively flat and all values are close to one. However, again P and Ti vary the most with slight enrichments for some samples of $Qvap_{1-2}$ (Figure 2.20a) to slight P depletions for some samples of $Qvap_6$ and Qvpp (Figures 2.20d and e). Compared to a basalt from

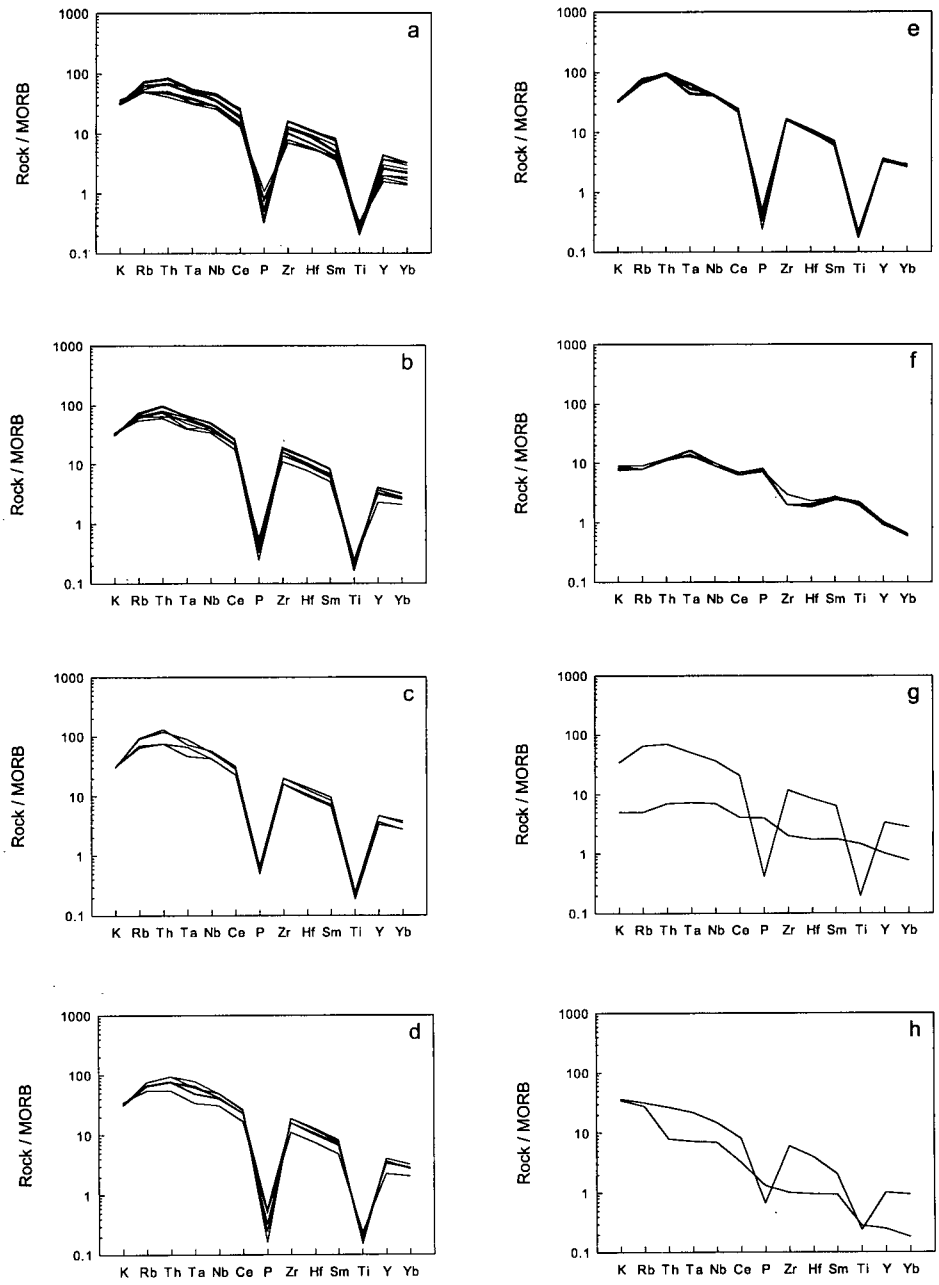

Figure 2.19. Multi-element plots of minor and trace element patterns normalized to values for a tholeiitic mid ocean ridge basalt (Pearce 1983) for: a) subunits $Qvap_{1-2}$, b) subunits $Qvap_{4-5}$, c) volcanic glass from Qvh and $Qvap_6$, d) subunit $Qvap_6$, e) unit Qvpp, f) unit Qvb, g) unit Qi, and h) xenoliths from *Little Bear Mountain* volcano.

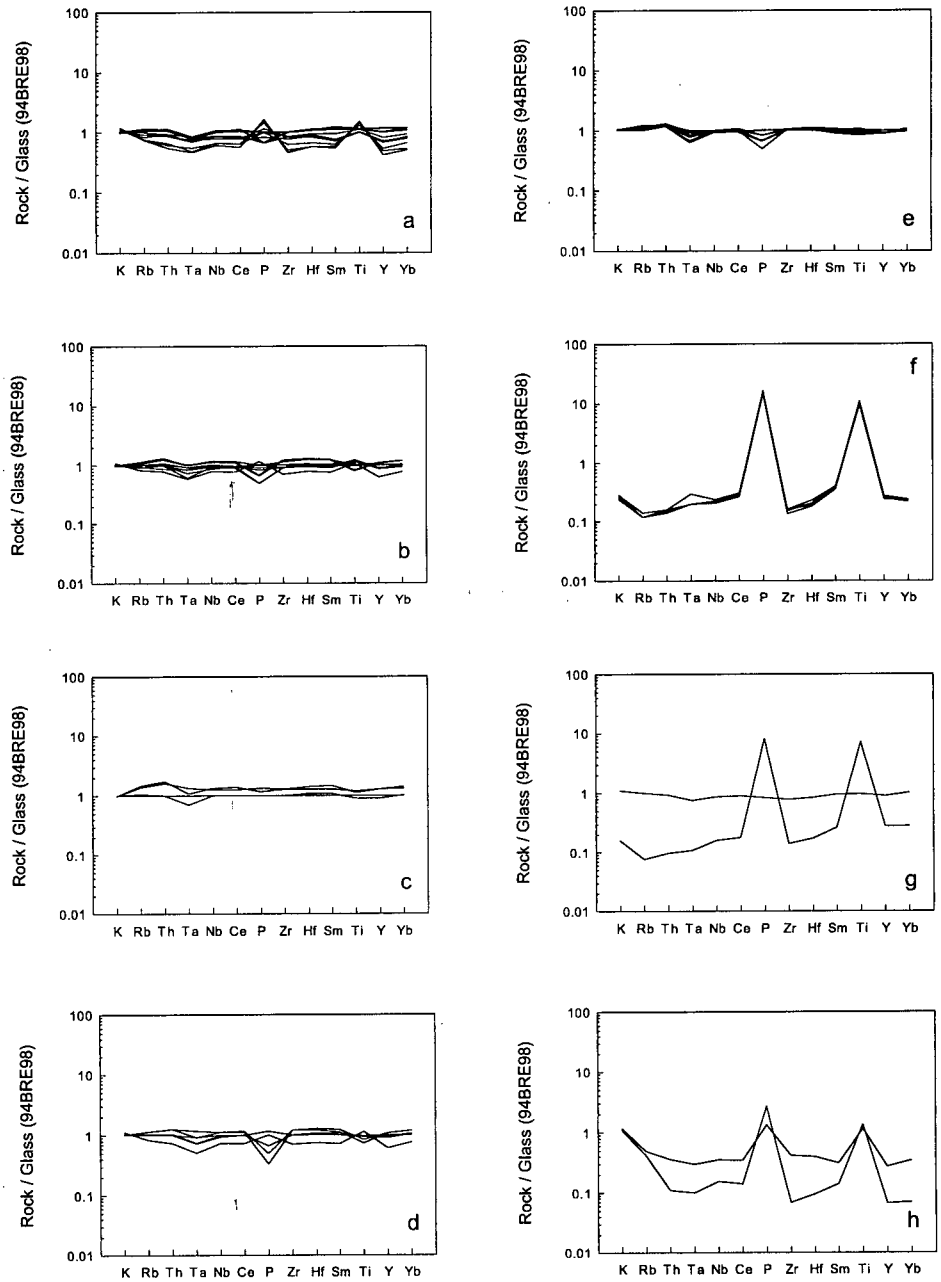

Figure 2.20. Multi-element plots of minor and trace element patterns normalized to values of volcanic glass from unit Qvh (94BRE98) for: a) subunits $Qvap_{1-2}$, b) subunits $Qvap_{4-5}$, c) volcanic glass from Qvh and $Qvap_6$, d) subunit $Qvap_6$, e) unit Qvpp, f) unit Qvb, g) unit Qi, and h) xenoliths from *Little Bear Mountain* volcano.

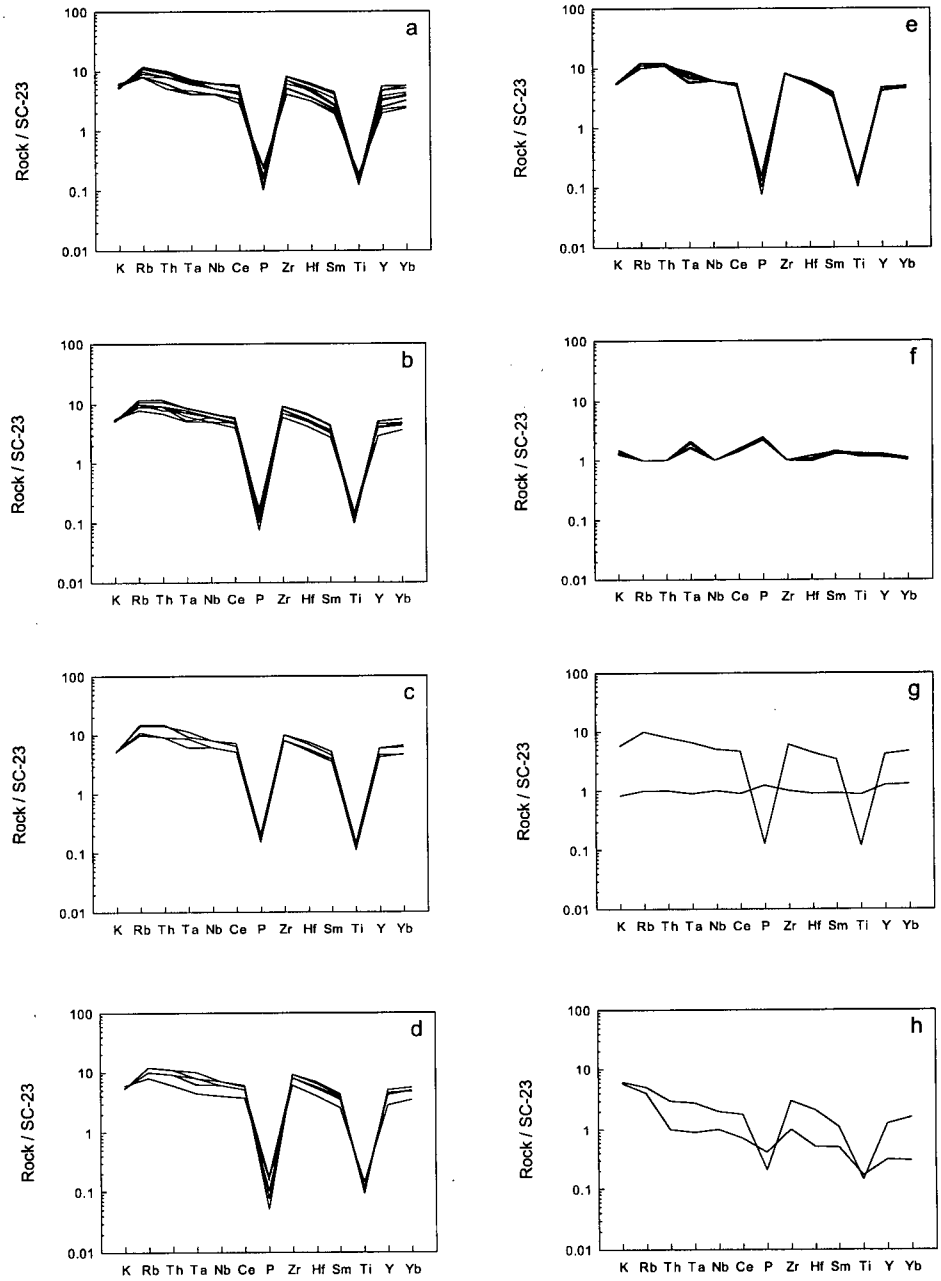

Figure 2.21. Multi-element plots of minor and trace element patterns normalized to values of the most Mg-rich Quaternary basalt in the Iskut area (SC-23; Hauksdóttir 1994) for: a) subunits $Qvap_{1-2}$, b) subunits $Qvap_{4-5}$, c) volcanic glass from Qvh and $Qvap_6$, d) subunit $Qvap_6$, e) unit Qvpp, f) unit Qvb, g) unit Qi, and h) xenoliths from Little Bear Mountain volcano.

Second Canyon lava flow (SC-23), the most primitive basalt in the Iskut area, the samples from Hoodoo Mountain are uniformly enriched in all elements except P and Ti from three to ten times (Figures 2.22a to e). Both P and Ti are depleted by a factor of ten. The P and Ti depletions are consistent with either a P- and Ti-bearing phase fractionating during crystallization or with a P- and Ti-bearing phase remaining in the source region during partial melting.

Little Bear Mountain volcano

MORB-normalized patterns for samples of basalts from *Little Bear Mountain* (Qvb) are similar to the patterns for samples from Hoodoo Mountain only in that both are enriched and have overall negative slopes. However, the Qvb patterns are only enriched by a factor of 20 and do not have P and Ti depletions (Figure 2.19f). In fact, the values for P and Ti are enriched by a factor of 10 relative to most of the Hoodoo samples (Figure 2.20f). The patterns for Qvb are very similar to that for the primitive Second Canyon basalt but slightly enriched in P and in Ta (Figure 2.21f). The similarity of patterns is consistent with the Little Bear Mountain samples having a source with chemical characteristics similar to the nearby, contemporaneous basalts from the Iskut-Unuk rivers centres like SC-23.

Dykes

The two dykes (Qi_2 and Qi_3) have normalized patterns similar to patterns for either *Little Bear Mountain* (Qi_2) or Hoodoo Mountain (Qi_3) (Figures 2.19g,

2.20g, and 2.21g). Both are relatively enriched compared to MORB (Figure 2.19g) and SC-23 (Figure 2.21g). The pattern for Qi_3 is flat and close to one when normalized to 94BRE98, while the pattern for Qi_2 has distinctive P and Ti peaks very similar to Qvb (Figure 2.20g).

Xenoliths

Patterns for the two analyzed xenolith samples are markedly different (Figures 2.19h, 2.20h, and 2.21h). Sample 94BRE23 has patterns similar to samples from Hoodoo Mountain: enriched relative to MORB with distinct P and Ti depletions (Figure 2.19h), relatively flat but slightly depleted relative to 94BRE98 except for small P and Ti enrichments (Figure 2.20h), and slightly enriched relative to SC-23 but again with P and Ti depletions (Figure 2.21h). However, the other xenolith sample, 93BRE153, shares pattern characteristics with both Hoodoo Mountain and *Little Bear Mountain* samples. Relative to MORB it is enriched for all elements except Ti, Y, and Yb (Figure 2.19h). Relative to 94BRE98 (Hoodoo glass) it is depleted except for K, P and Ti (Figure 2.20h). Relative to SC-23 it is enriched in K and Rb and slightly depleted in Ti, Y, and Yb.

Rare Earth Elements

The presentation of analyses of rare earth elements (REE) including La is the same as that for the trace elements. Concentrations are normalized to: i)

values for average chondrites (Boyton 1984) (Figures 2.22a-h), ii) values for 94BRE98 (Figures 2.24a-h), and iii) values for SC-23 (Figures 2.25a-h). The magnitude of the slopes for total REE, light REE (LREE), and heavy REE (HREE) of the chondrite normalized patterns ($_N$) are summarized in Figures 2.23a-e. The $(La / Yb)_N$ reflects the slope of the overall REE pattern (Figure 2.23a), and the relative degrees of fractionation among the LREE and among the HREE are represented by $(La / Sm)_N$ and $(Gd / Yb)_N$ (Figures 2.23b and c, respectively). Values of Sm_N and Yb_N, plotted on the abscissa in Figures 2.23a-c, correspond to degrees of overall enrichment relative to chondrite values. The size of the Eu_N anomaly is represented by $(Eu / Eu^*)_N$ (Figures 2.23d and e; method of Rollinson 1993).

Hoodoo Mountain volcano

All of the samples from Hoodoo Mountain volcano have very similar normalized REE patterns (Figures 2.22a-e, 2.23a-e, 2.24a-e, and 2.25a-e). Relative to average chondrite values, the samples are enriched from 30 to 500 times, have negative slopes, and have negative Eu_N anomalies (Figures 2.22a-e and 2.23a-e). Patterns for subunits $Qvap_{1,2}$ vary widely in degrees of enrichment (Figure 2.22a), while all the samples from unit Qvpp have uniformly enriched values (Figure 2.22e). The variance in the slopes for the overall REE patterns (Figure 2.23a), the relative fractionation among the LREE (Figure 2.23b), and the relative fractionation among the HREE (Figure 2.23c) are

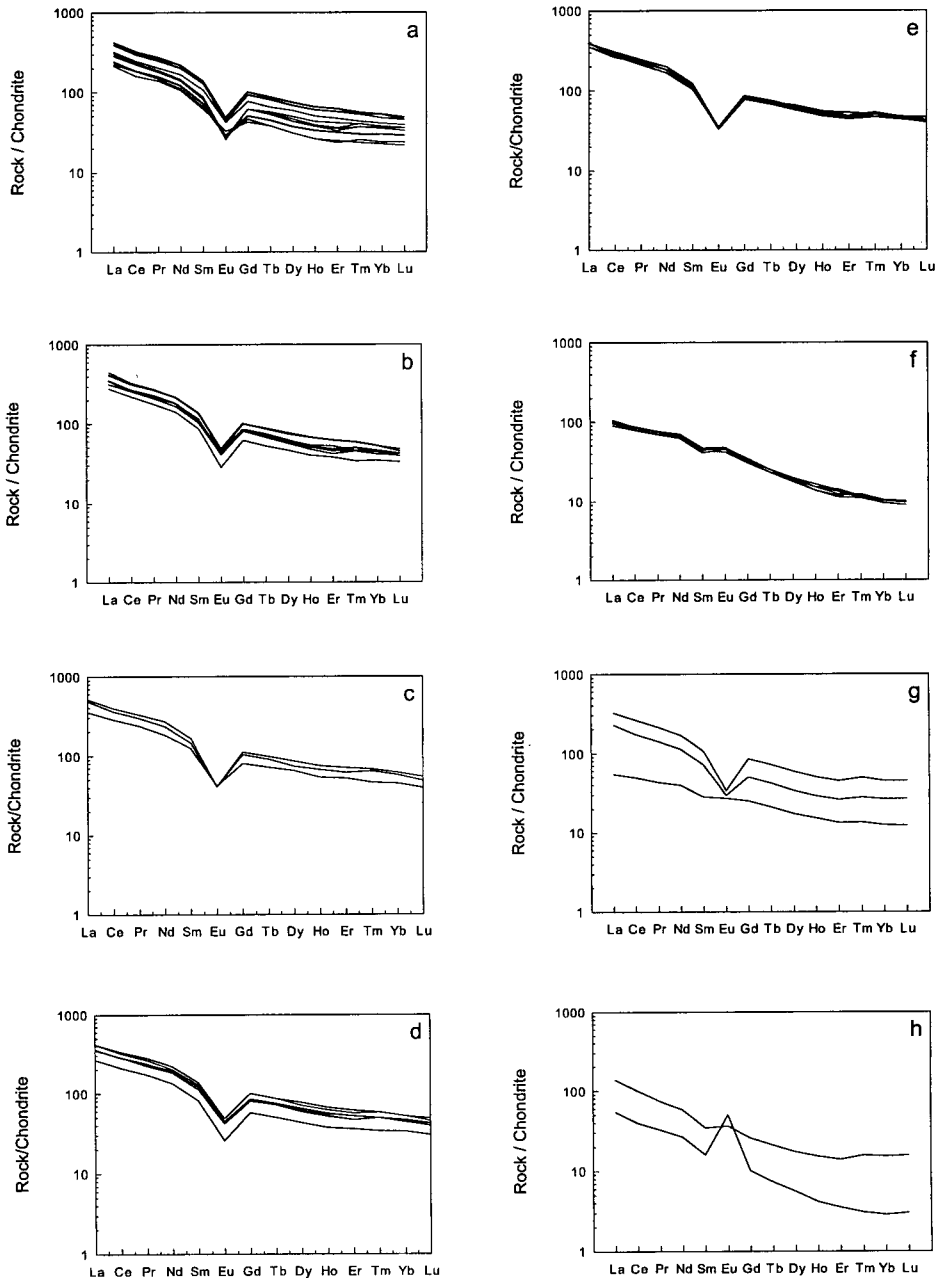

Figure 2.22. Multi-element plots of rare earth element patterns normalized to values of average chondritic meteorites (Boynton 1984) for: a) subunits $Qvap_{1-2}$, b) subunits $Qvap_{4-5}$, c) volcanic glass from Qvh and $Qvap_6$, d) subunit $Qvap_6$, e) unit Qvpp, f) unit Qvb, g) unit Qi, and h) xenoliths from *Little Bear Mountain* volcano.

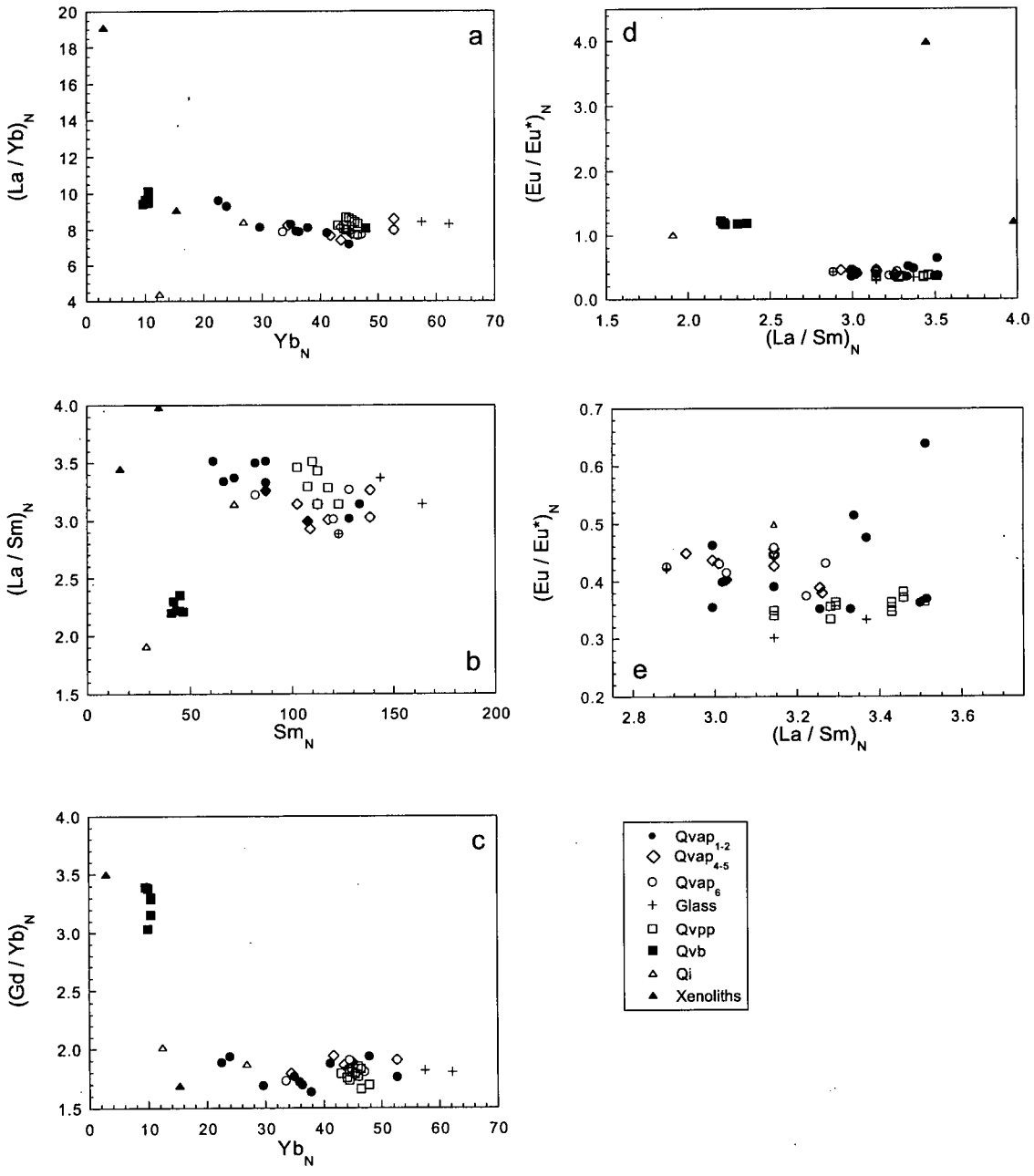

Figure 2.23. Quantification of chondrite normalized REE patterns expressed by: a) $(La / Yb)_N$ versus Yb_N, b) $(La / Sm)_N$ versus Sm_N, c) $(Gd / Yb)_N$ versus Yb_N, d) $(Eu / Eu^*)_N$ versus $(La / Sm)_N$ and e) $(Eu / Eu^*)_N$ versus $(La / Sm)_N$ for samples from Hoodoo Mountain only.

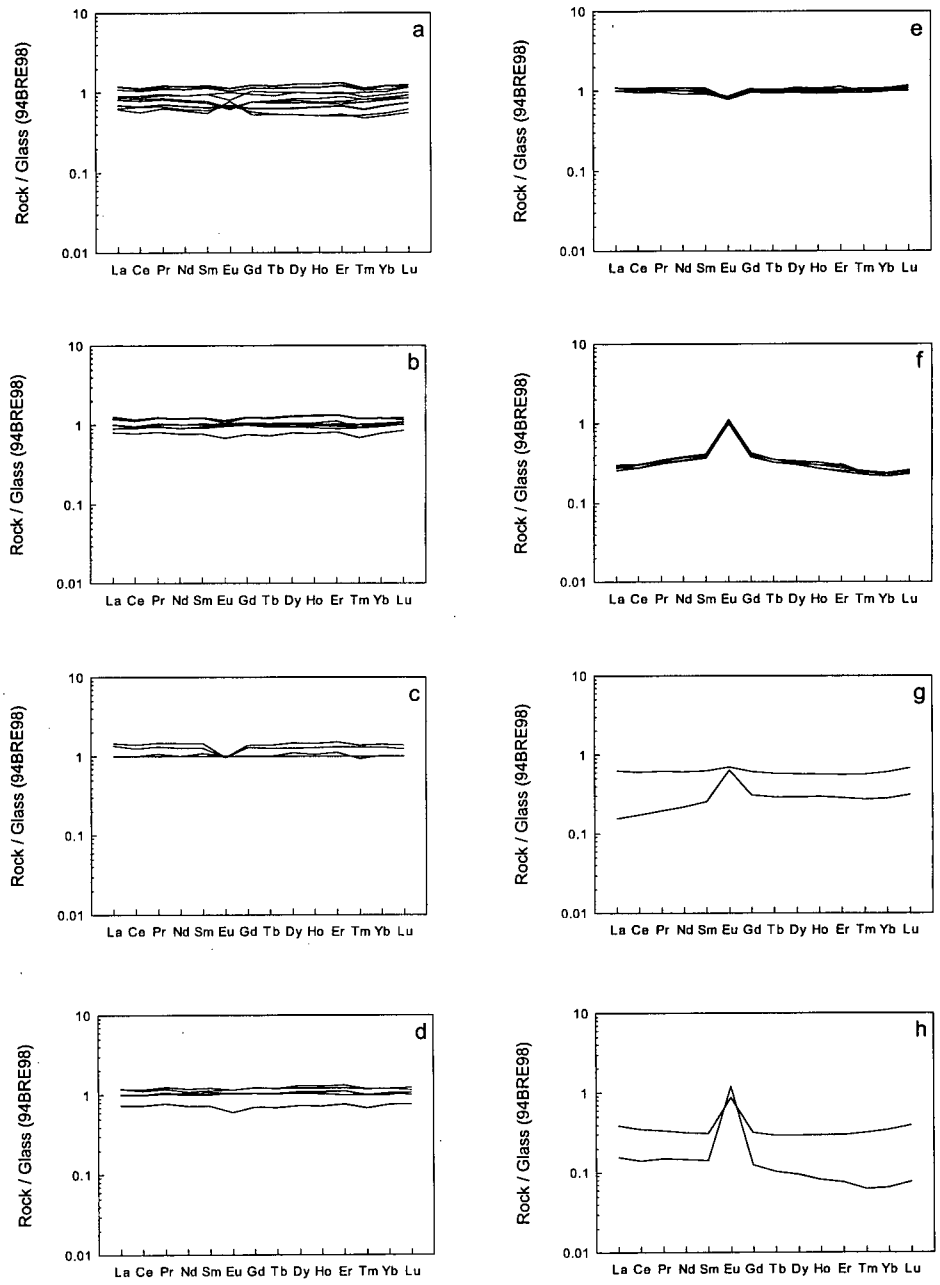

Figure 2.24. Multi-element plots of rare earth element patterns normalized to values of volcanic glass from unit Qvh (94BRE98) for: a) subunits $Qvap_{1-2}$, b) subunits $Qvap_{4-5}$, c) volcanic glass from Qvh and $Qvap_6$, d) subunit $Qvap_6$, e) unit Qvpp, f) unit Qvb, g) unit Qi, and h) xenoliths from *Little Bear Mountain* volcano.

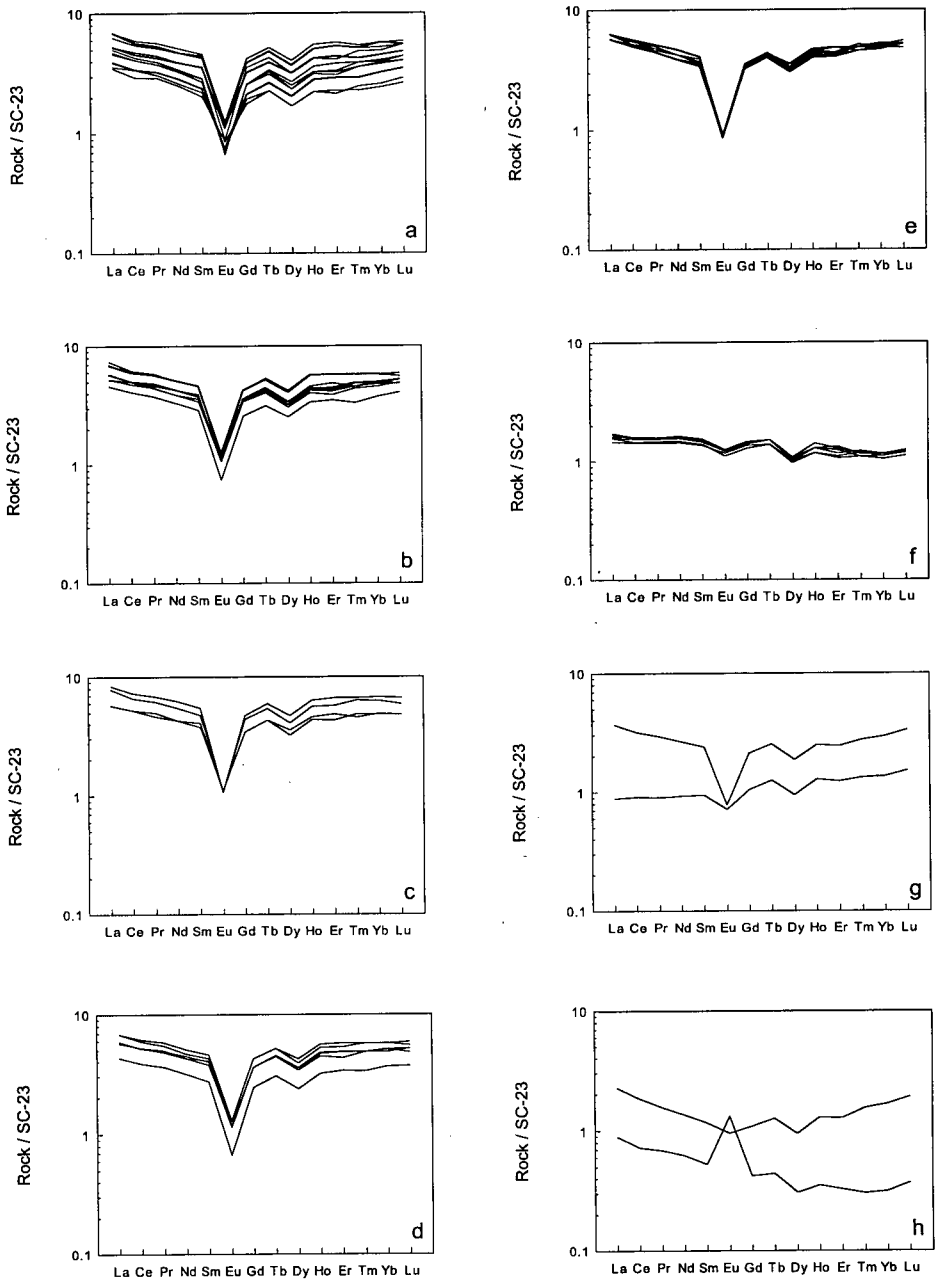

Figure 2.25. Multi-element plots of rare earth element patterns normalized to values of the most Mg-rich Quaternary basalt in the Iskut area (SC-23; Hauksdóttir 1994) for: a) subunits $Qvap_{1-2}$, b) subunits $Qvap_{4-5}$, c) volcanic glass from Qvh and $Qvap_6$, d) subunit $Qvap_6$, e) unit Qvpp, f) unit Qvb, g) unit Qi, and h) xenoliths from *Little Bear Mountain* volcano.

almost as great within units as between different units. However, unit Qvpp and the glass samples have the smallest values of $(Eu / Eu^*)_N$, which corresponds to the largest negative Eu_N anomalies (Figures 2.23d and e).

Compared to values for volcanic glass (94BRE98), all units at Hoodoo Mountain have uniformly flat patterns (Figures 2.24a-e). Samples from subunits $Qvap_{1,2}$ and $Qvap_{4,5}$ vary from slightly depleted to slightly enriched (Figures 2.24a and b). Two of the glass samples are slightly enriched relative to 94BRE98 for all REE except for Eu_N (Figure 2.24c) and one sample from subunit $Qvap_6$ is distinctly uniformly depleted (Figure 2.24d). Patterns for the other $Qvap_6$ samples and for all the Qvpp samples are identical to 94BRE98 (Figure 2.24d and e). Compared to REE values for the most Mg-rich basalt from the Iskut area (SC-23), all samples for units from Hoodoo Mountain are uniformly enriched by 3 to 8 times, with distinctive negative Eu_N and Dy_N anomalies (Figure 2.25a-e).

Little Bear Mountain volcano

The shapes of chondrite-normalized REE patterns for basalts from *Little Bear Mountain* (Qvb) are broadly similar those for Hoodoo Mountain samples in that the Qvb patterns are enriched and have negative slopes (Figures 2.22f and 2.23a). However, the Qvb patterns are less enriched (10 to 100 times; Figures 2.22), have less fractionated LREE (Figure 2.23b), and have more fractionated HREE (Figure 2.23c) than any of the units from Hoodoo Mountain. The Qvb

patterns also have no Eu_N anomaly (Figure 2.23d). Compared to the glass from Hoodoo Mountain (94BRE98), the patterns for Qvb are flat except for a large positive Eu_N anomaly (Figure 2.24f). The patterns for Qvb are also flat when normalized to SC-23 and are slightly enriched (Figure 2.25f).

Dykes

The normalized REE patterns for the two dykes, Qi_2 and Qi_3, are similar to patterns for Qvb and for samples from Hoodoo Mountain, respectively (Figures 2.22g, 2.24g, and 2.25g). However, the chondrite normalized pattern for Qi_2 is less fractionated than the pattern for Qvb for both LREE and HREE (Figures 2.23b and c). Both dykes are enriched relative to chondrite (Figure 2.22g) and depleted relative to 94BRE98 (Figure 2.24g). Compared to SC-23, the pattern for Qi_2 is flat with a small negative Eu anomaly and has a positive overall slope, indicating an enrichment in HREE relative to LREE (Figure 2.25g).

Xenoliths

Normalized REE patterns for the two xenoliths from *Little Bear Mountain* have LREE enrichment trends similar to those of the other analyzed samples (Figure 2.22h, 2.24h, and 2.25h). Sample 93BRE153 is relatively more enriched than sample 94BRE23 except for Eu_N; sample 94BRE23 has a large positive Eu_N anomaly (Figures 2.22h and 2.23d). Sample 94BRE23 also has the most highly fractionated LREE patterns and HREE patterns that are as

fractionated as those for Qvb (Figures 2.23b and c). Both xenoliths are depleted for all REE relative to 94BRE98 except for Eu; both xenoliths have large positive Eu anomalies (Figure 2.24h). Relative to SC-23, 94BRE153 is enriched for all REE and 94BRE23 is depleted for all REE except Eu.

Sr and Nd Isotopes

A small subset of samples from both *Little Bear Mountain* volcano (3 samples) and Hoodoo Mountain volcano (5 samples) was analyzed for ^{87}Sr / ^{86}Sr and ^{143}Nd / ^{144}Nd. The analyzed samples included two samples of basalt (93BRE150 & 93BRE151), four samples of trachyte (93BRE8, 93BRE16, 93BRE141, 93BRE190), and one xenolith (93BRE153). Values for the analyses are given in Table A2.7 and presented graphically in Figures 2.26a and 2.26b. In both figures values for ^{143}Nd / ^{144}Nd are given in terms of ε_{Nd}, which references the measured values to the chondritic uniform reservoir (CHUR) model (DePaolo & Wasserburg 1976). For comparison, fields are included for MORB (Hawkesworth et al. 1979; Cohen et al. 1980; Cohen & O'Nions 1982; Jahn et al. 1980; White & Hofmann 1982), island-arc volcanic rocks (IAV) (Samson et al. 1989), oceanic island basalts (OIB) (Zindler & Hart 1986), and Stikine terrane rocks (ST) (after Samson et al. 1989).

All of the samples have positive values of ε_{Nd}, with the trachyte samples from Hoodoo Mountain being slightly higher than those for basalts from *Little*

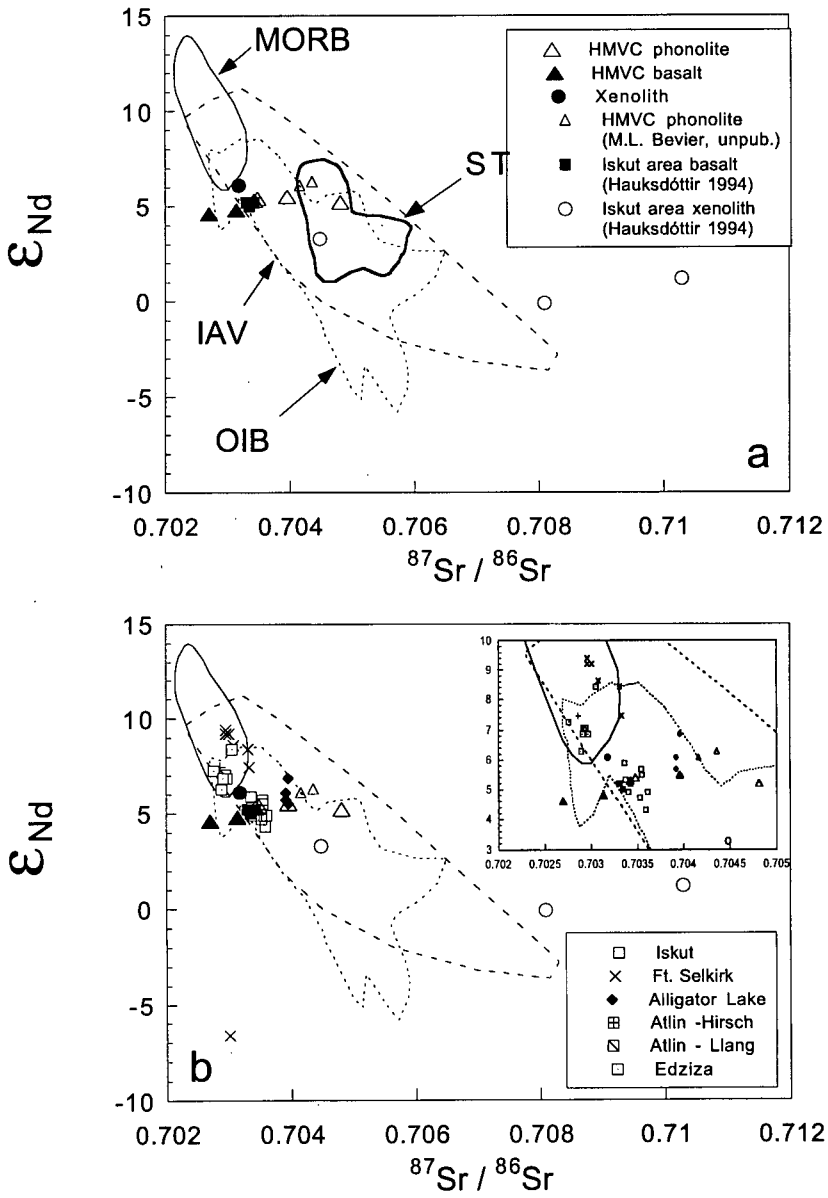

Figure 2.26. Epsilon Nd versus measured $^{87}Sr/^{86}Sr$ for: a) samples from the HMVC and the Stikine Terrane (ST - after Samson et al. 1989), and b) Quaternary volcanic rocks from the NCVP. Data for the NCVP are from Cousens and Bevier (1995; Iskut) and Carignan et al. (1994; Fort Selkirk, Alligator Lake, Atlin, Edziza). The labelled fields are for modern mid-ocean ridge basalts (MORB; Hawkesworth et al. 1979; Cohen et al. 1980; Cohen & O'Nions 1982; Jahn et al. 1980; White & Hofmann 1982), oceanic island basalts (OIB; Zindler & Hart 1986), and island-arc volcanic rocks (IAV; after Samson et al. 1989).

Bear Mountain (+5.2 to +5.5 versus +4.6 and +4.8; Figure 2.26a). However, the basalts have smaller values of $^{87}Sr / ^{86}Sr$ than the trachytes (0.7027 and 0.7031 versus 0.7034 to 0.7048). The xenolith has intermediate values of $^{87}Sr / ^{86}Sr$ (0.7032) but the highest value of ε_{Nd} (+6.1). All of the samples from Hoodoo Mountain plot within the field for the Stikine terrane (Figure 2.26a). Other analyzed mafic rocks from the NCVP have similar values to those for the Hoodoo samples, but commonly have higher values of ε_{Nd}.

Discussion and Summary of Petrography and Petrochemistry of the HMVC

Rocks from Hoodoo Mountain volcano are texturally diverse but are mineralogically and geochemically similar. The petrographic diversity is mainly in phenocryst sizes and abundances, with stratigraphically younger samples generally being more porphyritic. The increase in phenocryst size, phenocryst content, and glomerocryst content is consistent with the sequential eruption of lavas from a common magma chamber that is slowly cooling and crystallizing. Constraints from $^{40}Ar/^{39}Ar$ dating allow for 57 to 76 Ka if subunit $Qvap_1$ and unit Qvpp were sampling the same magma chamber. Evidence for disequilibrium processes or magma chamber recharge includes feldspar phenocrysts with rounded cores in one sample of Qvap (93BRE85) and the troctolite and gabbro xenoliths found in Qvpp.

The restricted compositional range of rocks from Hoodoo Mountain is consistent with the similarity of phenocryst and groundmass mineralogy. Most of the Hoodoo rocks have similar major element compositions, and the trace element and REE patterns are virtually identical throughout the stratigraphy; the only variations are in absolute abundances. The glasses and unit Qvpp samples generally are the most enriched samples, with unit Qvap having a wide range of abundances. Overall the rocks from Hoodoo Mountain volcano are enriched relative to mantle samples and relative to basalts from the Iskut area.

The basalts from *Little Bear Mountain* are mineralogically and geochemically distinct from Hoodoo Mountain trachytes. The basalts are characterized by both phenocrysts and xenocrysts of Cpx and Pl, similar to basalt from other volcanic centres in the Iskut area (Hauksdóttir 1994). The basalts also contain a diverse assemblage of inclusions including gabbro, troctolite, granite, and syenite, similar to inclusions from other Iskut centres. Rounded and embayed cores on phenocrysts and partly melted feldspathic xenoliths provide abundant evidence for chemical disequilibrium in the basalts. However, the groundmass assemblage of Ol + Pl + titanaugite indicates that the basalts are alkali olivine basalts, identical to the other Iskut basalts and like the majority of the basalts in the NCVP (cf. Chapter 1).

The *Little Bear Mountain* basalts have trace element and REE patterns that are very similar to the those for the most Mg-rich (hence most primitive) Iskut area basalt (SC-23); all samples are enriched relative to depleted mantle (MORB) and to bulk earth (chondrites). The Sr and Nd isotopic ratios are similar to those for other centres in the Iskut area and the NCVP.

One of the dykes, Qi_2, is petrographically and geochemically similar to the basalts from *Little Bear Mountain*. The trace element and REE patterns are virtually indestinguishable between the dyke and the *Little Bear Mountain* basalts. The other dyke, Qi_3, shares very close trace element and REE characteristics with the trachytes from Hoodoo Mountain and is tenatively correlated with that volcano.

Both xenoliths have major element compositions similar to those for Hoodoo Mountain, albeit with some differences (e.g., higher SiO_2). One of the xenoliths also has similar trace element and REE patterns to samples of Hoodoo trachyte, although the absolute abundances are not as enriched as most of the Hoodoo samples. However, the other xenolith has distinct trace element and REE characteristics, that are unique among all the analyzed samples in being less enriched and having a large positive (Eu and/or $Eu^*)_N$.

2.4. ORIGINS OF THE HMVC

Field and geochemical studies of the HMVC highlight at least two processes that have dominated its formation: i) interaction with surrounding glaciers and ii) magmatic assimilation.

The role of glaciation in the formation of the HMVC

The potential influence of glaciation on the evolution of the HMVC is obvious from its cross-sectional shape and the surrounding physiography (Figure 2.2) and has been recognized for over fifty years. Kerr (1948) first suggested that the high cliffs surrounding much of Hoodoo Mountain formed by lava flows abutting glaciers. He also recognized that tills occurred within the volcanic stratigraphy. Souther (1991) noted that the shape of Hoodoo Mountain was similar to that described by Mathews (1948) for subglacial volcanoes in the Tuya area, in the central NCVP.

Subsequent detailed stratigraphic work, presented in section 2.2, further documents the evidence for volcano-glacial interaction during the volcanic development of the HMVC. The new stratigraphy revised from Kerr (1948) includes additional evidence for tills within the volcanic stratigraphy and for glacially-influenced volcanic morphologies. However, the work presented above also provides the first evidence for direct glacio-volcanic interaction characteristic of subglacial volcanism. Recognition of subglacial deposits

coupled with the ^{40}Ar-^{39}Ar results provides new constraints for the glacial history of the Iskut area as well.

Evidence from Glacial Deposits

Tills occur within the volcanic stratigraphy in at least three different locations and in three or four different stratigraphic positions. At the boundary between Hoodoo and *Little Bear Mountain*s, the uppermost till (Qt_3) conformably overlies Qvbb and is itself overlain conformably by $Qvpp_2$. Near the northwestern edge of Hoodoo Mountain near Hoodoo Glacier, the same till overlies Qvh_2, which in turn overlies an older till (Qt_2). The lower till also overlies Qvu with possibly another till (Qt_1) in between the two. To the south lava flows of Qvap sit on top of a thick sequence of till, the upper portions of which contain clasts derived from Hoodoo Mountain and the lower sections of which only have clasts of country rock.

Evidence from Volcanic Deposits

Glaciation has affected primary volcanic deposits in two different ways: i) by controlling their morphologies, and ii) by physically interacting with erupting magma. Many of the deposits have also been subsequently glacially scoured by many episodes of glaciation (e.g., *Little Bear Mountain*).

Volcanic morphology

Many of the lava flows at Hoodoo Mountain thickened as they moved downslope from a few tens of metres to a few hundred metres to form cliffs that are in excess of 200 m in height and abut large valley glaciers (Figure 2.3e). Such cliffs are visible on all sides of the volcano and on aerial photographs (Figure 2.2); the cliffs are marked on Plate 1B as well. The shapes of the cliffs and stratigraphic relationships suggest impoundment of the lava flows against glacial ice.

The rounded and domical shapes of both Hoodoo Mountain and *Little Bear Mountain* are due to glacial action as well. *Little Bear Mountain* has a drumlin-like shape in being elongate NE-SW, which would have been the direction of ice flow when Twin and Hoodoo glaciers were connected (see Figure 2.2). Hoodoo Mountain, as mentioned by Souther (1991), has a gently rounded to flat top, similar in shape to the classic tuya morphology first described by Mathews (1948). However, the flat-topped shape of a tuya usually results from having a subaerial lava flow as a caprock (Mathews 1948). At Hoodoo Mountain, the uppermost part of the volcano comprises irregular lava flows and domes and voluminous breccia. Certainly part of the morphology of Hoodoo Mountain is due to the advancing and retreating icecap on top of the volcano.

Subglacial volcanism

Evidence for direct interaction between glaciers and volcanism comes from three different sources: i) *Little Bear Mountain*, ii) Qvap breccia, and iii) the intimate association of $Qvap_6$, Qvh_3, and Qvh_2. This type of volcanism is known as subglacial, intraglacial, or ice-contact volcanism (Smellie et al. 1993; Jones 1969; Cas & Wright 1987)

Little Bear Mountain volcano comprises predominantly proximal volcanic breccia, pillow lava breccia and hyaloclastite; locally pillow lavas are abundant. All of the units described at *Little Bear Mountain* volcano are similar to units described from subglacial / subaqueous volcanoes in other parts of British Columbia (Mathews 1947), the Yukon (Jackson et al. 1990), Iceland (Jones 1969, 1970), and Antarctica (cf. Smellie et al. 1993). Units Qvbb, Qvbh, and Qvbs are considered to be coeval with units Qvbp and Qvbm at *Little Bear Mountain* and are interpreted as having formed by the disruption of pillows during subaqueous / subglacial emplacement of the basaltic lavas. In a topographically lower basin to the southwest of *Little Bear Mountain*, the breccia was deposited by debris flows shed off the edifice. The entire Little Bear edifice is interpreted as having formed subglacially and/or subaqueously and has been subsequently shaped by glacial erosion.

Unlike *Little Bear Mountain*, only a limited number of units at Hoodoo Mountain can be directly tied to subglacial eruption. One of those units is the

Qvap breccia associated with $Qvap_5$. Complex, intermingled contact relationships between the breccia and subunit $Qvap_5$ are very similar to those described by Bergh and Sigvaldason (1991) between basaltic lavas and hyaloclastite in Iceland. Additionally, lobes of $Qvap_5$ that are completely surrounded by breccia have radial and convoluted columnar jointing, also characteristic of subaqueos and/or subglacial volcanism (Long & Wood 1986; Bergh & Sigvaldason 1991).

The other type of subglacial volcanic deposit found at Hoodoo Mountain volcano is interpreted as resulting from fissure eruptions through ice. The deposit has three different components represented by subunits $Qvap_6$, Qvh_2, and Qvh_3. The close spatial association between $Qvap_6$, Qvh_2, and Qvh_3 was first noted by Edwards and Russell (1994a) and discussed by Edwards et al. (1995); specifically subunit Qvh_3 is commonly found as a carapace around $Qvap_6$, and $Qvap_6$ directly overlies Qvh_2 in two of the three localities where Qvh_2 occurs. The close spatial association and complex, intermingled contact relationships between Qvh_3 and $Qvap_6$ suggest that these deposits are cogenetic (Figure 2.6d). The fine-grain size, vesicularity, and radial jointing common in $Qvap_6$ (Figure 2.6c) are all similar to deposits of dacitic and rhyolitic subglacial eruptions from Iceland (Furnes et al. 1980), as are the blocks and lapillus of woody pumice found in Qvh_3.

The three unit association is interpreted to have formed during fissure fed eruptions of subglacial lava flows. The most complete exposures of the subglacial lava flows are along *Pumice Ridge*, which is composed of: i) Qvh_3 comprising yellow, lithified hyaloclastite consisting of heterogeneously distributed, highly vesiculated and elongate lapillus and bombs in a yellow, palagonitized matrix, ii) Qvh_2 comprising green, nonlithified hyaloclastite of mainly lapillus and ash with local bombs of vesicular $Qvap_6$, and iii) columnar jointed $Qvap_6$. On the south side of the ridge, the subglacial lava flows cascaded down on top of domes of columnar jointed $Qvap_1$ and were subsequently covered by lava flows of Qvpp from vents higher up the volcano. At one location, three coarsening upwards sequences in Qvh_2 culminate in deposits of large, glass rimmed, grey bombs interpreted to be from $Qvap_6$.

The stratigraphic position of Qvh_2, directly overlying Qt_2 and locally directly overlain by Qt_3 (Figure 2.6f), is also consistent with a close temporal association between Qvh_2 and glaciation.

Physical Evolution of the HMVC

Hoodoo Mountain volcanic centre has a complex history marked by repeated interactions between volcanism and glaciation. The earliest known large deposits in the complex, from *Little Bear Mountain*, all formed in a subglacial and/or subaqeuous environment around 240 Ka. Subsequently the

edifice has been glacially scoured and shaped and presently has a drumlinoid appearance. Eruptions of $Qvap_2$, at 80 Ka, were dammed by glacial ice that must have surrounded but not covered Hoodoo Mountain volcano. Subsequent flows of $Qvap_4$ preserve no evidence for glacial confinement of interaction, thus at 54 Ka the volcano must have been relatively free of ice and this could mark an intraglacial period. Subunits $Qvap_5$ and $Qvap_6$ are strongly jointed with irregular columnar jointing and are intimately associated with breccia interpreted as hyaloclastites indicating that they formed subglacially. This suggests at least the later history (40 to 30 Ka) of the centre was dominated by subglacial volcanism. Between 28 Ka and 9-10 Ka, flows of Qvpp erupted subaerially as evidenced by the well preserved and non-glaciated lava levées and aa lava flow surfaces of Qvpp. The fact that Qvpp also underlies at least parts of Hoodoo and Twin glaciers currently confirms that this unit erupted during a period of glacial recession.

The role of magmatic assimilation at the HMVC

Volcanic rocks from *Little Bear Mountain* and Hoodoo Mountain preserve direct and indirect evidence for magmatic assimilation. Both volcanoes contain xenoliths and xenocrysts with disequilibrium textures (e.g., embayed, sieve-textured phenocrysts) which are direct indications of reaction between the host magma and foreign inclusions. Similar direct evidence of magmatic

assimilation is common throughout the volcanic centres in the NCVP (Chapter 1). Xenocrysts with or without accompanying partly-melted xenoliths have been recorded from the Iskut area (Stasiuk & Russell 1989; Hauksdóttir 1994), Level Mountain (Hamilton 1981), Mount Edziza (Souther 1992), the Tuya Buttes area (Watson & Mathews 1948), the Atlin area (Edwards et al. 1996), Alligator Lake (Eiché et al. 1987), Fort Selkirk (Francis & Ludden 1990), and Prindle volcano (Foster et al. 1966; Chapter 1).

Haukdóttir (1994) best documented the chemical effects of assimilation for valley-filling basalt flows and cinder cones in the Iskut area. She used a combination of mass balance modelling and element ratio plots to demonstrate that assimilation coupled with fractional crystallization controlled the chemical variation in at least three of the eight centres she studied. Subsequent work by Cousens and Bevier (1995) also found geochemical evidence for magmatic assimilation of crustal material in the Iskut area.

The potential for magmatic assimilation affecting the basalts from *Little Bear Mountain* was tested using the modified element ratio approach developed by Hauksdóttir (1994). She used a diagram refered to as the Or diagram to test for the effects of fractionation and assimilation. The ordinate for the diagram comprises a ratio that precisely reflects the effects on a silicate melt of fractionation of Ol, Pl, Cpx, versus the effects of assimilation. For example, basalts formed by fractional crystallization of those three phases in a

closed system should plot along a straight line with a slope of one. Figure 2.27a shows the Or diagram using samples from a 1968 Hawaiin eruption (Nicholls and Stout 1988); all of the samples (except one) fall on a straight line with a slope of one, even though the samples vary from picrite to basalt. However, when assimilation plays a role in the chemical evolution of the system, samples do not fall along a single line. Samples from Lava Fork, a centre in the Iskut area studied by Hauksdóttir (1994), plot to the right of a line with a slope of one that passes through the sample with the highest MgO content (Figure 2.27b). Likewise, samples from *Little Bear Mountain* also do not all fall on the line, demonstrating that they cannot be related by fractional crystallization alone (Figure 2.27c).

Direct evidence for assimilation at Hoodoo Mountain in the form of xenoliths and xenocrysts is not abundant. However, the large volume of evolved rock types at Hoodoo Mountain may be indirect evidence for magmatic assimilation. Trachytic / phonolitic melts may form in four ways: i) direct melting of the mantle, ii) direct melting of the crust, iii) fractionation from a more mafic parental magma, or iv) coupled fractional crystallization and assimilation (Hay et al 1995). Formation of trachyte by direct mantle melting has not been validated experimentally (Hay and Wendlandt 1995). Hay and Wendlandt (1995) interpret their experimental results as indicating that 15% partial fusion of alkali olivine basalt can produce phonolitic melts. Further geochemical modeling of

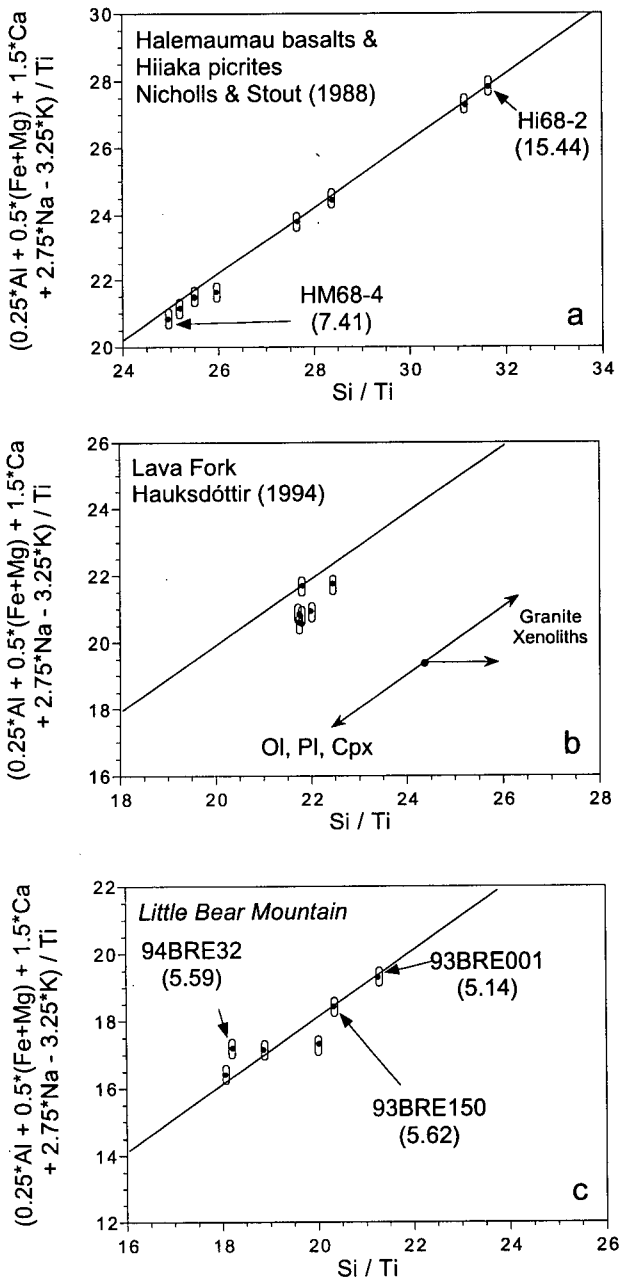

Figure 2.27. Element ratio plots for samples from: a) Hawaii, b) Lava Fork, and c) Little Bear Mountain. Ratios on ordinate are from Hauksdóttir (1994). Values in parentheses in a) and c) are weight percent MgO. Arrows in b) are vector displacements from any starting point caused by removal of Ol, Pl, and Cpx or addition of granite xenoliths (Hauksdóttir 1994).

the same suite of rocks by Hay et al. (1995) confirmed that the geochemistry of 4 of 6 samples of phonolite examined could be explained by partial melting alone, with the differences in the other two samples being related to incorporation of lower crustal material. Formation of trachyte / phonolite by fractional crystallization of basanite and/or alkali olivine basalt is possible in settings where the volumetric ratios of mafic to felsic magmas is high (Le Roex et al. 1990). However, fractional crystallization of 80% or more of a parental basaltic melt is required to produce the observed trachytic / phonolitic magmas. At the HMVC, the ratio of basaltic to trachytic / phonolitic magma is extremely low: 0.25 km^3 to 17.3 km^3. For the other two centres in the Stikine Subprovince, the ratios are much greater, but are still approximately 1:1 for Edziza (Souther 1992) and 4:1 for Level Mountain (Hamilton 1981).

The fourth method for producing trachyte / phonolite involves chemical contamination of a basaltic parental magma. This method maximizes the amount of evolved magma produced compared with volumes attributable to fractional crystallization alone (Figure 2.28). Liquid lines of descent for six different fractional crystallization (FC) scenarios, including FC alone, FC with assimilation of granite, FC with assimilation of biotite ($Phlogopite_{30}$), FC with assimilation of K feldspar, FC with assimilation of plagioclase (An_{10}), and FC with assimilation of quartz (Qtz) are shown in Figure 2.28. Also shown are samples from *Little Bear Mountain* (large open circles) and from Hoodoo

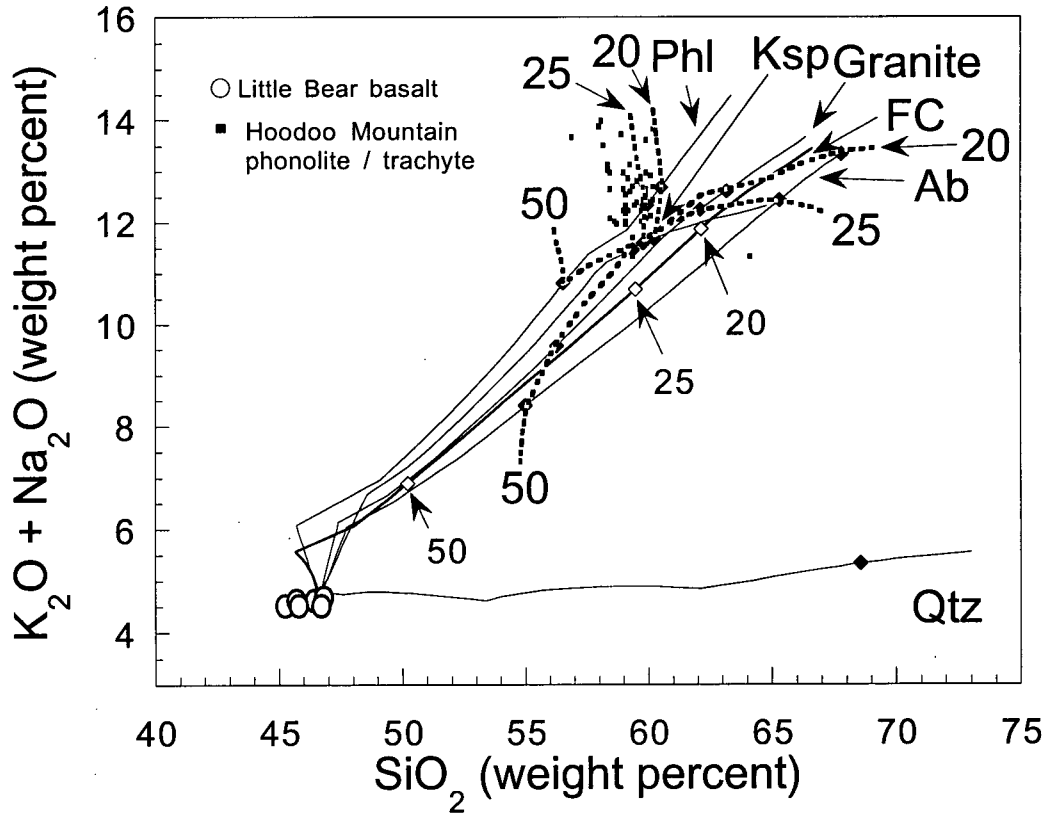

Figure 2.28. Weight percent total alkalies ($Na_2O + K_2O$) versus SiO_2 diagram for samples from Little Bear Mountain (open circles) and Hoodoo Mountain (filled squares). Model AFC paths are included for comparison. Paths correspond to fractional crystallization (FC) and FC plus assimilation of phlogopite (Phl), orthoclase (Ksp), granite, albite (Ab), and quartz (Qtz). For each model line three points are shown that represent the remaining mass fraction of original melt (50, 25 and 20 percent from low SiO_2 to high SiO_2 respectively). Details of modeling given in Chapter 4.

Mountain (small black squares). The liquid lines of descent were calculated using the MELTS software (Ghiorso 1995). For all six scenarios (labeled lines) shown, the starting composition was for a non-porphyritic sample from Lava Fork (sample SH-44 of Haukdóttir 1994; see Table 4.1), which has Pl on the liquidus at 10^5 Pa. Details of the model results are discussed in Chapter 4. For each model line three points are shown that represent the remaining mass fraction of original melt (50, 25 and 20 percent from low SiO_2 to high SiO_2 respectively). The liquid lines of descent illustrate that to derive Hoodoo Mountain trachytes from a basalt similar in composition to that of *Little Bear Mountain* requires assimilation of material rich in potassium (represented by AFC scenarios using either phlogopite or potassium feldspar). Eighty percent crystallization is required to produce trachyte from the basalt by fractional crystallization without assimilation. However, AFC of a K-rich phase drives the system to the trachyte / phonolite composition with only 50% crystallization; this allows the mafic magma to produce more felsic magma. Variations in $^{87}Sr / ^{86}Sr$ ratios are also consistent with this hypothesis in that all of the Hoodoo samples have values of $^{87}Sr / ^{86}Sr$ in between those for basalts from *Little Bear Mountain* and the field for rocks from the underlying basement to the HMVC, the Stikine terrane (Figure 2.26).

2.5. SUMMARY

The Hoodoo Mountain volcanic complex is the last of the major volcanic centres in the Stikine Subprovince of the Northern Cordilleran Volcanic Province to be studied in detail. It is now known to comprise phonolite, trachyte, and lesser alkali olivine basalt. The geology and stratigraphy of the volcano has been dominated for the last 240 Ka by processes that reflect close spatial and temporal association between volcanism and glaciation. Specifically the complex comprises units erupted subglacially and units whose morphology was controlled by bounding glacial ice.

The volcanic rocks from the complex are texturally diverse and the origin of the diversity is largely due to magmatic processes including magmatic assimilation. The chemical signature of assimilation is difficult to detect but is mineralogically evident in basalts from *Little Bear Mountain*. Moreover, the presence of volumetrically dominant evolved rocks at Hoodoo Mountain is consistent with derivation of the evolved rocks by chemical contamination of more basic magmas.

CHAPTER 3

Thermodynamic and Kinetic Controls on Magmatic Assimilation

3.1. INTRODUCTION

Plagioclase phenocrysts with rounded and embayed cores, plagioclase megacrysts with sieve-textured rims, rounded and embayed clinopyroxene megacrysts, and partly melted xenoliths are typical features in basalts from *Little Bear Mountain* that record complex mineral-melt reactions consistent with magmatic assimilation. The abundance of xenocrysts (e.g., Francis & Ludden 1990; Souther 1992; Hauksdóttir 1994) and partly melted xenoliths (e.g., Watson & Mathews 1948, Souther 1992, Hauksdóttir 1994) throughout the Northern Cordilleran Volcanic Province (NCVP) are evidence for pervasive assimilation throughout this magmatic province.

The role of thermodynamics and kinetics in the process of magmatic assimilation is critical to the quantitative modeling of assimilation at specific volcanic centres in the NCVP (Chapter 4). The following brief review expands the contribution of previous work on the well-established thermodynamic constraints on magmatic assimilation (Bowen 1922, Nicholls & Stout 1982, Ghiorso & Kelemen 1986, Russell et al. 1995) to present a model that links

kinetic constraints for mineral dissolution to the thermodynamic driving force for the dissolution reactions. Underlying the model is the examination of the kinetics of magmatic assimilation which includes a detailed examination of five published datasets of mineral dissolution experiments in natural magma compositions (Donaldson 1985 & 1989, Brearley & Scarfe 1986, Zhang et al. 1989, Thornber & Huebner 1985). A new model for predicting rates of mineral dissolution in natural silicate melts, a fundamental foundation for predictive models involving magmatic assimilation in the NCVP, is the result.

3.2. THERMODYNAMIC CONSTRAINTS

Bowen (1922) was one of the first petrologists to consider quantitatively the energetics of magmatic assimilation. He recognized the fundamental importance of heat balances attending reactions between the original magma and the xenolith. Bowen (1922) recognized that the solid material has to be heated to a temperature where it will fuse or react with the magma and that, since magmas probably are not commonly superheated (above liquidus temperatures), the heat available to the magma for completing this task is derived from the heat energy stored in the magma (the sensible heat) and from the latent heat of crystallization. Although Bowen did not have the information available to quantitatively calculate the entire heat balances for assimilation, he

outlined many of the important principles and established the groundwork for subsequent research.

Since Bowen (1922), a number of workers have used heat-balance considerations in their effort to quantify assimilation processes (e.g., Wilcox 1954; Myers & Marsh 1981). Nicholls and Stout (1982), however, presented the first detailed account of the heat budget attendant to assimilation. Their calculations considered the energy required to: i) unmix mineral solid solutions, ii) heat minerals to fusion temperatures, iii) fuse minerals at fusion temperatures, iv) heat (or cool) fused minerals to the temperature of the magma, and v) mix the fused mineral with the magma. The details of the enthalpy balance for the assimilation of alkali feldspar ($Or_{88}Ab_{12}$) initially at 500 ^{o} C by a basaltic magma at 1100 ^{o} C and 0.5 GPa are given in Table 3.1a (data from Table 4, Nicholls & Stout (1982), p. 336). They found that a perfect heat balance implied a ratio of assimilation to crystallization of 0.5. Most of the required energy (>85%) was used to heat the solids to their T_{fusion}. Fusion of the sanidine required about 24% of the total heat energy. For minerals with $T_{fusion} > T_{magma}$, some "calculated" energy (10%) is returned by cooling the fused mineral (now a liquid) down to T_{magma}. The heats of unmixing for mineral solid solutions and for mixing the silicate liquids are both small (-1.29% and +2.45%) and opposite in sign, and hence have commonly been neglected by other workers (e.g., Sparks 1986). Similar energy requirements are implied by

Table 3.1a. Detailed enthalpy budget for assimilation of alkali feldspar ($Or_{88}Ab_{12}$) in basaltic magma at P = 0.5 GPa (data from Table 4 of Nicholls & Stout 1982, p. 336).

Step	ΔH (Joules)	Percent of Total
1) unmix Sanidine solid solution	-118.9	-1.29
2) heat Or to its T_{fusion} (1473 K)	7163.3	86.88 (Or & Ab)
3) heat Ab to its T_{fusion} (1391 K)	845.9	
4) ΔH_{fus} for Or	1947.9	24.34 (Or & Ab)
5) ΔH_{fus} for Ab	295.1	
6) cooling Or to T_{magma}	-1113.1	-12.38 (Or & Ab)
7) cooling Ab to T_{magma}	-28.0	
8) mixing Or with magma	215.6	2.45 (Or & Ab)
9) mixing Ab with magma	10.5	

Table 3.1b. Modal mineralogy (in mole %) of five rock types used to calculate apparent ΔH_{fus} (kJ $mole^{-1}$) (after Russell et al. 1995; mineral abbreviations after Kretz 1983).

Rock Type	An	Ab	Kfs	Qtz	Cpx	Ol	En	Act	Ms	Chl	Ep
gabbro	28.6	19.3	0.0	0.0	31.9	13.8	6.4	0.0	0.0	0.0	0.0
granite	1.5	6.2	47.9	35.8	0.0	0.0	0.0	0.0	8.6	0.0	0.0
Bt schist	0.0	0.0	3.8	34.4	0.0	0.0	0.0	0.0	61.9	0.0	0.0
greenschist	4.0	4.0	0.0	8.8	0.0	0.0	0.0	11.9	0.0	42.4	28.9
Qtz arenite	0.0	5.8	5.4	88.8	0.0	0.0	0.0	0.0	0.0	0.0	0.0

Table 3.1c. Calculated apparent ΔH_{fus} (kJ $mole^{-1}$) for five rock types for several different ambient temperatures and a magmatic temperature of 1120 ° C (after Russell et al. 1995).

Rock Type	450 ° C	650 ° C	850 ° C	1050 ° C	1120 ° C
gabbro	73.45	59.98	45.97	31.56	26.44
granite	62.94	48.71	33.95	18.83	13.48
Bt schist	69.26	56.18	42.66	28.86	23.98
greenschist	79.70	66.23	52.15	37.61	32.43
Qtz arenite	55.20	41.59	27.50	13.09	8.00

the work of Ghiorso and Kelemen (1987) who found that isenthalpic assimilation of pelite by basalt magma required a six- to tenfold increase in the amounts of crystallization for pelite at 500 ° C as opposed to 1250 ° C. Both Nicholls and Stout (1982) and Ghiorso and Kelemen (1987) found that, in order for the magma to maintain a constant temperature as well as to assimilate solids, the mass of the crystallizing material must be at least twice as much as the mass of material being assimilated.

Different minerals have distinct thermodynamic properties. Thus, assimilation of different rock types requires significantly different amounts of energy. The apparent ΔH_{fus} is one way to quantify the amount of energy required for reaction of a mineral, given a $T_{initial}$ and T_{final} (Ghiorso & Kelemen 1987; Lange & Carmichael 1990). Apparent $\Delta H's_{fus}$ are calculated by summing the energy required to heat the mineral from $T_{initial}$ to T_{fusion}, the ΔH_{fus} at the T_{fusion}, and the amount of energy released (or required) by cooling (or heating) the fused mineral to T_{final}. Apparent $\Delta H's_{fus}$ for five xenoliths composed of common silicate minerals (Table 3.1b.) are shown in Table 3.1c. Table 3.1c highlights differences resulting from different heat capacity and ΔH_{fus}. For example, when the $T_{xenolith}$ = 450 ° C and T_{magma} = 1120 ° C, 44 % more energy (24.5 kJ) is required to assimilate one mole of greenschist than to assimilate one mole of quartz arenite.

3.3. KINETIC CONSTRAINTS

The kinetics of magmatic assimilation is strongly dependent on rates of reaction between minerals in the xenolith and the host magma. Numerous workers have published experimental results for rates of mineral dissolution reactions in silicate melts (Cooper & Kingery 1964; Kutolin & Agafonov 1978; Scarfe et al. 1980; Kuo 1982; Donaldson 1985; Kuo & Kirkpatrick 1985; Thornber & Huebner 1985; Brearley & Scarfe 1986; Zhang et al. 1989; Donaldson 1990). However, few systematic comparisons of the available data exist (Kuo & Kirkpatrick 1986; Brearley & Scarfe 1986; Edwards & Russell 1994) and none of the published dissolution studies have produced a quantitative predictive model for mineral dissolution rates in silicate melts.

The purpose of this section is to evaluate and compare the published experimental data on silicate mineral dissolution in naturally-occurring silicate melts. Calculated affinities (**A**) for dissolution reactions may prove useful to predict rates of mineral dissolution, where **A** is the difference in the chemical potential of the product(s) and the reactant(s) for the reaction. The section presents an analysis of five datasets of experimental measurements for silicate mineral dissolution in natural silicate melts as a function of melt composition, mineral composition, temperature (**T**), and pressure (**P**) and includes evaluation of the consistency of experiments conducted by different

workers, and of relationships between experimentally-determined values of reaction rates (v) and melt composition, mineral composition, **T**, and **P**. Finally, the possibility of using calculated values of **A** to predict experimentally-determined values of v is explored.

Methodology

This compilation of published mineral-dissolution experiments includes data for olivine (number = 120), plagioclase (N = 81), quartz (N = 37), spinel (N = 24), clinopyroxene (N = 25), orthopyroxene (N = 18), and garnet (N = 10). Table 3.2. summarizes the database which includes experiments using natural melt compositions ranging from basalt to rhyolite (Table 3.3.). Excluded from the current database are results from workers who report dissolution rates but do not report the data for individual experiments (e.g., Kutolin and Agafonov, 1978) or experiments using synthetic melt compositions (e.g., Kuo, 1982).

Evaluation of the datasets

Complete characterization of the experimental conditions and results is important for evaluating the internal consistency of the experiments and is critical for subsequent analysis and modeling. The experimental parameters that need to be reported include: i) temperature (**T**), ii) pressure (**P**), iii) time elapsed between the start and finish of the dissolution experiment (**t**), iv) initial

Table 3.2. Summary of silicate mineral dissolution experiments using both natural and synthetic melts. Underlined references are used in this work.

Minerals	Number of experiments	Researchers
Olivine	144	Kutolin and Agafonov (1978)[1]; Scarfe et al. (1980)[1]; Kuo (1982)[2]; Marvin and Walker (1985)[1]; Thornber and Huebner (1985); Donaldson (1985); Brearley and Scarfe(1986); Zhang et al. (1989), Donaldson (1990)
Orthopyroxene	41	Kutolin and Agafonov (1978)[1]; Scarfe et al. (1980)[1]; Kuo (1982)[2]; Brearley and Scarfe (1986);
Clinopyroxene	89	Kutolin and Agafonov (1978)[1]; Scarfe et al. (1980)[1]; Kuo (1982)[2]; Brearley and Scarfe (1986); Zhang et al. (1989)
Spinel	25	Scarfe et al. (1980)[1]; Brearley and Scarfe (1986); Zhang et al. (1989)
Garnet	17	Kutolin and Agafonov (1978)[1]; Scarfe et al. (1980)[1]; Brearley and Scarfe (1986)
Quartz	73	Watson (1982)[1]; Kuo (1982)[2]; Donaldson (1985); Zhang et al. (1989)
Alkali Feldspar	21	Watson (1982)[1]; Tsuchiyama (1985)[2]
Plagioclase	81	Marvin and Walker (1985)[1]; Donaldson (1985); Tsuchiyama (1985)[2]
Zircon, Apatite, Rutile	31	Harrison and Watson (1983, 1984); Zhang et al. (1989)

[1] initial sample geometries not reported
[2] experiments used synthetic melt compositions

Table 3.3. Compositions of melts used in mineral dissolution experiments.

Study	Thornber & Huebner (1985)		Donaldson (1985; 1990)			Brearley & Scarfe (1986)	Zhang et al. (1989)
Rock Type	high Al - basalt	Si-enrich. basalt	Qtz-norm basalt	andesite	rhyolite	alkaline basalt	andesite
Wt. % Oxides							
SiO_2	45.09	52.32	51.91	57.7	75.1	48.6	56.5
TiO_2	2.86	2.55	1.16	1.1	0.2	2.20	1.24
Al_2O_3	17.18	16.29	15.85	14.3	14.3	15.6	18.0
Cr_2O_3	na	na	0.06	na	na	na	na
Fe_2O_3	na	na	1.65	na	na	3.13	na
FeO	9.44[1]	8.38[1]	8.27	8.8[1]	0.9[1]	8.53	6.71[1]
MnO	0.02	0.01	0.15	0.2	0.1	0.16	0.13
MgO	10.67	9.09	7.01	6.4	0.2	6.30	3.96
CaO	12.00	9.59	8.66	7.6	0.6	9.85	7.73
Na_2O	1.60	0.67	3.03	2.6	3.9	3.50	3.75
K_2O	0.17	0.19	0.75	0.7	4.5	1.21	1.7
P_2O_5	na	na	0.17	na	na	0.51	0.38
H_2O	na	na	0.86	na	na	0.02	na
Total	99.03	99.09	99.53	99.4	99.8	99.61	100.1

na - not available
[1] Total Fe as FeO

size and shape of the starting material, v) final size of the starting material, vi) initial mineral and melt compositions, and vii) estimates of measurement errors. The datasets that best meet the above criteria and therefore form the basis for this analysis are Donaldson (1985; 1990), Brearley and Scarfe (1986), Thornber and Huebner (1985), and Zhang et al. (1989). Results are considered to be internally consistent if all the experiments at the same **T** and **P** produce dissolution rates that are within analytical error of each other and vary smoothly and continuously with time.

Multiple experiments at each **T** and **P** condition are also important as they serve as checks on the internal consistency of the experiments. In theory values of ν can be calculated on the basis of one experiment; however, such values of ν do not allow any estimation of uncertainty nor do they allow for assessment of time-dependent versus time-independent behavior.

Derivation of mineral dissolution rates

Data from experiments are reported as changes in dimensions (e.g., radii for spheres) for a given time at one value of **T** and **P**. Isothermal dissolution rates (ν) for each mineral are calculated by linear regression assuming a y-intercept of zero; ν is equal to the slope. Figure 3.1 illustrates the

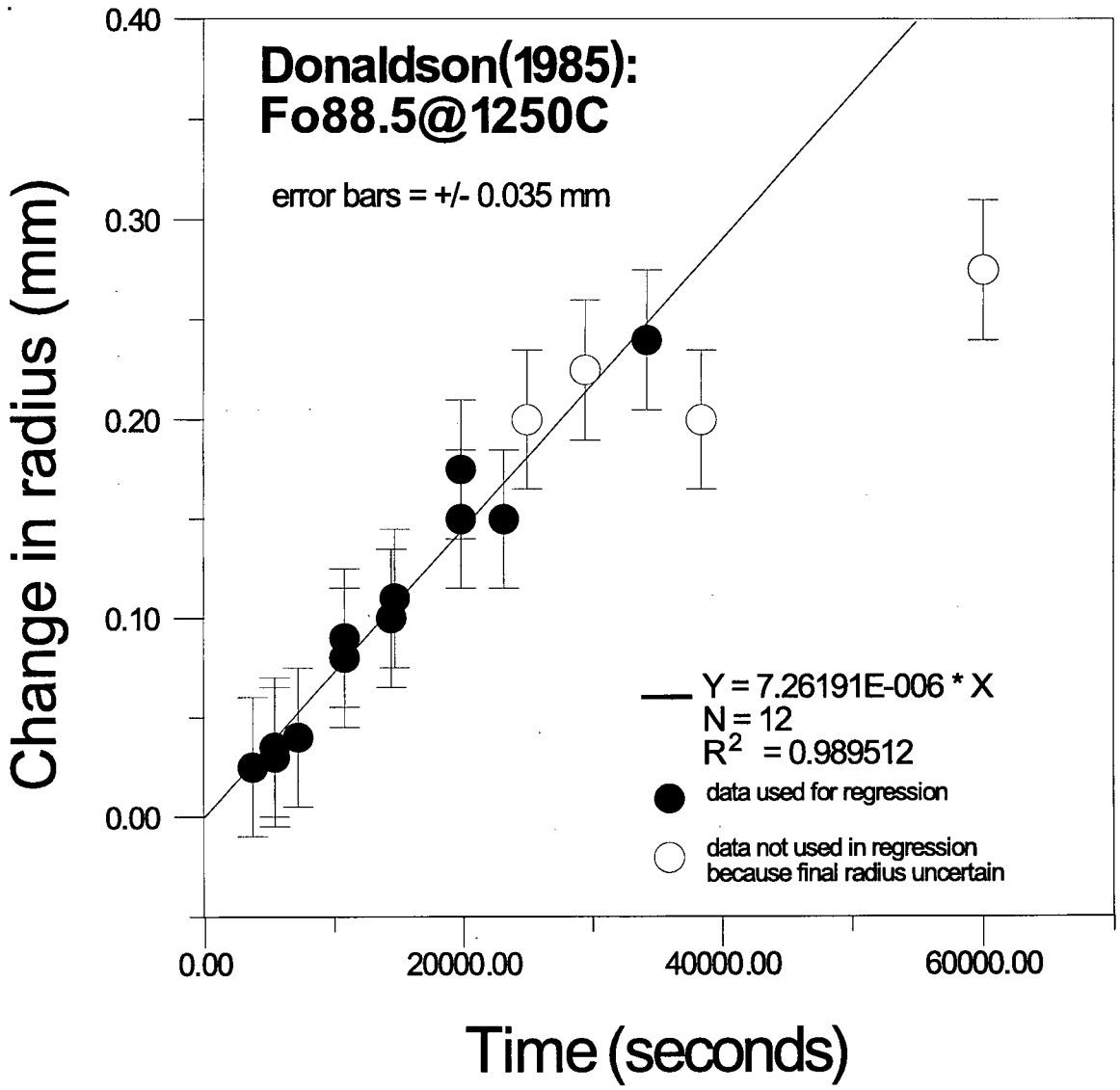

Figure 3.1. Experimental data from Donaldson (1985) for olivine ($Fo_{88.5}$) at 1250 ° C. Data are fit by linear regression to a line with a zero y-intercept; the slope of the fitted line is ν. Experiments in which the entire crystal dissolved (open symbols) were not used in the regression.

technique used to calculate ν at each **T** using dissolution data for olivine ($Fo_{88.5}$) at 1250 °C (Donaldson, 1985). The total change in radius of a mineral during each experiment is plotted against the time of the experiment. A total of 16 experiments are plotted; only the solid circles are used for the regression because of uncertainties in the final radius for 4 of the experiments (open circles). The best fit line for these experiments passes within the estimated measurement uncertainties for all data points used in the regression.

Normalization of experimental data

Normalization is required for direct comparison of experimental mineral dissolution data gathered under different **P** and **T** conditions and utilizing different experimental arrangements for two reasons. Firstly, the measured experimental values of ν are dependent on the initial shape of the crystal. For instance, a change in radius of 0.05 cm for a quartz sphere is not neccessarily equal to a shortening of a quartz parallelepiped by 0.05 cm in each dimension (Figure 3.2). Secondly, measured values of ν for different minerals are not directly comparable. A value of ν in units of cm of olivine ($(Fe,Mg)SiO_4$) s^{-1} is not directly comparable to a value of ν with units of cm of plagioclase ($(Na_x,Ca)Al_{2-x}Si_{2+x}O_8$) s^{-1} because the rates are not on an equivalent oxygen basis.

spherical geometry

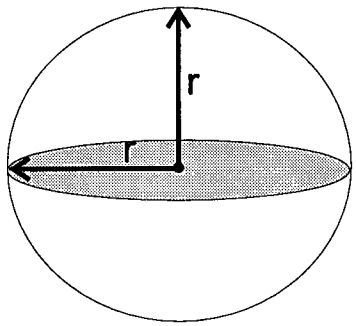

volume = $\frac{4}{3}\pi r^3$

surface area = $4\pi r^2$

$\frac{dV}{dr} = 4\pi r^2$

$\frac{dV}{dt} = \left(\frac{dV}{dr}\right)\left(\frac{dr}{dt}\right)$

volume = $\pi r^2 h$

exposed surface area = πr^2

$\frac{dV}{dh} = \pi r^2$

$\frac{dV}{dt} = \left(\frac{dV}{dh}\right)\left(\frac{dh}{dt}\right)$

cylindrical geometry

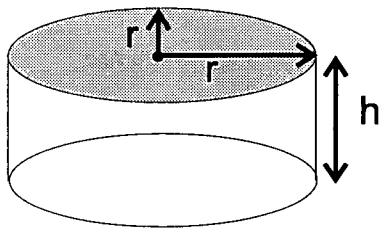

rectangular parallelepiped geometry

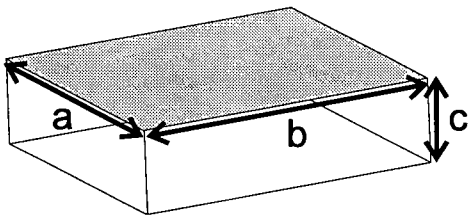

volume = abc

surface area = 2(ab + bc + ac)

$\left(\frac{dV}{da}\right) = bc \qquad \left(\frac{dV}{db}\right) = ac$

$\left(\frac{dV}{dc}\right) = ab$

$\frac{dV}{dt} = \left(\frac{dV}{da}\right)\left(\frac{da}{dt}\right) + \left(\frac{dV}{db}\right)\left(\frac{db}{dt}\right) + \left(\frac{dV}{dc}\right)\left(\frac{dc}{dt}\right)$

Figure 3.2. Mensuration formulas and volume derivatives for geometries of samples used in experiments.

The normalization procedure used is slightly modified from the method of Wood and Walther (1983) and Walther and Wood (1984). The regressed values of ν are converted from units of **cm s^{-1}** to **oxygen equivalent moles (o.e.m.) cm^{-2} s^{-1}** using the procedure outlined below:

1. Calculate values of ν (cm s^{-1}) by linear regression of isothermal experimental measurements of ***dr/dt*** (e.g., Figure 3.1).

2. Normalize values of ν (e.g., Walther and Wood, 1984) using:

$$(1) \qquad \nu = \frac{dm}{dt} = \frac{1}{s} \bullet \frac{dV}{dr} \bullet \frac{dr}{dt}$$

where *dm/dt* is the normalized dissolution rate (cm s^{-1}), *s* is the surface area of the dissolved crystal (cm^2), *dV/dr* is the change in volume with respect to change in radius (cm^3 cm^{-1}), and *dr/dt* is the measured change in radius over the duration of the experiment (cm s^{-1}). Because several different initial mineral geometries are possible, the *dV/dr* term and the *s* term have slightly different formulations depending on starting material geometry (Figure 3.2). For spherical geometries (Donaldson, 1985, 1990; Brearley & Scarfe, 1986), the surface area and the volume derivative with respect to changing radius are equal and thus cancel. Zhang et al. (1989) used a cylindrical geometry where only the upper and lower surfaces of the cylinder are exposed to the melt, so the volume derivative with respect to changing thickness and the exposed surface area are equal and also cancel. Thornber and Huebner (1985) used

rectangular parallelepiped geometries but only reported changes in one of the three dimensions. For their dataset, it was assumed that changes in all three dimensions were equal, which reduces the combined volume derivative and surface area terms to a constant (0.5). In summary, *dm/dt* = *dr/dt* for spherical or cylindrical geometries and *dm/dt* = 0.5 *dr/dt* for rectangular parallelopiped geometries.

3. Divide the values of ν by the molar volume (**V**) to convert to units of moles cm^{-2} s^{-1}. Molar volume properties are calculated at experimental **T** and **P** conditions using the thermodynamic database and methodology of Berman (1988) and assuming no excess volume of mixing.

4. Lastly, multiply the values of ν by the number of oxygens in the mineral formula to get o.e.m. cm^{-2} s^{-1}.

Results

Donaldson (1985; 1990)

Donaldson (1985; 1990) used the same experimental methodology and range of conditions to investigate several different mineral dissolution reactions (Table 3.4). Donaldson (1985) presented results of 110 dissolution experiments involving quartz normative tholeiitic basalt melt (Table 3.3) and 5 different mineral compositions (Table 3.4). Donaldson (1990) ran 26 experiments using three different melt compositions (Table 3.4) to dissolve

Table 3.4. Summary of dissolution rates at 10^{-4} GPa extracted from experimental data of Donaldson (1985; 1990).

mineral	**T (°C)**	**dr/dt ($cm\ s^{-1} \bullet 10^{-7}$)**	**N (number of experiments)**	**R^2**
Quartz	1122	0.1072	2	0.972
	1143	0.2947	5	0.884
	1210	9.636	4	0.991
	1250	13.57	11	0.993
	1300	22.26	5	0.995
Plagioclase (An_{29})	1150	0.2976	1	na
	1210	24.41	4	0.993
	1250	38.38	4	0.996
	1300	65.62	5	0.983
Plagioclase ($An_{52.5}$)	1210	13.18	5	0.923
	1250	29.80	5	0.994
	1300	56.57	5	0.989
Olivine ($Fo_{88.5}$)	1210	0.7645	3	0.912
	1250	7.262	12	0.990
	1300	17.40	2	0.999
Olivine ($Fo_{91.5}$)	1210	2.202	5	0.887
	1250	8.411	10	0.910
	1300	27.54	4	0.997
*	1300	27.02	6	0.990
*	1300	19.08[1]	5	0.975
*	1300	0.2504[2]	9	0.972

* Donaldson (1990)

[1] experiments with time > 5 hours were not used to calculate this **dr/dt** value

[2] experiments with time > 110 hours were not used to calculate this **dr/dt** value

spheres of olivine ($Fo_{91.5}$). For both datasets, values of change in radius for a given time interval (***dr/dt***) were determined by measuring initial and final radii of the spheres. Reported measurement errors are +/- 0.0035 cm.

The Donaldson (1985; 1990) datasets are the easiest to evaluate for internal consistency because, on average, 5 experiments were conducted at each set of experimental **T** and **P** conditions. The values of v Donaldson reported differ slightly from those reported in Table 3.4 because he did not constrain the regression to pass through the origin. However, this is a necessary constraint because at t = 0 the change in radius must be zero also.

Brearley and Scarfe (1986)

Brearley and Scarfe (1986) used an alkali basalt melt (Table 3.3) as a solvent for dissolving olivine, clinopyroxene, orthopyroxene, spinel, and garnet over a range of **T** (1250 - 1500 °C) and **P** (0.5 - 3.0 GPa) conditions (Table 3.5). They used spherical mineral geometries and reported initial and final radii for each experiment. Measurement errors are estimated at +/- 0.001 cm for most experiments but are as large as 0.003 cm (10% of the initial diameter of the crystals. They also conducted at least two experiments for each set of isothermal and isobaric conditions except for one garnet experiment (Table 3.5).

Table 3.5. Summary of dissolution rates extracted from experimental data of Brearley and Scarfe (1986).

mineral	T (°C)	P (GPa)	dr/dt ($cm\ s^{-1} \bullet 10^{-7}$)	N (number of experi-ments	R^2
Olivine ($Fo_{89.6}$)	1250	0.5	1.852	3	0.778
	1300	0.5	8.489	3	0.967
	1300	1.2	6.349	3	0.946
	1350	1.2	11.05	3	0.999
	1400	1.2	33.73	13	0.955
	1450	3.0	53.89	5	0.991
	1500	3.0	286.7	2	0.958
Clinopyroxene	1250	0.5	15.87	3	0.974
	1300	0.5	48.41	3	0.994
	1300	1.2	1.587	3	0.857
	1350	1.2	14.44	2	0.994
	1400	1.2	63.0	4	0.933
	1450	3.0	9.474	4	0.865
	1500	3.0	195.0	2	0.991
Orthopyroxene	1250	0.5	11.11	3	0.944
	1300	0.5	22.75	3	0.995
	1300	1.2	5.820	3	0.960
	1350	1.2	21.11	2	0.976
	1400	1.2	27.78	2	1
	1450	3.0	44.20	3	0.981
	1500	3.0	113.3	2	0.997
Spinel	1250	0.5	1.058	3	0.762
	1300	0.5	4.099	3	0.937
	1300	1.2	0.7508	4	0.338
	1350	1.2	1.058	3	0.762
	1400	1.2	2.889	4	0.751
	1450	3.0	6.053	4	0.964
	1500	3.0	55.74	3	0.998
Garnet	1300	1.2	290.5	3	0.900
	1400	1.2	1317.0	1	-
	1450	3.0	52.28	4	0.982
	1500	3.0	398.3	2	1.000

Thornber and Huebner (1985)

Thornber and Huebner (1985) studied olivine dissolution in melts of two different compositions (Table 3.3): lunar basalt #77115 and a silica-enriched variant of #77115 (Sil-77115). The experimental conditions and results are given in Table 3.6. They reported a total of 25 isothermal, superliquidus dissolution experiments including 18 on the basalt and another 7 using the silica-enriched melt. All of their experiments use olivine (Fo_{92}) cut into crystallographically-oriented rectangular parallelepipeds. Values of change in thickness with time (***dh/dt***) were determined by measuring the thickness perpendicular to the largest surface area of the mineral plates before and after the experiments. Reported measurement errors are +/- 0.0002 cm. The internal consistency of this dataset is not well-constrained because of the lack of repeated isothermal, isobaric experiments.

Zhang et al. (1989)

Zhang et al. (1989) used an andesitic melt (Table 3.3.) to dissolve crystals of forsterite (N = 3), diopside (N = 4), quartz (N = 1), spinel (N = 1), rutile (N = 1), as well as natural San Carlos olivine (N = 10) over a range of **T** (1215 to 1400 °C) and **P** (0.5 - 2.3 GPa) (Table 3.7). The starting crystals were cut and ground into cylinders to the exact diameter of the experimental charge, thereby isolating melt reservoirs on either side of the mineral. This dataset is similar to

Table 3.6. Summary of dissolution rates at 10^{-4} GPa extracted from experimental data of Thornber and Huebner (1985).

mineral	T(°C)	dh/dt (cm $s^{-1} \bullet 10^{-7}$)	N (number of experiments)	R^2
Olivine(Fo_{92})	1263	0.0579	1	-
	1265[1]	0.1196	3	0.999
	1280	0.934	1	-
	1285	1.452	2	0.970
	1297	1.90	1	-
	1315	5.741	2	0.992
	1326	5.35	1	-
	1330	5.951	2	0.986
	1450	171.0	1	-
*	1240	0.284	1	-
*	1270	2.05	1	-
*	1284	2.42	1	-
*	1315	9.72	1	-

[1] includes one experiment at 1266 °C

* silica-enriched melt composition (see Table 3.3)

Table 3.7. Summary of dissolution rates extracted from experimental data of Zhang et al. (1989).

mineral	T(°C)	P(GPa)	dh/dt ($cm\ s^{-1} \bullet 10^{-7}$)	N (number of experiments)	R^2
Olivine [1]	1270	0.55	0.9727	1	-
	1285	0.55	4.796	1	-
	1290	0.55	2.688	2	0.976
	1365	1.3	30.90	1	-
	1375	1.5	57.22	1	-
	1400	0.55	27.92	1	-
Olivine (Fo_{100})	1305	0.55	3.059	2	0.543
Clinopyroxene[2]	1305	1.05	10.40	2	0.871
	1365	1.3	30.93	1	-
	1375	2.15	79.78	1	-
Spinel	1385	1.3	7.865	1	-

[1] Olivine composition varies between Fo_{88} and Fo_{91} among experimental runs
[2] Clinopyroxene is diopside

that of Thornber and Huebner (1985) in that few isothermal, isobaric experiments were repeated (3 out of 11) making it difficult to assess the internal consistency of the experiments.

Comparison of reported data for olivine

The experimental dataset for olivine is by far the largest and serves to illustrate the effects of mineral stability, **T**, and **P** on values of ν. Figure 3.3a presents the datasets of Donaldson (1985; 1990) plotted as ln ν (o.e.m. cm^{-2} s^{-1}) vs. 1000 / **T** (K). The data, represented by filled circles ($Fo_{88.5}$) and open circles ($Fo_{91.5}$), demonstrate the small differences in values of ν for slightly different olivine compositions dissolving in the same melt composition at the same values of **T** and **P**. These 2 datasets strongly support an Arrhenian relationship between ν and **T**. Activation energies (E_A) are calculated from the slope of the best-fit line to the data divided by the gas constant and are reported in Table 3.8. Uncertainties in values of ln ν which arise from variances in the isothermal experimental data (e.g., Figure 3.1) are generally smaller than the symbol size in Figures 3.3 and 3.4 (Appendix A3.1).

Figure 3.3b gives a summary of all the **P** = 10^5 Pa data for olivine dissolution in basaltic melts and consists of data from Donaldson (1985; 1990) (dashed lines) and Thornber and Huebner (1985) (solid lines and

Table 3.8. Activation energies (kJ / oxygen equivalent moles) implied by fits to data shown in Figures 3.3 and 3.4.

Reference	Mineral	P(GPa)	Activation Energy (kJ / o.e.m)
Donaldson (1985)	Quartz	10^{-4}	180
	Plagioclase ($An_{59.5}$)	10^{-4}	310
	Plagioclase ($An_{29.5}$)	10^{-4}	210
	Olivine ($Fo_{91.5}$)	10^{-4}	550
	Olivine ($Fo_{88.5}$)	10^{-4}	650
Brearley & Scarfe (1986)	Olivine	0.5	610
		1.2	360
		3.0	850
	Clinopyroxene	0.5	440
		1.2	810
		3.0	1540
	Orthopyroxene	0.5	280
		1.2	340
		3.0	480
	Spinel	0.5	540
		1.2	290
		3.0	1130
	Garnet	1.2	330
		3.0	1030
Zhang et al. (1989)	Olivine[1]	0.55 - 1.5	590
	Clinopyroxene[1]	1.05 - 2.15	1800
Thornber & Huebner (1985)	Olivine	10^{-4}	870
	Olivine[2]	10^{-4}	920

[1] in andesitic melt (see Table 3.3)
[2] in Si-enriched basaltic melt (see Table 3.3)

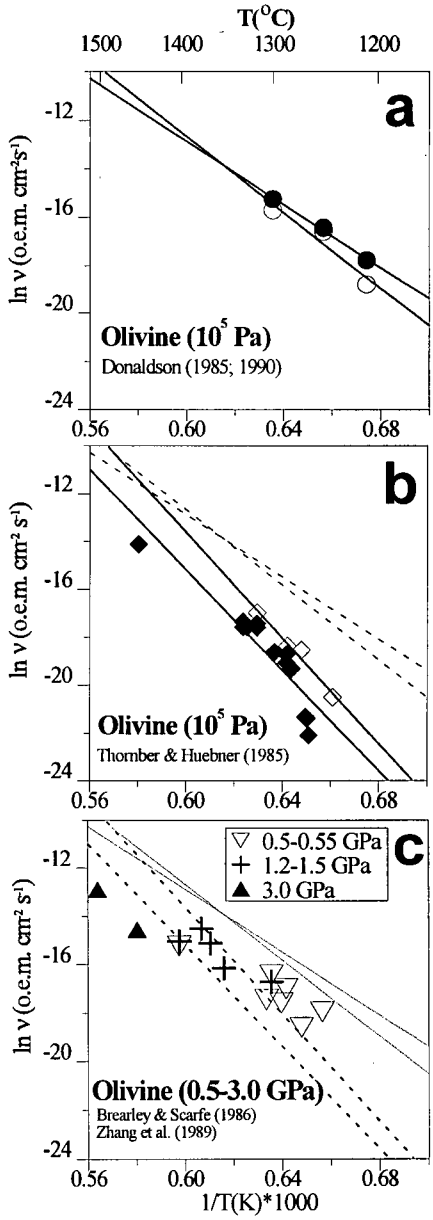

Figure 3.3. Normalized values of ν calculated from experimental data (oxygen equivalent moles (o.e.m.) $cm^{-2}s^{-1}$) for olivine are plotted as ln ν versus 1000 / T(K) for: a) 10^5 Pa data from Donaldson (1985) ($Fo_{88.5}$ = filled circles) and Donaldson (1990) ($Fo_{91.5}$ = open circles), b) 10^5 Pa data from Thornber and Huebner (1985) for Fo_{92} (high Al - basalt = filled diamonds, Si-enriched high Al - basalt = open diamonds) shown against fits (dashed lines) to Donaldson (1985, 1990) data, c) high P data (0.5 - 3.0 GPa) from Brearley and Scarfe (1986) and Zhang et al. (1989) compared to fits on 10^5 Pa experiments (dashed lines).

symbols). The data are Arrhenian for both sets of polythermal experiments. Olivine crystals studied by Thornber and Huebner (1985) dissolved at slower rates than those of Donaldson (1985; 1990), and the values of ν are higher in the silica-enriched melt. Calculated values of E_A for the Thornber and Huebner (1985) data are ~300 kJ o.e.m.$^{-1}$ higher than those for the Donaldson data (Table 3.8.).

Figure 3.3c shows data of the Zhang et al. (1989) and Brearley and Scarfe (1986) datasets for values of **P** ranging from 0.5 to 3.0 GPa. The values of ln ν fall in a narrow band between the two sets of 10^5 Pa data from Donaldson (1985; 1990) and Thornber and Huebner (1985). The 0.5, 1.2, and 3.0 GPa experiments define trends with slopes subparallel to the 10^5 Pa experiments with calculated values of E_A intermediate between the bounding sets of 10^5 Pa experiments (Table 3.8.).

Comparison between all reported mineral dissolution data

The datasets available for other minerals are fewer in number than the dataset for olivine. Figure 3.4a illustrates the Arrhenian behavior of quartz and plagioclase dissolution in basaltic melts at superliquidus temperatures and **P** = 10^5 Pa (Donaldson, 1985). The Arrhenian behavior of ln ν is disrupted for quartz and one of the plagioclase compositions (An_{29}) below the liquidus **T** of the melt. For quartz, the break corresponds with crystallization of pigeonite

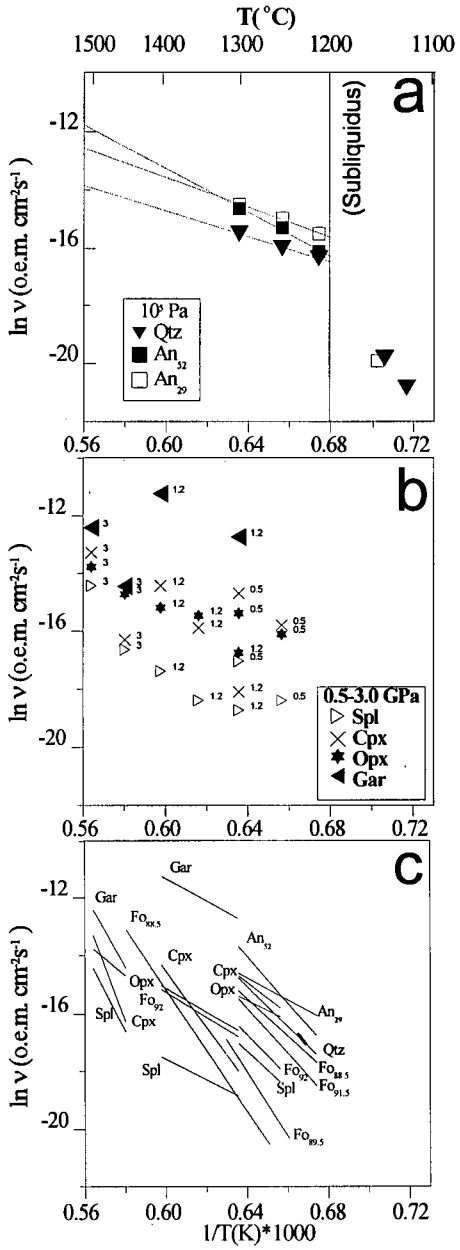

Figure 3.4. Diagram summarizing ln ν (measured) versus 1000 / **T**(K) relationships for: a) 10^5 Pa data from Donaldson (1985) for quartz and plagioclase ($An_{29.5}$ and $An_{52.5}$), b) higher P (0.5 - 3.0 GPa) data from Brearley and Scarfe (1986) for spinel, clinopyroxene, orthopyroxene, and garnet (numbers by symbols denote values of P in GPa), and c) all data in this database. The fits shown in 3.4a are based on superliquidus data only. Mineral abbreviations are from Kretz (1983).

around quartz during the experiment (Donaldson, 1985). Quartz has a smaller value of ν than either composition of plagioclase and has a lower calculated E_A than found for all other minerals in this study (Table 3.8).

Figure 3.4b illustrates the absolute differences in values of ν for spinel, clinopyroxene, orthopyroxene, and garnet dissolving in a basaltic melt (Brearley & Scarfe, 1986). The values of ln ν are Arrhenian and are given in Table 3.8. For all four minerals the calculated values of E_A increase between 0.5 to 3.0 GPa. Relative dissolution rates (ν) over the range of **P** (0.5 - 3.0 GPa) increase from spinel, to orthopyroxene ≅ clinopyroxene, to garnet.

The ln ν versus 1000/**T** relationships for the entire group of minerals included in this compilation are presented in Figure 3.4c. Over the range of values of **T** investigated, plagioclase and garnet have the highest values of ν while spinel and olivine have the lowest. The values of E_A are lowest for quartz, plagioclase, and garnet and highest for clinopyroxene and spinel (Table 3.8).

Discussion

Physicochemical Controls on Mineral Dissolution

Isothermal datasets commonly yield constant dissolution rates with respect to time (e.g., $d\nu/dt$ = constant) (Thornber & Huebner, 1985; Donaldson, 1985; Brearley & Scarfe, 1986). This implies that the mechanisms controlling

the process are also time-independent. Some workers have suggested that an interfacial mechanism is important in determining the rates of mineral dissolution (Wood & Walther 1983; Thornber & Huebner 1985). Other workers suggest that transport of material in the liquid (e.g. diffusion) is rate limiting (Cooper & Kingery 1964; Kuo & Kirkpatrick 1985; Zhang et al. 1989). The data analyzed in this work do not support diffusion nor any other time-dependent mechanism as the rate-limiting step for mineral dissolution in basaltic melts.

The values of ν systematically increase as a function of **T** for all of the minerals studied (Figures 3.3 and 3.4). The inferred Arrhenius relationship between ν and 1/**T**(K) suggests the possibility of predicting values of ν as a function of **T**.

Accurate and predictable dissolution rates are critical to understanding of the process of magmatic assimilation. For example, Figure 3.5 shows the length of time required to completely dissolve a one centimeter diameter sphere of quartz, olivine, or plagioclase in a basaltic melt of constant composition at at temperatures between 900 °C to 1450 °C. Intervals of one minute, one hour, and one day are marked for reference by heavy lines. Below 1300 °C olivine ($Fo_{88.5}$) takes the longest time to dissolve. At 1200 °C, plagioclase (An_{29}) would be completely dissolved in less than one day and quartz would last about three days, whereas olivine ($Fo_{88.5}$) would take over one

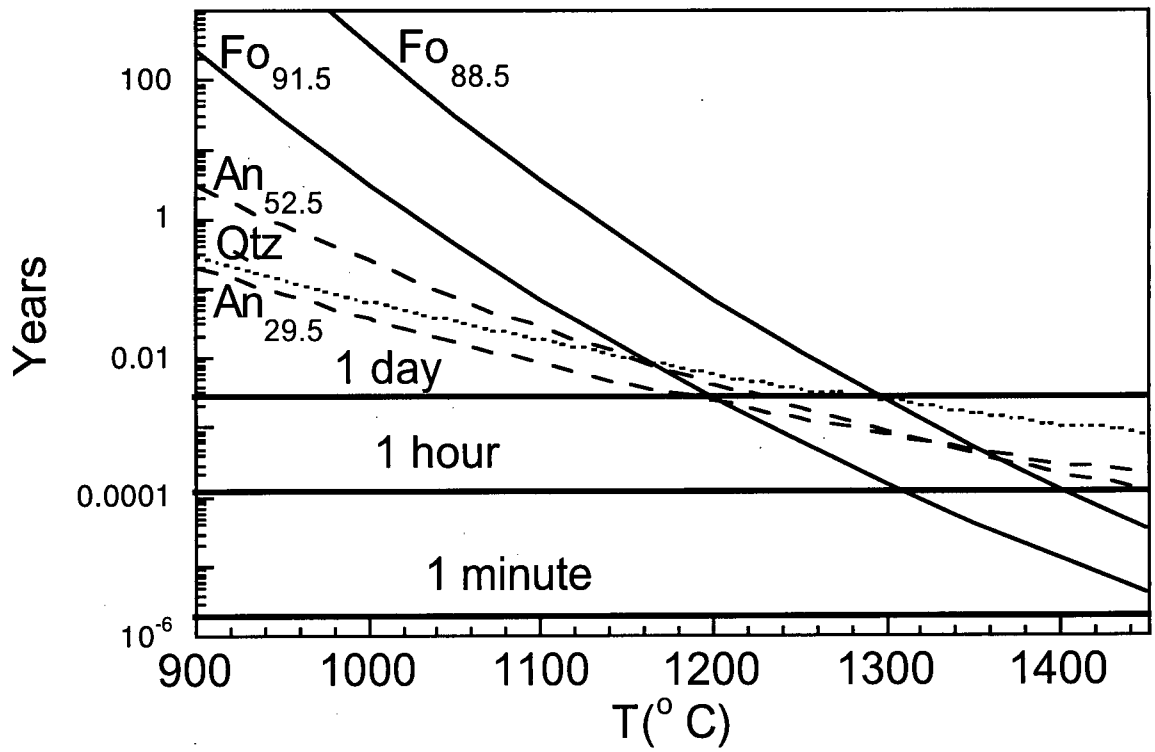

Figure 3.5. Time (years) versus T (° C) for complete dissolution of 1 cm diameter spheres of olivine ($Fo_{88.5}$ and $Fo_{91.5}$), plagioclase ($An_{52.5}$ and $An_{29.5}$), and quartz in a basaltic melt of constant composition at P = 10^5 Pa.

month to totally dissolve. However, above 1300 °C quartz and plagioclase dissolve more slowly than either olivine composition.

For a xenolith comprising any combination of these minerals, the rate at which the minerals dissolve varies with temperature and is different for each of the minerals. The implications of non-uniform, **T**-dependent dissolution rates on the dynamics of chemical contamination of host melts are very important and may result in a complex, nonlinear chemical evolution of a magmatic system undergoing assimilation (see Chapter 4).

The influence of **P** on the values of ν is not easy to evaluate from this database. For olivine (Fig. 3.3c), the high pressure experiments of Brearley and Scarfe (1986) have values intermediate between the 10^5 Pa experiments of Donaldson (1985) and Thornber and Huebner (1985). However, based on differences for calculated values of E_A for clinopyroxene at 0.5 and 3.0 GPa (443 and 1535 kJ/o.e.m. respectively), increasing pressure appears to be an important factor in controlling ν for some minerals.

Thermodynamic Controls on Mineral Dissolution

Relative rates of mineral dissolution of different mineral species depend on the relative thermodynamic stabilities of the minerals in the host melt (Kutolin & Agafonov 1978; Scarfe et al. 1980; Kuo & Kirkpatrick 1985; Thornber & Huebner 1985; Brearley & Scarfe 1986). The thermodynamic potential that

best represents the degree of disequilibrium between a crystal and a melt or the stability of that phase at a specific **P** and **T** is the affinity (**A**) (Prigogine, 1967; Lasaga, 1981a; Aagaard & Helegeson, 1982; Ghiorso,1987; Zhang et al. 1989). Values of **A** for a reaction are defined at constant **T** and **P** to be equal to the chemical potential of the reactant(s) minus the chemical potential of the product (s) (Prigogine, 1967). At equilibrium **A** is zero. Earlier workers were unable to quantify the "relative" stabilities of the different minerals (Brearley & Scarfe, 1986) because they lacked a comprehensive thermodynamic database for mineral-melt equilibria. The new thermodynamic melt parameterization of Ghiorso and Sack (1995) provides a method for obtaining quantitative estimates of the thermodynamic properties of silicate melts and thereby allows us to calculate values of **A** for reactions between minerals and silicate melts.

Following the lead of workers investigating mineral dissolution in aqueous systems (e.g., Wood & Walther 1984, Nagy et al. 1991, Sverjensky 1992), the dissolution rates presented above are related to the thermodynamic driving force for the dissolution reactions (Figure 3.6). Based on the Arrhenian relationship established for values of ν for the mineral dissolution experiments from Donaldson (1985) (Figure 3.6a), values of **A** for these mineral dissolution reactions are derived from the melt composition, **T**, and **P** of the experiments using the MELTS software package (Ghiorso & Sack 1995). Figure 3.6b demonstrates the relationship between calculated **A** (multiplied by o.e.m.) and

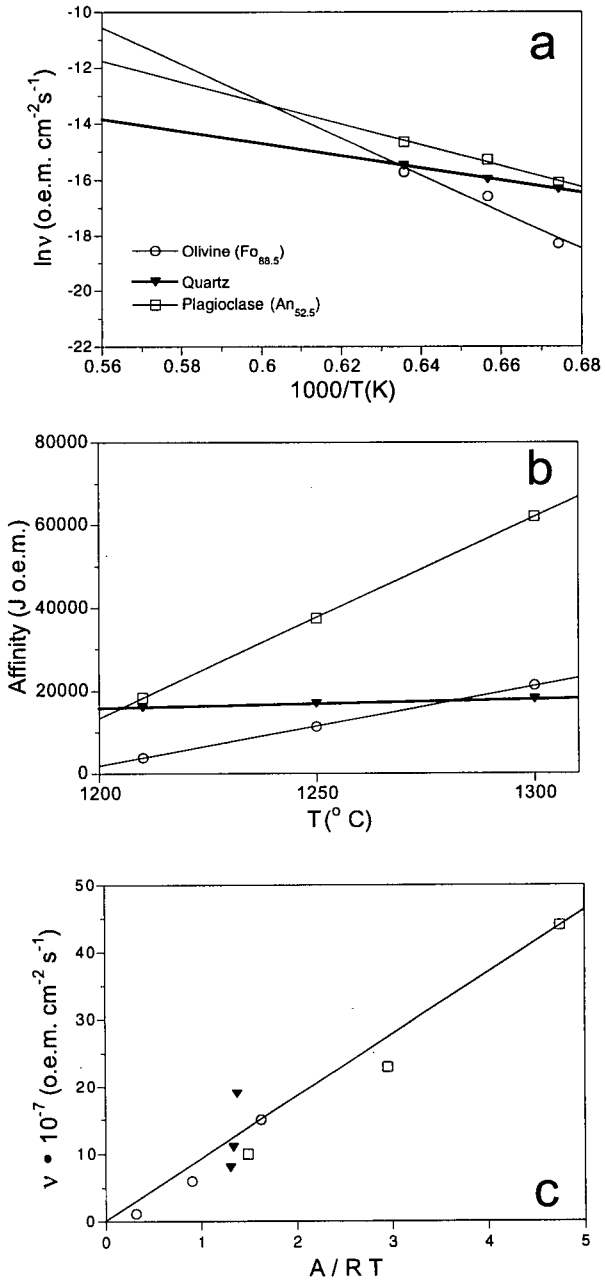

Figure 3.6. Relationships leading to predictive models for mineral dissolution in silicate melts illustrated with the 10^5 Pa experiments of Donaldson (1985): a) ln ν versus 1000 / **T**(K) for olivine, quartz, and plagioclase, b) calculated **A** versus **T** (° C) for olivine, quartz, and plagioclase at superliquidus conditions, c) ν • 10^{-7} versus calculated **A** / R**T**. Values of **A** are calculated using the MELTS software of Ghiorso (1994) and multiplied by o.e.m.

T(°C). The methodology for calculating the values of **A** is explained in Appendix A3.2. The experimentally-derived values of ν show a linear relationship to calculated **A** / **RT**(K) (Figure 3.6c). For values of **A** / **RT** <1, irreversible thermodynamics predicts this linear relationship (Aarsgaard & Helgeson, 1981; Lasaga, 1981a; 1981b). However, as discussed by Prigogine (1967, p. 60), even when values of **A** for the net reaction (as opposed to the elementary reactions) are much greater than unity, the linear phenomenological relationship between **A** / **RT** and ν may still hold as is the case for the limited data for mineral-melt pairs in Figure 3.6c.

3.4. SUMMARY AND CONCLUSIONS

Clearly, the study of mineral dissolution kinetics in silicate melts is still in its infancy. One observation from this study is that overall there is a paucity of data on the rates of dissolution for silicate minerals in natural silicate melt compositions. The published datasets are of variable quality, due mainly to incomplete descriptions of experimental conditions. In particular, information on sample geometries, measured sample dimensions and repeated isothermal experiments of different time-scales are critical. Notwithstanding the paucity of data, I can draw some important preliminary conclusions from this analysis. Mineral dissolution rates are Arrhenian for superliquidus conditions and for some minerals may be dependent on **P** as well. Preliminary

calculations suggest that experimentally-derived values of ν may have a systematic relationship to calculated values of **A**.

Equilibrium thermodynamics demonstrate that the energy balances attendant magmatic assimilation are important in determining the magmatic pathway taken by a given magma and assimilant and depend on the mineralogy of the assimilant. An understanding of the thermodynamic and kinetic controls on magmatic assimilation provides an opportunity to build calculational models for magmatic assimilation. Several purely thermodynamically-driven models have been produced by other workers (e.g., Nielsen 1988 and Ghiorso & Sack 1995). In Chapter Four, the capabilities of existing models are tested and discussed as a foundation for a new model that utilizes the kinetic control for mineral dissolution derived in this Chapter.

CHAPTER 4

Equilibrium Modeling of Magmatic Assimilation

4.1. INTRODUCTION

The previous chapter develops a predictive model for mineral dissolution rates, which is a required component in the kinetically-controlled thermodynamic model for magmatic assimilation presented in Chapter 5. This chapter explores the equilibrium thermodynamic consequences of assimilation-fractional crystallization (AFC) processes as a prelude to the dynamic model.

In this chapter, a pre-existing equilibrium thermodynamic model (MELTS, Ghiorso & Sack 1995) is used to test the effects of assimilation on mineral zoning in plagioclase and pyroxene growing in an alkali olivine basaltic magma. Five scenarios of magmatic assimilation are presented in terms of the expected mineral zoning patterns. The scenarios include: fractional crystallization (FC), fractional crystallization with concomitant assimilation (AFC) of bulk granite consisting of quartz (30 % by volume), plagioclase (30 %), K-feldspar (30 %), and biotite (10 %), and fractional crystallization coupled with assimilation of each mineral phase within the granite. For each scenario, the

physicochemical effects of assimilation of specific minerals on liquidus and solidus temperature, sequence of crystallization, mineral composition, and patterns of zoning in the constituent minerals of the host lava are summarized.

The modeling suggests that mineral zoning profiles are not only sensitive indicators of open-system behaviour but that the profiles can be used to identify different types of assimilation. An important conclusion is that the incorporation of both kinetic and thermodynamic constraints for chemical interaction between mineral growth and dissolution will provide distinctly new and more accurate constraints on the origins of mineral zoning patterns associated with open chemical systems and found in natural examples such as *Little Bear Mountain.*

4.2. MODEL PATHS OF ASSIMILATION

Overview

Assimilation can drastically change the nature and evolution of the host magma. It can change liquidus and solidus temperatures (Bowen 1922; Reiners et al. 1995), modify sequences of crystallization (Bowen 1922; Wilcox 1944; Nicholls & Stout 1982; Ghiorso & Kelemen 1987; Reiners et al. 1995; Russell et al. 1995), or cause significant changes in host magma compositions, especially trace element and isotopic compositions (Taylor 1980; DePaolo 1981; Myers et al. 1986; McBirney et al. 1987; Nielsen 1990;

Grunder 1992; McCulloch et al. 1994; Luhr et al. 1995; Reiners et al. 1995). Consequently, assimilation processes can result in substantially different liquid lines of descent and rock-types than fractional crystallization alone (e.g., Kelemen & Ghiorso 1986; Nielsen 1988).

Bulk assimilation and selective assimilation are recognized as two endmember processes in natural magmatic systems (e.g., Doe et al. 1969; Watson 1982; Blichert-Toft et al. 1992; Gerlach & Grove 1982; Philpotts & Asher 1993; Geist & White 1994; Reiners et al. 1995; Russell et al. 1995). Bulk assimilation occurs where the material being assimilated by a given melt is added in proportions equal to the bulk xenolith composition. Selective assimilation occurs where the composition of the assimilant added to the host melt is not equal to that of the bulk xenolith.

Thermodynamic, mass balance, and kinetic parameters need to be modeled together to accurately predict the consequences of magmatic assimilation. However, many of the consequences of bulk and selective assimilation can be demonstrated using existing models which combine only thermodynamic and mass balance constraints (e.g., Nielsen 1988; Ghiorso & Sack 1995). Modeling closed- and open-system (e.g., assimilation) behaviour in magmas has been substantially improved by the recent revision of a thermodynamic database for silicate melts and the release of a computer

program (MELTS) that simultaneously accounts for igneous phase equilibria and heat and mass-balance constraints (Ghiorso & Sack 1995).

The consequences of bulk versus selective assimilation on the model path of fractional crystallization of an alkali olivine basalt magma were examined using MELTS (Ghiorso & Sack 1995) (Table 4.1). The starting magma composition is that of a basalt from Lava Fork, a Quaternary volcanic centre in northwestern British Columbia (Hauksdóttir et al. 1994; Hauksdóttir 1994). This sample was chosen because: a) alkali olivine basalt is an important component of Quaternary magmatism in the Northern Cordilleran Volcanic Province (Chapters 1 & 2), b) it is chemically and petrographically well characterized, and c) Hauksdóttir (1994) documented the importance of assimilation of granite in explaining the chemical variations within and between Quaternary lavas from this region.

The model fractionation paths are coupled to bulk assimilation of a typical granite (30 % quartz, 30 % plagioclase, 30 % K-feldspar, 10 % biotite) or to assimilation of the individual minerals within the granite. The latter models represent potential endmembers of selective assimilation. Based on kinetic considerations for mineral dissolution in melts discussed below, these endmember models may be commonly approached in nature. Pressure was fixed at 10^5 Pa and fO_2 at the fayalite - magnetite - quartz buffer (FMQ) for all simulations. Assimilation scenarios used a total of 20 g of assimilant as input

Table 4.1. Chemical and modal composition of alkali olivine basalt SH-44[1] from Lava Fork, northwestern British Columbia.

Oxides	Wt. %	Minerals	Vol. %
SiO_2	46.46	Phenocrysts [Pl, Ol]	20
TiO_2	2.84		
Al_2O_3	16.92	Groundmass [Plagioclase, Olivine, Augite, Opaque phases]	55
Fe_2O_3	2.59		
FeO	10.10		
MnO	0.18		
MgO	6.52	Vesicles	25
CaO	8.87		
Na_2O	3.71		
K_2O	1.09		
P_2O_5	0.45		
H_2O	0.10		
Total	99.83		

[1]Hauksdóttir (1994), Table 4.1, p. 65

into an initial mass of 100 g of magma; the assimilant was added in intervals of 1 g per temperature step for the first 20 temperature steps. Each of the AFC simulations uses 20 g of either the bulk granite or one of the phases in the bulk granite (Qtz, An_{10}, Ksp, Phl_{30}). The cooling interval for each of the scenarios was 200 °C, from 1185 °C to 985 °C, using 5 °C temperature steps.

The model scenarios simulate a magmatic system open to mass transfer. Mass is added to the system via assimilation and removed via fractional crystallization. Heat is indirectly removed from the system in two ways as the assimilated solid is added. Firstly, the system is arbitrarily cooled in 5 °C temperature steps. This forces the magma to evolve heat via crystallization and cooling. The heat evolved is available to fuse the material being assimilated by the magma.

Details of the thermal energy required for assimilation have been outlined by previous workers (Chapter 3; Nicholls & Stout 1982; Ghiorso & Kelemen 1987; Russell et al. 1995). In summary, the overall thermal energy requirement for assimilation is dominated by the energy required to heat the solid material to the ambient magma temperature and the energy to fuse the solid at that temperature. Other workers have quantitatively explored the magnitude of the heating component relative to the overall thermal budget for assimilation and found it to have a potentially significant effect on the amount of crystallization and cooling necessary for assimilation (Ghiorso & Kelemen

1987; Reiners et al. 1995; Russell et al. 1995). The works listed above all demonstrate the potential effects for assimilation of xenoliths of the exact same compositions with different initial temperatures. For all of the model scenarios used in this paper, the initial solid temperature before assimilation was 500 °C.

Results of each simulation, including phase-saturation temperatures, saturation compositions, compositional ranges and total masses crystallized are summarized in Table 4.2. Figure 4.1 (a to f) shows the calculated sequences of crystallization and cumulative phase proportions from each of the five assimilation scenarios. Data for the FC alone scenario (Figure 4.1a) are shown in order to provide a contrast between the path of crystallization for the uncontaminated magma and the paths resulting from assimilation.

Results

The model FC path for the alkali olivine basalt SH-44 (Figure 4.1a) has plagioclase as the liquidus phase (1175 °C) followed closely by olivine (1170 °C), spinel (1125 °C) and clinopyroxene (1120 °C). Plagioclase precipitates over the entire interval of crystallization, with a continuous variation in composition from An_{71} to An_4. The sequence of crystallization produced by MELTS parallels that established petrographically for SH-44 (Hauksdóttir 1994; Table 4.1).

Table 4.2. Summary of sequence of crystallization for each of the model scenarios.

Model Scenario[1]	Phase[2]	Saturation T (°C)[3]	Saturation Composition[4]	Composition Range	Total mass crystallized in g[5]
1	Pl	1175 (1035)	An_{71}	An_{71-3}	53.2 (59.9)
	Ol	1170 (1035)	Fo_{79}	Fo_{79-62}	9.2 (10.4)
	Spl	1125	Spl_{47}	Spl_{47-17}	13.5 (15.2)
	Cpx	1120	Di_{44}	Di_{43-49}	12.9 (14.5)
2	Pl	1170 (1045)	An_{70}	An_{70-26}	46.7 (38.9)
	Ol	1170 (1050)	Fo_{79}	Fo_{79-65}	10.2 (8.5)
	Spl	1125	Spl_{45}	Spl_{45-19}	14.0 (11.7)
	Cpx	1115	Di_{44}	Di_{43-52}	12.1 (10.0)
	Kfs	1045	$Ab_{48}An_9Or_{43}$	$Ab_{48}An_9Or_{43}$-$Ab_{47}An_3Or_{49}$	18.3 (15.3)
3	Pl	1170	An_{68}	An_{68-34}	45.1 (37.6)
	Ol	1170 (1120)	Fo_{79}	Fo_{79-70}	7.0 (5.9)
	Opx	1115 (1065)	En_{84}	En_{84-75}	11.9 (9.9)
	Spl	1110 (995)	Spl_{33}	Spl_{33-14}	9.0 (7.5)
	Pig	1060	Di_{25}	Di_{25-28}	5.7 (4.7)
	Rhom	990	Ilm_{83}	Ilm_{83}	0.2 (0.2)
4	Pl	1175 (1015)	An_{71}	An_{71-5}	68.2 (56.9)
	Ol	1170 (1120)	Fo_{80}	Fo_{80-60}	10.7 (8.9)
	Spl	1130	Spl_{50}	Spl_{50-17}	12.9 (10.8)
	Cpx	1110	Di_{44}	Di_{44-40}	8.1 (6.7)
5	Pl	1170 (1065)	An_{71}	An_{71-35}	36.7 (30.6)
	Ol	1170 (1065)	Fo_{79}	Fo_{79-67}	9.5 (7.9)
	Spl	1125 (1030)	Spl_{41}	Spl_{41-30}	13.0 (10.8)
	Cpx	1115	Di_{44}	Di_{43-49}	14.69 (12.2)
	Rhom	1025	Ilm_{73}	Ilm_{73-78}	0.4 (0.3)
	Kfs	1060	$Ab_{39}An_8Or_{52}$	$Ab_{39}An_8Or_{52}$-$Ab_{37}An_2Or_{61}$	36.3 (30.3)
6	Ol	1170 (1055)	Fo_{79}	Fo_{79-62}	13.2 (11.0)
	Pl	1160 (1055)	An_{71}	An_{71-32}	38.4 (32.0)
	Spl	1120	Spl_{38}	Spl_{38-14}	19.4 (16.2)
	Cpx	1115	Di_{44}	Di_{43-50}	14.5 (12.1)
	Kfs	1050	$Ab_{42}An_8Or_{50}$	$Ab_{42}An_8Or_{50}$-$Ab_{46}An_4Or_{50}$	22.1 (18.4)

[1] Scenarios are defined as follows: 1: fractional crystallization of basaltic magma; 2: fractional crystallization coupled with assimilation of granite, 3: with Qtz, 4: with An_{10}, 5: with Ksp, and 6: with Phl_{30}
[2] All phases are solid solutions (e.g., Spl represents solid solution between chromite, hercynite, magnetite, spinel and ulvöspinel; Rhom represents solid solution between rhombohedral oxides including ilmenite, hematite, geikielite and pyrophanite)
[3] (- -) indicates temperature at which crystallization of phase stops
[4] Reported as mole fraction of selected endmember composition
[5] (- -) indicates percent of total system mass

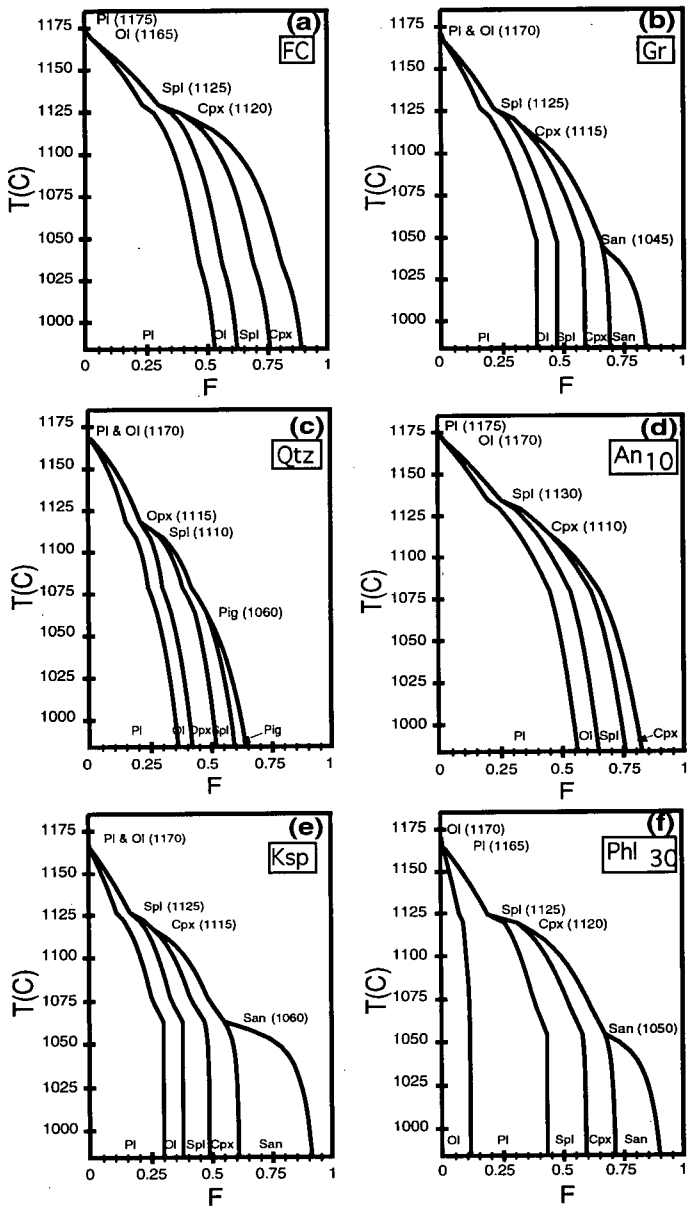

Figure 4.1. Six model simulations are represented as F (fraction of system crystallized) versus magmatic T (°C) for: a) fractional crystallization (FC) of basaltic magma; and FC combined with assimilation (AFC) of b) granite, c) Qtz, d) Pl (An_{10}), e) Ksp, and f) Bt (Phl_{30}). Saturation temperatures are shown for individual phases in parentheses. Mineral abbreviations are from Kretz (1983).

The second scenario (Figure 4.1b) models fractional crystallization and bulk assimilation of granite (AFC) consisting of 30% quartz, 30% plagioclase (An_{10}), 30% potassium feldspar, and 30% biotite [Phl_{30}: $K_2Fe_{4.2}Mg_{1.8}Al_2Si_6O_{20}(OH)_4$]. The changes in sequence of crystallization and the predicted ranges in mineral compositions are surprisingly small even though the total mass added to the system represents 20% by weight of the original magmatic system (Table 4.2). However, an important difference between this simulation and scenario 1 (FC only) is the abrupt appearance of sanidine as the equilibrium feldspar ($Ab_{48}An_9Or_{43}$) at 1045 °C (Figure 4.1b). Other differences arising from bulk assimilation of granite include coprecipitation of plagioclase and olivine as liquidus phases, 10 - 15 °C changes in their crystallization intervals (Table 4.2), and small differences in the composition of the crystallizing minerals [less than ~3 mole % for olivine (Fo), spinel (Spl) and pyroxene (Di)]. Overall, with the exception of the appearance of sanidine, the two scenarios produce similar results.

The last four simulations contrast the effects of selective assimilation of granite and its bulk assimilation (Figs. 4.1c to 4.1f; Table 4.2, scenarios 3-6). Paths of selective assimilation are markedly different from both the FC and bulk assimilation paths in terms of crystallization sequence, the phases crystallized and the range of mineral compositions. The only two characteristics common to all six simulations are the saturation compositions and temperatures for

olivine and plagioclase (Table 4.2), as the initial composition of the magma is affected only slightly by assimilation in the first 15 °C.

Fractional crystallization with assimilation of Qtz produces a crystallization path that is markedly different from either of the first two scenarios (Figure 4.1c; Table 4.2). Plagioclase crystallizes throughout the simulation yet has a relatively narrow range of compositions (An_{68} to An_{34}). Olivine has a shorter crystallization interval (55 °C) and is replaced by orthopyroxene at 1150 °C, which is in turn replaced by pigeonite at 1060 °C. Another minor change in the crystallization sequence is the late appearance of rhombohedral oxide (Ilm_{83}) replacing spinel in the crystallizing assemblage at 990 °C.

The fourth scenario involves FC with assimilation of An_{10}. The crystallization path is again distinct from the previous scenarios (Figure 4.1d; Table 4.2). The most distinctive feature of the path pertains to plagioclase; it is the first phase to precipitate at 1175 °C and its total mass crystallized is almost 50% more than in any of the other assimilation scenarios and 30% more than in the FC scenario. Similar to scenario 1, the composition of the plagioclase changes continuously from An_{71} to An_5, which is a broader range than for the Qtz assimilation scenario, yet without the abrupt appearance of sanidine as with bulk assimilation of granite.

The last two simulations both involve fractional crystallization with assimilation of a K-rich phase, either Ksp (Figure 4.1e; Table 4.2, scenario 5) or Phl_{30} (Figure 4.1f; Table 4.2, scenario 6). The important characteristics of both of these last two scenarios are the abbreviated intervals of crystallization for An-rich plagioclase, the abrupt compositional change from plagioclase to sanidine at 1060 °C for scenario 5 and at 1050 °C for scenario 6 ($Ab_{52}An_{35}Or_{13}$ to $Ab_{39}An_8Or_{52}$ and $Ab_{54}An_{32}Or_{14}$ to $Ab_{42}An_8Or_{50}$, respectively) and the large total mass of sanidine crystallized (Table 4.2). Scenario 5 produces a small amount of rhombohedral oxide, and in scenario 6, olivine replaces plagioclase as the liquidus phase at 1170 °C.

4.3. ASSIMILATION AND MINERAL ZONING

Compositional zoning in magmatic minerals can retain a record of the physicochemical conditions extant during crystallization (Pringle et al. 1974; Kuo & Kirkpatrick 1982; Anderson 1984; Pearce 1984, 1994; Nekvasil 1994). Patterns of growth of magmatic minerals can be used effectively to: a) record changes in the magmatic environment (Wiebe 1968; Pringle et al. 1974; Uebel 1978; Kuo & Kirkpatrick 1982; Pearce et al. 1987a, b); b) constrain crystallization histories and mechanisms (Sibley et al. 1976; Nixon & Pearce 1987; Russell et al. 1987); and / or c) constrain the dynamics of open systems (Nixon & Pearce 1987; Jamveit 1991). Most importantly, in the context of this

study, both compositional zoning and growth features in magmatic minerals have been used to identify the effects of open-system magmatic processes (e.g., Gerlach & Grove 1982; Pearce 1984; Nixon & Pearce 1987; Kowamoto 1992; Stimac & Pearce 1992; Hauksdóttir 1994).

As pointed out by Bowen (1928) and more recent investigators (Kelemen & Ghiorso 1986; Ghiorso & Kelemen 1987; Nielsen 1988; Reiners et al. 1995), one of the important consequences of assimilation is to change the crystallization temperature interval for individual phases as well as for the magma as a whole. Three of the AFC scenarios (granite, Qtz, An_{10}) effectively extend the crystallization interval for SH-44 beyond what it is predicted for the pure FC path. In constrast, AFC of either of the K-rich minerals (Ksp and Phl_{30}) results in a magmatic crystallization interval of intermediate temperature duration (Figure 4.1; Table 4.2).

The AFC paths simulated above also produce significant differences in the range of mineral compositions produced during crystallization (e.g., Figure 4.2). Variations in mineral compositions for plagioclase (Figure 4.3) and pyroxene (Figure 4.4) have been summarized as a function of T and crudely represent expected compositional profiles for crystals growing continuously in the melt without intercrystalline diffusional re-equilibration.

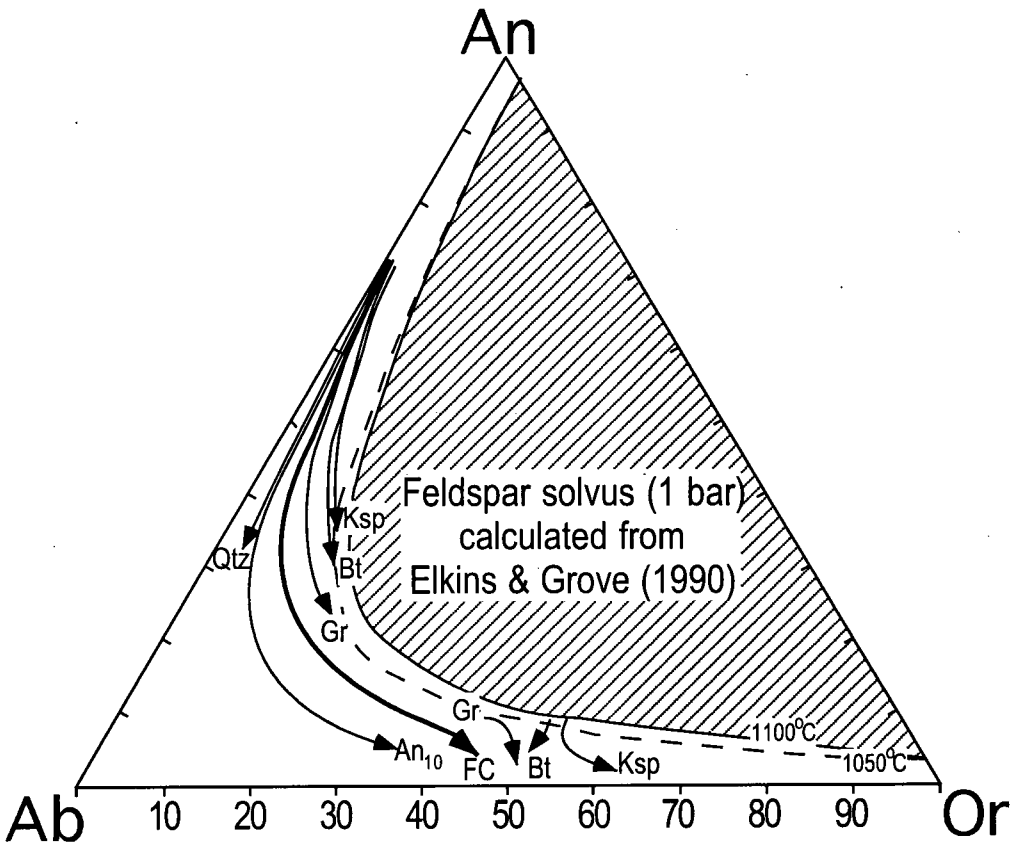

Figure 4.2. Ternary feldspar diagram showing distribution of model feldspar compositions derived from six model simulations (lines with arrows), including FC, and AFC of granite (Gr), Qtz, An_{10}, Ksp, and Phl_{30}. Projected feldspar solvus is for 10^5 Pa and 1100 ° C (solid) and 1050 ° C (dashed). Solvus is calculated using the solution model of Elkins and Grove (1990).

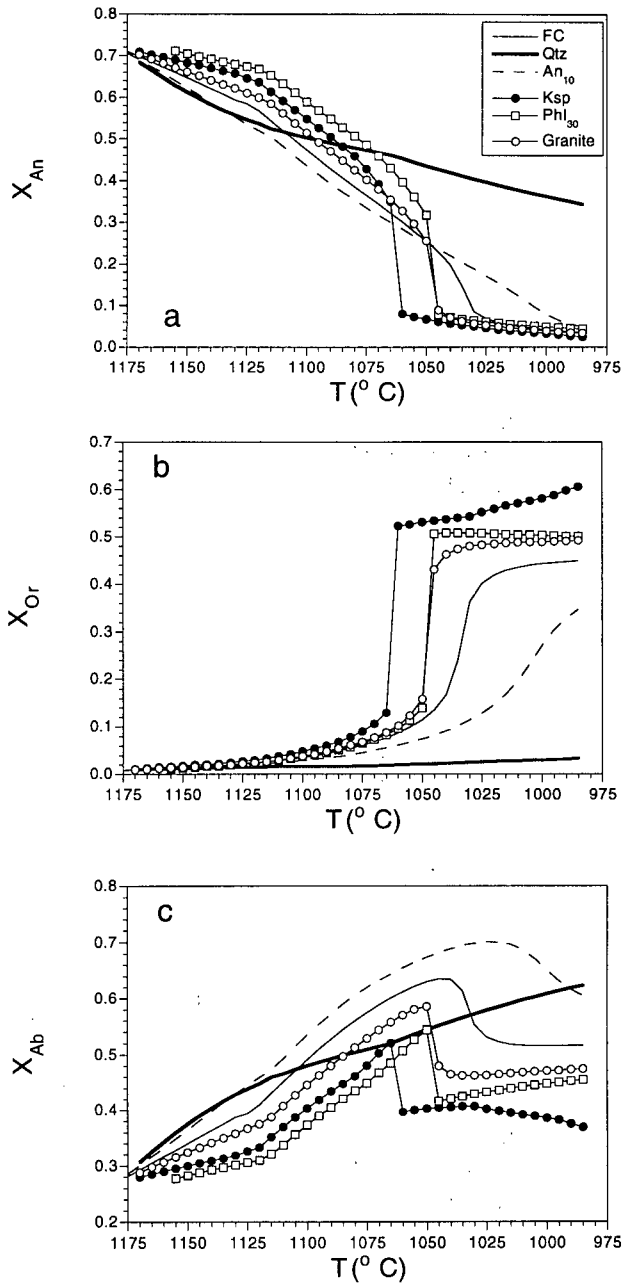

Figure 4.3. Model feldspar compositions are plotted against T (° C) as: a) X_{An}, b) X_{Or}, and c) X_{Ab}. Labels for the six simulations are as in Figure 4.2. Abrupt discontinuities in Ksp and Phl simulations correspond to the onset of San crystallization.

Feldspar

Plagioclase is an important product of crystallization in this basaltic system at P = 10^5 Pa because it is the liquidus phase in 5 of the 6 scenarios and crystallizes over more than 50% of the crystallization interval for every scenario. Consequently, its composition records part of the chemical path taken by the magma during crystallization and assimilation. The feldspar compositions for each of the scenarios are shown in Figure 4.2. The six scenarios produce three different patterns of zoning. The first, demonstrated by the Qtz assimilation scenario, has very little curvature, i.e. with decreasing X_{An} and increasing X_{Ab} there is little change in X_{Or}. This path also has a relatively narrow range in X_{An}. The second path, that of both the FC and the An_{10} assimilation scenarios, follows a continuous curve of decreasing X_{An} and increasing X_{Ab} and X_{Or}. The third pattern, generated by the other three scenarios (bulk granite, Ksp, Phl_{30}), is discontinuous.

Predicted patterns of composition for An, Or and Ab in feldspar in each of the scenarios are shown in Figure 4.3. The feldspar zoning profiles produced by the bulk granite, Ksp and Phl_{30} assimilation paths are similar in shape to the FC path except that at 1045 °C, 1060 °C and 1050 °C, respectively, sanidine replaces plagioclase as a crystallizing phase. However, the zoning paths for these three scenarios predict more An-rich, Or-rich, and Ab-poor compositions relative to the FC path. As a consequence, the rims of plagioclase crystals

produced by these three assimilation scenarios would be expected to be much more An-rich than the rim of plagioclase produced by fractional crystallization. Each of the three assimilation scenarios produce paths that could ultimately lead to the formation of sanidine mantles on plagioclase (anti-rapakivi texture) in the rock.

Both the Qtz and the An_{10} assimilation scenarios produce zoning paths that constrast sharply with the FC path (Figure 4.3). For the Qtz AFC path, plagioclase precipitates throughout the entire interval of crystallization, and K-feldspar does not crystallize at all. The Qtz path also produces a more uniform zoning profile in plagioclase from the core to the rim. The An_{10} path also has a strong buffering effect on the zoning profile and is quite similar in shape to the FC profile (Figure 4.2). At the low-T end of the crystallization interval, Ab decreases and Or increases for both the An_{10} and FC scenarios. However, unlike the FC scenario, the An_{10} scenario does not hava a flat compositional profile for all three feldspar components at low temperatures. And unlike the granite, Ksp and Phl_{30} scenarios, the compositional shift to Or-rich feldspar for the An_{10} scenario is gradual and occurs in the last 30 °C in the crystallization interval. Thus, the ternary feldspar solvus is never intersected (Figure 4.2).

The simulated zoning profiles (Figure 4.3) reproduce expected and somewhat unexpected characteristics. Bowen (1922) demonstrated that assimilation of plagioclase with a higher X_{Ab} content than the equilibrium

feldspar composition extends the total interval of crystallization of plagioclase. Similarly, adding quartz to this alkaline basalt destabilizes clinopyroxene, resulting in a more An-rich plagioclase. Also it seems intuitive that adding components rich in K to the system would stabilize sanidine. What is somewhat unexpected is that adding components rich in K early in the crystallization interval produces a plagioclase "core" with a relatively more An-rich composition than for FC alone. However, Kushiro (1975) qualitatively predicted this type of behavior based on experiments that showed the addition of monovalent cations to a silicate melts caused an expansion of the stability fields for higher temperature phases. The "rim" of plagioclase phenocrysts produced in the Ksp and Phl_{30} scenarios would have a lower X_{Or} than for the FC or An_{10} scenarios. Overall, the important point illustrated by these patterns is that they are highly dependent on the nature of contamination, either bulk or selective, and extent of assimilation. Such patterns should be recognizable in natural samples.

Pyroxene

As with feldspar, changes in mineral composition of the pyroxenes are sensitive recorders of the different model paths of assimilation (Figure 4.4). Clinopyroxene crystallization is predicted for the FC scenario and four of the five AFC scenarios; the Qtz scenario predicts only clinoenstatite (1115 °C) and

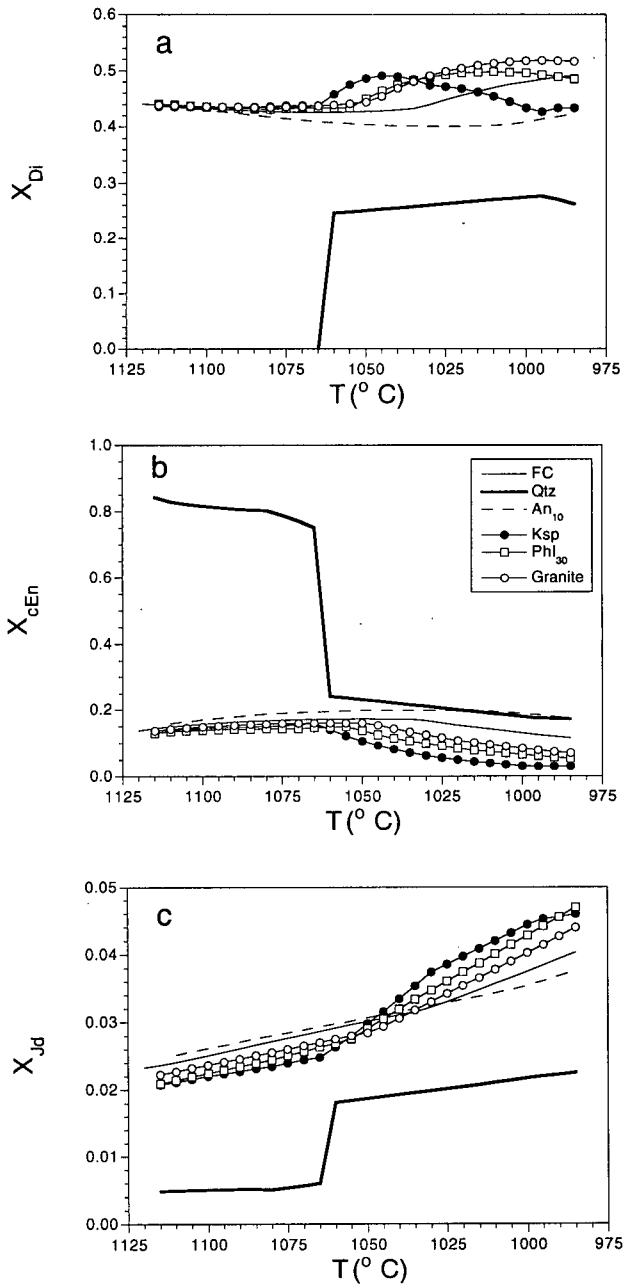

Figure 4.4. Model pyroxene compositions are plotted against T (° C) as: a) X_{cEn}, b) X_{Di}, and c) X_{Jd}. Labels are as in Figures 4.2 and 4.3. Abrupt discontinuity in Qtz simulation corresponds to the onset of pigeonite crystallization.

pigeonite (1060 °C) crystallization. In all cases, except for the Qtz scenario, the X_{Di} component in pyroxene initially decreases slightly. However, for the granite, Ksp and Phl_{30} scenarios, the X_{Di} component begins to increase steeply at the point where sanidine begins to crystallize. For the Ksp assimilation path, at 1060 °C the X_{Di} component shows a distinctive, sharp increase followed by a more gradual decrease to values less than the FC, granite or Phl_{30} scenarios. The An_{10} path maintains a relatively constant value of X_{Di}.

The clinoenstatite component (X_{cEn}) has a pattern distinctly different from that of the X_{Di} component. It first increases with clinopyroxene crystallization then decreases, for all scenarios. The change from increasing to decreasing X_{cEn} occurs again at the onset of sanidine crystallization for the Ksp, Phl_{30} and granite assimilation scenarios. The FC and An_{10} paths show much less variation in X_{cEn}.

The jadeite component (X_{Jd}) increases with decreasing temperature for all six of the scenarios. The only major variation occurs for the Ksp, Phl_{30} and granite assimilation scenarios, where the onset of sanidine crystallization produces overall variations of more than 50 % (0.02 X_{Jd}).

As with plagioclase, the assimilation paths initially produce pyroxenes with similar compositions to the case of fractional crystallization alone, with the exception of the Qtz assimilation scenario. However, as crystallization-assimilation proceeds, the compositional paths of the pyroxenes become

more distinct. The addition of K appears to have the most distinctive effect on implied profiles of pyroxene crystals as reflected in large variations in both X_{Di} and X_{Jd} components between the different paths.

4.4. DISCUSSION OF MELTS MODELING

As demonstrated above (Figures 4.1-4.4), each AFC simulation suggests a distinct chemical-mineralogical path. Mineral zoning patterns for plagioclase and pyroxene and the proportions of phases crystallized are particularly sensitive recorders of these different paths. For example, in the Qtz assimilation scenario both the plagioclase compositions (Figure 4.3) and the proportions of phases crystallized (Table 4.2) are very different from those generated by the FC scenario. On the basis of these observations, patterns of mineral growth and zoning seem a promising way to recognize open-system behaviour and, possibly, to identify the type of assimilation (e.g., bulk versus selective) responsible for the patterns.

Recently two different investigations have attributed distinct chemical zoning patterns in magmatic minerals in mafic dykes to assimilation (Kitchen 1989; Philpotts & Asher 1993). Kitchen (1989) found that in clinopyroxene-bearing dolerite dykes assimilation of granitic wallrock produced both pigeonite and orthopyroxene, as well as a diverse group of pyroxene zoning patterns. Kitchen (1989) also attributed enrichments in Na and K in plagioclase to

assimilation. Philpotts and Asher (1993) reported that sections of oscillatory zoning in plagioclase phenocrysts in a contaminated diabase dyke consistently contained an "orthoclase spike" which, along with elevated X_{Or} in the cores of the phenocrysts, they attributed to assimilation. Two other important reaction textures commonly reported in contaminated magmas are pyroxene or amphibole reaction rims on quartz xenocrysts and overgrowths of plagioclase on K-feldspar (e.g., Doe et al. 1969; Sato 1974; cf. Stimac & Wark 1992; many others).

However, it is important to note that mineral zoning affected by assimilation need not be recorded in all phenocrysts of the contaminated magma. One of the trademarks of mineral growth and zoning studies is the amount of variation seen within any one population of minerals (Wiebe 1968; Pringle et al. 1974; Kitchen 1989; Stimac & Wark 1992; Philpotts & Asher 1993; Hausdottir 1994). Many workers (e.g., Pringle et al 1974; Pearce & coworkers) have suggested that growth features and compositional zoning in minerals record both local and global magma conditions. Depending on the physical mechanism and spatial distribution of xenoliths, minerals crystallizing and growing immediately adjacent to the xenoliths are most likely to record the chemical changes caused by assimilation.

Types of Assimilation

An important question for workers trying to recognize assimilation processes in magmatic systems is whether the type of contamination was bulk or selective. Several lines of evidence are consistent with selective assimilation being dominant over bulk assimilation in natural systems; these include measurements of mineral-dissolution rates (Watson 1982; cf. Chapter 3, Edwards and Russell 1996), the presence of isolated xenocrysts in host magmas (Wilcox 1954; Sato 1975; Kitchen 1989; Blichert-Toft et al. 1992; Luhr et al. 1995; among others), and the composition of glass in partly melted xenoliths (LeMaitre 1974; Philpotts & Asher 1993; Hauksdóttir 1994; among others). In particular, experimentally observed rates of dissolution suggest that the mineral phases in xenoliths do not react with the host magma at the same rate (Figure 4.5, inset).

The consequences of misidentifying bulk versus selective assimilation can be severe in modeling the chemical evolution of open magmatic systems. For example, trace element or isotope mass-balance calculations based on the assumption of bulk assimilation may drastically overestimate the amount of actual contamination. One of the most important parameters used for such mass-balance models is the ratio of assimilation to crystallization (DePaolo 1981). Reiners et al. (1995) demonstrated that this ratio is highly dependent on the composition of the material being assimilated and that the isotopic differences resulting from bulk assimilation of pelite versus the assimilation of

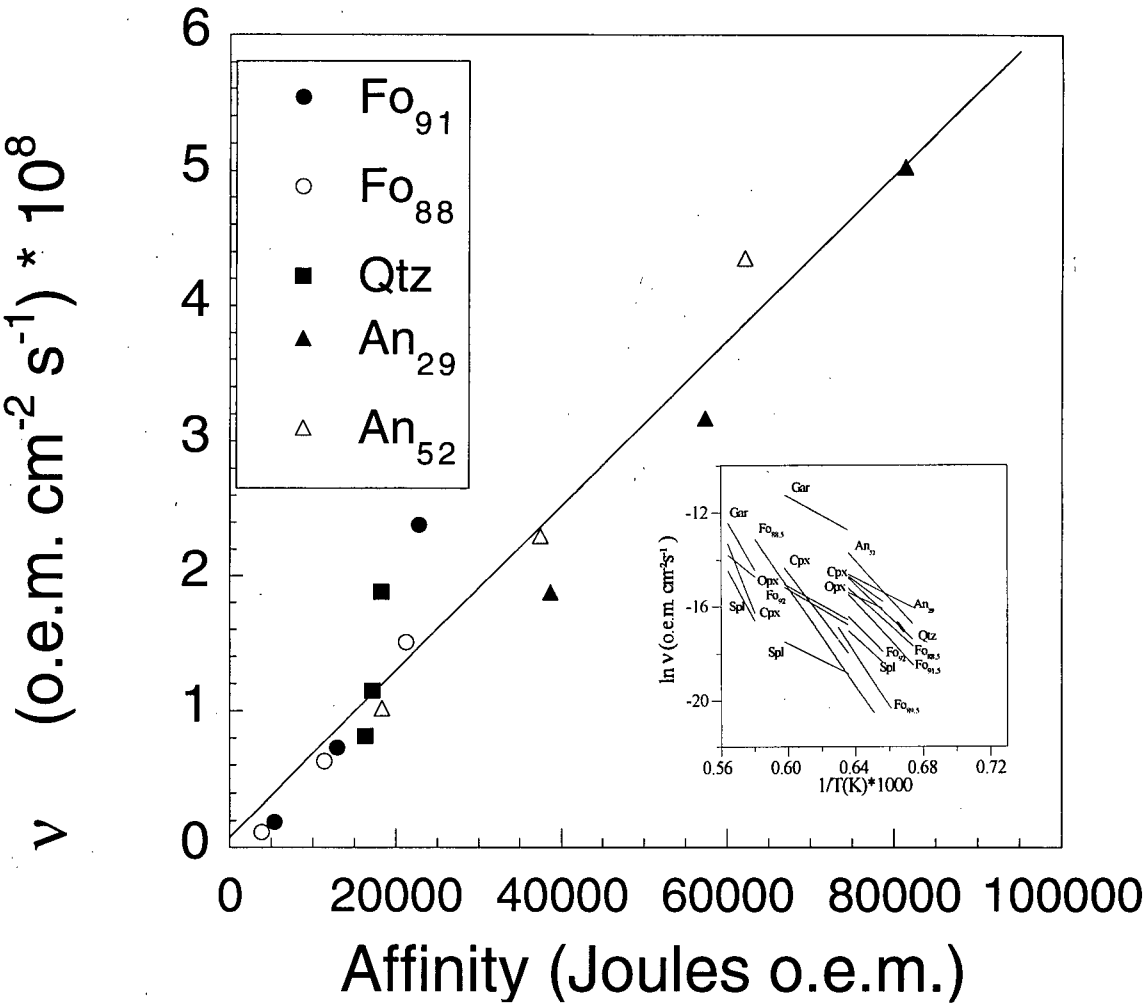

Figure 4.5. Diagram of v (oxygen equivalent moles $cm^{-2}s^{-1}$) versus **A** (J • number of oxygen atoms $mole^{-1}$ of mineral) for Qtz, Pl, and Ol derived from 10^{-4} GPa, mineral dissolution experiments of Donaldson (1985). Values of **A** were calculated using thermodynamic data from Ghiorso and Sack (1995), Sack and Ghiorso (1989), Berman (1988), and Elkins and Grove (1990). Inset is a summary of normalized rates of mineral dissolution plotted against 1000 / T (K) (see Chapter 3 for details).

a partial melt of the pelite are significant. Figures 4.3 and 4.4 show that selective assimilation of the individual phases in a granite xenolith produces distinctly different patterns of zoning than does bulk assimilation of granite. Thus, as demonstrated above, the variation in compositional zoning in minerals could provide an alternative means for identifying the extent and chemical pathways of assimilation.

Models for chemical zoning in open systems

The equilibrium models establish some of the linkages between patterns of mineral zoning and different styles of magmatic assimilation. The next step is to model rates of mineral dissolution in basaltic magma using the calculated thermodynamic potential affinity (Figure 4.5; Edwards & Russell 1996). Based on the model presented in Figure 4.5, the calculated rates of dissolution (ν) for granitic minerals at a liquidus temperature of 1175 °C (e.g., Scenario 2) are, in decreasing order, $\nu_{biotite}$, $\nu_{K\text{-}feldspar}$, $\nu_{plagioclase}$, and ν_{quartz}. Table 4.3 shows the calculated rates of mineral dissolution as well as the total time required to dissolve 1 cm diameter spheres of each mineral. This predicted order of mineral dissolution is consistent with observations on partly melted granitic xenoliths found in basaltic magmas. For examples, hydrous phases react significantly faster than quartz, plagioclase, or K-feldspar (e.g., Larsen & Switzer 1939; Watson & Mathews 1948; Al-Rawi & Carmichael 1967;

Table 4.3. Calculated values of **A** and ν for minerals (1 cm diameter spheres) in granite at 1175 °C and 10^{-4} GPa[1].

Mineral	**A** (J mole $^{-1}$)[2]	ν• 10^{-7} (oxygen equiv. moles cm^{-2} s^{-1})[3]	Time to dissolve 1 cm sphere
Qtz	10,231	1.13	4.5 days
An_{10}	9,205	4.62	0.95 days
Ksp	25,879	13.37	7 hours
Phl_{30}	139,473	100.43	1 hour

[1] Model line used to calculate mineral dissolution rates (ν) is ν = 6.56 E-5 **A** - 0.213; values of **A** and ν vary as a function of T and P

[2] **A** is the thermodynamic potential affinity and for chemical reactions at a specific T and P is equal to the sum of the chemical potentials of the reactants multiplied by their stoichiometric coefficients minus the sum of the chemical potentials of the products multiplied by their stoichiometric coefficients

[3] ν is the predicted rate of mineral dissolution at a given T and P

Table 4.4. Model prediction of time required to incorporate granite (1 cm diameter sphere) by selective assimilation.

Time	% Qtz	% Pl	% Ksp	% Phl	% Granite
1 hour	3	14	45	100	28.6
2 hours	6	29	89	100	47.2
1 day	74	100	100	100	82.2
100% dissolution (hours)	33	6.9	2.2	0.11	33

Kaczor et al. 1988; Hauksdóttir 1994).

Such calculations also model the temporal changes in composition of the granite (Table 4.4), which is also initially a 1 cm diameter sphere comprising the same volumetric proportions of Qtz, An_{10}, Ksp, and Phl_{30} as in the MELTS scenario (30%, 30%, 30%, and 10% respectively). The first melts produced are very K-rich as biotite and K-feldspar both dissolve in the first two hours. Plagioclase continues to dissolve for an additional four hours, whereas quartz requires 33 hours to assimilate completely. The implications for concomitant plagioclase crystallization over this 33-hour period are clear. The expected plagioclase crystallization path includes the formation of an An-rich core with a higher X_{Or} than predicted for FC only due to the rapid initial influx of K, a steady decrease in X_{Or} and concomitant increase in X_{Ab} as K-rich phases are consumed and Na input from plagioclase becomes more important. Finally, as Si becomes the only component being added to the magma, the X_{An} might again increase if clinopyroxene is replaced by clinoenstatite, generating reversed zoning in the crystal near the rim. This example describing the pattern of zoning expected in plagioclase due to selective assimilation indicates possible complexities expected from the selective assimilation process.

4.5. SUMMARY OF EQUILIBRIUM THERMODYNAMIC MODELING

Patterns of mineral zoning record some of the chemical paths taken by the host magma during crystallization with or without assimilation processes. An existing equilibrium thermodynamic model indicates distinct, recognizable mineral growth and zoning patterns attributable to bulk and selective assimilation. Accordingly, patterns of compositional zoning in minerals can help to constrain hypotheses dealing with open- versus closed-system behaviour in magmatic systems.

CHAPTER 5

A New Model for Assimilation-Fractional Crystallization (AFC)

5.1. INTRODUCTION

Chapter 5 presents a new paradigm for predicting the chemical and temporal consequences of magmatic assimilation. The model is unique because it incorporates both kinetic and thermodynamic constraints on AFC processes. Justification for a new AFC model comes from field and experimental observations discussed in Chapters 2, 3, and 4. The observations demonstrate that in nature rates of assimilation reactions control AFC paths and that rates of assimilation (e.g., mineral-melt) reactions vary for different mineral-melt pairs. Secondly, predicted AFC paths are dependent on rates of mineral reaction (see Chapter 4). Coupling the kinetic (temporal) constraints for AFC processes with the static, equilibrium thermodynamic constraints improves our ability to model natural processes.

A computer code that uses pre-existing thermodynamic databases (e.g., Berman 1988, Ghiorso & Sack 1995) coupled to a model for predicting rates of mineral dissolution (e.g., Chapter 3 and Chapter 4) is used to demonstrate the new paradigm. The resultant model makes quantitative predictions about the

mineral and liquid compositions generated by specific magmatic assimilation-fractional crystallization scenarios. The model differs from other thermodynamic-based AFC models (e.g., Nielsen 1990, Ghiorso & Sack 1995) because it uses time-steps to drive the AFC process. Thus, the model predicts both cooling and crystallization rates attendant to specific isenthalpic AFC paths. This model is unique because it predicts the chemical, physical, and **temporal** consequences of AFC.

This chapter starts by developing a fractional crystallization (FC) algorithm and testing it against a pre-existing model (MELTS). A modified FC algorithm that approximates isenthalpic assimilation-fractional crystallization (AFC) shows how variations in pressure (P), temperature of the assimilant (T_a), and assimilant composition affect the compositions of olivine (Ol) and plagioclase (Pl) crystallizing from the melt and the liquid lines of descent, the cooling rates, and the crystallization rates for the system. The chapter ends by discussing the implications of the model results for AFC processes in the southern Northern Cordilleran Volcanic Province (NCVP) and for magmatic processes in general.

5.2. DEVELOPMENT OF A FORWARD MODEL FOR TIME-DEPENDENT AFC

A new, quantitative model for simulating magmatic AFC was created using a three step process. First a general theoretical and numerical approach

was developed based largely on previous work, particularly that of Russell and Nicholls (1985). The result was an algorithm to simulate FC alone (**Petros**). The FC algorithm was then modified to simulate isenthalpic assimilation-fractional crystallization (**Petros-AFC**).

General Theoretical and Numerical Philosophy

Previous workers have developed strategies for solving problems of chemical equilibria in silicate systems of high variance (e.g., Nicholls 1977, Reed 1982, Ghiorso & Carmichael 1983, Russell & Nicholls 1985). This task has three components: defining the system of interest, adopting theoretical guidelines, and implementing a numerical technique to solve the defined problem.

The system of interest is an anhydrous silicate melt represented by the eleven chemical components listed in Table 5.1. The chosen components are linearly independent and are based on the chemical components used by Ghiorso and Sack (1995) in their regular solution model for silicate liquids. The number of phases in the system varies between one and three, and includes a silicate melt +/- olivine +/- plagioclase. Other solid phases are not considered. The variance of the system, defined by the Gibb's Phase Rule, is 10 or more.

Duhem's Theorem states that if the bulk composition of a closed system

Table 5.1 Variables required to define a magma system containing three phases (silicate liquid, Ol, Pl).

Components (after Ghiorso & Sack 1995)

SiO_2
TiO_2
Al_2O_3
Fe_2O_3
$MgCr_2O_4$
Fe_2SiO_4
Mg_2SiO_4
$CaSiO_3$
Na_2SiO_3
$KAlSiO_4$
$Ca_3(PO_4)_2$

(N =11)

System variables

T, P
$n_{i,liq}$, i = 1 to 11
n_{melt}
n_{Ol}
n_{Pl}
$X_{i,liq}$, i = 1 to 11
X_{Fo}
X_{An}, X_{Ab}

(total of 30 system variables)

Independent variables: N + 2

Dependent variables: 30 - (N+2) = 17

is known, the equilibrium state of the system is completely determined when two independent system variables are fixed (Prigogine & Defay 1954, Nicholls 1977, Russell & Nicholls 1984, Nicholls 1990). Because of the high variance of the system, the two independent variables can be either extensive or intensive (Russell & Nicholls 1985).

The total number of variables in the system is 30 (Table 5.1). Duhem's Theorem guarantees that all but 17 variables are dependent. This requires 17 equations that relate the unknown variables. Eleven of the 17 equations are mass balance equations for the system components and the twelfth equation guarantees mass conservation in the system (Table 5.2). The remaining five equations are thermodynamic equilibria, relating the chemical potentials of components in the melt to those in the solids (Table 5.2). To solve the thermodynamic equilibria I used the database of Ghiorso and Sack (1995) for the thermodynamic properties of the melt, the database of Berman (1988) for the standard state thermodynamic properties of the solids, the symmetric binary solution model of Sack and Ghiorso (1989) for olivine, and the asymmetric ternary solution model of Elkins and Grove (1990) for plagioclase. All of the solid solution models used are internally consistent with the adopted thermodynamic data (cf. Ghiorso & Sack 1995).

Both the FC and the assimilation-fractional crystallization paths were approximated using step-wise equilibrium calculations. Computer program

Table 5.2. System of equations describing the equilibrium state of an Ol + Pl saturated melt. Functions F1-F17 are minimized for each fractionation step.

$F1 = X_{SiO2,l} * n_l + n_{fsp} * (X_{An} + 2.5 * X_{Ab} + 2.0 * (1.0 - X_{An} - X_{ab})) - M_{SiO2};$

$F2 = X_{TiO2,l} * n_l - M_{TiO2};$

$F3 = X_{Al2O3,l} * n_l + n_{Fsp} * (X_{An} + 0.5 * X_{Ab}) - M_{Al2O3};$

$F4 = X_{Fe2O3,l} * n_l - M_{Fe2O3};$

$F5 = X_{MgCr2O4,l} * n_l - M_{MgCr2O4};$

$F6 = X_{Fe2SiO4,l} * n_l + n_{Ol} * (1.0 - X_{Fo}) - M_{Fe2SiO4};$

$F7 = X_{Mg2SiO4,l} * n_l + n_{Ol} * X_{Fo} - M_{Mg2SiO4};$

$F8 = X_{CaSiO3,l} * n_l + n_{Fsp} * X_{An} - M_{CaSiO3};$

$F9 = X_{Na2SiO3,l} * n_l + n_{Fsp} * 0.5 * X_{Ab} - M_{Na2SiO3};$

$F10 = X_{KAlSiO4,l} * n_l + n_{Fsp} * (1.0 - X_{An} - X_{Ab}) - M_{KAlSiO4};$

$F11 = X_{Ca3(PO4)2,l} * n_l - M_{Ca3(PO4)2};$

$F12 = X_{SiO2,l} + X_{TiO2,l} + X_{Al2O3,l} + X_{Fe2O3,l} + X_{MgCr2O4,l} + X_{Fe2SiO4,l} + X_{Mg2SiO4,l} + X_{CaSiO3,l} + X_{Na2SiO3,l} + X_{KAlSiO4,l} + X_{Ca3(PO4)2,l} - 1.0;$

$F13 = (\mu_{SiO2,l} + \mu_{Al2O3,l} + \mu_{CaSiO3,l}) - (\mu_{CaAl2Si2O8,Pl} + R * T * \ln(a_{An}));$

$F14 = (2.5 * \mu_{SiO2,l} + 0.5 * \mu_{Al2O3,l} + 0.5 * \mu_{Na2SiO3,l}) - (\mu_{NaAlSi3O8,Pl} + R * T * \ln(a_{Ab}));$

$F15 = (2.0 * \mu_{SiO2,l} + \mu_{KAlSiO4,l}) - (\mu_{KAlSi3O8,Pl} + R * T * \ln(a_{San}));$

$F16 = (\mu_{Mg2SiO4,l}) - (\mu_{Mg2SiO4,Ol} + 2.0 * R * T * \ln(a_{Fo});$

$F17 = (\mu_{Fe2SiO4,l}) - (\mu_{Fe2SiO4,Ol} + 2.0 * R * T * \ln(a_{Fa});$

Petros is an ANSI C code that simultaneously solves the mass balance equations and thermodynamic equilibria given in Table 5.2 using Newton-Raphson technique for non-linear equations. The Newton-Raphson technique works well as long as the Jacobian matrix is not singular (i.e. the matrix must be invertible) and the initial guesses are close to the correct values (Reed 1982; Russell & Nicholls 1985). In the case of FC, the Jacobian matrix appears to be invertible as long as positive quantities of crystallized material are removed at each step. For the first step of each simulation the starting guesses are equal to the saturation temperature and composition for the liquidus phase(s). Subsequent initial guesses for each step are the components of the solution vector for the previous step, and since the steps are small, the initial guesses are always close to the correct values. For the simulations presented below the algorithm converged to a stable solution in 17 or fewer iterations.

Fractional Crystallization Algorithm

The algorithm for the FC calculation is shown in Figure 5.1. The initial conditions include the composition of the system and the initial total moles of liquid, which is set to one. Throughout the calculations pressure (P) is held constant; the model is driven by fixing the amount of solid crystallized at each step. The initial calculation determines the liquidus temperature and liquidus phase for the system. At that temperature, the equilibrium state of the system is

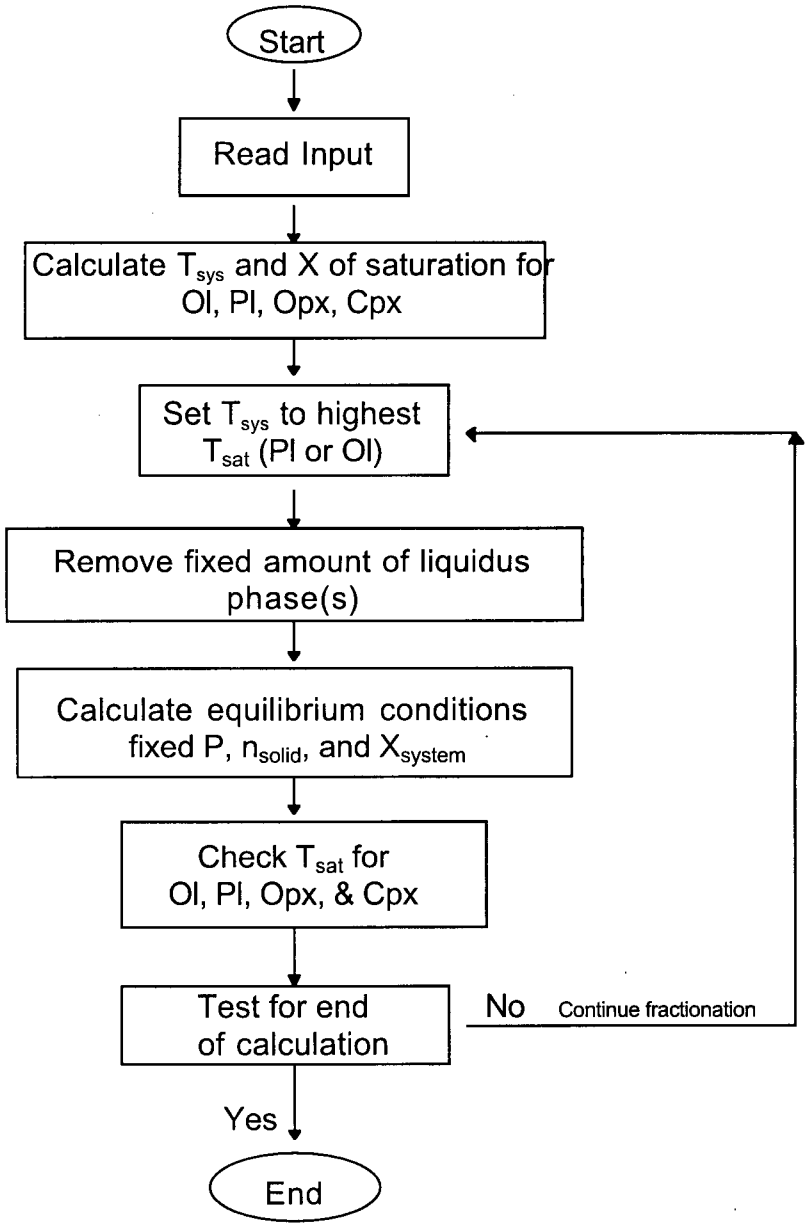

Figure 5.1. Flow diagram for the fractional crystallization (FC) algorithm.

melt plus an infinitesmal amount of the solid phase. Using the liquidus temperature and the composition of the liquidus phase as starting guesses, the program finds the first solution vector. That solution vector contains all the information about the new equilibrium state of the system, including the temperature and the new, stable liquid and solid compositions. After the first calculation is complete, the program checks the saturation state of the system to insure that the fractionated phase is still the only stable solid and that no cotectic surfaces have been reached. If true, then the program loops back to the start and the fractionation calculation continues. When the temperature of the system drops to within 0.5 $^{\circ}$ C of a cotectic surface, the size of the liquid decrement decreases, to insure that the cotectic surface is not overstepped.

When two phases are determined to be saturated within the temperature tolerance of the program (0.05 $^{\circ}$ C), the FC algorithm includes mass balance and thermodynamic equations for both solid phases. Crystallization continues until the moles of liquid remaining in the system reaches a pre-determined amount (generally 0.7).

Petros-MELTS Comparison

As a check of the FC algorithm, the liquid lines of descent for two different starting melt compositions were calculated. The algorithm used in **Petros** is validated by comparing these model results to results from MELTS

Table 5.3. Calculated chemical composition and saturation conditions[1] of alkali olivine basalts SH-44 and SC-23, from northwestern British Columbia[2].

Oxides (Wt. %)	SH-44	SC-23
SiO_2	46.46	46.06
TiO_2	2.84	2.57
Al_2O_3	16.92	14.89
Fe_2O_3	2.59	4.30
FeO	10.10	8.28
MnO	0.18	0.18
MgO	6.52	9.25
CaO	8.87	10.24
Na_2O	3.71	2.85
K_2O	1.09	0.91
P_2O_5	0.45	0.39
H_2O	0.10	0.62
Total	99.83	100.52

SH-44	Petros	MELTS	Obs.[3]
T_L	1180.06	1179.84	
T_{Pl}	1180.06	1179.84	
T_{Ol}	1172.21	1173.64	
X_{An}	71.17	71.15	69.6
X_{Fo}	81.53	81.18[4] (80.25)	78.3

SC-23	Petros	MELTS	Obs.[3]
T_L	1208.14	1211.46	
T_{Pl}	1184.78	1185.38	
T_{Ol}	1208.14	1211.46	
X_{An}	74.93	75.00	70.5
X_{Fo}	87.78	87.56[4] (86.52)	81.9

[1] for pressure equal to 10^5 Pa
[2] SH-44 from Lava Fork volcanic centre, SC-23 from Second Canyon volcanic centre (Hauksdóttir 1994)
[3] Maximum observed X_{An} in plagioclase and X_{Fo} in olivine in samples from Lava Fork (SH-50, SH-54) and in SC-23 reported by Hauksdóttir (1994)
[4] reported value is Fo/(Fo + Fe); value in parentheses is Fo/(Fo + Ca + Fe)

(Ghiorso & Sack 1995) for the same two melt compositions (Table 5.3). The two programs use the same thermodynamic database and thus should give similar results. Table 5.3 gives the major element compositions of the two samples used for the comparison and lists the liquidus temperatures, saturation temperatures, and compositions for olivine and plagioclase predicted by the two programs. The petrology of both samples (SH-44 and SC-23) is discussed in detail by Hauksdóttir (1994). For comparison Table 5.3 also gives measured compositions for plagioclase and olivine from the volcanic centres where the samples were collected (SH-44 from Lava Fork and SC-23 from Second Canyon). Results of the runs are summarized in Figures 5.2 to 5.5.

SH-44 is an olivine-plagioclase, porphyritic basalt that has plagioclase on the liquidus at 10^{-4} GPa (Table 5.3). Results for SH-44 from both **Petros** and MELTS for the FC of Pl and Ol + Pl at a pressure of 10^{-4} GPa are very similar (Figures 5.2 and 5.3). Liquidus temperatures agree to within 0.22 $^{\circ}$ C (Table 5.3). Temperatures for the plagioclase-olivine cotectic agree to within 1.5 $^{\circ}$ C (Table 5.3). Changes in predicted plagioclase and olivine compositions (X_{An} and X_{Fo} respectivley), plotted against the T (Figures 5.2a and b), are also similar. Results from MELTS are plotted as Fo/(Fo + Fa) (Figure 5.2b). In both figures horizontal lines show the fields for liquid, liquid plus plagioclase, and liquid plus plagioclase plus olivine. At the liquidus the plagioclase

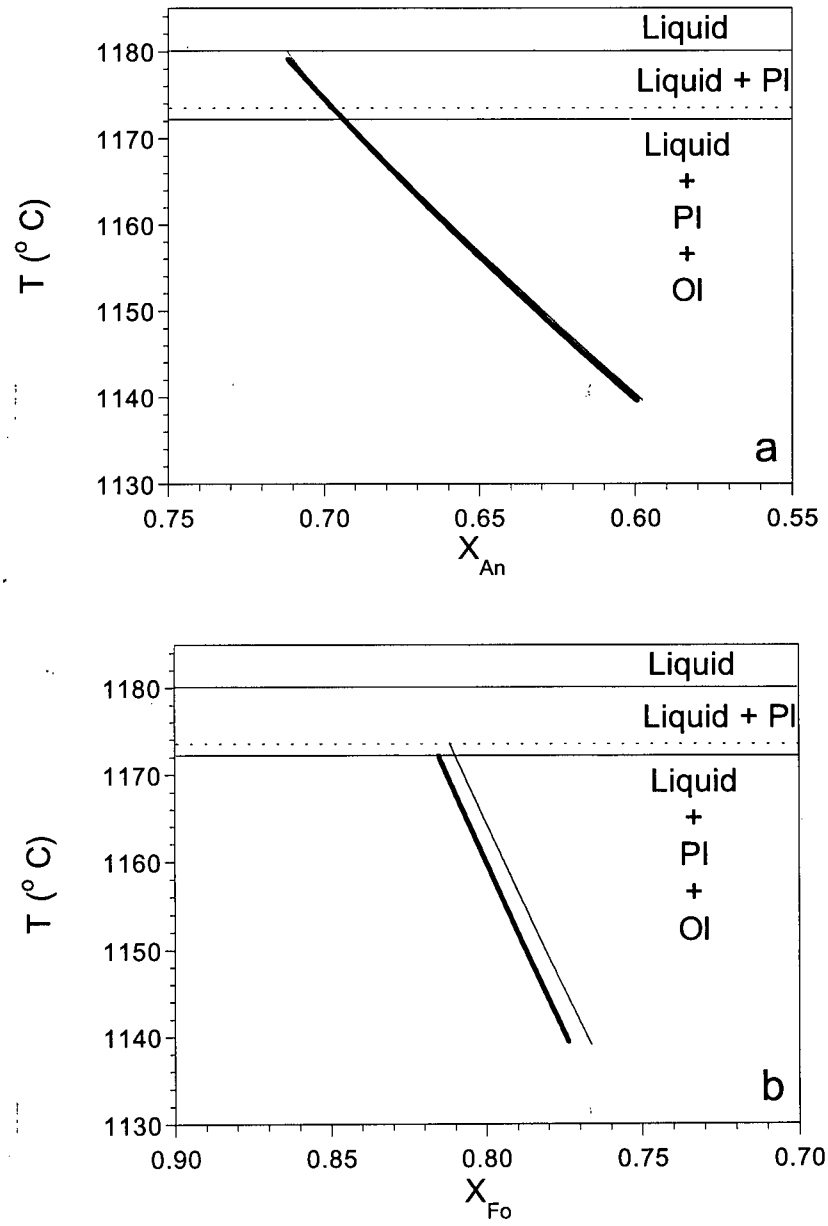

Figure 5.2. T(° C) versus predicted values of a) X_{an} and b) X_{fo} for a liquid of composition SH-44. Predicted values are from **Petros** (bold) and MELTS (light). Pressure is equal to 10^{-4} GPa.

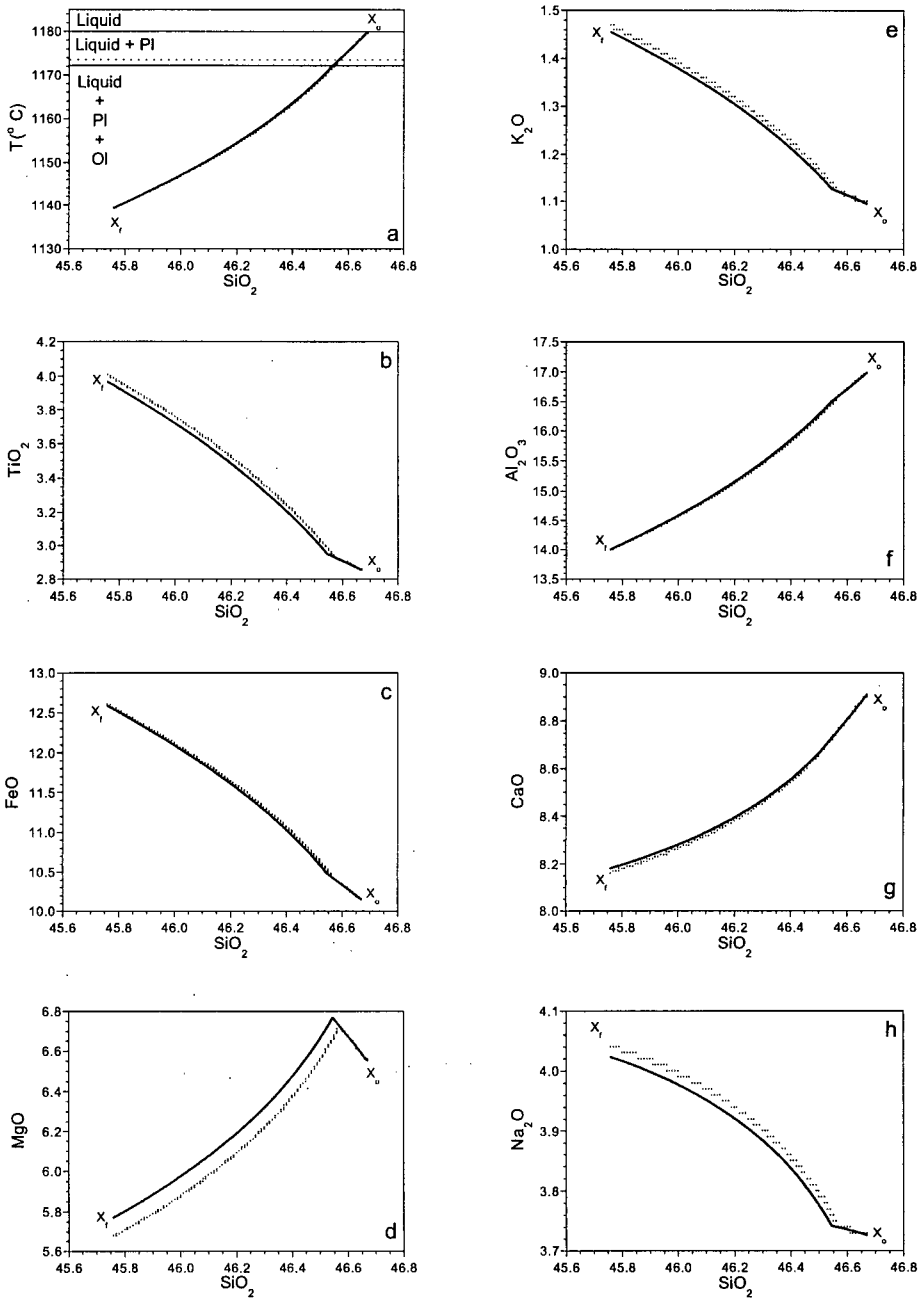

Figure 5.3. SiO_2 (wt. %) versus predicted values of a) T, b) TiO_2 (wt. %), c) FeO (wt. %), d) MgO (wt. %), e) K_2O (wt. %), f) Al_2O_3(wt. %), g) CaO (wt. %) and h) Na_2O (wt. %) for a liquid of composition SH-44. Predicted values are from **Petros** (bold) and MELTS (light). Pressure is equal to 10^{-4} GPa.

compositions predicted by both programs differ by 0.02 mole percent; they remain in close agreement until the cotectic is reached. Below the cotectic the plagioclase compositions predicted by MELTS become slightly poorer in X_{An} than those predicted by **Petros**. Predicted olivine compositions show more differences. MELTS predicts slightly less Mg-rich olivine (~0.35 mole % Fo).

The predicted differences in composition of the residual melt are given in Table 5.4 as differences in absolute weight percents of the oxides (see Figure 5.3). The differences were calculated for values of F (moles of liquid remaining) equal to 0.75. The largest differences between MELTS and **Petros** are for MgO and Al_2O_3 (0.13 wt. %).

SC-23 is an olivine porphyritic basalt that has olivine on the liquidus at 10^{-4} GPa (Table 5.3). Figures 5.4 and 5.5 show results for SC-23 from both **Petros** and MELTS for the FC of Ol, Pl, and Ol + Pl at a pressure of 10^{-4} GPa. Liquidus temperatures for sample SC-23 agree to within 3.3 $^{\circ}$ C. The predicted temperatures for the plagioclase-olivine cotectic agree to within 1.5 $^{\circ}$ C (Table 5.3). Figures 5.4a and 5.4b show the variations in predicted olivine and plagioclase compositions plotted against T for both models. In Figure 5.4a the MELTS results are plotted as Fo/(Fo + Fa). At the liquidus the Fo/(Fo + Fa) ratios for olivine predicted by both programs differ by 0.22 mole percent; Petros predicts slightly more Mg-rich olivine compositions than MELTS. The difference

Table 5.4. Comparison of results from Petros and MELTS for predicted liquid lines of descent for alkali olivine basalts SH-44 and SC-23. Delta values are for values of F = 0.75.

Oxides[1]	SH-44 (ΔWt. %)	SC-23 (ΔWt. %)
ΔSiO_2	-0.05	-0.01
ΔTiO_2	0.09	0.07
ΔAl_2O_3	-0.13	-0.11
ΔFe_2O_3	0.08	0.10
ΔFeO	0.11	0.06
ΔMgO	-0.13	-0.13
ΔCaO	-0.03	-0.02
ΔNa_2O	0.03	0.01
ΔK_2O	0.03	0.02
ΔP_2O_5	0.01	0.01

[1] value for MELTS minus value for Petros

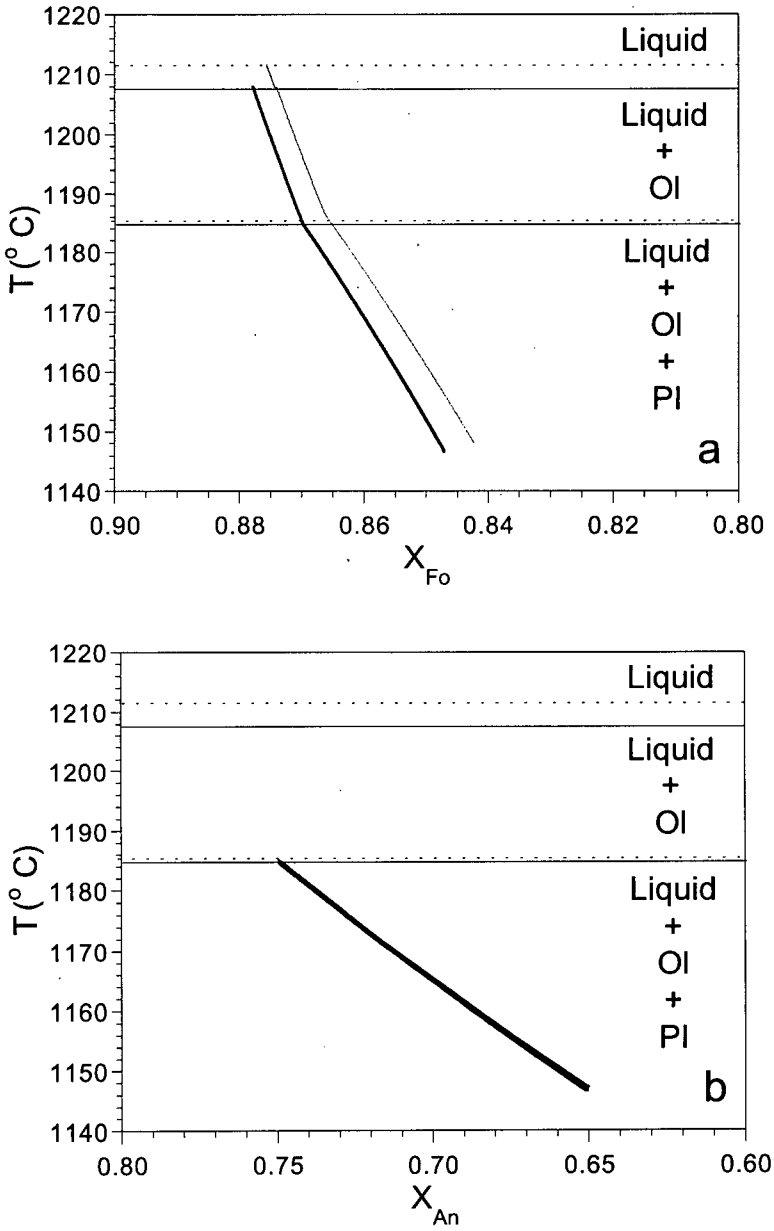

Figure 5.4. T(° C) versus a) X_{Fo} and b) X_{An} for a liquid of composition SC-23. Predicted values are from **Petros** (bold) and MELTS (light). Pressure is equal to 10^{-4} GPa.

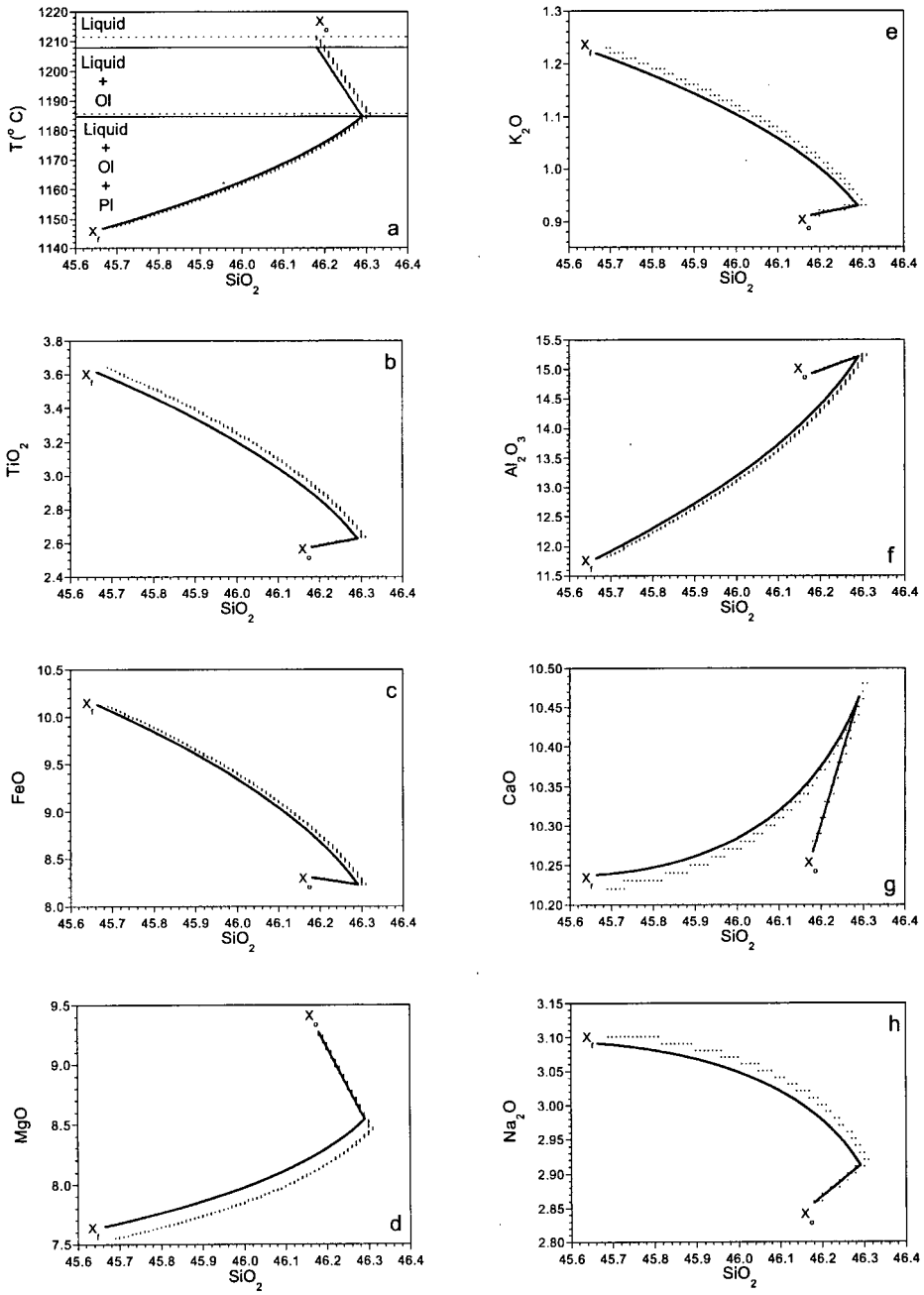

Figure 5.5. SiO_2 (wt. %) versus predicted values of a) T (^{o} C), b) TiO_2 (wt. %), c) FeO (wt. %), d) MgO (wt. %), e) K_2O (wt. %), f) Al_2O_3(wt. %), g) CaO (wt. %) and h) Na_2O (wt. %) for a liquid of composition SC-23. Predicted values are from **Petros** (bold) and MELTS (light). Pressure is equal to 10^{-4} GPa.

in the predicted Fo/(Fo + Fa) ratio remains constant to the cotectic. The initial predicted plagioclase compositions agree to within 0.07 mole percent.

Figure 5.5a-h shows some of the variations in the predicted liquid compositions between the two programs for SH-44. The liquid lines of descent differ slightly as summarized in Table 5.4 for values of F (moles of liquid remaining) equal to 0.75. The largest differences between MELTS and **Petros** are for MgO and Al_2O_3 (0.13 weight percent). In general, the two programs produce very similar results for SC-23.

The discrepancies between results from **Petros** and MELTS in liquidus temperatures, solid compositions, and liquid composition derive soley from using different olivine solution models. **Petros** uses a binary solution model for olivine (Mg-Fe: Sack & Ghiorso 1989) while MELTS uses a ternary olivine solution model (Ca-Mg-Fe: Hirschman 1991). Allowing for incorporation of Ca into olivine (e.g., MELTS) changes slightly the olivine and plagioclase saturation temperatures and the composition of the crystallized olivine.

Isenthalpic Assimilation - FC Algorithm

The previous section illustrates that the FC algorithm in **Petros** reproduces the results of an established model. The final step in building a new model for simulating coupled assimilation-fractional crystallization is to link the FC algorithm with an algorithm that describes the mass changes,

thermodynamic relationships, and kinetics of reactions attending assimilation. For the new model it is assumed that the assimilation reactions are congruent mineral dissolution reactions, where the assimilant (feldspar) reacts with the melt to form a new melt. This assumption is consistent with experiments for dissolution of feldspar in mafic melts (Donaldson 1985).

First, the affinity for the assimilation reaction is calculated using the following general equation:

$$A_{rx} = \nu_{solid} \bullet \mu_{solid} - \nu_{melt} \bullet \mu_{melt}$$

where A_{rx} is the affinity for the reaction in Joules, ν_{solid} and ν_{melt} are the stoichiometric reaction coefficients in moles for the solid and melt, and μ_{solid} and μ_{melt} are the chemical potentials of the solid and melt. The μ_{solid} and μ_{melt} are calculated at the temperature of the system (T_{sys}). The A_{rx} is used to calculate a reaction rate based on the model developed in Chapter 3 and given in Chapter 4, which relates affinity to rate of mineral dissolution. The equation is

$$\upsilon = 7.682 \bullet 10^{-11} \bullet A_{rx} - 5.27049 \bullet 10^{-8}$$

where υ is reaction rate in moles cm^{-2} s^{-1}. The value of υ is converted from units of moles cm^{-2} s^{-1} to units of moles by multiplying by a time increment and a surface area factor (SA_x; Table 5.5).

Table 5.5. Formulae for converting reaction rate (moles cm^{-2} s^{-1}) to moles for a spherical xenolith.

Variables

V_x = volume of xenoliths

V_m = volume of magma (calculated at T and P of the system)

SA_x = total surface area of xenoliths

r_x = radius of single xenolith

N = number of xenoliths

R_v = ratio of V_x to V_m (constant)

$$R_v = \frac{V_x}{V_m}$$

$$V_x = R_v \bullet V_m = N \bullet 4 \bullet \pi \bullet r_x^3$$

$$N = \frac{R_v \bullet V_m}{4 \bullet \pi \bullet r_x^3}$$

$$SA_x = N \bullet \frac{4}{3} \bullet \pi \bullet r_x^2 = \frac{4}{3} \bullet \pi \bullet r_x^2 \bullet \frac{R_v \bullet V_m}{4 \bullet \pi \bullet r_x^3} = \frac{R_v \bullet V_m}{3 \bullet r_x}$$

Multiplication of υ by SA_x converts the rate to moles s^{-1}; SA_x is held constant throughout the entire simulation. To calculate SA_x, the volumetric ratio of assimilant to magma (R_v), the initial volume of the magma (V_m), and the radius of the assimilant (r_x) must be specified (Table 5.5). For all the calculations the volumetric ratio of xenolith to melt (R_v) is set to 0.05 and the radius for the xenolith (r_x) is set to 10 cm. These values are based on field observations from the NCVP on common abundances of xenoliths and their average sizes. V_m is calculated for the starting melt composition at the initial T_{sys} and is held constant. Finally, υ, now in units of moles s^{-1}, is multiplied by the time-step (5000 seconds for Ol crystallization and 25000 for Ol + Pl crystallization) to convert the rate into a finite amount of moles of assimilant. This amount of assimilant is added to the melt, to produce the new melt composition.

One of the significant differences between the new algorithm and the old algorithm is that for the new algorithm the enthalpy of the system is fixed at each step (i.e., the process is considered to be isenthalpic). The isenthalpic assumption links the energy requirements of assimilation, heating the assimilant to the temperature of the magma and fusing the assimilant (cf. Chapters 3 and 4), to the energy available from the magma through cooling and crystallization. Several other workers have made this assumption when

modeling AFC processes (Nicholls & Stout 1982; Ghiorso & Kelemen 1987; Reiners et al. 1995, Russell et al. 1995).

The enthalpy of the assimilant is calculated by multiplying the molar enthalpy of the assimilant at T_a by the number of moles of assimilant. The enthalpy for the magma is calculated by multiplying the molar enthalpy for each of the liquid components by the number of moles of each of the liquid components. The enthalpy of the liquid is calculated before the composition of the liquid is changed by adding the assimilant. The equation illustrating this calculation is given in Table 5.6 along with the partial derivatives used in the Jacobian matrix to calculate the new thermodynamic state of the system. The equation for the enthalpy of the system (H_{sys}) given in Table 5.6 has the following components: the number of moles of the new liquid (n_{l^*}), the liquid mole fractions ($X_i^{l^*}$), the standard state molar enthalpy for the new liquid ($\Delta\bar{H}_i^{o,l^*}$), the excess molar enthalpy of the new liquid ($\Delta\bar{H}_i^{ex,l^*}$), the number of moles of Pl crystallized ($n_{Fsp}{}^s$), the Pl endmember mole fractions ($X_i^{s,Fsp}$), the standard state molar enthalpy of the Pl ($\Delta\bar{H}_i^{o,s,Fsp}$), the excess molar enthalpy of the Pl ($\Delta\bar{H}_i^{ex,s,Fsp}$), the number of moles of Ol crystallized ($n_{Ol}{}^s$), the Ol endmember mole fractions ($X_i^{s,Ol}$), the standard state molar enthalpy of the Ol ($\Delta\bar{H}_i^{o,s,Ol}$), the excess molar enthalpy of the Ol ($\Delta\bar{H}_i^{ex,s,Ol}$), the number of moles of the old liquid (n_l), the liquid mole fractions for the old liquid (X_j^l), the standard state molar enthalpy for the old liquid ($\Delta\bar{H}_j^{o,l}$), the excess molar enthalpy of the new liquid

Table 5.6. Enthalpy balance equation and first derivatives.

$$H_{sys} = n_{l^*} \bullet \sum_{i-1}^{11}[X_i^{l^*} \bullet (\Delta\overline{H}_i^{o,l^*} + \Delta\overline{H}_i^{ex,l^*})] \quad + n_{Fsp}^{s} \bullet \Sigma[X_i^{s,Fsp} \bullet (\Delta\overline{H}_i^{o,s,Fsp} + \Delta\overline{H}_i^{ex,s,Fsp})]$$
$$+ n_{Ol}^{s} \bullet \Sigma[X_i^{s,Ol} \bullet (\Delta\overline{H}_i^{o,s,Ol} + \Delta\overline{H}_i^{ex,s,Ol})]$$
$$= [n_{l^o} \bullet \Sigma[X_j^{l^o} \bullet (\Delta\overline{H}_j^{o,l^o} + \Delta\overline{H}_j^{ex,l^o})] \quad + n^{ass} \bullet \Sigma[X_i^{ass} \bullet (\Delta\overline{H}_i^{o,ass} + \Delta\overline{H}_i^{ex,ass})]]$$

$$\left(\frac{\partial H_{sys}}{\partial n_{l^*}}\right) = \Sigma[X_i^{l^*} \bullet (\Delta\overline{H}_i^{o,l^*} + \Delta\overline{H}_i^{ex,l^*})]$$

$$\left(\frac{\partial H_{sys}}{\partial n_{Fsp}^{s}}\right) = \Sigma[X_i^{s,Fsp} \bullet (\Delta\overline{H}_i^{o,s,Fsp} + \Delta\overline{H}_i^{ex,s,Fsp})]$$

$$\left(\frac{\partial H_{sys}}{\partial n_{Ol}^{s}}\right) = \Sigma[X_i^{s,Ol} \bullet (\Delta\overline{H}_i^{o,s,Ol} + \Delta\overline{H}_i^{ex,s,Ol})]$$

$$\left(\frac{\partial H_{sys}}{\partial T}\right) = n_{l^*} \bullet \Sigma[X_i^{l^*} \bullet C_p^{l^*}] + n_{Fsp}^{s} \bullet \Sigma[X_i^{s,Fsp} \bullet \left(\frac{\partial C_p^{s,Fsp}}{\partial T}\right)] + n_{Ol}^{s} \bullet \Sigma[X_i^{s,Ol} \bullet \left(\frac{\partial C_p^{s,Ol}}{\partial T}\right)]$$

$$\left(\frac{\partial H_{sys}}{\partial X_i^{l^*}}\right) = n_{l^*} \bullet \Sigma[\Delta\overline{H}_i^{o,l^*} + X_i^{l^*} \bullet \left(\frac{\partial \Delta\overline{H}_i^{ex,l^*}}{\partial X_i^{l^*}}\right) + \Delta\overline{H}_i^{ex,l^*})]$$

$$\left(\frac{\partial H_{sys}}{\partial X_i^{s,Fsp}}\right) = n_{Fsp}^{s} \bullet \Sigma[\Delta\overline{H}_i^{s,Fsp} + X_i^{s,Fsp} \bullet \left(\frac{\partial \Delta\overline{H}_i^{ex,s,Fsp}}{\partial X_i^{s}}\right) + \Delta\overline{H}_i^{ex,s,Fsp})]$$

$$\left(\frac{\partial H_{sys}}{\partial X_i^{s,Ol}}\right) = n_{Ol}^{s} \bullet \Sigma[\Delta\overline{H}_i^{s,Ol} + X_i^{s,Ol} \bullet \left(\frac{\partial \Delta\overline{H}_i^{ex,s,Ol}}{\partial X_i^{s,Ol}}\right) + \Delta\overline{H}_i^{ex,s,Ol})]$$

($\Delta\bar{H}_j^{ex,l}$), the number of moles of Fsp assimilated (n^{ass}), the assimilated Fsp endmember mole fractions (X_i^{ass}), the standard state molar enthalpy of the assimilated Fsp ($\Delta\bar{H}_i^{o,ass}$), and the excess molar enthalpy of the assimilated Fsp ($\Delta\bar{H}_i^{ex,ass}$).

Figure 5.6 illustrates the resulting algorithm for combined assimilation-fractional crystallization (**Petros-AFC**). The first four steps in the algorithm are exactly the same as for FC alone, except that **Petros-AFC** is driven by ***time increments*** as opposed to increments of extracted melt. Once the initial T_{sys} is determined, the enthalpy of the melt is calculated. Then the affinity, enthalpy, and amount of the assimilant are computed. Next the new enthalpy for the system is calculated. The final two steps return to the **Petros** routine established above for FC. The only difference is that for **Petros-AFC** the two fixed intensive parameters are pressure and the enthalpy of the system, as opposed to pressure and moles of solid. This slightly modifies the set of equations used to find the equilibrium state of the system to account for the fixed system enthalpy. Once the new equilibrium state is found and the saturation state of the melt is confirmed, the algorithm loops back to the melt enthalpy calculation. The algorithm runs until the moles of melt remaining, initially set to 1.0, reaches a pre-set value (e.g., 0.75).

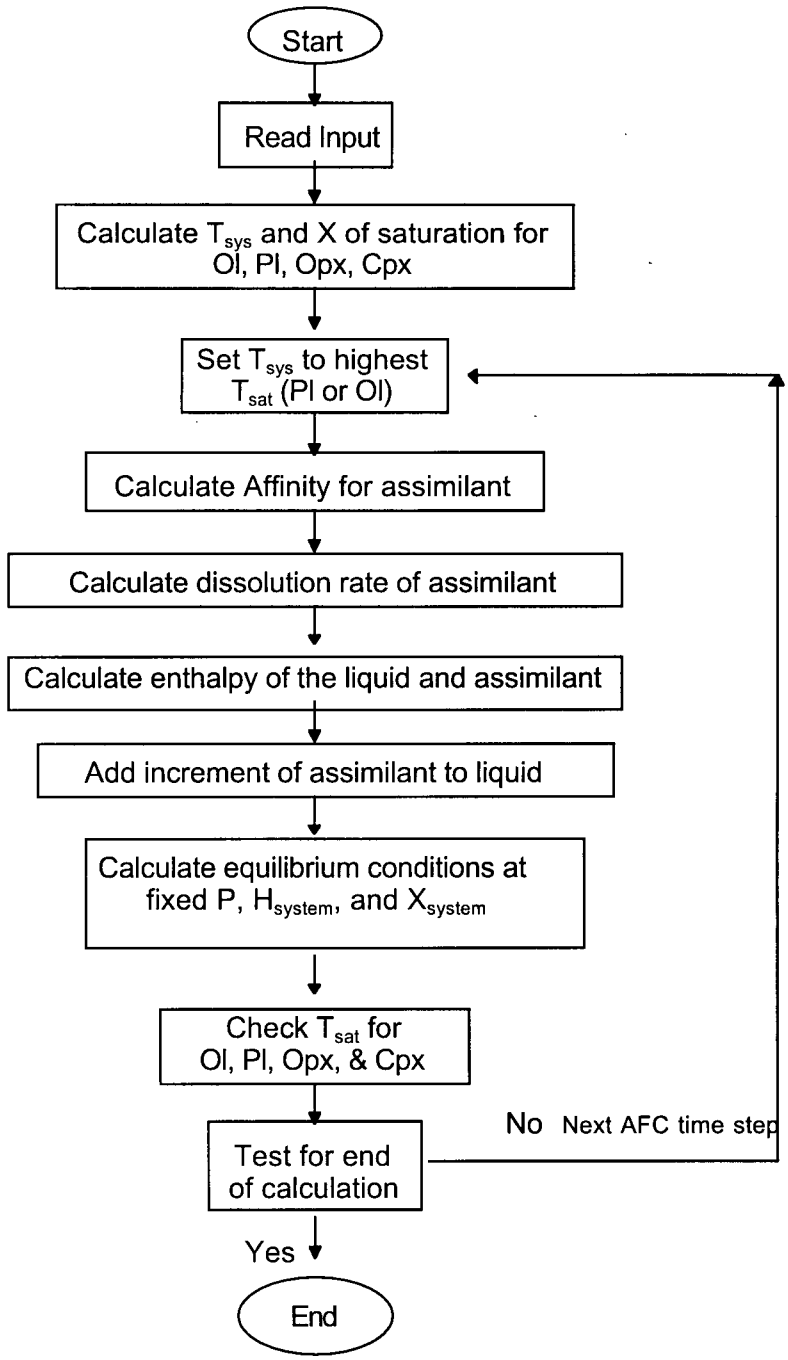

Figure 5.6. Algorithm for kinetically-driven AFC model.

An Isenthalpic AFC Simulation for SC-23

Hauksdóttir (1994) documented that assimilation was important at the Iskut River volcanic centres and results from Chapter 2 extend this conclusion to the Hoodoo Mountain volcanic complex. Program **Petros-AFC** was used to model seven assimilation scenarios, based on examples from the Iskut area, to illustrate the new AFC model and also gain new insight into AFC processes in the southern NCVP. The assimilation scenarios model assimilation of plagioclase and alkali feldspar by an alkali olivine basalt (SC-23). The specific conditions for this simulation (AFC1) are listed in Table 5.7. Sample SC-23 is a MgO-rich, sparsely porphyritic olivine basalt from the Second Canyon basalt flow (cf. Chapter 2, Figure 2.1). This sample was chosen as the initial melt composition because it has the highest MgO (wt %) content of all the basalts in the Iskut volcanic centres and is the best candidate for a primitive mantle magma from the southern NCVP (Hauksdóttir 1994). Plagioclase was chosen as an assimilant because it is a common xenocryst at Little Bear Mountain (Chapter 2) and at many other of the Iskut River centres (Hauksdóttir 1994).

Figures 5.7a and b show the compositions of olivine and plagioclase as the temperature of the system decreases. Open circles represent moles of mineral crystallized from the system and are given in 0.5 mole increments. For the given conditions, the composition of the olivine changes little between the AFC and the FC scenarios until the

Table 5.7. Summary of assimilation-fractional crystallization scenarios using SC-23 as the starting melt composition.

Model Scenario	Parameters varied from Scenario 1	P (GPa)	Assimilant Composition[1]	T_a (^{o} C)
AFC 1	-	10^{-4}	$An_{24.73}\ Ab_{67.2}\ San_{8.07}$	500
AFC 2	P	0.1	$An_{24.73}\ Ab_{67.2}\ San_{8.07}$	500
AFC 3	P	0.5	$An_{24.73}\ Ab_{67.2}\ San_{8.07}$	500
AFC 4	X_a	10^{-4}	$An_{93.26}\ Ab_{6.7}\ San_{0.04}$	500
AFC 5	X_a	10^{-4}	$An_{7.3}\ Ab_{54.7}\ San_{38.0}$	500
AFC 6	T_a	10^{-4}	$An_{24.73}\ Ab_{67.2}\ San_{8.07}$	200
AFC 7	T_a	10^{-4}	$An_{24.73}\ Ab_{67.2}\ San_{8.07}$	800

[1] Reported as mole fraction of Feldspar endmember compositions

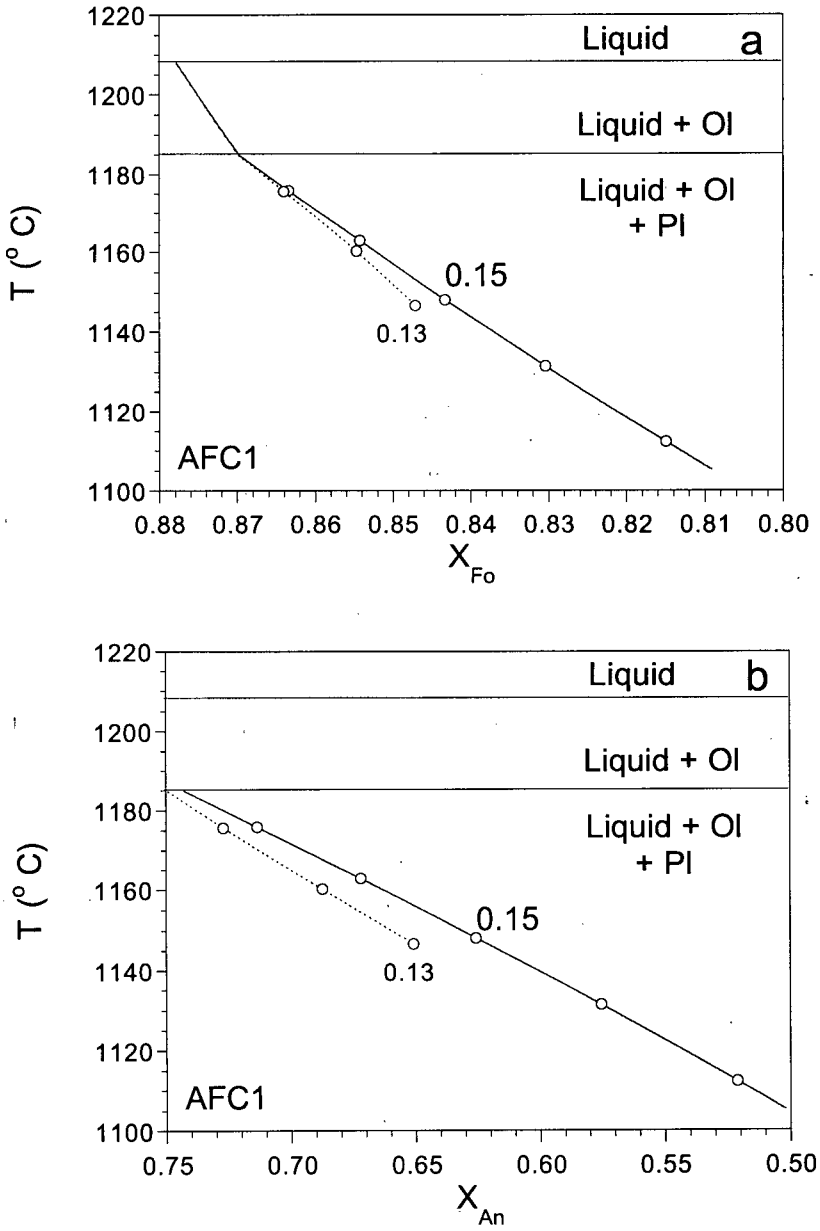

Figure 5.7. T(° C) versus a) X_{Fo} and b) X_{an} for a liquid of composition SC-23. Predicted values are from **Petros-AFC** (bold) and Petros (light). Pressure is equal to 10^{-4} GPa. Open circles denote total moles crystallized (0.05 increments).

plagioclase-olivine cotectic (Figure 5.7a). However, the plagioclase composition does vary (Figure 5.7b), because the liquid composition is enriched in Na in the AFC scenario faster than in the FC scenario.

Figure 5.8 illustrates variations in the liquid line of descent for AFC1. The open circles in this diagram represent common temperature points to facilitate comparison between the AFC and the FC scenarios. The liquid lines of descent for AFC1 versus FC are distinctly different. The most striking difference is the SiO_2 content of the melt. For FC alone, the SiO_2 increases slightly during olivine crystallization, because the olivine crystallizing from the system has a lower SiO_2 content than the melt. However, because the SiO_2 content of the plagioclase is greater than that of the melt, once plagioclase starts to crystallize the SiO_2 content drops. In contrast, assimilation of the Ab-rich plagioclase causes the melt to become enriched in SiO_2 relatively rapidly; this enrichment continues from the Ol crystallization field to the Ol plus Pl crystallization field. Another important difference between the two scenarios is the amount of melt remaining in the system at a given temperature. Assimilation-fractional crystallization produces new melt for each mole of solid that is removed from the system. Hence, at a given temperature, the amount of melt in the system is greater for the AFC scenario than for the FC alone scenario. This AFC scenario effectively extends the crystallization potential of the original melt.

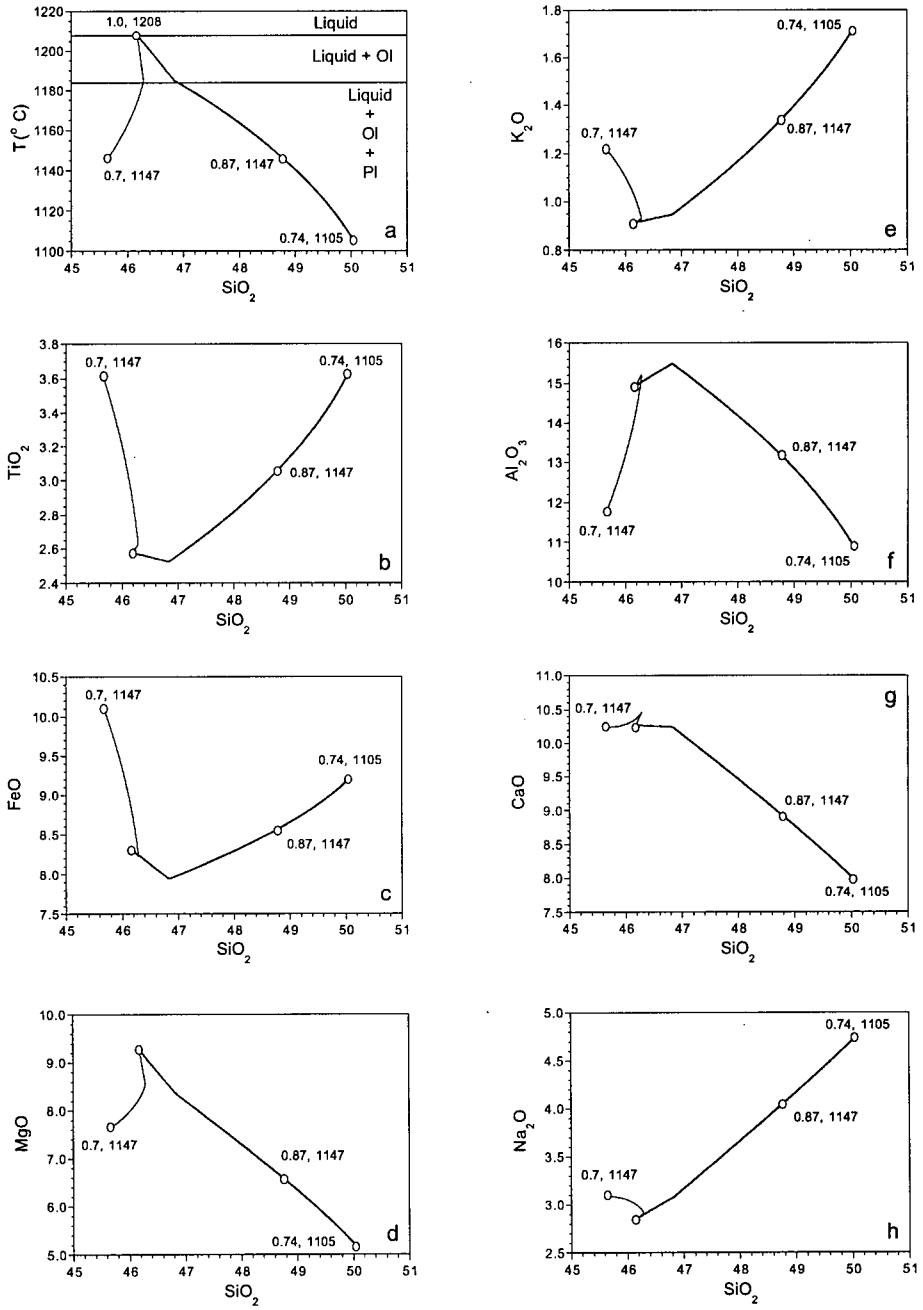

Figure 5.8. SiO_2 (wt. %) versus a) T (^{o} C), b) TiO_2 (wt. %), c) FeO (wt. %), d) MgO (wt. %), e K_2O (wt. %), f) Al_2O_3(wt. %), g) CaO (wt. %) and h) Na_2O (wt. %) for a liquid of composition SC-23. Predicted values are from **Petros-AFC** (bold) and **Petros** (light). Pressure is equal to 10^{-4} GPa. Open circles denote total moles crystallized (0.05 increments).

Figures 5.7 and 5.8 present information that is important to the study of assimilation in magmatic systems; but the same information can be obtained from pre-existing programs (e.g., MELTS). Figures 5.9 and 5.10 illustrate the temporal implications of AFC1. Program **Petros-AFC** is the first computer model that can produce this information because it is driven by rates of reaction. Figure 5.9a illustrates how the amount of melt in the system changes as a function of time. The solid horizontal line marks the original number of moles of melt and the vertical line (dotted) separates the field of olivine crystallization from that of olivine plus plagioclase crystallization. The dotted vertical line is the same for figures 5.9b and c and 5.10a-c. In general, the moles of melt initially increase for Ol crystallization, and then start to decrease when the Ol-Pl cotectic is reached. The moles of melt increase while Ol alone is crystallizing for two reasons. The first reason is that the latent heat of crystallization for olivine is large relative to the energy needed to assimilate the feldspar. The second reason is that, as the concentration of MgO in the melt becomes diluted by addition of the feldspar components, the liquidus for olivine is also moving to lower temperatures. Thus a larger component of the energy necessary for assimilation comes from the cooling of the melt (i.e. sensible heat; cf. Reiners et al. 1995, Chapters 3 and 4). However, once Pl begins to crystallize, the relative amount of material assimilated per amount crystallized drops drastically, so that overall the amount of melt in the system decreases.

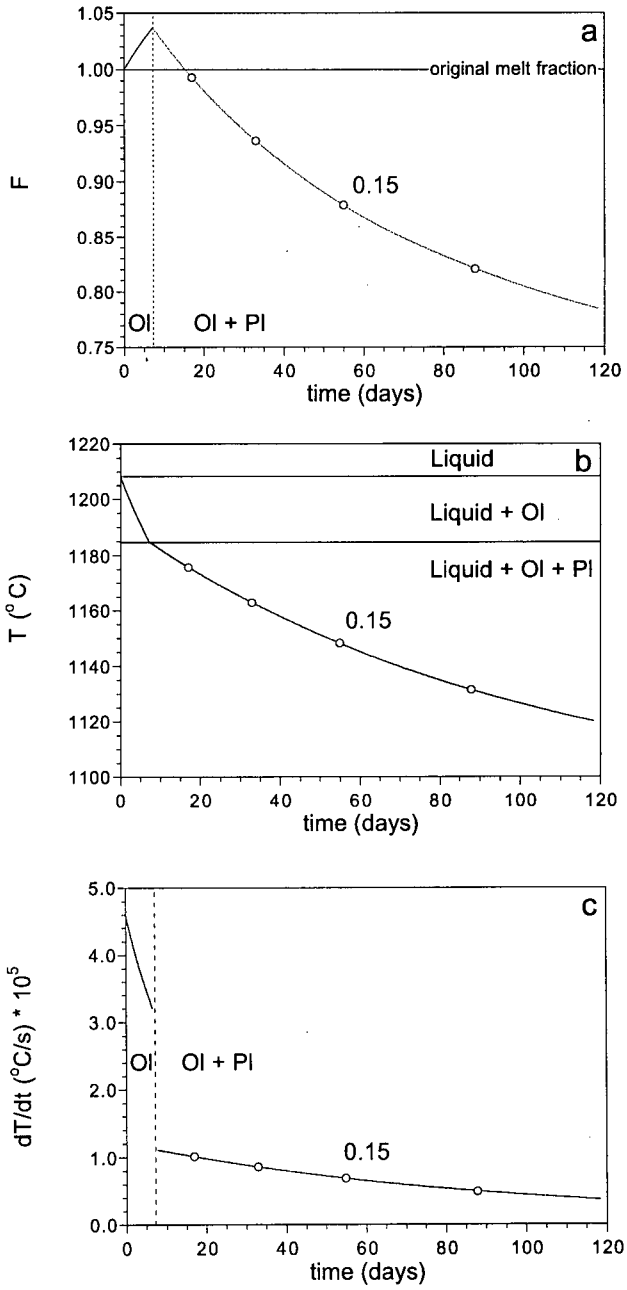

Figure 5.9. Time (days) versus a) F (moles of melt), b) T (° C), and c) cooling rate (° C s^{-1}) for a liquid of composition SC-23. Predicted values are from **Petros-AFC** for scenario AFC1 (Table 5.7). Pressure is equal to 10^{-4} GPa. Open circles denote total moles crystallized (0.05 increments).

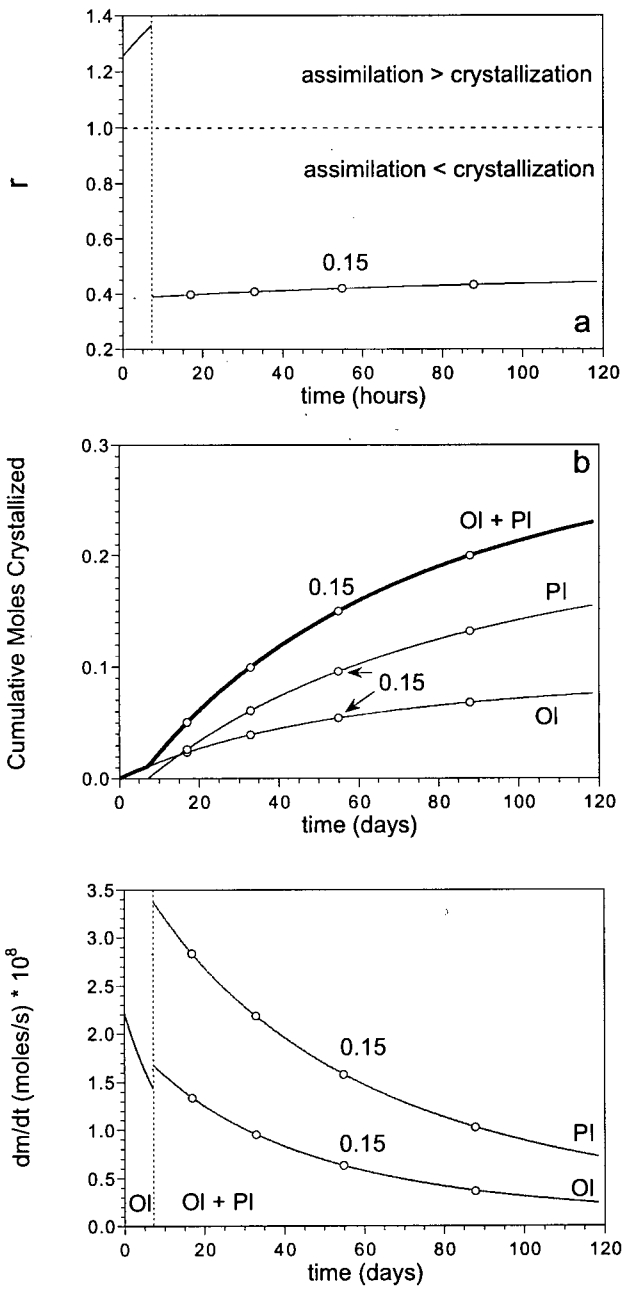

Figure 5.10. Time (days) versus a) r (moles assimilated divided by moles crystallized), b) cumulative moles crystallized, and c) crystallization rates (moles s^{-1}) for a liquid of composition SC-23. Predicted values are from **Petros-AFC** for scenario AFC1 (Table 5.7). Pressure is equal to 10^{-4} GPa. Open circles denote total moles crystallized (0.05 increments).

Thus, after the first 15 days of concomitant crystallization and assimilation, the amount of liquid in the system is the same as the starting amount even though the liquid has crystallized five percent of its initial molar amount.

The cooling rate of the system for scenario AFC1 is illustrated by Figures 5.9b and c. In Figure 5.9b, the temperature of the system (^{o} C) is plotted versus time; horizontal lines on the figure separate the fields of phase stability (e.g., liquid only, liquid plus Ol, liquid plus Ol plus Pl). The Ol crystallization interval lasts for seven days and spans a temperature range of 23 ^{o} C. Figure 5.9c shows the change in the instantaneous cooling rate (^{o} C per second) as a function of time. For the Ol alone crystallization interval the instantaneous cooling rate varies from 0.000045 to 0.000032 $^{o}C\ s^{-1}$ and it decreases with time; however, once the cotectic is reached, the cooling rate drops to 0.00001 $^{o}C\ s^{-1}$ and continues to slowly decrease with time.

The ratio of material assimilated to material crystallized, defined as **r**, is a very important parameter for assimilation studies. It has been discussed in detail by DePaolo (1981) as well as by many subsequent workers (e.g., Reiners et al. 1995). **Petros-AFC** demonstrates one of the most important aspects of incorporating kinetic constraints into assimilation scenarios, namely that values of **r** are time-dependent (Figure 5.10a). As detailed by Reiners et al. (1995), the fact that values of **r** change throughout the process of assimilation is very important to workers using isotopes and trace elements to constrain

amounts of assimilation. For the AFC1 path values of **r** change by an order of magnitude when the melt intersects the olivine-plagioclase cotectic (1.3 versus 0.4).

The last important pieces of new information gleaned from **Petros-AFC** are crystallization rates. Note that the calculated crystallization rates assume that the kinetics of crystallization can keep track with the energetic and temporal demands of assimilation. Figure 5.10b gives the cumulate molar amounts of Ol, Pl, and Ol plus Pl crystallized as a function of time. Figure 5.10b illustrates the importance of plagioclase crystallization in this system. Plagioclase crystallization quickly dominates the total amount of solids produced by the system, because plagioclase crystallizes twice as fast as olivine ($3.4 \cdot 10^{-8}$ moles s^{-1} versus $1.7 \cdot 10^{-6}$ moles s^{-1} respectively, Figure 5.10c). The instantaneous crystallization rate of Ol decreases for the first seven days of the simulation, and then jumps to a rate slightly higher than that immediately before the cotectic (Figure 5.10c). With time, the rates of crystallization for both Ol and Pl steadily decrease. The concavitity for the crystallization rate curves is the same and indicates that with time the crystallization rates steadily decrease.

The importance of the predictions from **Petros-AFC** are:

- they demonstrate how assimilation can change mineral compositions and the liquid lines of descent versus FC,
- they allow us to estimate how fast a magma would cool if it were undergoing isenthalpic assimilation,
- they give crystallization rates implied by a specific AFC path,
- they show that temporal changes in crystallization rates are unique for different minerals, and
- they show us how a magmatic system evolves as a function of time.

5.3. EFFECTS OF VARYING P, T_a, AND ASSIMILANT COMPOSITION

Overview

Three of the most important parameters that must be set *a priori* to investigate a specific AFC path using **Petros-AFC** are the pressure (P), the initial temperature of the assimilant (T_a), and the composition of the assimilant. I ran simulations using SC-23 as a starting melt composition at three different values for each of the three parameters to investigate how P, T_a, and assimilant composition affect the predicted liquid lines of descent, cooling rates, and crystallization rates for AFC paths.

Table 5.7 lists the fixed parameters for the seven investigated AFC scenarios and shows how each scenario differs from AFC1. For each of the parameters, the choice of values was guided by petrological variations

constrained by basalts in the Iskut-Hoodoo volcanic centres. For example, the three various assimilant compositions are from measured compositions of a xenocryst from Little Bear mountain volcanic centre, a xenolith from Little Bear mountain volcanic centre, and a xenocryst from the Iskut River volcanic centre.

Effects of varying P on AFC paths

The effect of varying P on assimilation-fractional crystallization was examined for three different pressures (10^{-4} GPa - AFC1, 0.1 GPa - AFC2, 0.3 GPa - AFC3; Table 5.7). All other run parameters for the three scenarios were the same. 0.3 GPa was chosen as a maximum pressure based on the observation that SC-23 has phenocrysts of olivine but not clinopyroxene. Clinopyroxene replaces olivine as the liquidus phase at pressures near 0.3 GPa. The lack of abundant clinopyroxene phenocrysts for the lavas in the Iskut-Hoodoo volcanic field is consistent with most of the crystallization history of the lavas occurring at relatively low pressures (Hauksdóttir 1994; Chapter Two).

As pressure increases, values of X_{an} decrease and the initial temperatures of plagioclase crystallization increase (Figure 5.11a). The effect of decreasing X_{an} in plagioclase and of increasing the temperature of the olivine-plagioclase cotectic as pressure increases is a well documented effect (e.g., Ghiorso & Carmichael 1985). The increase from 10^{-4} GPa to 0.1 GPa has

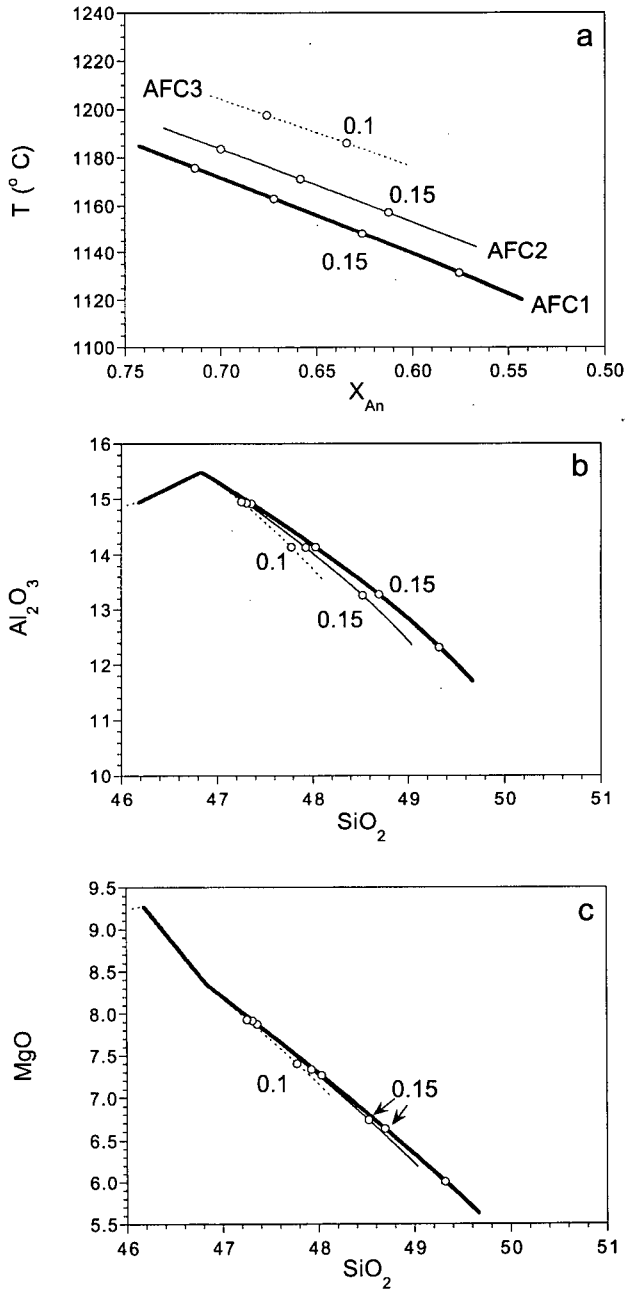

Figure 5.11. Effects of P on AFC simulations for a liquid of composition SC-23: a) X_{An} versus T (° C), b) SiO_2 (wt. %) versus Al_2O_3 (wt. %), and c) SiO_2 (wt. %) versus MgO (wt. %). Predicted values are from **Petros-AFC** for P=10^{-4} GPa (bold), P=0.1 GPa (light), and P=0.3 GPa (dashed). Open circles denote total moles crystallized (0.05 increments).

a much smaller effect on the predicted plagioclase and liquid compositions than does the increase from 0.1 to 0.3 GPa (Figures 5.11a-c). For the two lowest pressure runs the variation in the concentrations by weight percent of Al_2O_3 and MgO are similar and have parallel trends. However, for the 0.3 GPa run, clinopyroxene saturates the melt at 1177 ^{o} C; below this temperature the model is not valid.

Figure 5.12 shows the effects of changing pressure for the total amount of melt in the system and the cooling rates. The effect of changing P on the amount of moles of liquid remaining in the system is small. However, the cooling rates do reflect the changes in P. For the highest P scenario, the cooling rate is the lowest for olivine and for plagioclase (Figure 5.12c).

The cumulative amounts of material crystallized as a function of time are relatively insensitive to changes in P as well (Figure 5.13). For Ol crystallization, changes in pressure result in virtually no change in cumulative amounts crystallized (Figure 5.13a). Similarly for Pl, increasing only slightly decreases the amount of Pl crystallized for equivalent time intervals.

Changes in pressure do not have dramatic changes on the values of **r** (Figure 5.14a) or on the rates of Ol crystallization rates (Figure 5.14b). Increasing P causes a slight decrease in the crystallization rate of plagioclase (Figure 5.14c).

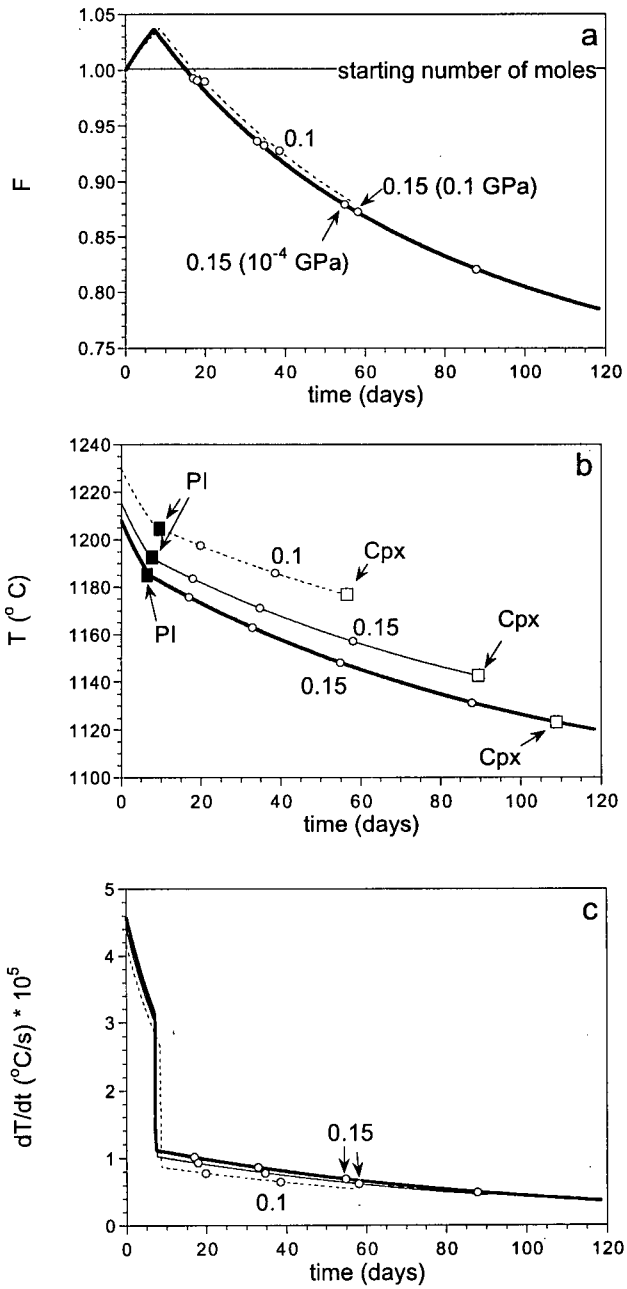

Figure 5.12. Time (days) versus a) F (moles of melt), b) T (° C), and c) cooling rate (° C s^{-1}). Predicted values are from **Petros-AFC** for a liquid of composition SC-23 and P=10^{-4} GPa (bold), P=0.1 GPa (light), and P=0.3 GPa (dashed). Open circles denote total moles crystallized (0.05 increments).

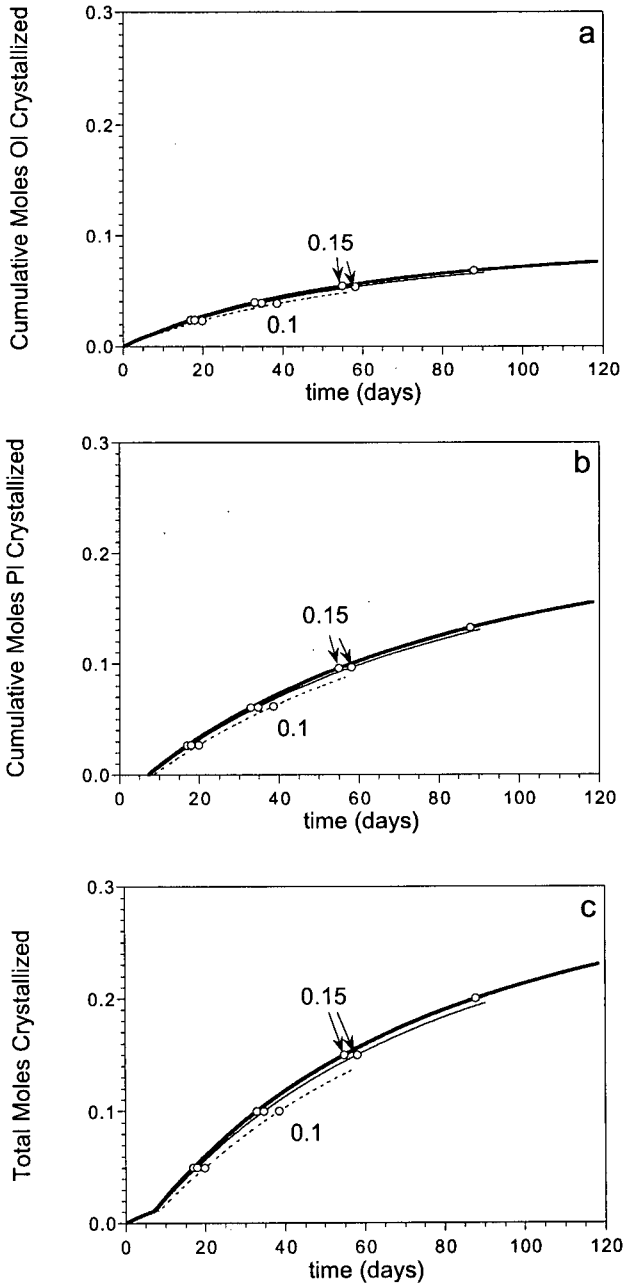

Figure 5.13. Time (days) versus a) cumulative moles of Ol crystallized, b) cumulative moles of Pl crystallized, and c) total moles crystallized (Ol + Pl). Predicted values are from **Petros-AFC** for a liquid of composition SC-23 and $P=10^{-4}$ GPa (bold), P=0.1 GPa (light), and P=0.3 GPa (dashed). Open circles denote total moles crystallized (0.05 increments).

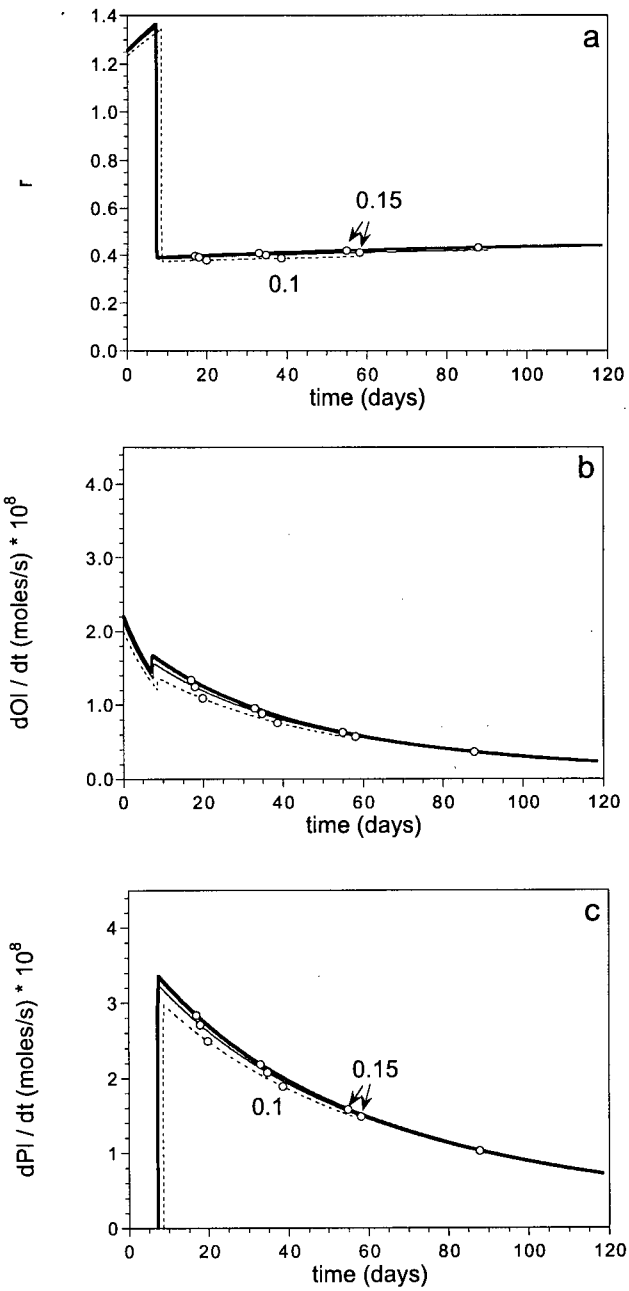

Figure 5.14. Time (days) versus a) r (moles assimilated divided by moles crystallized), b) Ol crystallization rates (moles s^{-1}), and c) Pl crystallization rates (moles s^{-1}). Predicted values are from **Petros-AFC** for a liquid of composition SC-23 and P=10^{-4} GPa (bold), P=0.1 GPa (light), and P=0.3 GPa (dashed). Open circles denote total moles crystallized (0.05 increments).

Effects of varying T_a on AFC paths

The initial temperature of the assimilant (T_a) is another important system parameter for defining a specific AFC path (cf. Chapters 3 and 4); comparison of scenarios AFC1, AFC6, and AFC7 demonstrate this quantitatively. All other parameters were held constant for these three scenarios (Table 5.7). The three scenarios cover a range of T_a from 200 ° C (AFC6) to 500 ° C (AFC1) to 800 ° C (AFC7) and represent ambient temperatures from the upper crust to the lower crust. The range of temperatures is consistent with the range of xenoliths found in lavas from the Iskut-Hoodoo volcanic field, where xenoliths have been derived from sources exposed at the surface as well as deeper sources, including granulite grade metamorphic rocks (Hauksdóttir 1994; Chapter 1 and 2; Nicholls et al. 1982).

Varying T_a causes recognizable changes in the composition of crystallizing phases and of the melt. For plagioclase, the effects are greater for increasing T_a from 500 to 800 ° C than from 200 to 500 ° C (Figure 5.15a). At a T_{sys} of 1130 ° C, the predicted X_{an} for AFC7 is 0.02 higher than that predicted by AFC1 for the same temperature. Scenario AFC7 also produces the largest changes in the melt composition (Figures 5.15b and c) for the same total amount of crystallization. For example, the difference between the initial SiO_2 of the melt (weight percent) and the predicted SiO_2 when a total of 0.2 moles of material have crystallized is 4.5 for AFC7, compared to 3.2 for AFC1 and 2.4 for

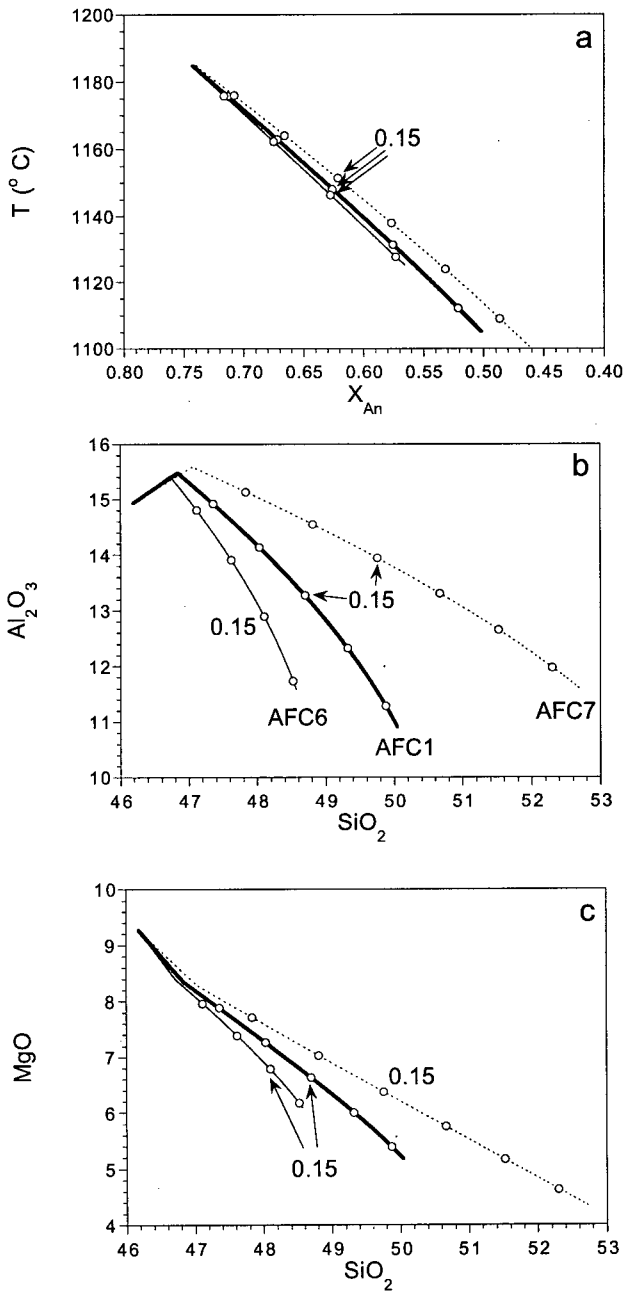

Figure 5.15. Effects of T_a on AFC simulations: a) X_{An} versus T (° C), b) SiO_2 (wt. %) versus Al_2O_3 (wt. %), and c) SiO_2 (wt. %) versus MgO (wt. %). Predicted values are from **Petros-AFC** for a liquid of composition SC-23 and T_a = 500 ° C (bold), T_a = 200 ° C (light), and T_a = 800 ° C (dashed). Open circles denote total moles crystallized (0.05 increments).

AFC6. Surprisingly, the temperature of the Ol-Pl cotectic remains almost constant (Table 5.8), even though melt composition at the cotectic is different.

The differences in T_a are even more strongly reflected in the total amount of melt in the system (Figure 5.16a), the cooling rate of the system (Figures 5.16b and c), and the crystallization rates (Figures 5.17 and 5.18). The amount of melt produced during olivine crystallization is greatest for AFC7, and decreases for both AFC1 and AFC6 (Figure 5.16a). For AFC7, the system has the same amount of liquid (in moles) as it started with after cooling and crystallizing for 56 days and converting ten percent of its original molar mass from melt into Ol and Pl. The overall cooling rate (Figure 5.16b) and the instantaneous cooling rates (Figure 5.16c) increase as T_a decreases. The instantaneous cooling rate is 1.8 times as fast for AFC6 ($5.77 \cdot 10^{-5}$ °C s^{-1}; T_a = 200 ° C) as for AFC7 ($3.24 \cdot 10^{-5}$ °C s^{-1}; T_a = 800 ° C) (Table 5.8). The slower cooling rate for scenario AFC7 extends the crystallization time before reaching clinopyroxene saturation from 66 days (AFC6) to 462 days (Figure 5.16b, Table 5.8). The cooling rates for all three simulations decrease with time (i.e. the curves are concave up in Figure 5.16b), although the change in cooling rates is most rapid for AFC6.

Total amounts of olivine and plagioclase crystallized also reflect the faster cooling rate for AFC6 compared to AFC1 and AFC7 (Figure 5.17a-c). After

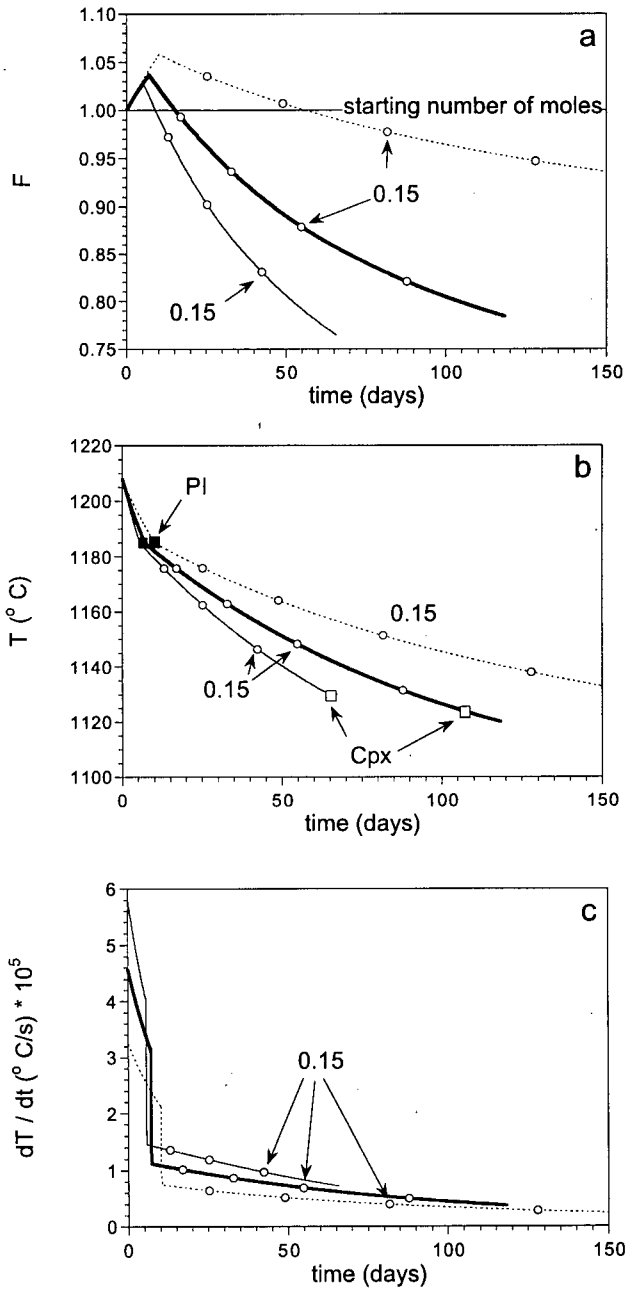

Figure 5.16. Time (days) versus a) F (moles of melt), b) T (° C), and c) cooling rate (° C s^{-1}). Predicted values are from **Petros-AFC** for a liquid of composition SC-23 and T_a = 500 ° C (bold), T_a = 200 ° C (light), and T_a = 800 ° C (dashed). Open circles denote total moles crystallized (0.05 increments).

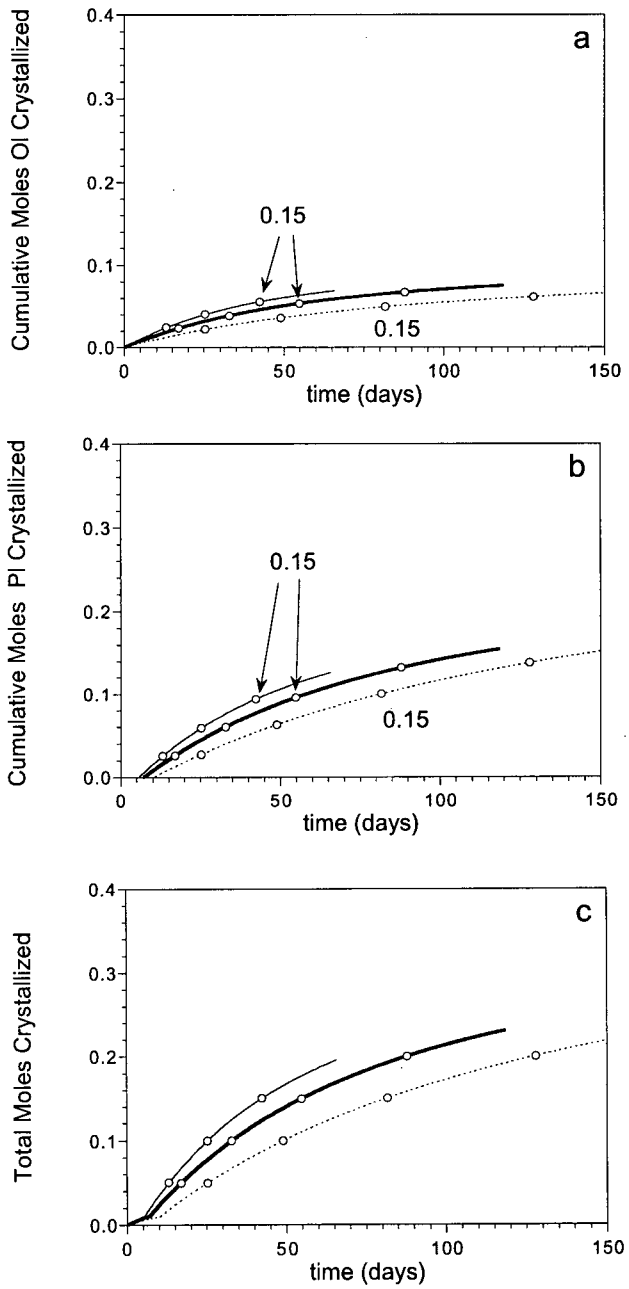

Figure 5.17. Time (days) versus a) cumulative moles of Ol crystallized, b) cumulative moles of Pl crystallized, and c) total moles crystallized (Ol + Pl). Predicted values are from **Petros-AFC** for a liquid of composition SC-23 and T_a = 500 ° C (bold), T_a = 200 ° C (light), and T_a = 800 ° C (dashed). Open circles denote total moles crystallized (0.05 increments).

25 days of assimilation-fractional crystallization AFC6 predicts twice as much Ol (0.04 moles versus 0.02 moles) and 2.5 times as much Pl crystallization (0.06 versus 0.02) as does AFC7.

The faster cooling rates result in large changes for values of **r** (Figure 5.18a) and for the instantaneous crystallization rates of Ol and Pl (Figures 5.18b and c respectively). AFC7 has maximum values of **r** that are twice that for AFC6 (2.15 versus 1.02; Table 5.8) and one and a half that for AFC1 (2.15 versus 1.36; Table 5.8). Conversely, the instantaneous crystallization rates are more than two times as great for AFC6 as for AFC7 (Figure 5.18b, Table 5.8).

Effects of varying assimilant compositions on AFC paths

A diverse range of xenoliths and xenocrysts have been found in the Iskut-Hoodoo volcanic field (Hauksdóttir 1994; Chapter 2) and throughout the rest of the Northern Cordilleran Volcanic Province. To test the effects on assimilation of some of the most common xenolithic components, two additional AFC scenarios were run to cover the range of feldspar compositions representative of the xenolithic material from the Iskut-Hoodoo volcanic field (Table 5.7). The purpose of these runs was to determine the effect of assimilating only feldspar components on predicted liquid lines of descent, cooling rates, and crystallization rates (Table 5.7). The Ab-rich plagioclase composition assimilated in AFC1 is from a plagioclase xenocryst at Little Bear mountain.

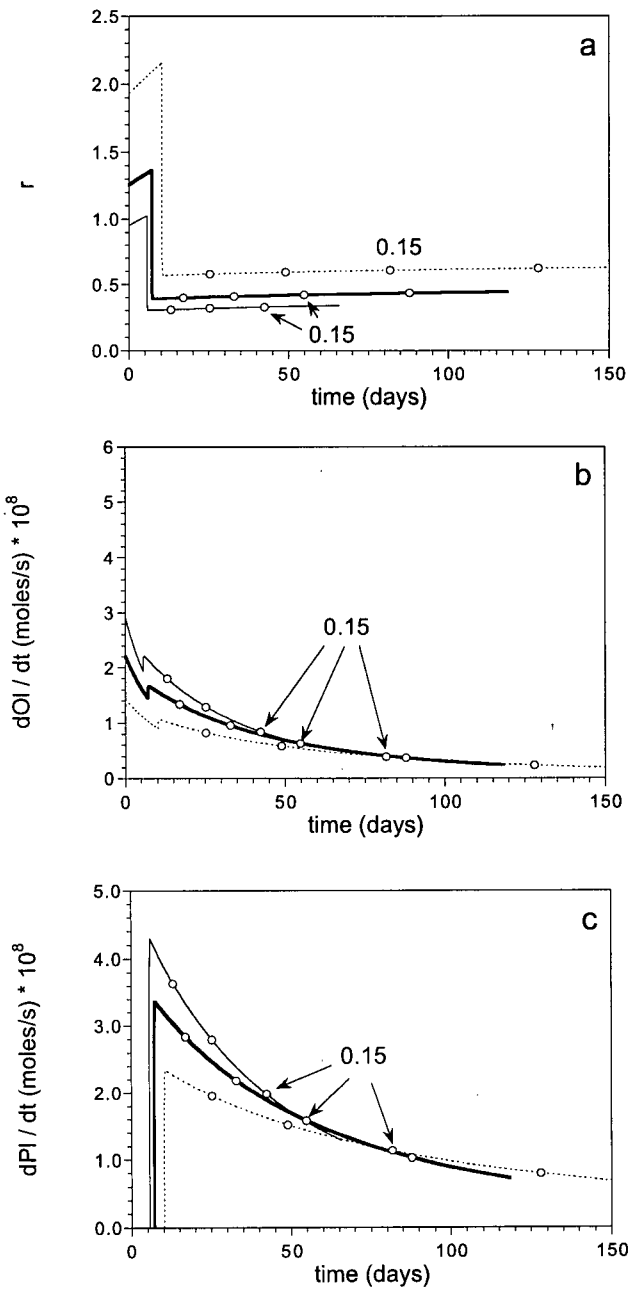

Figure 5.18. Time (days) versus a) r (moles assimilated divided by moles crystallized), b) Ol crystallization rates (moles s^{-1}), and c) Pl crystallization rates (moles s^{-1}). Predicted values are from **Petros-AFC** for a liquid of composition SC-23 and T_a = 500 ° C (bold), T_a = 200 ° C (light), and T_a = 800 ° C (dashed). Open circles denote total moles crystallized (0.05 increments).

The An-rich plagioclase composition used in AFC4 is from a xenocryst found in the Iskut River lava flows and may be a fragment of a lower crustal granulite (Nicholls et al. 1982). The feldspar composition used in AFC5 is the normative feldspar composition calculated from a bulk rock analysis of a xenolith from Little Bear mountain and is Or-rich. Figures 5.19 to 5.25 show the effects of these changes in assimilant composition for AFC processes.

Varying the composition of the assimilant subtly changes the compositions of solids crystallizing from the melt. The compositions of olivine predicted for scenarios AFC1, AFC4, and AFC5 are not very different from those predicted for FC (Figure 5.19), especially when assimilating Ab-rich plagioclase (Figure 5.19a). However, AFC of An-rich plagioclase generates a much narrower range in X_{Fo} for the same amount of total crystallization compared to FC ($Fo_{87.7}$ to $Fo_{86.0}$ versus $Fo_{87.7}$ to $Fo_{84.6}$). Assimilation-fractional crystallization of Or-rich feldspar has the opposite effect; for a comparable amount of assimilation AFC5 predicts a much broader range in X_{Fo} than FC ($Fo_{87.7}$ to $Fo_{82.4}$ versus $Fo_{87.7}$ to $Fo_{84.6}$). At temperatures below the cotectic, which are marked by breaks in slope for the curves in Figure 5.19, the concavities of the curves for AFC1 (Figure 5.19a) and AFC5 (Figure 5.19c) are opposite in direction from AFC4 and from FC. This implies that the rate of change in Ol composition becomes more sensitive to decreases in T for assimilation of Ab- and Or-rich phases.

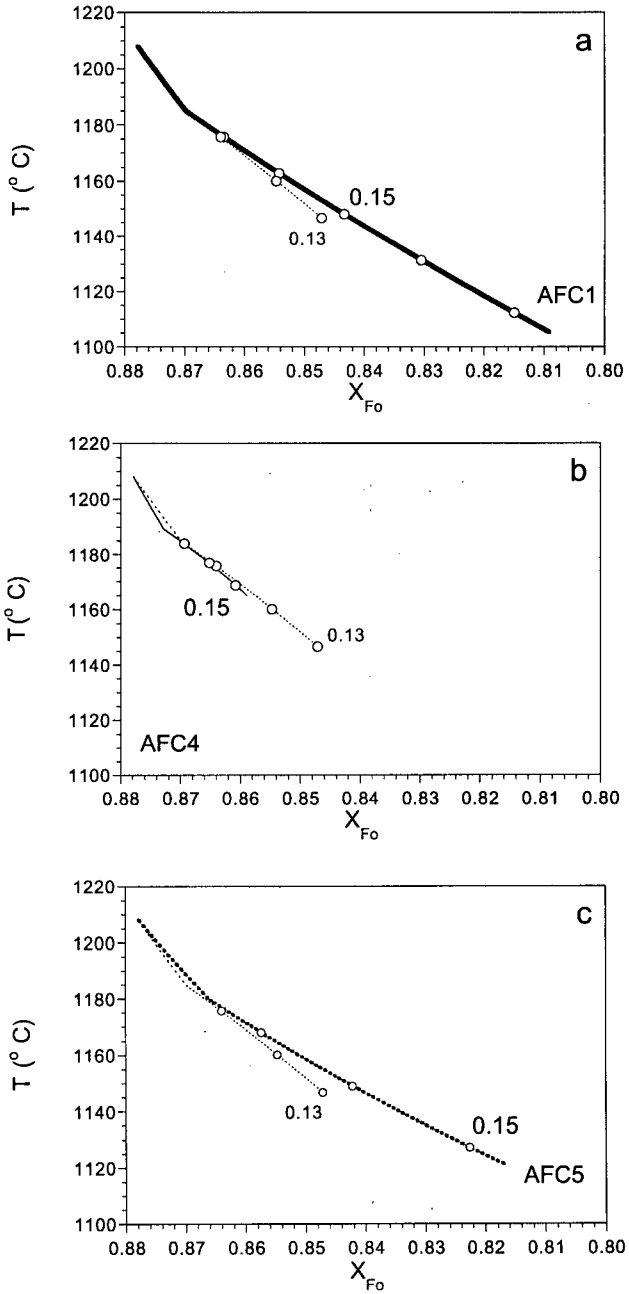

Figure 5.19. T(° C) versus X_{Fo} for a liquid of composition SC-23 and three different xenolith compositions: a) $An_{25}Ab_{67}San_{8}$ (AFC1 - bold line), b) $An_{93}Ab_{7}San_{0.04}$ (AFC4 - light line), and c) $An_{7}Ab_{55}San_{38}$ (AFC5 - bold dashes). Predicted values are from **Petros-AFC** and **Petros** (light dashes). Pressure is equal to 10^{-4} GPa. Open circles denote total moles crystallized (0.05 increments).

The composition of Pl crystallizing in the system is a more sensitive recorder of variations in assimilant composition. For scenario AFC1 the compositions of Pl become increasing more Ab-rich relative to FC for comparable amounts of crystallization (Figure 5.20a). Assimilation of An-rich Pl (AFC4) restricts the compositional range of crystallizing Pl compositions relative to the FC simulation (An_{76} to An_{72} versus An_{75} to An_{64}), increases the Ol-Pl cotectic temperature by 4 ^{o} C, and produces Pl with higher X_{An}. Assimilation of Or-rich feldspar (AFC5) has the opposite effects. It predicts a 5 ^{o} C lowering of the cotectic temperature and slightly less An-rich Pl compositions compared to FC (Figure 5.20c).

The liquid lines of descent are more sensitive to changes in assimilant compositions than the compositions of the minerals, at least for the early stages of crystallization (Figure 5.21). On Figure 5.21 all of the major changes in slope correspond to the onset of cotectic crystallization. In general, the variations in melt compositions are bracketed by scenarios AFC4 and AFC5, with AFC1 and FC falling in between for comparable amounts of crystallization.

Two trends in SiO_2 concentrations are apparent (Figures 5.21a-h). Both FC and AFC4 produce melts with progressively less SiO_2, while both AFC1 and AFC5 produce melts with progressively more SiO_2. All three of the AFC simulations produce a larger range in SiO_2 than the FC simulation (Figures 5.21a-h). The concentration of TiO_2 initially decreases slightly for the AFC

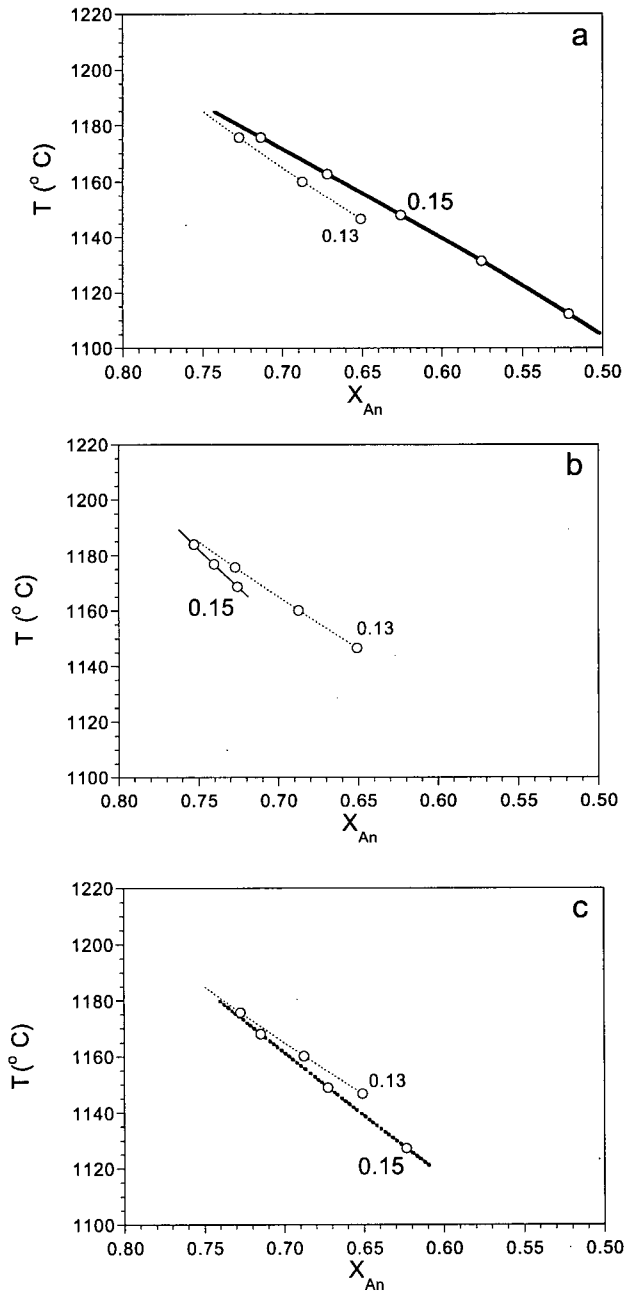

Figure 5.20. T(° C) versus X_{An} for a liquid of composition SC-23 and three different xenolith compositions: a) $An_{25}Ab_{67}San_{8}$ (AFC1 - bold line), b) $An_{93}Ab_{7}San_{0.04}$ (AFC4 - light line), and c) $An_{7}Ab_{55}San_{38}$ (AFC5 - bold dashes). Predicted values are from **Petros-AFC** and **Petros** (light dashes). Pressure is equal to 10^{-4} GPa. Open circles denote total moles crystallized (0.05 increments).

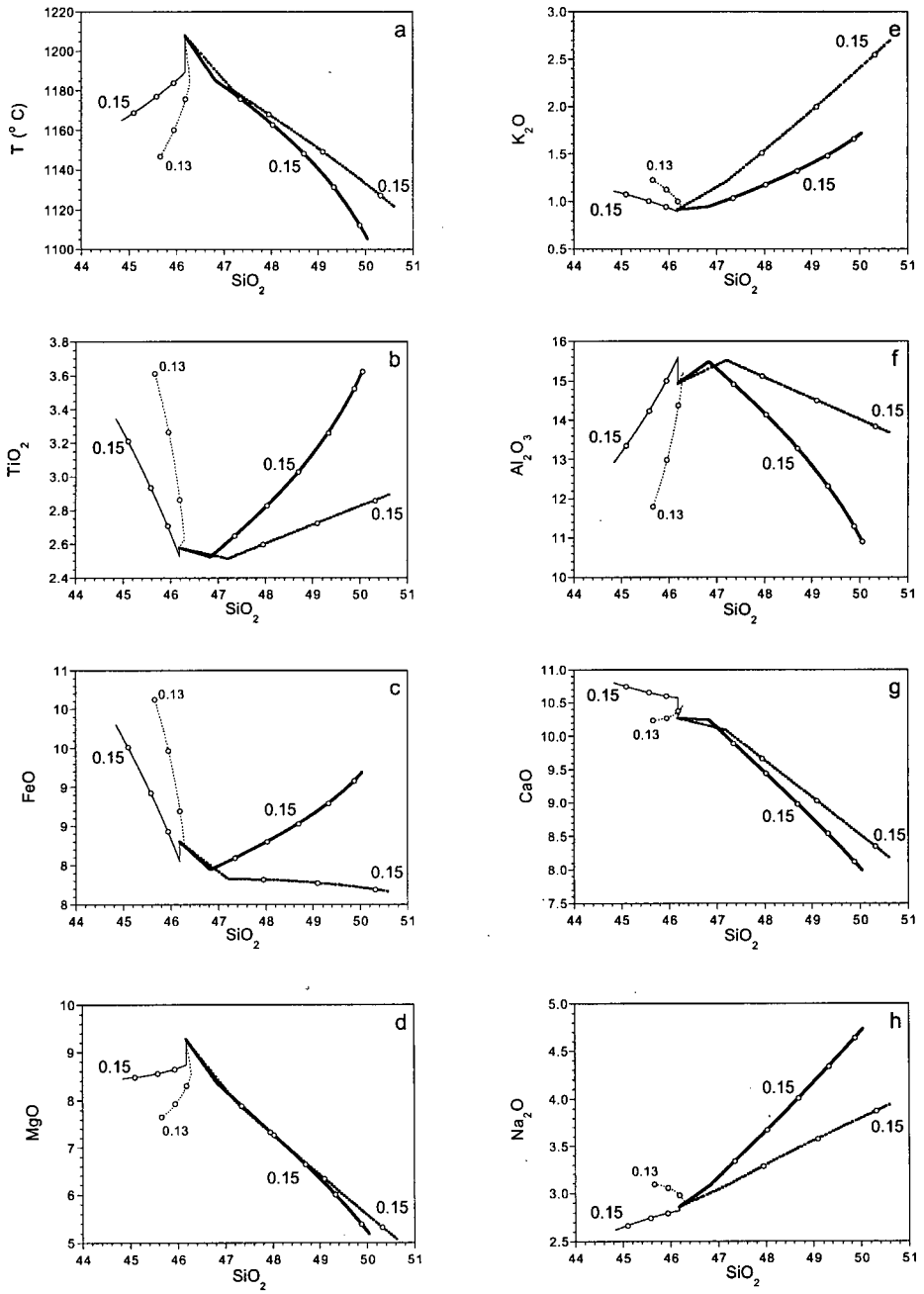

Figure 5.21. SiO_2 (wt. %) versus a) T (° C), b) TiO_2 (wt. %), c) FeO (wt. %), d) MgO (wt. %), e) K_2O (wt. %), f) Al_2O_3(wt. %), g) CaO (wt. %) and h) Na_2O (wt. %). Results are from **Petros-AFC** for a liquid of composition SC-23 and three different xenolith compositions: $An_{25}Ab_{67}San_8$ (bold line), $An_{93}Ab_7San_{0.04}$ (light line), and $An_7Ab_{55}San_{38}$ (bold dashs). Predicted values from **Petros** (light dashs) are included for comparison. Pressure is equal to 10^{-4} GPa. Open circles denote total moles crystallized (0.05 increments).

simulations, but it increases for all scenarios after the cotectic, although much less so for AFC5 than for AFC1, AFC4, or FC (Figure 5.21b). The concentrations of both FeO and MgO initially decrease when Ol is the only crystallizing phase for all simulations (Figures 5.21c and d). However, after the cotectic the FeO begins to increase for all the scenarios except for AFC5, where it remains relatively constant at the cotectic concentration. The concentration of MgO steadily decreases throughout all the of simulations, although the range of values of MgO for comparative amounts of crystallization varies from small (9.4 to 8.5 wt. % for AFC4) to large (9.4 to 5.5 wt. % for AFC5). Similarly, the concentration of K_2O has a small range for AFC4 and and large range for AFC5, where it increases threefold (0.8 to 2.5 wt. %; Figure 5.21e). The concentrations of Al_2O_3 also increase to the cotectic for all four scenarios, and then steadily decrease (Figure 5.21f). Scenario AFC5 produces the smallest range of Al_2O_3 concentrations (15 to 13.8 wt. %) and the FC scenario results in the greatest decrease of Al_2O_3. The concentrations of CaO and Na_2O do not vary much for the FC and AFC4 scenarios, but vary more for scenarios AFC1 and AFC5 (Figures 5.21g and h). The concentration of CaO steadily increases throughout the simulation for AFC4, while it remains constant or decreases for AFC1 and AFC5. Lastly, Na_2O decreases slightly in concentration for AFC4 while it increases by almost 25% for both AFC1 and AFC5.

The changes in melt composition are more broadly reflected by changes in the saturation temperatures for Ol, Pl, clinopyroxene (Cpx), and orthopyroxene (Opx) as a function of time (Figures 5.22a-c). The two most important observations from these figures are that the size and shape of the Ol crystallization field (bounded in each of the figures by the Ol and Pl lines and the ordinate) changes for each of the scenarios and that the concavity of the predicted Cpx saturation surface for AFC4 is opposite to that for AFC1 and AFC5. As in Figure 5.21, scenarios AFC4 and AFC5 bracket the extremes in chemical variation (Figures 5.22b and c). For AFC1, the system reaches the Ol-Pl cotectic after seven days and meets the subhorizontal Cpx saturation surface after 108 days of assimilation-fractional crystallization. At that point, over 20 percent of the initial moles of the system has crystallized. For AFC4 the Ol crystallization field is larger and the system reaches the cotectic in 27 days (Table 5.8). For AFC4 the Cpx saturation surface is concave up and probably would intersect the Ol-Pl cotectic after approximately 500 days. Scenario AFC5 takes 4.5 days to reach the cotectic but only 35 days to reach the Cpx saturation surface.

The values of F (moles of melt remaining) are also sensitive to the composition of the assimilant (Figure 5.23a). The values of F decrease most slowly for AFC4, where after 76 days of reaction the amount of melt is the same as at the start of the simulation, and only 2% of the initial moles of

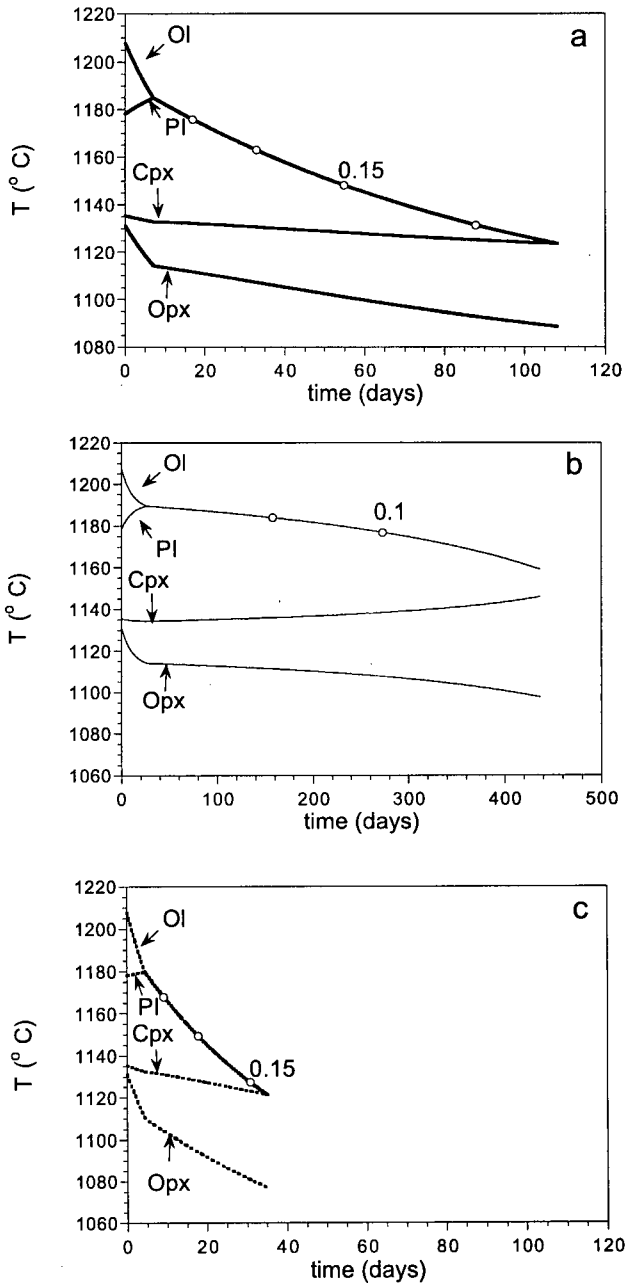

Figure 5.22. Time (days) versus T (° C) for three different xenolith compositions: a) $An_{25}Ab_{67}San_{8}$ (AFC1 - bold line), b) $An_{93}Ab_{7}San_{0.04}$ (AFC4 - light line), and c) $An_{7}Ab_{55}San_{38}$ (AFC5 - bold dashes). Labelled lines indicate predicted values of T_{sat} for Ol, Pl, Cpx, and Opx using a liquid of composition SC-23. Pressure is equal to 10^{-4} GPa. Open circles denote total moles crystallized (0.05 increments). Note longer time-scale in b).

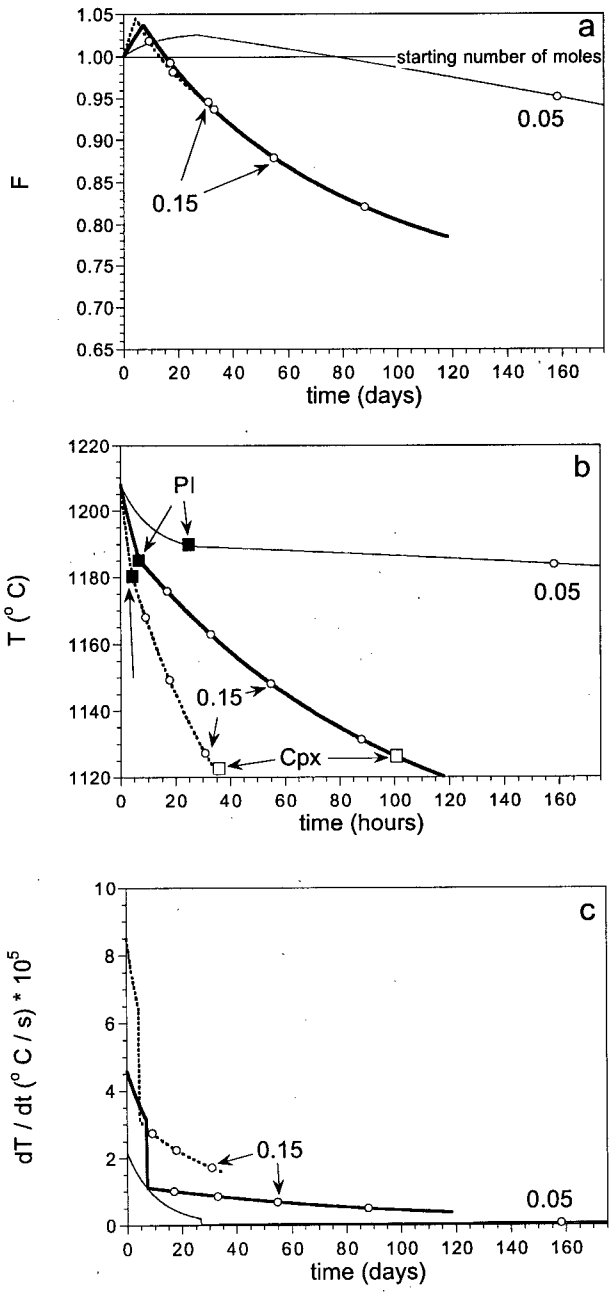

Figure 5.23. Time (days) versus a) F (moles of melt), b) T (° C), and c) cooling rate (° C s^{-1}). Plots show results from **Petros-AFC** for a liquid of composition SC-23 and three different xenolith compositions: $An_{25}Ab_{67}San_8$ (bold), $An_{93}Ab_7San_{0.04}$ (light), and $An_7Ab_{55}San_{38}$ (bold dashs). Pressure is equal to 10^{-4} GPa. Open circles denote total moles crystallized (0.05 increments).

melt have crystallized (Figure 5.23a). After the same amount of time, the moles of melt has decreased to 0.83 for AFC1; AFC4 is well below the Cpx saturation surface at that time.

The maximum cooling rate for the three AFC scenarios decreases 100 % after the cotectic (Figure 5.23c; Table 5.8) . However, scenario AFC5 has the fastest overall cooling rate (Figure 5.23b). After 30 days, the temperature of the system for scenario AFC5 is 1126 $^{\circ}$ C, compared to 1165 $^{\circ}$ C for AFC1 and 1190 $^{\circ}$ C for AFC4. The instantaneous cooling rate for Ol crystallization is always fastest for AFC5 and slowest for AFC4 (Figure 5.23c; Table 5.8). At the cotectic, the cooling rate for AFC4 drops from 0.000025 to <0.000005 $^{\circ}$ C s^{-1}, while that for AFC5 drops from 0.000065 to 0.00003 $^{\circ}$ C s^{-1}.

The cumulative crystallization rates for AFC1, AFC4, and AFC5 vary the most for Pl and the least for Ol (Figure 5.24). Total amounts of Ol crystallized are much less for AFC4 (<0.02 moles) than for either AFC1 or AFC5 (Figure 5.24a), with twice as much Ol crystallization in scenario AFC5 as in AFC1. For a given amount of time, seven times as much Pl crystallizes in AFC1 and AFC5 as in AFC4 (Figure 5.24b). The total amounts crystallized are dominated by plagioclase crystallization after 30 days for AFC1 and 160 days for AFC4, but AFC5 crystallizes subequal amounts of Ol and Pl for the first 35 days of assimilation-fractional crystallization (Figures 5.24a and b). Overall scenario AFC5 has the highest cumulative crystallization rate (Figure 5.24c).

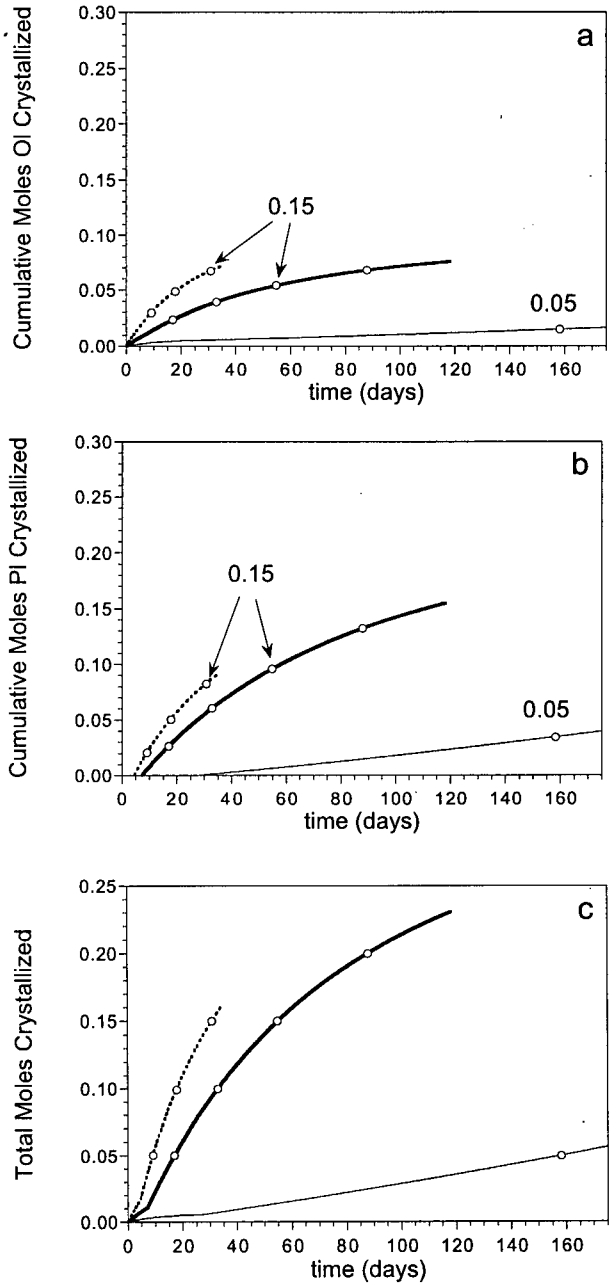

Figure 5.24. Time (days) versus a) cumulative moles of Ol crystallized, b) cumulative moles of Pl crystallized, and c) total moles crystallized (Ol + Pl). Plots show results from **Petros-AFC** for a liquid of composition SC-23 and three different xenolith compositions: $An_{25}Ab_{67}San_{8}$ (bold), $An_{93}Ab_{7}San_{0.04}$ (light), and $An_{7}Ab_{55}San_{38}$ (bold dashs). Open circles denote total moles crystallized (0.05 increments).

The values of **r** and instantaneous crystallization rates are broadly similar to the cooling rates and are sensitive to the composition of the assimilant (Figure 5.25). Scenario AFC4 has the highest value of **r** of the three scenarios (1.9), which is almost twice that for AFC5 (1.2) and 1.5 times that for AFC1. However, after reaching the cotectic, the ordering of values of **r** reverses, and AFC4 reverts to having the lowest value of the three scenarios (0.32 versus 0.39 for AFC1 and 0.45 for AFC5; Figure 5.25a and Table 5.8). The Ol crystallization rates for AFC5 at least five times those for AFC4 and over twice that of AFC1 before the cotectic (Figure 5.25b, Table 5.8). The Ol crystallization rates for AFC5 and AFC1 are decay to similar values after 35 days, although at that point the rate for AFC5 is still decreases rapidly. The maximum Pl crystallization rates for AFC4 are also nearly ten times smaller than those of AFC5 ($0.05 \cdot 10^{-8}$ versus $5.6 \cdot 10^{-8}$ moles s^{-1}) at the cotectic and are much less than those for AFC1 as well ($3.4 \cdot 10^{-8}$ moles s^{-1}).

5.4. DISCUSSION

Relative effects of P, T_a, and assimilant composition

Table 5.8 is a summary of data taken from Figures 5.11 to 5.25 and comprises results for all seven of the AFC scenarios investigated. Data given in Table 5.8 include: liquidus temperature (T_L), temperature of the cotectic (T_{cot}), the difference between T_L and T_{cot} (ΔT_{cot}), the amount of time elapsed before the

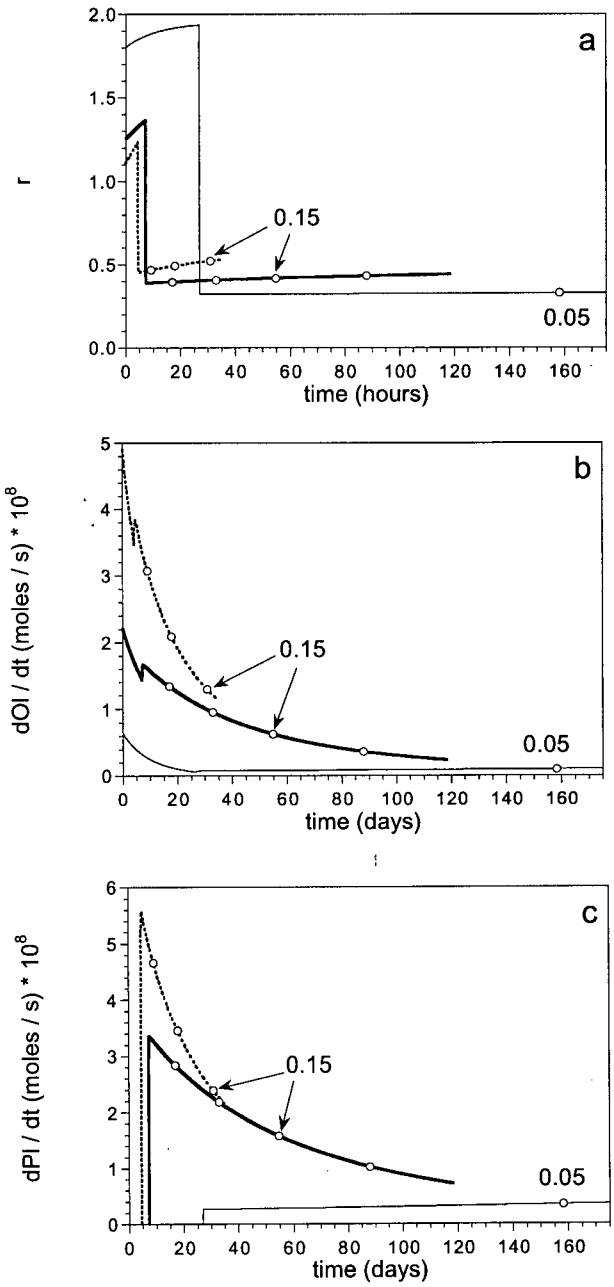

Figure 5.25. Time (days) versus a) r (moles assimilated divided by moles crystallized), b) Ol crystallization rate (moles s^{-1}), and c) Pl crystallization rate (moles s^{-1}). Plots show results from **Petros-AFC** for a liquid of composition SC-23 and three different xenolith compositions: $An_{25}Ab_{67}San_{8}$ (bold), $An_{93}Ab_{7}San_{0.04}$ (light), and $An_{7}Ab_{55}San_{38}$ (bold dashs). Pressure is equal to 10^{-4} GPa. Open circles denote total moles crystallized (0.05 increments).

Table 5.8. Summary of temperatures, cooling rates, crystallization rates, and r-values for AFC scenarios.

	AFC1	AFC2	AFC3	AFC4	AFC5	AFC6	AFC7
T_L (° C)	1208	1216	1244	1208	1208	1208	1208
T_{cot} (° C)	1185	1192	1217	1189	1180	1185	1185
ΔT_{cot} (° C)	23.24	23.18	27.12	18.78	28.40	23.32	23.19
Δt_{cot} (hr)	2.01	1.98	2.20	1.47	2.56	1.22	4.67
T_{cpx} (° C)	1123	1142	1208	<1164	1121	1129	1102
ΔT_{cpx} (° C)	84.68	73.37	35.83		86.76	78.84	106.0
Δt_{cpx} (hr)	15.04	12.93	4.47	>9.61	13.18	7.86	55.73
$(dT/dt)_{max} \cdot 10^3$	3.35	3.40	3.59	3.69	3.24	5.48	1.49
$(dT/dt)_{min} \cdot 10^3$	1.11	1.10	1.03	0.68	1.43	1.88	0.42
r_{max}	1.36	1.36	1.34	1.94	1.23	1.02	2.15
r_{min}	0.39	0.38	0.36	0.32	0.45	0.30	0.57
$(dOl/dt)_{max} \cdot 10^6$	1.66	1.67	1.72	1.10	1.87	2.87	0.66
$(dOl/dt)_{min} \cdot 10^6$	1.01	1.11	1.54	0.99	1.14	1.95	0.24
$(dPl/dt)_{max} \cdot 10^6$	3.35	3.45	3.82	4.58	2.58	5.55	1.43
$(dPl/dt)_{min} \cdot 10^6$	2.96	2.60	3.77	4.13	1.77	5.00	1.14

melt reaches the cotectic (Δt_{cot}), the temperature of Cpx saturation (T_{cpx}), the difference between T_L and T_{cpx} (ΔT_{cpx}), the amount of time elapsed before the melt reaches T_{cpx} (Δt_{cpx}), the maximum and minimum cooling rates (dT/dt_{max} and dT/dt_{min}), the maximum and minimum values of r, the maximum and minimum instantaneous Ol crystallization rates (dOl/dt_{max} and dOl/dt_{min}), and the maximum and minimum instantaneous Pl crystallization rates (dPl/dt_{max} and dPl/dt_{min}). The values of Δt_{cpx} and Δt_{cpx} are in units of hours, the cooling rates are in units of $^{o}C\ s^{-1} \bullet 10^{5}$, and the crystallization rates are in units of moles $s^{-1} \bullet 10^{8}$.

Comparison of the results from the seven AFC scenarios leads to several generalizations. Variations in P mainly affect the sequence of crystallization and have comparatively small effects on the cooling and crystallization rates (Table 5.8). However, variations in T_a and assimilant composition strongly affect AFC paths. Variations in T_a produce the smallest changes in both crystallization rates and cooling rates, with cooling rates varying by an order of magnitude over the range of T_a's investigated (0.0000577 versus 0.0000043 $^{o}C\ s^{-1}$; Table 5.8). Relative to AFC1, assimilation of An-rich plagioclase has similarities both to increasing T_a and at the same time to decreasing T_a. For example, as with increasing T_a assimilation of An-rich plagioclase causes an decrease in the maximum cooling rate and a decrease in the minimum value of **r**. However, it also causes a decrease in Pl

crystallization rate in the minimum cooling rate, and increase in $\mathbf{r}_{max}$, and a decrease in the Ol crystallization rate just as increasing T_a does. Assimilation of alkali feldspar has exactly the opposite effects.

Thus, variations in P, T_a, and assimilant composition can operate together to enhance assimilation or to retard assimilation. Two examples illustrate the potential for complex interplay between changes in P, T_a, and assimilant composition. First consider a melt of composition SC-23 at high P undergoing AFC of An-rich Pl with a high T_a (i.e., close to the T of the magma). The effect of higher P is to promote Cpx crystallization. However, the effect of a high T_a is to postpone Cpx crystallization. In contrast, the high T_a and An-rich assimilant both promote lower cooling rates, lower Pl crystallization rates, higher values of **r**, and lower Ol crystallization rates; high P has little effect on these values. The resulting AFC path is one where lots of assimilation can occur with moderate amounts of crystallization. The potential suppression of Cpx crystallization could mask the high P assimilation-fractional crystallization history of the magma that would be preserved in a derivative rock sample.

The second example is for AFC of an Or-rich assimilant at low P with a low T_a. Although low P favors crystallization of Ol and Pl over Cpx, the Or-rich assimilant and low T_a both tend to drive the system towards Cpx saturation. Both the cooling rates and the Ol crystallization rates are relatively fast for the Or-rich assimilant and low T_a. However, the maximum values of **r** would be low

and the minimum values of **r** would be intermediate compared to the other scenarios. The end result would be a porphyritic rock that is moderately contaminated, with phenocrysts of Ol, Pl, and Cpx. This would make the rock look like the product of higher P crystallization.

Implications for assimilation in the southern NCVP

Scenarios AFC1-7 were designed to simulate potential AFC paths relevant to the Iskut-Hoodoo volcanic centres. The model paths are shown on an AFM diagram in Figure 5.26 along with data from Hauksdóttir (1994) for the eight Iskut-Unuk rivers centres and from Chapter 2 for Little Bear Mountain. In Figure 5.26, all of the predicted AFC paths start at the composition of SC-23 (large diamond), which is the best candidate for a parental magma from all of the Iskut-Unuk-Hoodoo centres.

The liquid lines of descent from the AFC models reproduce some to the chemical variation found among the Iskut centres (Figure 5.26). The trend for fractional crystallization (FC) and for AFC4 both are too steep to intersect any of the sampled lava compositions. However, all of the other AFC scenarios pass through at least some of the lava datapoints. The effect of increasing P slightly steepens the slopes of the model paths producing a slight Fe enrichment

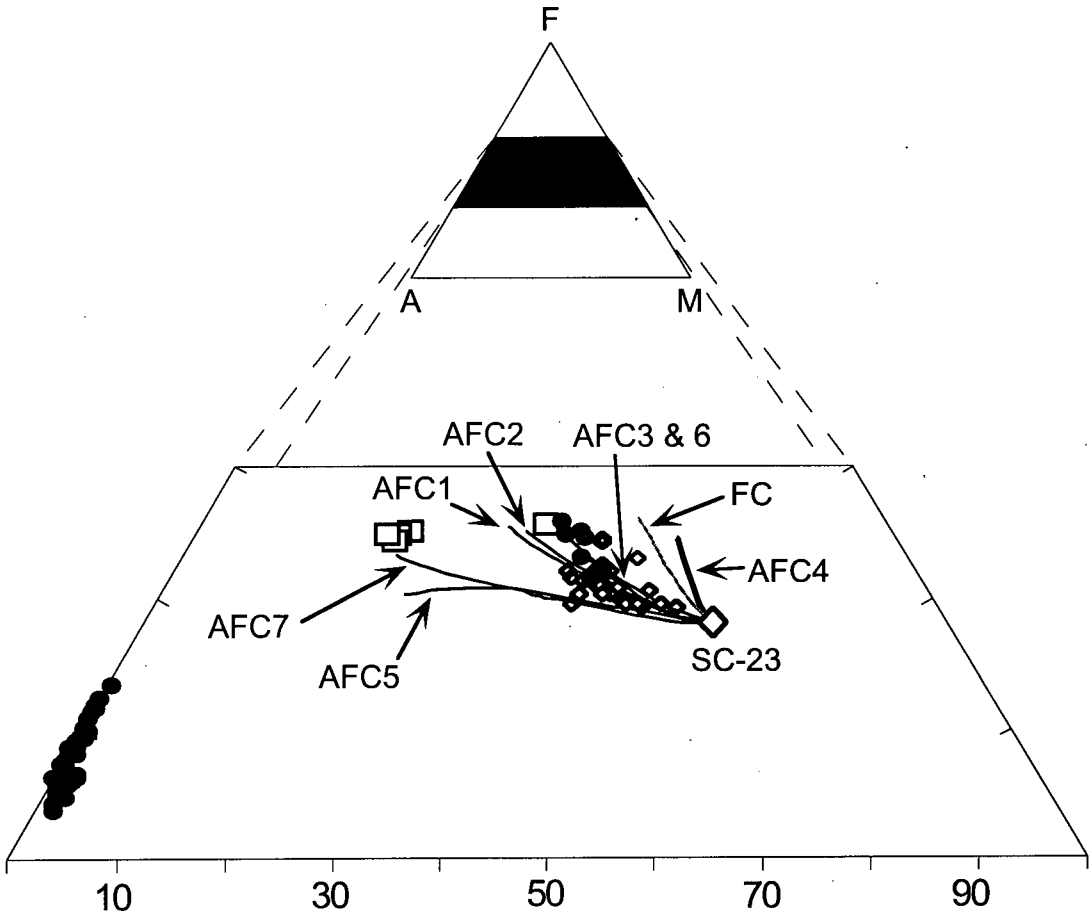

Figure 5.26. AFM (A = $Na_2O + K_2O$, F = FeO, M = MgO) diagram for AFC scenarios 1 to 7 (labelled lines). Data for Cinder Mountain (squares), the other Iskut-Unuk centres (diamonds), the HMVC (filled circles), and SC-23 are shown for comparison.

trend. Decreasing T_a from 500 ° C to 200 ° C has a similar effect. Scenarios AFC1-3,6 all produce liquid lines of descent that are consistent with deriving the sampled lavas from all of the Iskut centres from SC-23 by AFC processes. The hawaiites from Cinder Mountain (open squares) could be produced by AFC when the T_a is high (800 ° C).

One of the significant general observations pertaining to the production of phonolites from Hoodoo Mountain is that AFC of either Na-rich or Or-rich feldspar drives the liquid lines of descent rapidly towards enrichment in Na_2O and K_2O (e.g., Figures 2.28 and 5.21). This makes producing the HMVC phonolites and trachytes from a basaltic parental magma much more tractable than FC, which would require much larger degrees of fractionation to produce such evolved compositions.

AFC rates and rates of other petrological processes

The main difference between the new AFC paradigm and existing models is the incorporation of time. Why is this important? Figure 5.27a shows the relative timescales for various petrologic rates as well as for predicted crystallization and cooling rates for scenarios AFC1-7. All the rates are normalized to a common length scale (1 cm or 1 cm^2). Kinematic viscocities are calculated using silicate melt viscocities from Scarfe (1973, 1986) and silicate melt densities from Scarfe (1986). Growth rates are taken from Table 4

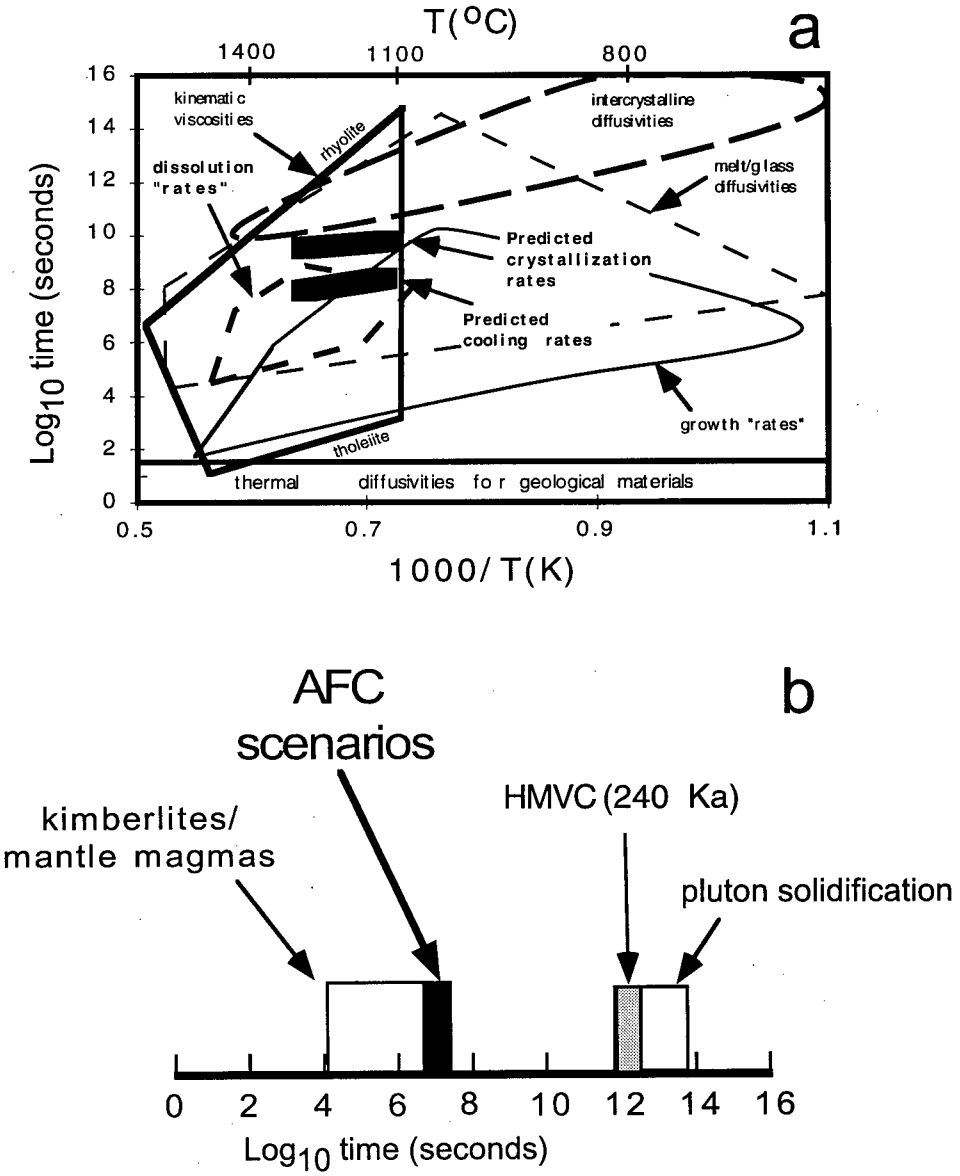

Figure 5.27. Logarithm$_{10}$ of time (seconds) for various important petrological rates (a) and several important petrological processes (b). In a) the rates are plotted against 1000/T(K). In b) the time-scales for a variety of igneous processes including pluton solidification, the timespan for the development of the HMVC, and transport of kimberlitic and other mafic magmas are compared to that for the AFC scenarios discussed above

of Cashman (1990). Solid, melt, and glass diffusivities are from a literature summary by Freer (1981) and from Dunn (1986). Rates for mineral dissolution are from data summarized in Chapter Two. The predicted crystallization rates are slower than crystal growth rates measured by other researchers (cf. Cashman 1990). Figure 5.27b shows ranges of timescales of several important magmatic processes including: pluton solidification, transport rates for kimberlites and other mantle derived magmas, and the timescale of the development of the Hoodoo Mountain volcanic complex (Chapter Two).

The rates of assimilation and crystallization predicted by **Petros-AFC** would not be important on the timescale of extremely rapid magma transport from the mantle. Mantle-derived magmas that reach the surface carrying mantle xenoliths must have traveled at rates of 0.1 to 30 km hr^{-1} (Spera 1984; Eggler 1986). Depending on the depth of origin of the magmas (e.g., 300 km or 100 km), transport times range from a maximum of approximately 125 days to a minimum of three hours. All of the AFC scenarios investigated reach the Ol-Pl cotectic in 30 days or less. This suggests that even during transport of mantle-derived magmas at intermediate to slow rates, AFC processes can play an important role. Indeed, over the timescale of the evolution of the HMVC or the solidification of a pluton (~200 to 500 Ka; Bowers et al. 1990), the AFC processes have sufficient time to operate.

5.5. CONCLUSIONS

The newly developed model for AFC processes (**Petros-AFC**) provides the means of investigating the temporal consequences of isenthalpic assimilation-fractional crystallization. The model shows how cooling rates, crystallization rates, and values of **r** will change as a function of time. The paths also are consistent with field observations from the southern NCVP that magmatic assimilation is important in this area. Finally, the timescales of cooling and crystallization implied by the model are consistent with AFC processes being important on the timescale of many igneous processes.

CHAPTER 6

Summary

The main purpose of this thesis was to develop new, quantitative insights into the process of magmatic assimilation. The thesis presents the first calculational model that combines kinetic and thermodynamic constraints on assimilation processes. The model is applied to volcanic rocks from the Northern Cordilleran Volcanic Province (NCVP), where the importance of magmatic assimilation is well documented (Chapter One). The results of these models show for the first time the temporal evolution of a magmatic system undergoing AFC processes.

The thesis also makes several broader contributions to the fields of igneous petrology, physical volcanology, and Cordilleran geology. Chapter One defines a new volcanic province, the Northern Cordilleran Volcanic Province (NCVP). The NCVP supplants the ill-defined "Stikine Volcanic Belt" as a more appropriate nomenclature for the Neogene to Recent volcanism in northern British Columbia and the Yukon. The chapter also provides the most comprehensive summary of the ages, petrology, and volcanology for this region of magmatism, and ends by presenting evidence for the widespread influence of magmatic assimilation throughout the NCVP.

Chapter Two documents the importance of assimilation at one of the largest volcanic complexes in the NCVP, the Hoodoo Mountain volcanic complex. The chapter also provides the first detailed stratigraphy, petrography, geochemistry, and geology for the HMVC. This centre is one of the last major, Quaternary, unstudied volcanic complexes in the northern Canadian Cordillera. The descriptive petrology shows that the complex is dominated by subaerial and subglacial, peralkaline phonolites and trachytes (Hoodoo Mountain volcano) with subordinate alkali olivine basalt (Little Bear Mountain volcano). The basalts contain abundant xenocrysts and the variations in their major element geochemistry cannot be explained by closed system processes. The petrography and geochemistry together strongly support the role of AFC processes.

Thermodynamic and kinetic constraints on the process of magmatic assimilation are reviewed in Chapters Three and Four. A comprehensive review of published experiments leads to the development of a new model for predicting rates of mineral dissolution in mafic silicate melts (Chapter Three). The new model was combined with pre-existing thermodynamic datasets (e.g., Ghiorso & Sack 1995 and Berman 1988) to produce a algorithm to simulate isobaric, isenthalpic assimilation-fractional crystallization. The new algorithm formed the basis for a computer code written in ANSI C (Petros-AFC); the code predicts the temporal evolution of a magma for specific AFC scenarios. The

predicted cooling and crystallization rates for simulations constrained by observations from the Iskut volcanic field demonstrate that the timescales for magmatic assimilation are similar to those for slow rates of magma transport (~0.1 km hr^{-1}) and are smaller (e.g., faster) than the timescale of development of the HMVC or timescales for the solidification of plutons.

REFERENCES

Aagaard, P. and Helegeson, H.C. 1982. Thermodynamic and kinetic constraints on reactions rates among minerals and aqueous solutions. I. theoretical considerations. *American Journal of Science*, Vol. 282: 237-285.

Aitken, J.D. 1959. Atlin, British Columbia, Geological Survey of Canada Memoir 307, 89p.

Allen, C. 1991. Tuya Butte. in *Volcanoes of North America*, C.A. Wood and J. Kienle (eds.). Cambridge University Press: New York: 119-120.

Allen, C.C., Jercinovic, M.J. and Allen, J.S.B. 1982. Subglacial volcanism in north-central British Columbia and Iceland. *Journal of Geology*, Vol. 90: 699-715.

Al-Rawi, Y. and Carmichael, I.S.E. 1967. A note on the natural fusion of granite. *American Mineralogist*, Vol. 52: 1806-1814.

Anderson, A.T. 1984. Probable relations between plagioclase zoning and magma dynamics, Fuego volcano, Guatemala. *American Mineralogist*, Vol. 69: 660-676.

Anderson, R.G. 1993. A Mesozoic stratigraphic and plutonic framework for northwestern Stikinia (Iskut River area), northwestern British Columbia,

Canada in *Mesozoic Paleogeography of the Western United States--II*, G. Dunne and K. McDougall, (eds.), Society of Economic Palaeontologists and Mineralogists, Pacific Section, Vol. 71: 477-494.

Anonymous. 1899. An active volcano. *The Klondike Nugget*, January 28: 4 p.

Barker, D.S. 1996. Nephelinite-phonolite volcanism. in *Undersaturated alkaline rocks: mineralogy, petrogenesis, and economic potential*, R.H. Mitchell (ed.). Mineralogical Association of Canada Short Course Series, Vol. 24: 23-44.

BC-Hydro. 1985. Stikine-Iskut development, Iskut Canyon and More Creek Projects, 1982-1984. *Geotechnical Investigations*, Main Report, Vol. 1, Report No. H1614. BC-Hydro Information Centre.

Berman, R.G. 1988. Internally-consistent thermodynamic data for minerals in the system Na_2O-K_2O-CaO-MgO-FeO-Fe_2O_3-Al_2O_3-SiO_2-TiO_2-H_2O-CO_2. *Journal of Petrology,* Vol. 29: 445-522.

Bevier, M.L. 1992. A dominant asthenospheric mantle source for Late Miocene-Quaternary volcanic rocks, Stikine Volcanic Belt, British Columbia and Yukon Territory, Canada. EOS (American Geophysical Union Transactions), Spring Meeting Supplement, Vol. 73: 334.

Blichert-Toft, J., Lesher, C.E., and Rosing, M.T. 1992. Selectively contaminated magmas of the Tertiary East Greenland macrodike complex. *Contributions to Mineralogy and Petrology,* Vol. 110: 154-172.

Bloodgood, M.A. and Bellefontaine, K.A. 1990. The geology of the Atlin area (Dixie Lake and Teresa Island) (104N/6 and parts of 104N/5 and 12) in *Geological Fieldwork 1989*, British Columbia Ministry of Energy, Mines, and Petroleum Resources, Paper 1990-1: 205-215.

Bostock, H.S. 1936. Carmacks District, Yukon. Geological Survey of Canada Memoir 189: 67p.

Bowen, N.L. 1922. The behavior of inclusions in igneous magmas. *Journal of Geology,* Vol. 30: 513-570.

Bowen, N.L. 1928. *The evolution of the igneous rocks.* Dover Press: 332p.

Bowers, J.R., Kerrick, D.M. and Furlong, K.P. 1990. Conduction model for the thermal evolution of the Cupsuptic aureole, Maine. *American Journal of Science*, Vol. 290: 644-665.

Brearley, M. and Scarfe, C.M. 1986. Dissolution rates of upper mantle minerals in an alkali basalt melt at high pressure: an experimental study and implications of ultramafic xenolith survival. *Journal of Petrology,* Vol. 27: 1157-1182.

Bultman, T.R. 1979. Geology and tectonic history of the Whitehorse trough west of Atlin, British Columbia; Ph.D. thesis, Yale University, New Haven, Connecticut: 296p.

Carignan, J., Ludden, J. and Francis, D. 1994. Isotopic characteristics of mantle sources for Quaternary continental alkaline magmas in the northern

Canadian Cordillera. *Earth and Planetary Science Letters,* Vol. 128: 271-286.

Carignan, J., Ludden, J., and Francis, D. 1995. Asthenosphere-lithosphere interaction during the formation of continental alkaline basalts in the northern Canadian Cordillera. EOS, Transactions, Fall 1995, F587.

Carignan, J., Ludden, J., and Francis, D. 1996. On the recent enrichment of subcontinental lithosphere: A detailed U-Pb study of spinel lherzolite xenoliths, Yukon, Canada. *Geochemica et Cosmochimica Acta*, Vol. 60: 4241-4252.

Carmichael, I.S.E. 1964. The petrology of Thingmuli, a Tertiary volcano in eastern Iceland. *Journal of Petrology*, Vol. 5: 435-460.

Carmichael, I.S.E. and Ghiorso, M.S. 1990. The effect of oxygen fugacity on the redox state of natural liquids and their crystallizing phases in *Modern methods of igneous petrology: understanding magmatic processes*, J. Nicholls and J.K. Russell (eds.). Reviews in Mineralogy, Vol. 24: 191-212.

Carmichael, I.S.E., Nicholls, J., and Smith, A.L. 1970. Silica activity in igneous rocks. *American Mineralogist* , Vol. 55: 246-263.

Casey, J.J. 1980. Geology of the Heart Peaks Volcanic Centre, Northwestern British Columbia; unpub. M.S. thesis, The University of Alberta, Edmonton: 116p.

Casey, J.J., and Scarfe, C.M. 1980. Summary of the petrology of the Heart Peaks volcanic centre, northwestern British Columbia in *Current Research, Part A*, Geolgoical Survey of Canada, 80-1A: 356.

Cashman, K.V. 1990. Textural constraints on the kinetics of crystallization of igneous rocks. in *Modern methods of igneous petrology: understanding magmatic processes*, J. Nicholls and J.K. Russell (eds.). Reviews in Mineralogy, Vol. 24: 259-314.

Clague, J.J. 1991. Quaternary glaciation and sedimentation; Chapter 12 in *Geology of the Cordilleran Orogen in Canada*, H. Gabrielse and C.J. Yorath (eds.). Geological Survey of Canada, Geology of Canada, No. 4: 419-434.

Clark, A.H., Pearce, T.H., Roeder, P.L. and Wolfson, I. 1986. Oscillatory zoning and other microstructures in magmatic olivine and augite: Normarski interference contrast observations on etched polished surfaces. *American Mineralogist*, Vol. 71: 734-741.

Cohen, R.S., Evensen, N.M., Hamilton, P.J., and O'Nions, R.K. 1980. U-Pb, Sm-Nd and Rb-Sr systematics of mid-oceanic ridge basalt glasses. *Nature*, Vol. 283: 149-153.

Cohen, R.S., and O'Nions, R.K. 1982. The lead, neodymium and strontium isotopic structure of ocean ridge basalts. *Journal of Petrology,* Vol. 23: 299-324.

Cooper, A.R. and Kingery, W.D. 1964. Dissolution in ceramic systems: I. molecular diffusion, natural convection, and forced convection studies of sapphire dissolution in calcium aluminum silicate. *American Ceramic Society Journal*, Vol. 47: 37-43.

Cousens, B.L. and Bevier, M.L. 1995. Discerning asthenospheric, lithospheric and crustal influences on the geochemistry of Quaternary basalts from the Iskut-Unuk rivers area, northwestern British Columbia. *Canadian Journal of Earth Science*, Vol. 32;9: 1451-1461.

De P. Watson, K. and Mathews, W.H. 1948. Partly vitrified xenoliths in pillow basalt. *American Journal of Science,* Vol. 246: 601-614.

DePaolo, D.J., and Wasserburg, G.J. 1976. Nd isotopic variations and petrogenetic models. *Geophysical Research Letters*, Vol. 3: 249-252.

Doe, B.R., Lipman, P.W., Hedge, C.E. and Kurasawa, H. 1969. Primitive and contaminated basalts from the southern Rocky Mountains, U.S.A. *Contributions to Mineralogy and Petrology,* Vol. 21: 142-156.

Donaldson, C.H. 1985. The rates of dissolution of olivine, plagioclase and quartz in a basalt melt. *Mineralogical Magazine,* Vol. 69: 683-693.

Donaldson, C.H. 1990. Forsterite dissolution in superheated basaltic, andesitic and rhyolitic melts. *Mineralogical Magazine*, Vol. 54: 67-74.

Dunn, T. 1986. Diffusion in silicate melts: an introduction and literature review. in *Silicate Melts: their properties and structures applied to problems in*

geochemistry, petrology, economic geology, and planetary geology, C.M. Scarfe (ed.). Mineralogical Association of Canada Short Course Series, Vol. 12: 57-92.

Edwards, B.R., Anderson, R.G., and Russell, J.K. 1997. Geology of the Quaternary Hoodoo Mountain Volcanic Complex and adjacent Paleozoic and Mesozoic basement rocks, parts of Hoodoo Mountain (NTS 104B/14) and Craig River (NTS 104B/11) map areas, northwestern British Columbia. Geological Survey of Canada, Open File 3321.

Edwards, B.R., Edwards, G. and Russell, J.K. 1995. Revised stratigraphy for the Hoodoo Mountain volcanic centre, northwestern British Columbia in *Current Research, Part A;* Geological Survey of Canada, Paper 95-A: 105-115.

Edwards, B.R., Hamilton, T.S., Nicholls, J., Stout, M.Z., Russell, J.K., and Simpson, K. 1996. Late Tertiary to Quaternary volcanism in the Atlin area, northwestern British Columbia in *Current Research Part A*; Geological Survey of Canada, Paper 96-1A: 29-36.

Edwards, B.R. and Russell, J.K. 1994a. Preliminary stratigraphy of Hoodoo Mountain volcano, northwestern British Columbia in *Current Research Part A*; Geological Survey of Canada, Paper 94-1A: 69-76.

Edwards, B.R., and Russell, J.K. 1994b. Preliminary stratigraphy, petrography and melt compositions of volcanic rocks from Hoodoo Mountain,

northwestern British Columbia, Canada. GAC-MAC 1994 Annual Meeting, Waterloo 19: 32.

Edwards, B.R. and Russell, J.K. 1996. An overview of the nature, distribution and tectonic significance of xenoliths from the Stikine Volcanic Belt, northern Cordillera in 1996 Slave-Northern Cordillera Lithospheric Evolution (SNORCLE) Transect and Cordilleran Tectonics Workshop Meeting (March 1-3), F. Cook and P. Erdmer (compilers), University of Calgary, Lithoprobe Report No. 50: 96-107.

Edwards, B.R. and Russell, J.K. 1996. A review and analysis of mineral dissolution rates in naturally occurring silicate melts. *Chemical Geology.* Vol. 1130: 233-245.

Eiché, G.E. 1986. Petrogenesis of the basalts of the Alligator Lake alkaline complex, Yukon Territory; unpub. M.Sc., McGill University.

Eiché, G.E., Francis, D.M., and Ludden, J.N. 1985a. Geochemistry and petrogenesis of Quaternary alkaline basalts from the Alligator Lake volcanic complex, Yukon Territory. Program with Abstracts, Geological Association of Canada-Mineralogical Association of Canada Joint Annual Meeting, Fredericton, N.B.: A16.

Eiché, G.E., Francis, D.M., and Ludden, J.N. 1985b. Temporal evolution of alkaline magmatism in the northern Canadian Cordillera. Abstracts with Programs - *Geological Society of America*, Vol. 17: 157.

Eiché, G.E., Francis, D.M., and Ludden, J.N. 1987. Primary alkaline magmas associated with the Quaternary Alligator lake volcanic complex, Yukon Territory, Canada. *Contributions to Mineralogy and Petrology*, Vol. 95: 191-201.

Elkins, L.T. and Grove, T.L. 1990. Ternary feldspar experiments and thermodynamic models. *American Mineralogist,* Vol. 75: 544-559.

Elliott, R.L., Koch, R.D. and Robinson, S.W. 1981. Age of basalt flows in the Blue River Valley, Bradfield Canal Quadrangle in *The U.S. Geological Survey of Alaska*, Accomplishments during 1979, U.S.G.S. Circular 823-B, B115-B116.

Evenchick, C.A. and Thorkelson, D.J. 1993. Geology, Spatzizi River, British Columbia (104H). Geological Survey of Canada, Open File 2719, scale 1:250 000.

Fillipone, J.A., and Ross, J.V. 1989. Stratigraphy and structure in the Twin Glacier-Hoodoo Mountain area, northwestern British Columbia (104B/14) in *Geological Fieldwork*, 1988, British Columbia Ministry of Energy, Mines and Petroleum Resources, Paper 1989-1: 285-292.

Foster, H.L., Forbes, R.B., and Ragan, D.L. 1966. Granulite and peridotite inclusions from Prindle Volcano, Yukon-Tanana Upland, Alaska. *U.S.G.S. Prof. Paper 550-B*: B115-B119.

Francis, D. 1987. Mantle-melt interaction recorded in spinel lherzolite xenoliths from the Alligator Lake volcanic complex, Yukon, Canada. *Journal of Petrology*, Vol. 28: 569-597.

Francis, D. 1991a. Volcano Mountain in *Volcanoes of North America*, C.A. Wood and J. Kienle (eds.). Cambridge University Press: New York. 118-119.

Francis, D. 1991b. Some implications of xenolith glasses for the mantle sources of alkaline mafic magmas. *Contributions to Mineralogy and Petrology*, Vol. 108: 175-180.

Francis, D., Abraham, A.C., Rowins, S., Shi, L., Carignan, J., and Ludden, J. 1996. A chemo-isotopic transect of the lithospheric upper mantle across the northern Canadian Cordillera in 1996 Slave-Northern Cordillera Lithospheric Evolution (SNORCLE) Transect and Cordilleran Tectonics Workshop Meeting (March 1-3), F. Cook and P. Erdmer (compilers), University of Calgary, Lithoprobe Report No. 50: 108.

Francis, D. and Ludden, J. 1990. The mantle source for olivine nephelinite, basanite and alkaline olivine basalts at Fort Selkirk, Yukon, Canada. *Journal of Petrology*, Vol. 31: 371-400.

Francis, D. and Ludden, J. 1995. The signature of amphibole in mafic alkaline lavas, a study in the northern Canadian Cordillera. *Journal of Petrology,* Vol. 36: 1171-1191.

Freer, R. 1981. Diffusion in silicate minerals and glasses: a data digest and guide to the literature. *Contributions to Mineralogy and Petrology*, Vol. 76: 440-454.

Gabrielse, H. 1963. McDame map-area, Cassiar District, British Columbia. Geological Survey of Canada Memoir 319: 138p..

Gabrielse, H. 1969. Geology of the Jennings River map-area, British Columbia. Geological Survey of Canada, Paper 68-55, 37p.

Gabrielse, H. and Souther, J.G. 1962. Dease Lake map-area, British Columbia. Geological Survey of Canada Map 21.

Geist, D. and White, C. 1994. Assimilation and fractionation in adjacent parts of the same magma chamber: Vandfaldsdalen macrodike, East Greenland. *Contributions to Mineralogy and Petrology*, Vol. 116: 92-107.

Gerlach, D.C., and Grove, T.L. 1982. Petrology of Medicine Lake Highland volcanics: characterization of endmembers in magma mixing. *Contributions to Mineralogy and Petrology*, Vol. 80: 147-159.

Ghiorso, M.S. 1987. Chemical mass transfer in magmatic processes: III. crystal growth, chemical diffusion and thermal diffusion in multicomponent silicate melts. *Contributions to Mineralogy and Petrology*, Vol. 96: 291-313.

Ghiorso, M.S. and Carmichael, I.S.E. 1987. Modelling magmatic systems: petrologic applications in *Thermodynamic Modeling of Geological*

Materials: Minerals, Fluids and Melts. I.S.E. Carmichael and H.P. Eugster (eds.). Reviews in Mineralogy, Vol. 17: 467-499.

Ghiorso, M.S. and Kelemen, P.B. 1987. Evaluating reaction stoichiometry in magmatic systems evolving under generalized thermodynamic constraints: examples comparing isothermal and isenthalpic assimilation in *Magmatic Processes: Physicochemical Principles,* B.O. Mysen (ed.). The Geochemical Society Special Publication No. 1: 319-336.

Ghiorso, M.S. and Sack, R.O. 1995. Chemical mass transfer in magmatic processes: IV. A revised and internally consistent thermodynamic model for the interpolation and extrapolation of liquid-solid equilibria in magmatic systems at elevated temperatures and pressures. *Contributions to Mineralogy and Petrology,* Vol. 119: 197-212.

Grove, E. W. 1974. Deglaciation - a possible triggering mechanism for Recent volcanism. International Association of Volcanology and Chemistry of the Earth's Interior, Proceedings of the Symposium on Andean and Antarctic Volcanology Problems, Santiago, Chile, September 1974: 88-97.

Grove, E.W. 1986. Geology and mineral deposits of the Unuk River - Salmon River - Anyox Area. B.C. Ministry of Energy, Mines and Petroleum Resources Bulletin 63: 152.

Grunder, A.L. 1992. Two-stage contamination during crustal assimilation: isotopic evidence from volcanic rocks in eastern Nevada. *Contributions to Mineralogy and Petrology*, Vol. 112: 219-229.

Hall, A. 1987. *Igneous Petrology*, First Edition: 573p.

Hamilton, T.S. 1981. Late Cenozoic Alkaline Volcanics of the Level Mountain Range, Northwestern British Columbia: Geology, Petrology, and Paleomagnetism; unpub. Ph.D. dissertation. The University of Alberta, Edmonton, 490p.

Hamilton, T.S. 1991. Level Mountain in *Volcanoes of North America*, C.A. Wood and J. Kienle (eds.). Cambridge University Press: New York: 121-123.

Hamilton, T.S., Baadsgaard, H. and Scarfe, C.M. 1978. Petrogenesis of the late Cenozoic volcanics, Level Mountain, northern British Columbia. GAC/MAC/GSA Annual Meeting Program with Abstracts, Vol. 10: 414-415.

Hamilton, T.S. and Evans, M.E. 1983. A magnetostratigraphic and secular variation study of Level Mountain, northern British Columbia. *Geophysical Journal of the Royal Astronomical Society*, Vol. 73: 39-49.

Hamilton, T.S. and Muehlenbachs, K. 1977. The 18O geochemistry of Cenozoic lavas from the Level Mountain volcanic centre, British Columbia. EOS (American Geophysical Union Transactions), Vol. 58: 1248.

Hamilton, T.S. and Scarfe, C.M. 1976. Cenozoic alkaline lavas from the Level Mountain volcanic centre. Abstracts of the Geological Association of Canada/Mineralogical Association of Canada Annual Meeting, Vol. 1: 47.

Hamilton, T.S. and Scarfe, C.M. 1977. Preliminary report on the Petrology of the Level Mountain volcanic centre, northwestern British Columbia. Geological Survey of Canada Report of Activities, Paper 77-1A: 429-434.

Harrison, T.M. and Watson, E.B. 1983. Kinetics of zircon dissolution and zirconium diffusion in granitic melts of variable water content. *Contributions to Mineralogy and Petrology*, Vol. 84: 66-67.

Harrison, T.M. and Watson, E.B. 1984. The behavior of apatite during crustal anatexis: equilibrium and kinetic considerations. *Geochemica et Cosmochimica Acta*, Vol. 48: 1467-1477.

Hasik, V., Francis, D., and Ludden, J. 1993. Volcanic evidence for a compositional contrast in the lithospheric upper mantle across the Tintina Trench, SE Yukon. GAC-MAC Abstracts with Program, Vol. 18: A-41.

Hauksdóttir, S. 1994. Petrography, geochemistry and petrogenesis of the Iskut-Unuk rivers volcanic centres, northwestern British Columbia; unpub. M.Sc. thesis, University of British Columbia, 253p.

Hauksdóttir, S., Enegren, E.G. and Russell, J.K. 1994. Recent basaltic volcanism in the Iskut-Unuk rivers area, northwestern B.C. in Current Research Part A; Geological Survey of Canada, Paper 94-1A: 57-67.

Hauksdóttir, S. and Russell, J.K. 1994. Assimilation-crystallization reactions in recent basalts of the Iskut-Unuk rivers area, northwestern British Columbia. 1994 GAC-MAC abstract, Vol. 19: 48.

Hickson, C.J. 1991. Volcano vent map and table in *Volcanoes of North America,* C.A. Wood and J. Kienle (eds.). Cambridge University Press: New York. 116-118.

Higgins, M.D. and Allen, J.M. 1984. A new locality for primary xenolith-bearing nephelinites in northwestern British Columbia. *Canadian Journal of Earth Science*, Vol. 22: 1556-1559.

Higman, S.L. and Pearce, T.H. 1993. Spatiotemporal dynamics in oscillatory zoned magmatic plagioclase. *Geophysical Research Letters,* Vol. 20: 1935-1938.

Hunt, P.A., and Roddick, J.C. 1992. A compiliation of K-Ar and $^{40}Ar^{-39}Ar$ ages: Report 22 in *Radiogenic Age and Isotopic Studies: Report 6,* Geological Survey of Canada, Paper 92-2: 179-226.

Jackson, L.E., Jr. 1989. Pleistocene subglacial volcanism near Fort Selkirk, Yukon Territory in *Current Research, Part E*, Geological Survey of Canada, Paper 89-1E: 251-256.

Jackson, L.E., Jr., Barendregt, R., Irving, E. and Ward, B. 1990. Magnetostratigraphy of early to middle Pleistocene basalts and sediments, Fort Selkirk area, Yukon Territory in *Current Research, Part E*, Geological Survey of Canada, Paper 90-1E: 277-286.

Jackson, L.E., Jr., Barendregt, R., Baker, J. and Irving, E. 1996. Early Pleistocene volcanism and glaciation in central Yukon: a new chronology from field studies and paleomagnetism. *Canadian Journal of Earth Science*, Vol. 33: 904-916.

Jackson, L.E., Jr., and Stevens, W. 1992. A recent eruptive history of Volcano Mountain, Yukon Territory in *Current Research, Part E*, Geological Survey of Canada, Paper 92-1A: 33-39.

Jamveit, B. 1991. Oscillatory zonation patterns in hydrothermal grossular-andradite garnet: nonlinear dynamics in regions of immiscibility. *American Mineralogist*, Vol. 76: 1319-1327.

Kaczor, S.M., Hanson, G.N., and Peterman, Z.E. 1988. Disequilibrium melting of granite at the contact with a basic plug: a geochemical and petrographic study. *Journal of Geology*, Vol. 96: 61-78.

Kawamoto, T. 1992. Dusty and honeycomb plagioclase: indicators of processes in the Uchino stratified magma chamber, Izu Peninsula, Japan. *Journal of Volcanology and Geothermal Research,* Vol. 49: 191-208.

Kelemen, P.B. and Ghiorso, M.S. 1986. Assimilation of peridotite in zoned calc-alkaline plutonic complexes: evidence from the Big Jim complex, Washington Cascades. *Contributions to Mineralogy and Petrology*, Vol. 94: 12-28.

Kerr, F.A. 1926. Dease Lake area, Cassiar District, B.C. in Geological Survey of Canada Summary Report, 1925, Part A: 75-99.

Kerr, F.A. 1948. Lower Stikine and western Iskut river areas, British Columbia; Geological Survey of Canada, Memoir 246: 94p.

Kesler, S.E. 1968. Mechanisms of magmatic assimilation at a marble contact, northern Haiti. *Lithos* 1: 219-229.

Kitchen, D.E. 1988. The disequilibrium partial melting and assimilation of Caledonian granite by Tertiary basalt at Barnesmore, Co. Donegal. *Mineralogical Magazine,* Vol. 126: 397-405.

Klassen, R.W. 1987. The Tertiary Pleistocene stratigraphy of the Liard Plain, southeastern Yukon Territory. Geological Survey of Canada Paper 86-17, 16p.

Kretz, R. 1983. Symbols for rock-forming minerals. *American Mineralogist,* Vol. 68: 277-279.

Kuo, L.-C. 1982. Kinetics of crystal dissolution in the system diopside-forsterite-silica; unpub. Ph.D., University of Illinois at Urbana-Champaign: 124p.

Kuo, L.-C., and Kirkpatrick, R.J. 1982. Pre-eruption history of phyric basalts from DSDP legs 45 and 46: evidence from morphology and zoning patterns in plagioclase. *Contributions to Mineralogy and Petrology*, Vol. 79: 13-27.

Kuo, L.-C. and Kirkpatrick, R.J. 1985. Dissolution of mafic minerals and its implications for the ascent velocities of peridotite-bearing basaltic magmas. *Journal of Geology*, Vol. 93: 691-700.

Kuo, L.-C. and Kirkpatrick, R.J. 1985. Kinetics of crystal dissolution in the system diopside-forsterite-silica. *American Journal of Science*, Vol. 285: 51-90.

Kushiro, I. 1975. On the nature of silicate melt and its significance in magma genesis: regularities in the shift of the liquidus boundaries involving olivine, pyroxene, and silica minerals. *American Journal of Science*, Vol. 275: 411-431.

Kutolin, V. A. and Agafonov, L.V. 1978. Composition of the upper mantle in light of the relative stability of ultrabasic nodules. *Geologiya i Geofizika*, Vol. 19: 3-13.

Larsen, E.S. and Switzer, G. 1939. An obsidian-like rock formed from the melting of a granodiorite. *American Journal of Science*. Vol. 237: 562-568.

Lasaga, A.C. 1981a. Transition State Theory in *Kinetics of Geochemical Processes* (A.C. Lasaga and R.J. Kirkpatrick, eds.). Reviews in Mineralogy, Vol. 8, Mineralogical Society of America: 135-169.

Lasaga, A.C. 1981b. Rate laws of chemical reactions in *Kinetics of Geochemical Processes,* A.C. Lasaga and R.J. Kirkpatrick (eds.). Reviews in Mineralogy, Vol. 8, Mineralogical Society of America: 1-68.

LeBas, M.J., LeMaitre, R.W., Streckeisen, A., and Zanettin, B. 1986. A chemical classification of volcanic rocks based on the total alkali-silica diagram. *Journal of Petrology*, Vol. 27, Part 3: 745-750.

LeMaitre, R.W. 1974. Partially fused granite blocks from Mt. Elephant, Victoria, Australia. *Journal of Petrology*, Vol. 15: 403-412.

Levson, V. M. 1992. Quaternary geology of the Atlin area (104N/11W, 12E); in Geological Fieldwork 1992, British Columbia Ministry of Energy, Mines, and Petroleum Resources, Paper 1992-1: 375-390.

LíHeureux, I. and Fowler, A.D. 1994. A non-linear dynamical model of oscillatory zoning in plagioclase. *American Mineralogist*, Vol. 79: 885-891.

Littlejohn, A.L. and Greenwood, H.J. 1974. Lherzolite nodules in basalts from British Columbia, Canada. *Canadian Journal of Earth Sciences*, Vol. 11: 1288-1308.

Lord, C.S. 1944. Geological Reconnaissance along the Alaska Highway between Watson Lake and Teslin River, Yukon and British Columbia. Geological Survey of Canada Paper 44-25: 20p.

Lord, C.S. 1948. McConnell Creek map-area, Cassiar District, British Columbia. Geological Survey of Canada Memoir 251: 72p.

Luhr, J.F., Pier, J.G., Aranda-Gomez, J.J., and Podosek, F.A. 1995. Crustal contamination in early Basin-and-Range hawaiites of the Los Encinos Volcanic Field, central Mexico. *Contributions to Mineralogy and Petrology*, Vol. 118: 321-339.

Mathews, W.H. 1947. "Tuyas", flat-topped volcanoes in northern British Columbia. *American Journal of Science*, Vol. 245: 560-570.

Mathews, W.H. 1986. Physiography of the Canadian Cordillera. Geological Survey of Canada Map 1701A.

McBirney, A.R., Taylor, H.P., and Armstrong, R.L. 1987. Paricutin re-examined: a classic example of crustal assimilation in calc-alkaline magma. *Contributions to Mineralogy and Petrology,* Vol. 95: 4-20.

McCulloch, M.T., Kyser, T.K., Woodhead, J.D. and Kinsley, L. 1994. Pb-Sr-Nd-O isotopic constraints on the origin of rhyolites from the Taupo Volcanic Zone of New Zealand: evidence of assimilation followed by fractionation from basalt. *Contributions to Mineralogy and Petrology,* Vol. 115: 303-312.

Monger, J.W.H. 1977. Upper Paleozoic rocks of the western Canadian Cordillera and their bearing on Cordilleran evolution. *Canadian Journal of Earth Sciences,* Vol. 14: 1832-1859.

Moore, J.G., Hickson, C.J. and Calk, L. 1995. Tholeiitic-alkalic transition at subglacial volcanoes, Tuya region, British Columbia; *Journal of Geophysical Research*, Solid Earth, Vol. 100;12: 24577-24592.

Mortensen, J.K. 1992. British Columbia, GSC 92-29 in *Radiogenic Age and Isotopic Studies: Report 6*, Geological Survey of Canada, Paper 92-2: 192.

Mortensen, J.K. and Roddick, J.C. 1989. Miocene ^{40}Ar-^{39}Ar and K-Ar ages for basaltic volcanic rocks in southwestern Dawson map area, western Yukon Territory in *Radiogenic Age and Isotopic Studies: Report 3*, Geological Survey of Canada, Paper 89-2: 17-22.

Mortensen, J.K. and Wirth, K. 1992. Isotopic ages GSC 92-97 and GSC-92-98 in *Radiogenic Age and Isotopic Studies: Report 6.* Geological Survey of Canada Paper 92-2: 215.

Myers, J.D., Frost, C.D. and Angevine, C.L. 1986. A test of a quartz eclogite source for parental Aleutian magmas: a mass balance approach. *Journal of Geology*, Vol. 94: 811-828.

Naeser, Nancy D., Westgate, John A., Hughes, Owen L., Pewe, Troy L. 1982. Fission-track ages of late Cenozoic distal tephra beds in the Yukon

Territory and Alaska. *Canadian Journal of Earth Sciences*, Vol. 19: 2167-2178.

Nagy, K.L., Blum, A.E., and Lasaga, A.C. 1991. Dissolution and precipitation kinetics of kaoliinite at 80 °C and pH 3: the dependence on solution saturation state. *American Journal of Science*, Vol. 291: 649-686.

Naranjo, J.A., Sparks, R.S.J., Stasiuk, M.V., Moreno, H., and Ablay, G.J. 1992. Morphological, structural and textural variations in the 1988-1990 andesite lava of Lonquimay Volcano, Chile. *Geological Magazine*, Vol. 129: 657-678.

Nekvasil, H. 1994. Ternary feldspar/melt equilibria: a review in *Feldspars and Their Reactions,* I. Parsons, (ed.). Kluwer Academic Publishing: Netherlands: 195-219.

Nicholls, J. 1977. The calculation of mineral compositions and modes of olivine-two pyroxene-spinel assemblages. problems and possibilities. *Contributions to Mineralogy and Petrology,* Vol. 60: 119-142.

Nicholls, J. 1990. Principles of thermodynamic modeling of igneous processes, in *Modern Methods of Igneous Petrology,* J. Nicholls and J.K. Russell (eds.). Reviews in Mineralogy, Vol. 24: 1-23.

Nicholls, J. and Stout, M.Z. 1982. Heat effects of assimilation, crystallization and vesiculation in magmas. *Contributions to Mineralogy and Petrology,* Vol. 81: 328-339.

Nicholls, J. and Stout, M.Z. 1996. Basaltic lava flows and enclosed xenoliths as samples of the lithosphere and low velocity zone beneath northern British Columbia, a progress report. 1996 Slave-Northern Cordillera Lithospheric Evolution (SNORCLE) Transect and Cordilleran Tectonics Workshop Meeting (March 1-3), F. Cook and P. Erdmer (compilers), University of Calgary, Lithoprobe Report No. 50: 109-115.

Nicholls, J. and Stout, M.Z. 1997. Pressures and temperatures for ultramafic xenoliths, Atlin Lake area, British Columbia. Slave-Northern Cordillera Lithospheric Evolution (SNORCLE) Transect and Cordilleran Tectonics Workshop Meeting (March 7-9), F. Cook and P. Erdmer (compilers), University of Calgary, Lithoprobe Report No. 56: 245pp.

Nicholls, J., Stout, M.Z., and Fiesinger, D.W. 1982. Petrologic variations in Quaternary volcanic rocks, British Columbia, and the nature of the underlying upper mantle. *Contributions to Mineralogy and Petrology*, Vol. 79: 201-218.

Nielsen, R.L. 1988. A model for the simulation of combined major and trace element liquid lines of descent. *Geochem. Cosmochem. Acta,* Vol. 52: 27-38.

Nielsen, R.L. 1990. Phase equilibria constraints on liquid lines of descent generated by paired assimilation and fractional crystallization: trace

elements and Sr and Nd isotopes. *Journal of Geophysical Research,* Vol. 94: 787-794.

Nixon, G.T. and Pearce, T.H. 1987. Laser-interferometry study of oscillatory zoning in plagioclase: the record of magma mixing and phenocryst recycling in calc-alkaline magma chambers, Iztaccihuatl Volcano, Mexico. *American Mineralogist,* Vol. 72: 1144-1162.

Pearce, J.A. 1983. Role of the sub-continental lithosphere in magma genesis at active continental margins in *Continental Basalts and Mantle Xenoliths.* C.J. Hawkesworth and M.J. Norry (eds.). Shiva Press: Nantwich: 230-249.

Pearce, T.H. 1994. Recent work on oscillatory zoning in plagioclase in *Feldspars and Their Reactions*, I. Parsons (ed.). Kluwer Academic Publishing, Netherlands: 313-349.

Pearce, T.H., Griffin, M.P. and Kolisnik, A.M. 1987a. Magmatic crystal stratigraphy and constraints on magma chamber dynamics: Laser interference results on individual phenocrysts. *Journal of Geophysical Research,* Vol. 92: 13,745-13,752.

Pearce, T.H. and Kolisnik, A.M. 1990. Observations of plagioclase zoning using interference imaging. *Earth Science Research,* Vol. 29: 9-26.

Pearce, T.H., Russell, J.K. and Wolfson, I. 1987b. Laser interference and Normarski interference imaging of zoning profiles in plagioclase

phenocrysts from the May 18, 1986 eruption of Mt. St. Helen's, Washington. *American Mineralogist,* Vol. 72: 1131-1143.

Philpotts, A.R. and Asher, P.M. 1993. Wallrock melting and reaction effects along the Higganum diabase dike in Connecticut: contamination of a continental flood basalt feeder. *Journal of Petrology,* Vol. 34: 1029-1058.

Prescott, J. 1983. Petrogenesis of ultramafic xenoliths from the Canadian Cordillera and Alaska; unpub. M.Sc., McGill University: 185p.

Prigogine, I. 1967. *Introduction to Thermodynamics of Irreversible Processes.* 3rd ed. John Wiley and Sons, N.Y.: 147p.

Prigogine, I. and Defay, R. 1954. *Chemical Thermodynamics*. Longmans, Green and Co., Ltd., London, 543p.

Pringle, G.J., Trembath, L.T. and Parjari, G.E. 1974. Crystallization history of a zoned plagioclase. *Mineralogical Magazine,* Vol. 39: 867-877.

Reed, M. H. 1982. Calculation of multicomponent chemical equilibria and reaction processes in systems involving minerals, gases and an aqueous phase. *Geochimica et Cosmochimica Acta,* Vol. 46: 513-528.

Reiners, P.W., Nelson, B.K. and Ghiorso, M.S. 1995. Assimilation of felsic crust by basaltic magma: thermal limits and extents of crustal contamination of mantle-derived magmas. *Geology,* Vol. 23: 563-566.

Ross, J.V. 1983. The nature and rheology of the Cordilleran upper mantle of British Columbia: inferences from peridotite xenoliths. *Tectonophysics,* Vol. 100: 321-357.

Russell, J.K., Edwards, B.R., and Snyder, L.D. 1995. Volatile production possibilities during magmatic assimilation: heat and mass-balance constraints. in *Magmas, Fluids and Ore Deposits,* J.F.H. Thompson (ed.). Mineralogical Association of Canada Short Course Series, Vol. 23:1-24.

Russell, J.K. and Nicholls J. 1985. Application of Duhem's Theorem to the estimation of extensive and intensive properties of basaltic systems. *Canadian Mineralogist,* Vol. 23: 479-488.

Russell, J.K., Nixon, G.T., and Pearce, T.H. 1987. Petrographc constraints on modelling the crystallization of basalt magma, Cow Lakes, southeast Oregon. *Canadian Journal of Earth Science,* Vol. 25: 86-494.

Sack, R.O. and Ghiorso, M.S. 1989. Importance of considerations of mixing properties in establishing an internally consistent thermodynamic database: thermochemistry of minerals in the system Mg_2SiO_4-Fe_2SiO_4-SiO_2. *Contributions to Mineralogy and Petrology*, Vol. 102: 41-68.

Samson, S.D., McClelland, W.C., Patchett, P.J., Gehrels, G.E., and Anderson, R.G. 1989. Evidence from neodymium isotopes for mantle contributions to Phanerozoic crustal genesis in the Canadian Cordillera. *Nature*, Vol. 337: 705-709.

Samson, S.D., Patchett, P.J., Gehrels, G.E. ,and Anderson, R.G. 1990. Nd and Sr isotopic characterization of the Wrangellia terrane and implications for crustal growth of the Canadian Cordillera. *Journal of Geology*, Vol. 98: 749-762.

Sato, H. 1975. Diffusion coronas around quartz xenocrysts in andesite and basalt from Tertiary volcanic regions in northeastern Shikoku, Japan. *Contributions to Mineralogy and Petrology,* Vol. 50: 49-64.

Scarfe, C.M. 1973. Viscosity of basic magmas at varying pressure. *Nature*, Vol. 241: 101-102.

Scarfe, C.M. 1986. Viscosity and density of silicate melts. in *Silicate Melts: their properties and structures applied to problems in geochemistry, petrology, economic geology, and planetary geology,* C.M. Scarfe (ed.). Mineralogical Association of Canada Short Course Series, Vol. 12: 36-56.

Sigvaldason, G.E., Annertz, K., and Nilsson, M. 1992. Effect of glacier loading/deloading on volcanism: postglacial volcanic production rate of the Dyngjufjoll area, central Iceland. *Bulletin of Volcanology*, Vol. 54: 385-392.

Simpson, K. 1996. The geology, geochemistry and geomorphology of Mathews Tuya: a subglacial volcano in northwestern British Columbia. unpub. B.Sc. thesis, University of British Columbia: 97 p.

Sinclair, P.D., Templeman-Kluit, D.J. and Medaris, L.G. Jr. 1978. Lherzolite nodules from a Pleistocene cinder cone in central Yukon. *Canadian Journal of Earth Sciences*, Vol. 15: 220-226.

Souther, J.G. 1971. Telegraph Creek map-area, British Columbia. Geological Survey of Canada Paper 71-44: 38p.

Souther, J.G. 1977. Volcanism and tectonic environments in the Canadian Cordillera - a second look in *Volcanic Regimes in Canada*, W.R.A. Baragar, L.C. Coleman and J.M. Hall (eds.). Geological Association of Canada, Special Paper 16: 3-24.

Souther, J.G. 1990. Volcano tectonics of Canada in *Volcanoes of North America*, C.A. Wood and J. Kienle (eds.). Cambridge University Press, New York: 110-116.

Souther, J.G. 1991. Chapter 15, Volcanic Regimes in *Geology of the Cordilleran Orogen in Canada*, H. Gabrielse and C.J. Yorath (eds.). Canada Geological Survey, Geology of Canada, No. 4: 457-490 (*also* Geological Society of America, The Geology of North America, No. G-.2).

Souther, J.G. 1991a. Volcano tectonics of Canada in *Volcanoes of North America*, C.A. Wood and J. Kienle (eds.). Cambridge University Press: New York: 111-116.

Souther, J.G. 1991b. Edziza in *Volcanoes of North America*, C.A. Wood and J. Kienle (eds.). Cambridge University Press: New York: 124-126.

Souther, J.G. 1991c. Hoodoo in *Volcanoes of North America*, C.A. Wood and J. Kienle (eds.). Cambridge University Press: New York: 127-128.

Souther, J.G. 1991d Iskut-Unuk River cones in *Volcanoes of North America*, C.A. Wood and J. Kienle (eds.). Cambridge University Press: New York: 128-129.

Souther, J.G. 1991e. Maitland in *Volcanoes of North America*, C.A. Wood and J. Kienle (eds.). Cambridge University Press: New York: 126-127.

Souther, J.G. 1991f. The Thumb in *Volcanoes of North America*, C.A. Wood and J. Kienle (eds.). Cambridge University Press: New York: 129-130.

Souther, J.G. 1992. The late Cenozoic Mount Edziza Volcanic Complex, British Columbia; Geological Survey of Canada, Memoir 420: 320 p.

Souther, J.G., Armstrong, R.L., and Harakal, J. 1984. Chronology of the peralkaline, late Cenozoic Mount Edziza volcanic complex, northern British Columbia. *Geological Society of America* Bulletin 95: 337-349.

Souther, J.G. and Hickson, C.J. 1984. Crystal fractionation of the basalt comendite series of the Mount Edziza volcanic complex, British Columbia: major and trace elements. *Journal of Volcanology and Geothermal Research*, Vol. 21: 79-106.

Souther, J.G., and Yorath, C.J. 1991. Neogene assemblages. Chapter 10 in *Geology of the Cordilleran Orogen in Canada*. H. Gabrielse and C.J.

Yorath (eds.). Geological Survey of Canada. Geology of Canada. No. 4: 373-401.

Stasiuk, M. and Russell, J.K. 1989. Quaternary volcanic rocks of the Iskut River region, northwestern British Columbia in *Current Research*, Geological Survey of Canada Paper 90-1E: 53-157.

Stimac, J.A. and Pearce, T.H. 1992. Textural evidence of mafic-felsic magma interaction in dacite lavas, Clear Lake, California. *American Mineralogist*, Vol. 77: 795-809.

Stimac, J.A. and Wark, D.A. 1992. Plagioclase mantles on sanidine in silicic lavas, Clear Lake, California: implications for the origin of rapakivi texture. *Geological Society of America,* Bull.104: 728-744.

Sutherland-Brown, A. 1969. Aiyansh lava flow, British Columbia. *Canadian Journal of Earth Sciences*, Vol. 6: 1460-1468.

Sverjensky, D.A. 1992. Linear free energy relations for predicting dissolution rates of solids. *Nature*, Vol. 358: 310-313.

Symons, D.T.A. 1975. Age and flow direction from magnetic measurements on the Historic Aiyansh flow, British Columbia. *Journal of Geophysical Research*, Vol. 80, No. 17: 2622-2626.

Taylor, H.P. 1980. The effects of assimilating country rock by magmas on the 18O/16O and 87Sr/86Sr systematics of igneous rocks. *Earth and Planetary Science Letters*, Vol. 47: 243-254.

Thorkelson, D.J. 1992. Volcanic and tectonic evolution of the Hazelton Group in the Spatzizi River (104H) map-area, north-central British Columbia. unpub. Ph.D. thesis, Carleton University, Ottawa: 281p.

Thornber, C.R. and Huebner, J.S. 1985. Dissolution of olivine in basaltic liquids: experimental observations and applications. *American Mineralogist*, Vol. 70: 934-945.

Thornton, C.P. and Tuttle, O.F. 1960. Chemistry of Igneous Rocks I. Differentiation Index. *American Journal of Science*, Vol. 258: 664-684.

Trupia, S. 1992. Petrology of nephelinites and associated ultramafic nodules of Volcano Mountain, Yukon Territory. M.Sc. thesis, Unversity of Calgary 123p.

Trupia, S. and Nicholls, J. 1996. Petrology of Recent lava flows, Volcano Mountain, Yukon Territory, Canada. *Lithos*. Vol. 37: 61-78.

Uebel, P.J. 1978. The zoning of plagioclase as record of petrogenetic development of the Ben Nevis Ring-Intrusion, Scotland. *Neues. Jahrb. Abh.*, Vol. 132: 182-213.

Walther, J.V. and Wood, B.J. 1984. Rate and mechanism in prograde metamorphism. *Contributions to Mineralogy and Petrology*, Vol. 88: 246-259.

Watson, E.B. 1982. Basalt contamination by continental crust: some experiments and models. *Contributions to Mineralogy and Petrology*, Vol. 80: 73-87.

Watson, K. De P. and Mathews, W.H. 1944. The Tuya-Teslin area, northern British Columbia. British Columbia Department of Mines Bulletin No. 19: 52p.

Watson, K. De P. and Mathews, W.H. 1948. Partly vitrified xenoliths in pillow basalt. *American Journal of Science*, Vol. 244: 601-614.

Wheeler, J.O. 1961. Whitehorse map-area, Yukon Territory. Geological Survey of Canada Memoir 312: 156p.

White, W.M., and Hofmann, A.W. 1982. Sr and Nd isotope geochemistry of oceanic basalts and mantle evolution. *Nature*, Vol. 296: 821-825.

Wiebe, R.A. 1968. Plagioclase stratigraphy: a record of magmatic conditions and events in a granite stock. *American Journal of Science,* Vol. 266: 690-703.

Wilcox, R.E. 1954: Petrology of the Paricutin volcano. *U.S.G.S. Bulletin 965-C*: 281-353.

Wirth, K.R. 1991. Processes of lithosphere evolution: geochemistry and tectonics of mafic rocks in the Brooks Range and Yukon-Tanana region, Alaska. Ph. D. thesis, Cornell University.

Wood, B.J., and Walther, J.V. 1983. Rates of hydrothermal reactions. *Science*, Vol. 22: 413-415.

Woodsworth, G.J., Anderson, R.G., and Armstrong, R.L. 1991. Plutonic regimes, Chapter 15 in *Geology of the Cordilleran Orogen in Canada*, H. Gabrielse and C.J. Yorath (eds.). Geological Survey of Canada, Geology of Canada, No. 4: 491-531.

Wuorinen, VL. 1978. Age of Aiyansh volcano, British Columbia. *Canadian Journal of Earth Sciences*, Vol. 15: 1037-1038.

Zhang, Y., Walker, D., and Lesher, C.E. 1989. Diffusive crystal dissolution. *Contributions to Mineralogy and Petrology*, Vol. 102: 492-513.

Zindler, A., and Hart, S. 1986. Chemical geodynamics. *Annual Reviews of Earth and Planetary Sciences*, Vol. 14: 493-571.

APPENDIX A2

Sample information and geochemical data for the Hoodoo Mountain volcanic complex

The tables in Appendix A2 contain sample information and geochemical analyses for samples from the Hoodoo Mountain volcanic complex (Chapter 2). Major, minor, and trace element and rare earth element analyses are given in Tables A2.2 and A2.3. All analyses in these tables were made at the Geological Survey of Canada Analytical Chemistry Section in Ottawa, Ontario. Major elements were analyzed using standard XRF techniques except for FeO, H_2O, CO_2, $S_{(total)}$, and LOI, which were analyzed using chemical methods. Hauksdóttir (1994) presented precision and accuracy estimates for analyses from the GSC laboratory (see Hauksdóttir 1994, Appendix I, p. 242-253). In Tables A2.2 and A2.3, trace element analyses done by ICP-MS are given in rows with **bold** headings; all other trace element analyses are by XRF. Rare earth analyses are by ICP-MS as well. I acknowledge R.G. Anderson for providing the access to the GSC analytical laboratories and N. Bertrand for performing the ICP-MS analyses.

Analyses of samples for Sr and Nd isotopes were by R. Thériault also at the GSC analytical laboratories in Ottawa (Table A2.5). The techniques used were standard isotope dilution techniques (cf. Thériault, R.J. and Tella, S. 1997. Sm-Nd isotopic study on mafic volcanic rocks from the Rankin Inlet and Tarani regions, District of Keewatin, Northwest Territories. in Radiogenic and Isotopic

Studies: Report 10, Geological Survey of Canada, *Current Research 1997-F*, p. 61-66).

Analyses of plagioclase grains from sample 94BRE02 are given in Table A2.4. The analyses were done on the Cameca SX-50 electron microprobe at the University of British Columbia. Analyses were done by Drs. M. Raudsepp and M. Kopylova under standard operating conditions (15 kV and 20 nA) with a 5 micron spot-fixed beam.

Table A2.1. Sample information for samples analyzed for whole rock chemistry (including major, minor, and trace elements, and rare earth element), Sr and Nd isotopes and $^{40}Ar/^{39}Ar$ dating.

Sample No.	UTM Easthings (zone 9)	UTM Northings	Unit	TAS name	Sr & Nd	Ar/Ar
93BRE2	358703	6296773	Qvap2a	trachyte		
93BRE7	359002	6296971	Qvap2a	phon/trach		
93BRE16	359671	6296880	Qvap4	trachyte	X	X
93BRE28	360749	6290959	Qvap2b	trachyte		
93BRE29	359251	6292008	Qvap5	phonolite		
93BRE32	362215	6294348	Qvap4	trachyte		
93BRE50	361809	6295660	Qvap4	phonolite		
93BRE74	361376	6296447	Qvap2a	phonolite		
93BRE85	363901	6293430	Qvap	phon/trach		X
93BRE106	361914	6295747	Qvap2a	trachyte		
93BRE141	359602	6296642	Qvap4	phon/trach	X	
93BRE168	358607	6297462	Qvap1	phon/trach		X
94BRE44	361013	6296869	Qvap2a	trachyte		
94BRE45	361682	6296645	Qvap2a	phonolite		X
94BRE49	361372	6296542	Qvap2a	trachyte		
94BRE65	359857	6297003	Qvap4	trachyte		
94BRE66	358537	6297003	Qvap4	trachyte		
94BRE69	359245	6296602	Qvap4	trachyte		
94BRE76	357167	6296952	Qvub	trachyte		X
94BRE87	358864	6296560	Qvap4	trachyte		
94BRE111	360900	6296663	Qvap2a	trachyte		
94BRE119	356773	6294243	Qvap2b	trachyte		X
94BRE151	358080	6294659	Qvap5	phonolite		
94BRE158	358821	6293770	Qvap5	phonolite		
93BRE5	358446	6296287	Qvap6	phonolite		
93BRE9	358565	6296605	Qvap6	phonolite		
93BRE76	358685	6292837	Qvap6	phonolite		
93BRE83	364338	6292852	Qvap6	phon/trach		
94BRE62	360269	6295385	Qvap6	phonolite		
94BRE78	357215	6297147	Qvap6u	trachyte		X
93BRE107	362066	6295800	Qvh3	phonolite		
93BRE190g	357932	6297034	Qvap6	phonolite	X	
94BRE98	357458	6296583	Qvap6	phonolite		
94BRE165	362085	6295783	Qvh3	phonolite		
93BRE8	358774	6296791	Qvpp1	trachyte	X	X
93BRE12	358598	6296621	Qvpp2	trachyte		
93BRE23	357773	6295591	Qvpp1	trachyte		
93BRE26	357813	6294910	Qvpp1	trachyte		
93BRE31	362429	6294340	Qvpp1	phon/trach		
93BRE44	362237	6294643	Qvpp1	phon/trach		X
93BRE58	364917	6293220	Qvpp2	phon/trach		
93BRE109	361006	6293120	Qvpp2	phon/trach		
94BRE72	357416	6297808	Qvpp	trachyte		
94BRE86	358986	6296523	Qvpp1	trachyte		
94BRE91	358537	6296073	Qvpp1	trachyte		
94BRE94	358537	6296073	Qvpp1	trachyte		
94BRE100	357216	6296611	Qvpp1	phon/trach		
94BRE108	360809	6296580	Qvpp1	phonolite		
93BRE1	359002	6298630	Qvbb	basalt		
93BRE150	359373	6298053	Qvbb	basalt	X	
93BRE151	359378	6298494	Qvbm	basalt	X	
94BRE2	359637	6298777	Qvbm	basalt		X
94BRE10	359694	6298767	Qvbm	basalt		
94BRE32	359401	6298460	Qvbp	basalt		
94BRE75	357287	6297494	Qi in uTs	tephrite		X
94BRE74	357287	6297496	Qi in uTs	trachyandesite		X
93BRE153	359413	6298868	xenolith in Qvbb	trachyte	X	
94BRE23	358960	6299108	xenolith in Qvbb	trachyte		

Table A2.2. List of all major, minor, and trace element and rare earth element analyses for samples from Hoodoo Mountain volcano.

Sample No.	93BRE2	93BRE7	93BRE16	93BRE28	93BRE29	93BRE32	93BRE50	93BRE74	93BRE85	93BRE106	93BRE141	93BRE168	94BRE44	94BRE45
Map Unit	Qvap	Qvap	Qvap	Qvap	Qvap	Qvap	Qvap	Qvap	Qvap	Qvap	Qvap	Qvap	Qvap	Qvap
TAS name	trachyte	phon/tract	trachyte	trachyte	phonolite	trachyte	phonolite	phonolite	phon/tracl	trachyte	phon/trach	phon/trach	trachyte	phonolite
Major and Minor Elements														
SiO_2	59.4	59.1	59.7	59.1	58.4	59.0	59.3	59.2	59.8	59.7	59.2	59.1	58.7	59.0
TiO_2	0.36	0.35	0.37	0.35	0.25	0.34	0.32	0.31	0.48	0.41	0.37	0.35	0.31	0.32
Al_2O_3	14.9	14.5	14.9	15.1	15.3	15.7	14.5	16.3	16.8	16.2	14.8	14.5	16.6	16.5
Fe_2O_3(total)	9.60	9.80	9.60	9.20	9.10	8.60	9.70	8.10	7.20	8.40	9.40	9.80	8.20	8.30
Fe_2O_3	4.20	6.80	5.90	4.50	4.50	3.50	3.70	2.80	3.20	5.50	4.60	5.20	6.00	3.70
FeO	4.90	2.70	3.30	4.20	4.10	4.60	5.40	4.80	3.60	2.60	4.30	4.10	2.00	4.10
MnO	0.28	0.24	0.21	0.23	0.21	0.22	0.23	0.20	0.18	0.19	0.22	0.23	0.23	0.21
MgO						0.04			0.21	0.04			0.11	0.09
CaO	1.87	1.75	1.53	1.67	1.06	1.86	1.23	1.68	1.88	1.94	1.65	1.84	2.10	1.87
Na_2O	6.40	7.20	7.10	6.80	8.30	7.00	8.40	7.60	6.70	6.60	7.40	7.50	6.80	7.80
K_2O	4.82	4.70	4.83	5.08	4.61	5.15	4.66	5.15	5.63	5.30	4.73	4.60	5.04	5.08
P_2O_5	0.04	0.06	0.03	0.04	0.04	0.07	0.06	0.06	0.10	0.06	0.05	0.06	0.06	0.07
H_2O(total)	2.30	1.40	1.10	1.60	2.50	1.70	1.10	1.20	0.50	0.80	1.60	1.60	1.90	1.20
CO_2(total)	0.30	0.50	0.60	0.20	0.20	0.30	0.30	0.30	0.20	0.10	0.40	0.30	0.50	
S(total)	0.06	0.03		0.02	0.03	0.04	0.04	0.03			0.03	0.11	0.18	0.09
Total	100.20	99.70	100.00	99.30	100.00	99.90	99.70	100.00	99.60	99.80	99.80	99.90	100.70	100.30
Trace Elements														
Ag	0.9	1.4	0.9	0.9	1.0	0.7	1.1	0.8	0.5	0.6	0.8	0.9		
Ba	60	30			40	70	50	60	260	70	50		80	50
Be	10	9	8.1	7.2	10	6.1	11	7.1	4.2	5.2	7.7	9.5	7	7
Co			6						5		10		6	13
Cr														
Cs	1.7	1.7	0.42	1.3	1.5	1.1	2.2	1.5	0.8	0.98	1.5	1.9	1.1	1.3
Cu														
Ga	50	49	47	47	55	42	52	44	35	39	48	50	39	39
Hf	26	26	25	23	31	19	30	22	14	16	24	27	20	20
In	0.19	0.18	0.26	0.23	0.15	0.20	0.18	0.24	0.09	0.13	0.19	0.19	0.21	0.24
La	130	120	110	100	130	88	130	95	67	75	110	130	89	88
La	140	110	100	94	130	83	140	97	68	79	100	130	89	89
Mo	4.5	9.3	3.7	5.3	14	7.3	12	9.7	6.1	3.6	8.2	11	6.6	9.7
Nb									94					
Nb	150	150	130	130	170	120	180	130	92	100	140	160	130	120
Ni					15									
Pb	16	17	15	13	17	11	19	13	2	8	14	16	14	15
Rb						89		100	80	86	95		95	
Rb	140	150	120	130	140	110	150	130	98	100	120	140	110	120
Sc	0.5					1.1	0.5	0.6	2.6	1.5			0.8	0.8
Sr									30		-20			
Ta	9.4	9.9	8.8	8.3	12	7.1	12	8.4	5.6	5.8	7.4	10	10	10
Th	16	17	15	13	19	12	20	14	8.2	9.9	15	17	14	14
Tl	0.24	0.12	0.11	0.30	0.45	0.27	0.42	0.19	0.05	0.07	0.22	0.32	0.24	0.25
U	5.3	5.8	2.9	4.8	6.7	4.3	7.2	4.8	2.9	2.5	5.3	6.4	4.7	4.7
V														
Y	130	110	97	90	120	70	120	77	47	59	96	110	80	80
Y	130	110	92	87	120	68	130	79	49	63	94	120	72	72
Yb	11	10	9.5	8.60	11.00	7.20	11.00	7.90	4.70	6.20	9.10	11.00	7.60	7.50
Yb	10	8.3	7.5	6.9	8.8	5.7	10	6.7	4.1	5.5	7.7	9.2	7	7
Zn	310	280	250	240	300	190	330	210	140	170	260	300	200	200
Zr	1400	1400	1300	1200	1700	1000	1600	1200	650	890	1300	1400	1200	1200
Rare Earth Elements														
La	130	120	110	100	130	88	140	95	67	75	110	130	89	88
Ce	260	240	220	200	260	180	270	190	130	150	220	250	180	180
Pr	33	30	28	25	33	22	34	23	17	19	27	31	22	22
Nd	130	120	110	100	130	85	130	88	64	73	110	120	84	85
Sm	27	25	23	21	27	17	27	17	12	14	22	26	16	17
Eu	3.5	3.2	3.1	3.1	3.5	2.1	3.3	2.0	2.4	2.1	3.0	3.2	1.9	1.9
Gd	26	24	21	20	26	16	26	16	11	13	21	24	16	16
Tb	4.1	3.8	3.4	3.1	4.1	2.5	4.2	2.7	1.8	2.1	3.3	3.8	2.6	2.6
Dy	24	22	20	19	24	15	25	16	10	12	20	22	15	15
Ho	4.7	4.3	3.9	3.6	4.8	2.9	4.9	3.1	1.9	2.4	3.8	4.3	2.8	2.8
Er	13	12	11	9.9	13	8.0	13	8.7	5.2	6.6	10	12	7.6	7.4
Tm	1.8	1.7	1.5	1.4	1.9	1.1	1.9	1.3	0.76	0.97	1.5	1.7	1.3	1.2
Yb	11	10	9.5	8.6	11	7.2	11	7.9	4.7	6.2	9.1	11	7.6	7.5
Lu	1.6	1.5	1.3	1.3	1.5	1.1	1.6	1.2	0.72	0.95	1.3	1.5	1.2	1.2

Table A2.2. (continued).

Sample No.	94BRE49	94BRE65	94BRE66	94BRE69	94BRE76	94BRE87	94BRE111	94BRE119	94BRE151	94BRE158	93BRE5	93BRE9	93BRE76
Map Unit	Qvap	Qvap	Qvap	Qvap	Qvap	Qvap	Qvap	Qvap	Qvap	Qvap	Qvap6	Qvap6	Qvap6
TAS name	trachyte	trachyte	trachyte	trachyte	trachyte	trachyte	trachyte	trachyte	phonolite	phonolite	phonolite	phonolite	phonolite
Major and Minor Elements													
SiO_2	58.6	59.1	59.6	60.0	64.1	59.4	59.4	60.1	58.9	58.5	58.4	58.2	58.2
TiO_2	0.32	0.36	0.38	0.37	0.30	0.37	0.32	0.46	0.30	0.31	0.29	0.29	0.26
Al_2O_3	16.5	15.2	15.3	15.2	15.4	15.5	16.8	17.3	15.6	15.6	15.3	15.3	15.6
Fe_2O_3(total)	8.30	9.60	9.50	9.60	6.20	9.60	8.20	7.30	9.50	9.60	9.30	9.40	9.20
Fe_2O_3	5.30	4.40	3.70	7.40	3.20	4.70	5.50	3.00	3.10	4.20	5.40	5.36	6.80
FeO	2.70	4.70	5.20	2.00	2.70	4.40	2.40	3.90	5.80	4.90	3.50	3.64	2.20
MnO	0.22	0.23	0.22	0.23	0.15	0.24	0.17	0.18	0.22	0.22	0.21	0.22	0.20
MgO	0.11		0.07		0.06		0.10	0.25					
CaO	2.11	1.61	1.63	1.60	0.63	1.89	1.85	2.08	1.46	1.63	1.22	1.22	0.97
Na_2O	7.00	7.50	8.00	8.03	6.10	6.80	7.50	6.60	8.90	7.70	8.20	8.04	8.70
K_2O	4.93	4.74	4.71	4.79	5.13	4.82	5.11	5.45	4.71	4.83	4.85	4.78	4.72
P_2O_5	0.07	0.05	0.06	0.06	0.05	0.03	0.05	0.09	0.06	0.06	0.04	0.04	0.03
H_2O(total)	2.30	1.60	1.20	0.63	0.70	1.60	1.10	0.80	1.20	1.80	2.30	2.34	2.00
CO_2(total)	0.10		0.10		1.60	0.60			0.10	0.40	0.40	0.14	0.20
S(total)	0.06	0.06	0.03		0.02	0.04	0.08		0.07	0.06	0.04		
Total	100.50	99.70	100.40	100.70	100.44	100.60	100.60	100.30	100.60	100.40	100.40	100.40	100.30
Trace Elements													
Ag					0.5		0.2				0.8	0.9	1.0
Ba	90		50	63	80	90	80	150	80	60	30	30	
Be	7	8	8	8	6	8	7	5	9	9	9	8.68	11
Co				6	6	6	10	6	5				
Cr													
Cs	1.1	1.3	1.6	1.1	0.52	0.72	0.7	0.7	1.7	1.6	2.0	1.82	2.2
Cu													
Ga	39	43	42	42	40	42	39	32	43	44	50	50.4	56
Hf	20	23	23	23	20	23	21	14	25	25	26	25.2	31
In	0.22	0.19	0.19	0.21	0.26	0.19	0.26	0.16	0.18	0.18	0.17	0.188	0.15
La	88	100	100	99	100	100	90	69	110	110	110	116	130
La	87	100	100		100	100	88	67	110	100	120		150
Mo	5.9	7.6	9.0	2.6	4.4	5.0	2.0	5.3	11.0	9.8	7.6	3.46	8.6
Nb								99					
Nb	120	140	140	140	130	140	130		150	140	140	148	170
Ni													
Pb	14	27	14	16	15	14	12	8	13	13	13	13.6	16
Rb						98		88					
Rb	120	130	130	125	130	120	130	100	130	130	130	136	150
Sc	0.7	0.6	0.5		1	0.5	0.7	2.4	0.6	0.6			0.5
Sr													
Ta	8.9	10	10	10.3	9.1	10	9.1	6.6	11	11	8.7	9	11
Th	13	15	15	13	14	15	13	9.2	16	16	15	16	19
Tl	0.21	0.24	0.18	0.18	0.28	0.18	0.25	0.20	0.34	0.26	0.35	0.35	0.42
U	4.6	5.2	5.3	3.8	3.6	5.0	1.0	2.3	5.3	5.2	5.3	4.6	6.7
V													
Y	79	100	100	96	100	100	76	54	110	110	100	106	120
Y	72	92	94		94	92	70	49	99	97	110		130
Yb	7.50	9.10	9.10	8.23	9.4	9.10	7.30	5.00	9.50	9.40	9.7	9.8	11.0
Yb	7	8	8		9	8	6	4	8	8	8.6	8.28	10
Zn	190	250	260	260	210	250	190	140	260	260	280	278	320
Zr	1200	1300	1300	1300	1100	1300	1100	720	1400	1400	1400	1400	1700
Rare Earth Elements													
La	88	100	100	99	100	100	90	69	110	110	110	114	130
Ce	180	220	210	220	210	210	180	150	220	220	230	232	270
Pr	22	26	26	25.75	26	26	22	18	28	27	29	28.8	34
Nd	84	100	100	100	100	100	84	67	110	110	110	116	130
Sm	17	21	21	21.25	21	20	17	13	22	22	24	23.8	27
Eu	1.9	3	3	3.1	2.5	3	1.9	2.1	3.2	3.2	3.2	3.2	3.6
Gd	16	21	21	21	22	21	16	12	21	22	22	22	26
Tb	2.6	3.3	3.2	3.3	3.4	3.3	2.5	1.8	3.5	3.5	3.5	3.58	4.1
Dy	14	18	18	18	19	19	14	10	20	19	21	21	25
Ho	2.8	3.6	3.6	3.4	3.6	3.6	2.7	1.9	3.7	3.7	4	4.1	4.8
Er	7.4	9.5	9.4	8.8	9.4	9.4	7	4.9	10	9.8	11	11	13
Tm	1.2	1.5	1.5	1.45	1.6	1.6	1.2	0.83	1.6	1.6	1.6	1.6	1.9
Yb	7.5	9.1	9.1	8.7	9.4	9.1	7.3	5	9.5	9.4	9.7	9.82	11
Lu	1.1	1.4	1.4	1.3	1.5	1.4	1.1	0.79	1.4	1.4	1.3	1.4	1.5

Table A2.2.(continued).

Sample No.	93BRE83	94BRE62	94BRE78	93BRE107	93BRE190g	94BRE98	94BRE165	93BRE8	93BRE12	93BRE23	93BRE26	93BRE31
Map Unit	Qvap6	Qvap6	Qvap6	Qvh	Qvh	Qvh	Qvh	Qvpp	Qvpp	Qvpp	Qvpp	Qvpp
TAS name	phon/trach	phonolite	trachyte	phonolite	phonolite	phonolite	phonolite	trachyte	trachyte	trachyte	trachyte	trach/phon
Major and Minor Elements												
SiO_2	59.1	56.9	58.5	60.2	58.0	58.1	59.9	59.7	59.9	59.5	59.9	59.9
TiO_2	0.36	0.23	0.30	0.35	0.28	0.31	0.37	0.32	0.33	0.32	0.32	0.29
Al_2O_3	16.4	15.7	16.0	14.2	15.1	15.2	14.5	16.1	16.2	16.0	16.3	16.1
Fe_2O_3(total)	8.40	9.20	9.70	9.90	9.20	9.20	9.90	8.00	7.90	8.00	7.90	7.70
Fe_2O_3	4.30	5.30	4.90	2.20	1.90	1.80	2.80	5.30	5.10	4.60	4.50	3.70
FeO	3.70	3.50	4.30	6.90	6.60	6.70	6.40	2.40	2.50	3.10	3.10	3.60
MnO	0.21	0.21	0.22	0.24	0.22	0.21	0.24	0.18	0.18	0.18	0.18	0.18
MgO							0.10	0.21	0.23	0.21	0.25	0.18
CaO	1.76	1.04	1.64	1.22	1.27	1.39	1.53	1.61	1.78	1.71	1.65	1.67
Na_2O	7.20	8.80	7.20	9.10	9.10	9.20	8.90	7.30	7.20	7.40	7.60	7.70
K_2O	5.25	4.77	4.78	4.60	4.69	4.66	4.59	4.84	4.78	4.85	4.87	4.88
P_2O_5	0.06	0.02	0.07	0.07	0.06	0.06	0.08	0.05	0.05	0.05	0.05	0.05
H_2O(total)	1.10	3.30	2.00	0.20	2.10	2.00	0.40	1.20	1.10	1.30	1.00	0.80
CO_2(total)	0.20		0.10	0.20	0.30	0.10		0.30	0.20	0.20	0.20	0.20
S(total)	0.03	0.03	0.05	0.04	0.03	0.04	0.05	0.03		0.02	0.02	
Total	100.00	100.10	100.30	100.00	100.00	99.90	100.10	100.00	100.00	99.80	100.30	99.70
Trace Elements												
Ag	0.5	0.1		1.4	0.8	0.1	0.1	1.0	0.8	0.9	0.9	0.9
Ba		50	80	40	40		100		60	60	60	50
Be	5.9	11	8	13	8.7	8.7	12	9.3	9.1	9.3	9.0	9.4
Co	5		12		14	8	7	11	6	6	5	5
Cr												
Cs	1.3	2.4	1.9	3.5	1.8	1.8	3	2.5	3.7	2.6	2.2	2.6
Cu												
Ga	41	48	45	53	50	44	46	48	48	47	48	48
Hf	18	29	24	34	26	24	31	26	25	26	26	26
In	0.2	0.15	0.18	0.25	0.18	0.22	0.20	0.14	0.15	0.14	0.2	0.15
La	82	130	110	160	110	110	150	120	120	110	120	120
La	82	130	110	160	120	110	150	120	120	110	110	120
Mo	5.8	5.7	6.6	16	12	12	16	8.3	8	8.6	9.1	8.6
Nb												
Nb	110	170	150	200	150	150	190	150	140	140	150	150
Ni												
Pb	10	20	14	26	13	17	28	13	13	14	15	15
Rb	92											
Rb	110	150	130	190	140	130	180	140	150	160	150	150
Sc	0.8	0.7	0.6	0.7		0.5	1.2	1.0	0.9	0.9	0.9	0.8
Sr								21				21
Ta	6.1	14	11	13	8.4	12	16	8.2	8.0	10	9.4	9.3
Th	11	19	15	26	15	15	24	18	18	18	18	19
Tl	0.17	0.42	0.40	0.61	0.36	0.34	0.55	0.23	0.21	0.19	0.25	0.32
U	3.9	6.6	5.1	9.5	5.3	5.2	8.5	6.5	6.2	6.6	6.7	6.8
V												
Y	68	120	110	140	100	110	140	100	100	97	99	98
Y	68	120	98	140	100	96	130	100	100	97	97	99
Yb	7.0	11.0	9.3	13.00	9.40	9.20	12.00	9.50	9.40	9.30	9.30	9.50
Yb	5.9	10	8	11	8.3	8	11	8.1	8.0	8.0	7.9	8.1
Zn	190	300	270	350	280	260	320	230	240	230	220	220
Zr	990	1700	1400	1800	1400	1400	1800	1400	1400	1400	1400	1400
Rare Earth Elements												
La	82	130	110	160	110	110	150	120	120	110	120	120
Ce	170	260	230	320	230	230	290	230	230	230	230	230
Pr	21	32	28	40	29	27	36	29	29	28	28	29
Nd	81	120	110	160	110	110	140	110	110	110	110	110
Sm	16	25	22	32	24	22	28	23	22	22	22	22
Eu	1.9	3.6	3.3	3.0	3.1	3.1	3	2.4	2.5	2.4	2.5	2.5
Gd	15	26	22	29	21	21	27	21	21	20	20	21
Tb	2.4	4.1	3.5	4.7	3.4	3.4	4.3	3.3	3.3	3.2	3.3	3.3
Dy	14	23	20	28	21	19	24	20	20	19	20	20
Ho	2.7	4.5	3.8	5.4	3.9	3.7	4.8	3.8	3.8	3.8	3.8	3.9
Er	7.6	12	9.8	15	11	9.8	13	11	11	11	11	11
Tm	1.1	1.9	1.6	2.2	1.5	1.6	2.1	1.5	1.5	1.5	1.5	1.6
Yb	7.00	11	9.3	13	9.4	9.2	12	9.5	9.4	9.3	9.3	9.5
Lu	1.0	1.6	1.4	1.8	1.3	1.3	1.6	1.3	1.3	1.3	1.3	1.4

Table A2.2. (continued).

Sample No.	93BRE44	93BRE58	93BRE109	94BRE72	94BRE86	94BRE91	94BRE94	94BRE100	94BRE108
Map Unit	Qvpp	Qvpp	Qvpp	Qvpp	Qvpp	Qvpp	Qvpp	Qvpp	Qvpp
TAS name	trach/phon	trach/phon	trach/phon	trachyte	trachyte	trachyte	trachyte	trach/phon	phonolite
Major and Minor Elements									
SiO_2	59.7	59.7	59.9	60.1	59.9	59.6	60.2	59.3	59.0
TiO_2	0.30	0.30	0.30	0.33	0.33	0.33	0.26	0.27	0.28
Al_2O_3	16.0	16.3	16.1	16.7	16.5	16.5	16.8	16.9	16.5
Fe_2O_3(total)	7.90	7.50	8.10	8.00	8.10	8.00	7.50	7.70	8.10
Fe_2O_3	4.50	3.80	5.90	6.20	6.10	4.70	4.80	4.10	4.50
FeO	3.10	3.30	2.00	1.60	1.80	3.00	2.40	3.20	3.20
MnO	0.18	0.17	0.18	0.18	0.18	0.18	0.18	0.18	0.19
MgO	0.12	0.16	0.08	0.28	0.25	0.27	0.20	0.22	0.21
CaO	1.55	1.67	1.33	1.73	1.54	1.80	1.59	1.60	1.65
Na_2O	7.80	7.70	8.00	7.45	7.70	7.50	7.70	7.60	7.60
K_2O	4.87	4.94	4.85	4.86	4.77	4.78	4.90	4.90	4.94
P_2O_5	0.04	0.04	0.05	0.03	0.06	0.04	0.06	0.06	0.06
H_2O(total)	0.90	1.20	0.70	0.85	0.90	1.60	1.00	0.70	1.20
CO_2(total)	0.20	0.20	0.10				0.10		
S(total)			0.03		0.02	0.05		0.04	
Total	99.60	99.90	99.90	100.90	100.30	100.60	100.50	99.30	99.60
Trace Elements									
Ag	0.8	0.8	0.9			0.3			
Ba	70	60	70	120	50	100	70	100	90
Be	9.2	9.1	10	10	10	9	10	10	10
Co			5	12	16	7	6	8	6
Cr									
Cs	2	2	2.6	1.8	2.3	2.1	2.5	2.5	2.6
Cu									
Ga	48	48	49	42	41	41	42	42	42
Hf	26	26	27	26	25	24	25	26	26
In	0.19	0.14	0.21	0.16	0.14	0.15	0.14	0.15	0.20
La	120	110	120	120	110	110	110	110	120
La	110	110	120	120	110	110	110	110	120
Mo	6.8	5.9	11	3	8.9	6.8	8.5	9.3	9.0
Nb									
Nb	140	140	150	145	140	140	140	150	150
Ni									
Pb	16	15	17	12	14	13	15	15	20
Rb									
Rb	150	150	150	150.0	140	130	150	160	150
Sc	0.7	0.7	0.6	1	1.3	1.2	0.8	0.8	0.9
Sr								31	
Ta	8	8	10	12	10	11	11	12	10
Th	18	18	20	20.00	19	18	19	19	20
Tl	0.23	0.33	0.26	0.3	0.15	0.22	0.29	0.34	0.35
U	6.9	6.8	6.9	4	6.5	6.2	5.8	6.7	7.0
V									
Y	99	96	100	110	100	100	100	110	110
Y	98	96	100	110	97	94	96	96	100
Yb	9.70	9.20	10.00	9.60	9.20	9.00	9.30	9.60	9.70
Yb	8.0	7.8	8.3	10	9	8	8	8	9
Zn	220	220	230	8.5	220	300	210	210	220
Zr	1400	1400	1500	245	1400	1400	1400	1500	1500
				1450					
Rare Earth Elements									
La	120	110	120	120	110	110	110	110	120
Ce	240	2.1	250	230	220	220	220	230	230
Pr	29	28	30	28	26	26	26	27	28
Nd	110	110	120	110	100	100	100	110	110
Sm	23	22	24	21	20	21	20	21	22
Eu	2.5	2.4	2.5	2.6	2.5	2.4	2.5	2.5	2.5
Gd	20	20	21	22	20	20	21	21	22
Tb	3.3	3.2	3.4	3.5	3.3	3.2	3.3	3.4	3.5
Dy	20	19	21	20	19	18	18	19	20
Ho	3.8	3.7	4.0	3.9	3.5	3.4	3.6	3.7	3.8
Er	11	11	11	10	9.5	9.2	9.7	9.9	10
Tm	1.6	1.5	1.6	1.7	1.6	1.5	1.6	1.6	1.7
Yb	9.7	9.2	10	9.6	9.2	9	9.3	9.6	9.7
Lu	1.3	1.3	1.4	1.4	1.4	1.4	1.4	1.4	1.5

Table A2.3. List of all major, minor, and trace element and rare earth element analyses for samples from Little Bear Mountain volcano.

Sample No.	93BRE1	93BRE150	93BRE151	94BRE2	94BRE10	94BRE32	94BRE75	94BRE74	93BRE153	94BRE23
Map Unit	Qvb	Qvb	Qvb	Qvb	Qvb	Qvb	Qi	Qi	xenolith	xenolith
TAS name	basalt	basalt	basalt	basalt	basalt	basalt	tephrite	trachyandesite	trachyte	trachyte
Major Elements										
SiO_2	46.4	46.8	46.7	45.5	45.7	45.8	44.3	57.3	61.5	63.2
TiO_2	2.90	3.06	3.10	3.35	3.22	3.34	2.2	0.51	0.42	0.36
Al_2O_3	17.3	16.9	16.6	16.0	16.5	16.7	15.1	15.5	18.5	17.8
Fe_2O_3(total)	12.70	13.00	13.30	13.87	13.30	13.60	11.95	7.60	3.30	4.40
Fe_2O_3	2.80	2.90	4.00	4.17	4.20	3.70	3.25	1.30	0.90	0.50
FeO	8.90	9.10	8.40	8.70	8.20	8.90	7.8	5.70	2.20	3.50
MnO	0.17	0.17	0.17	0.19	0.18	0.18	0.18	0.18	0.06	0.11
MgO	5.14	5.62	4.90	5.53	5.13	5.59	5.29	0.95	0.35	0.22
CaO	9.30	9.44	9.31	10.2	10.2	10.1	11.3	2.54	1.85	2.01
Na_2O	3.40	3.40	3.20	3.10	3.20	3.30	3	4.60	6.10	5.70
K_2O	1.13	1.19	1.25	1.35	1.35	1.16	0.75	4.56	5.17	5.51
P_2O_5	0.88	0.86	0.98	0.96	0.92	0.88	0.485	0.13	0.16	0.08
H_2O(total)	1.20	0.70	0.80	1.23	1.40	0.70	1.2	1.50	1.80	0.70
CO_2(total)	0.10	0.20	0.20				5.3	5.50	0.40	
S(total)	0.06	0.07	0.02	0.05	0.02	0.02	0.07	0.04	0.02	
Total	100.10	100.80	100.00	100.30	100.40	100.60	101.13	100.40	99.80	99.90
Trace Elements										
Ag	0.2	0.2	0.2	0.1					0.1	
Ba	420	430	430	450	430	410	230	340	1600	950
Be	21	22	23	1	1	1	1.2	3	2.6	3.1
Co	34	43	37	35	31	34	37		10	8
Cr	52	66	47	48	40	51				
Cs	0.17	0.18	0.12	0.17	0.13	0.15	0.49	0.41	0.14	
Cu	20	22	20	22	23	22				
Ga	25	25	25	22	22	22	19	32	21	
Hf	5.5	5	5	4.8	4.6	4.4	4.1	13	2.3	
In	0.12	0.14	0.09	0.09	0.12	0.08	0.11	0.27		
La	33.00	30.00	32.00	31.00	30.00	28.00	17.5	70	17.00	43.00
La	29	27	29	30	29	27	16.5	66	15	46
Mo	1.8	2.1	1.9	2	1.3	1.2	1.65	6.7	1.6	
Nb	34	33	33	36	34	31			12	
Nb	28	30	28					100	23	
Ni	33	41	25	30	27	32				
Pb	3	3	2	2	3	2	2	6	4	
Rb	15	16	16	18	16	16		82	16	
Rb								100	55	
Sc	19	20	20	19	18	18	23	4	2.6	3.5
Sr	920	850	920	820	930	850		77	230	160
Ta	2.3	2.6	2.4	3.0	2.8	2.9	1.3	7	1.3	
Th	2.4	2.2	2.2	2.4	2.3	2.1	1.45	10	1.6	
Tl	0.05	0.04	0.05	0.04	0.04	0.04	0.035	0	0.09	
U	0.83	0.78	0.89	0.77	0.74	1	0.485	3.1	0.54	
V	160	190	160	177	160	170				
Y	28	27	29	31	30	28	30.5	60	7.4	
Y	28	26	28	27	26	25	26.50	53	7	29
Yb	2.20	2.10	2.20	2.20	2.10	2.00	2.6	5.6	0.60	3.20
Yb	1.8	1.7	1.8	2	2	1	2	5	0.5	3
Zn	85	85	90	100	100	100	135	140	33	79
Zr	230	210	220	223	220	190	195	650	95	580
Rare Earth Elements										
La	33	30	32	31	30	28	17.5	70	17.0	43.0
Ce	70	64	69	70	68	63	41	140	32.0	81.0
Pr	9.2	8.6	9.3	9.27	9.0	8.4	5.35	17	4.0	9.1
Nd	41	38	42	41	40	37	24	68	16.0	35.0
Sm	8.8	8.2	9.1	8.77	8.5	8.0	5.75	14	3.1	6.8
Eu	3.4	3.1	3.5	3.4	3.4	3.3	2.05	2.2	3.7	2.7
Gd	8.6	7.9	9.0	8.97	8.8	8.4	6.5	13	2.6	6.7
Tb	1.2	1.1	1.2	1.2	1.2	1.1	1	2	0.35	1.0
Dy	6.3	6.0	6.4	6.2	6.0	5.7	5.55	11	1.80	5.6
Ho	1.1	1.1	1.2	1.1	1.0	1.0	1.1	2.1	0.30	1.1
Er	3.0	2.8	2.9	2.63	2.5	2.4	2.8	5.5	0.74	2.9
Tm	0.38	0.36	0.38	0.40	0.39	0.36	0.44	0.91	0.1	0.51
Yb	2.2	2.1	2.2	2.2	2.1	2.0	2.6	5.6	0.6	3.20
Lu	0.33	0.32	0.32	0.34	0.33	0.30	0.395	0.9	0.1	0.52

Table A2.4. Electron microprobe analyses for plagioclase from Little Bear mountain (94BRE02).

Analysis No.	be-pl2	be-pl4	be-pl5	be-pl6	be-pl7	be-pl8	be-pl9	be-pl10	be-pl11	be-pl12	be-pl13	be-pl14
SiO_2	52.55	57.09	52.08	50.16	50.90	51.24	52.24	52.10	52.52	55.20	55.42	55.71
Al_2O_3	29.28	26.34	29.16	30.63	30.09	30.20	29.42	29.42	29.12	27.48	27.35	27.17
Fe_2O_3	0.73	0.31	0.69	0.51	0.55	0.56	0.50	0.53	0.52	0.39	0.41	0.39
BaO	0.00	0.10	0.04	0.02	0.02	0.03	0.00	0.05	0.00	0.02	0.06	0.01
MgO	0.10	0.03	0.08	0.09	0.07	0.08	0.09	0.09	0.11	0.06	0.05	0.04
CaO	12.30	8.70	12.13	13.76	13.31	13.77	12.26	12.49	12.06	9.99	10.01	9.72
Na_2O	4.27	6.00	4.18	3.19	3.66	3.38	3.98	4.03	4.26	5.30	5.25	5.41
K_2O	0.35	0.71	0.32	0.22	0.27	0.24	0.31	0.31	0.36	0.54	0.51	0.57
Total	99.24	98.57	98.37	98.36	98.60	99.25	98.50	98.70	98.59	98.44	98.57	98.46
				Cation calculation of plagioclase based on 8 oxygens								
Si	2.3971	2.5837	2.3962	2.3174	2.3444	2.3449	2.3964	2.3894	2.4071	2.5132	2.5203	2.5323
Al	1.5740	1.4048	1.5810	1.6676	1.6330	1.6288	1.5907	1.5900	1.5728	1.4747	1.4661	1.4557
Fe^{3+}	0.0252	0.0106	0.0239	0.0178	0.0190	0.0192	0.0174	0.0183	0.0179	0.0133	0.0141	0.0134
Ba	0.0000	0.0017	0.0007	0.0003	0.0004	0.0005	0.0000	0.0009	0.0000	0.0004	0.0011	0.0002
Mg	0.0067	0.0023	0.0057	0.0065	0.0050	0.0056	0.0061	0.0058	0.0075	0.0038	0.0036	0.0030
Ca	0.6012	0.4217	0.5979	0.6810	0.6566	0.6752	0.6028	0.6137	0.5923	0.4875	0.4880	0.4736
Na	0.3774	0.5268	0.3732	0.2859	0.3267	0.3001	0.3542	0.3587	0.3786	0.4683	0.4628	0.4769
K	0.0204	0.0413	0.0187	0.0126	0.0158	0.0139	0.0179	0.0181	0.0207	0.0316	0.0296	0.0330
Sum	5.0022	4.9929	4.9973	4.9891	5.0008	4.9881	4.9856	4.9948	4.9971	4.9928	4.9858	4.9881
An %	60.18	42.60	60.41	69.52	65.72	68.26	61.83	61.96	59.73	49.37	49.77	48.16
Ab %	37.78	53.22	37.70	29.19	32.70	30.34	36.33	36.21	38.18	47.43	47.20	48.48
Or %	2.04	4.18	1.89	1.29	1.58	1.40	1.84	1.83	2.09	3.20	3.02	3.36

Table A2.4. (continued).

Analysis No.	be-pl15	be-pl16	be-pl17	be-pl18	be-pl19	be-pl20	be-pl21	be-pl22	be-pl23	be-pl24	be-pl25	be-pl26	be-pl27
SiO_2	55.30	53.56	57.58	57.38	57.96	52.84	52.46	54.28	57.12	56.42	53.06	51.19	49.77
Al_2O_3	27.48	28.28	25.91	25.85	25.69	28.70	29.19	27.79	26.24	26.46	28.32	30.05	30.82
Fe_2O_3	0.50	0.81	0.34	0.34	0.36	0.67	0.62	0.50	0.27	0.38	0.66	0.48	0.53
BaO	0.02	0.03	0.04	0.18	0.10	0.07	0.00	0.00	0.08	0.11	0.04	0.00	0.04
MgO	0.06	0.09	0.03	0.02	0.04	0.09	0.07	0.08	0.03	0.05	0.08	0.08	0.08
CaO	9.87	10.90	8.19	8.05	8.01	11.83	12.28	10.57	8.54	8.86	11.51	13.14	13.99
Na_2O	5.45	4.77	6.25	6.26	6.34	4.41	4.24	5.11	6.11	5.92	4.50	3.66	3.16
K_2O	0.48	0.45	0.73	0.74	0.80	0.36	0.34	0.46	0.70	0.64	0.38	0.26	0.19
Total	98.68	98.44	98.33	98.08	98.50	98.63	98.87	98.32	98.39	98.20	98.16	98.60	98.38
Cation calculation of plagioclase based on 8 oxygens													
Si	2.5136	2.4516	2.6067	2.6065	2.6185	2.4221	2.4006	2.4824	2.5885	2.5673	2.4395	2.3542	2.3025
Al	1.4722	1.5257	1.3825	1.3838	1.3677	1.5504	1.5742	1.4977	1.4015	1.4193	1.5346	1.6287	1.6802
Fe^{3+}	0.0173	0.0280	0.0115	0.0115	0.0123	0.0231	0.0215	0.0171	0.0094	0.0130	0.0230	0.0167	0.0184
Ba	0.0003	0.0005	0.0008	0.0032	0.0018	0.0013	0.0000	0.0000	0.0014	0.0020	0.0007	0.0000	0.0008
Mg	0.0038	0.0058	0.0022	0.0015	0.0027	0.0063	0.0049	0.0052	0.0023	0.0031	0.0054	0.0053	0.0055
Ca	0.4807	0.5348	0.3972	0.3920	0.3877	0.5811	0.6023	0.5178	0.4145	0.4322	0.5670	0.6473	0.6935
Na	0.4799	0.4237	0.5483	0.5515	0.5551	0.3922	0.3761	0.4531	0.5364	0.5223	0.4008	0.3264	0.2833
K	0.0277	0.0264	0.0425	0.0432	0.0466	0.0209	0.0198	0.0268	0.0408	0.0371	0.0222	0.0152	0.0110
Sum	4.9955	4.9966	4.9918	4.9933	4.9925	4.9976	4.9995	5.0001	4.9948	4.9963	4.9931	4.9938	4.9952
An %	48.64	54.30	40.20	39.73	39.18	58.45	60.34	51.90	41.80	43.58	57.27	65.46	70.21
Ab %	48.56	43.02	55.49	55.89	56.10	39.45	37.68	45.41	54.09	52.67	40.48	33.01	28.68
Or %	2.80	2.68	4.30	4.38	4.71	2.10	1.99	2.68	4.12	3.74	2.24	1.53	1.11

Table A2.4. (continued).

Analysis No.	be-pl28	be-pl29	be-pl30	be-pl31	be-pl32	be-pl33	be-pl34	be-pl35	be-pl36	be-pl37	be-pl38	be-pl39	be-pl40
SiO_2	49.20	52.44	52.52	53.66	56.89	59.66	59.82	59.82	61.51	51.85	52.39	53.46	50.88
Al_2O_3	31.01	28.92	29.06	28.31	26.83	24.55	24.41	24.53	23.43	29.76	29.24	28.36	30.24
Fe_2O_3	0.54	0.59	0.57	0.64	0.19	0.23	0.22	0.17	0.30	0.78	0.64	0.74	0.51
BaO	0.04	0.00	0.00	0.00	0.15	0.15	0.20	0.17	0.10	0.04	0.04	0.04	0.02
MgO	0.07	0.08	0.09	0.09	0.01	0.02	0.01	0.02	0.01	0.10	0.10	0.10	0.11
CaO	14.38	11.97	11.97	11.27	8.76	6.13	6.27	6.00	5.12	12.31	11.74	11.37	13.43
Na_2O	2.89	4.25	4.18	4.67	6.13	7.21	7.11	7.23	7.68	4.10	4.34	4.65	3.41
K_2O	0.19	0.32	0.33	0.44	0.61	1.08	1.08	1.05	1.38	0.32	0.35	0.43	0.27
Total	98.14	98.24	98.40	98.65	98.96	97.94	98.03	97.94	98.14	98.93	98.49	98.71	98.60
Cation calculation of plagioclase based on 8 oxygens													
Si	2.2843	2.4122	2.4107	2.4516	2.5682	2.6920	2.6971	2.6976	2.7547	2.3742	2.4037	2.4439	2.3416
Al	1.6972	1.5675	1.5722	1.5240	1.4274	1.3053	1.2970	1.3035	1.2366	1.6059	1.5809	1.5276	1.6400
Fe^{3+}	0.0190	0.0202	0.0198	0.0220	0.0064	0.0079	0.0075	0.0058	0.0100	0.0269	0.0222	0.0254	0.0176
Ba	0.0008	0.0000	0.0000	0.0000	0.0027	0.0026	0.0036	0.0031	0.0017	0.0006	0.0007	0.0006	0.0003
Mg	0.0050	0.0052	0.0065	0.0062	0.0009	0.0012	0.0010	0.0012	0.0006	0.0069	0.0066	0.0067	0.0076
Ca	0.7156	0.5902	0.5887	0.5518	0.4235	0.2963	0.3027	0.2900	0.2455	0.6037	0.5772	0.5570	0.6623
Na	0.2600	0.3788	0.3715	0.4138	0.5363	0.6307	0.6212	0.6325	0.6671	0.3643	0.3864	0.4120	0.3047
K	0.0112	0.0184	0.0190	0.0256	0.0356	0.0627	0.0631	0.0611	0.0801	0.0184	0.0206	0.0250	0.0155
Sum	4.9931	4.9925	4.9885	4.9951	5.0011	4.9985	4.9932	4.9948	4.9963	5.0008	4.9982	4.9981	4.9896
An %	72.51	59.77	60.12	55.67	42.55	29.94	30.67	29.48	24.73	61.21	58.64	56.04	67.41
Ab %	26.35	38.37	37.94	41.75	53.88	63.73	62.94	64.31	67.20	36.93	39.26	41.45	31.01
Or %	1.14	1.86	1.94	2.59	3.57	6.34	6.39	6.21	8.07	1.86	2.09	2.51	1.57

Table A2.4. (continued).

Analysis No.	be-pl41	be-pl42	be-pl43	be-pl44	be-pl45	be-pl46	be-pl47	be-pl48_1	be-pl48_2	be-pl48_3	be-pl48_4	be-pl48_5
SiO_2	51.00	57.87	59.35	57.33	57.23	53.63	54.10	54.79	54.58	54.71	53.09	54.96
Al_2O_3	29.93	25.48	24.69	26.20	25.99	27.89	28.09	27.57	27.83	27.77	26.18	27.51
Fe_2O_3	0.50	0.84	0.81	0.32	0.38	0.68	0.68	0.46	0.37	0.46	0.43	0.44
BaO	0.00	0.09	0.08	0.07	0.09	0.00	0.04	0.05	0.10	0.07	0.03	0.01
MgO	0.11	0.06	0.06	0.03	0.04	0.10	0.10	0.05	0.05	0.06	0.05	0.06
CaO	13.35	7.75	7.57	8.39	8.17	11.26	11.00	10.41	10.29	10.42	9.69	9.99
Na_2O	3.54	6.25	6.68	6.10	6.14	4.78	4.89	5.24	5.14	5.02	5.05	5.37
K_2O	0.26	1.02	1.06	0.78	0.79	0.42	0.47	0.49	0.49	0.44	0.50	0.50
Total	98.43	98.33	99.24	98.43	98.03	98.35	98.90	98.55	98.35	98.50	94.53	98.33
					Cation calculation of plagioclase based on 8 oxygens							
Si	2.3509	2.6176	2.6576	2.5941	2.5996	2.4594	2.4644	2.4980	2.4923	2.4945	2.5186	2.5073
Al	1.6263	1.3583	1.3033	1.3970	1.3911	1.5071	1.5079	1.4816	1.4976	1.4924	1.4638	1.4789
Fe^{3+}	0.0173	0.0285	0.0274	0.0108	0.0129	0.0236	0.0234	0.0157	0.0125	0.0158	0.0152	0.0150
Ba	0.0000	0.0016	0.0015	0.0012	0.0016	0.0000	0.0007	0.0008	0.0019	0.0012	0.0005	0.0001
Mg	0.0075	0.0040	0.0039	0.0019	0.0024	0.0071	0.0069	0.0032	0.0031	0.0037	0.0039	0.0039
Ca	0.6595	0.3758	0.3630	0.4070	0.3976	0.5533	0.5369	0.5084	0.5035	0.5091	0.4926	0.4886
Na	0.3166	0.5480	0.5801	0.5353	0.5404	0.4246	0.4319	0.4628	0.4552	0.4440	0.4644	0.4751
K	0.0151	0.0591	0.0619	0.0451	0.0459	0.0246	0.0274	0.0283	0.0283	0.0255	0.0292	0.0290
Sum	4.9931	4.9928	4.9986	4.9924	4.9916	4.9998	4.9996	4.9989	4.9943	4.9861	4.9882	4.9978
An %	66.54	38.23	36.12	41.22	40.41	55.19	53.90	50.87	51.01	52.02	49.95	49.22
Ab %	31.94	55.75	57.72	54.21	54.92	42.35	43.35	46.30	46.12	45.37	47.08	47.86
Or %	1.52	6.01	6.16	4.57	4.67	2.46	2.75	2.83	2.86	2.60	2.96	2.93

Table A2.4. (continued).

Analysis No.	be-pl48_6	be-pl48_7	be-pl48_8	be-pl48_9	be-pl48_10	be-pl49	be-pl50	be-pl51	be-pl52	be-pl53	be-pl54	be-pl55
SiO_2	56.90	55.57	54.86	55.89	54.32	53.90	51.15	49.34	50.65	49.60	56.13	52.90
Al_2O_3	24.66	27.24	27.65	26.86	28.11	27.92	30.33	31.35	30.36	30.64	26.81	28.61
Fe_2O_3	0.39	0.40	0.39	0.49	0.44	0.68	0.43	0.57	0.58	0.60	0.74	0.96
BaO	0.02	0.04	0.09	0.07	0.05	0.10	0.03	0.00	0.05	0.02	0.03	0.03
MgO	0.04	0.06	0.06	0.07	0.07	0.11	0.09	0.08	0.08	0.07	0.10	0.12
CaO	9.91	9.90	10.24	9.36	10.93	11.10	13.20	14.62	13.55	14.73	9.66	11.73
Na_2O	5.93	5.50	5.18	5.65	4.99	4.85	3.49	2.88	3.26	2.83	5.59	4.36
K_2O	0.48	0.54	0.49	0.60	0.46	0.41	0.26	0.17	0.21	0.16	0.63	0.38
Total	97.86	98.71	98.47	98.38	98.92	98.67	98.73	98.83	98.53	98.51	99.06	98.72
					Cation calculation of plagioclase based on 8 oxygens							
Si	2.6075	2.5238	2.5011	2.5431	2.4719	2.4642	2.3484	2.2761	2.3342	2.2963	2.5394	2.4224
Al	1.3317	1.4581	1.4855	1.4403	1.5076	1.5041	1.6412	1.7044	1.6493	1.6718	1.4295	1.5443
Fe^{3+}	0.0134	0.0136	0.0133	0.0168	0.0151	0.0235	0.0149	0.0196	0.0202	0.0211	0.0253	0.0332
Ba	0.0004	0.0008	0.0017	0.0012	0.0008	0.0018	0.0006	0.0000	0.0010	0.0004	0.0005	0.0006
Mg	0.0027	0.0040	0.0043	0.0044	0.0048	0.0072	0.0063	0.0052	0.0056	0.0049	0.0068	0.0084
Ca	0.4867	0.4820	0.5002	0.4561	0.5330	0.5439	0.6493	0.7225	0.6690	0.7308	0.4681	0.5755
Na	0.5271	0.4844	0.4581	0.4981	0.4402	0.4303	0.3107	0.2579	0.2909	0.2544	0.4906	0.3872
K	0.0280	0.0317	0.0286	0.0348	0.0267	0.0239	0.0149	0.0099	0.0123	0.0094	0.0367	0.0219
Sum	4.9975	4.9984	4.9929	4.9949	5.0002	4.9990	4.9863	4.9957	4.9826	4.9891	4.9970	4.9934
An %	46.71	48.29	50.69	46.12	53.30	54.50	66.60	72.96	68.81	73.48	47.03	58.45
Ab %	50.59	48.53	46.41	50.36	44.02	43.11	31.87	26.04	29.92	25.58	49.29	39.33
Or %	2.69	3.17	2.90	3.52	2.67	2.39	1.53	1.00	1.27	0.94	3.69	2.22

Table A2.5. Isotopic data for samples from the Hoodoo Mountain Volcanic Complex.

Sample	Rock type	Unit	Rb (ppm)	Sr (ppm)	Sm (ppm)	Nd (ppm)	$^{87}Sr/^{86}Sr$[1]	$^{143}Nd/^{144}Nd$[1]	ε_{Nd}
93BRE8	trachyte	Qvpp	107.0	22.91	21.4	103.7	0.703479(28)	0.512916(7)	+5.4
93BRE16	trachyte	$Qvap_4$	101.6	2.15	11.3	51.47	0.704812(47)	0.512905(4)	+5.2
93BRE141	trachyte	Qvap	83.38	23.99	21.96	103.6	0.703427(19)	0.512909(12)	+5.3
93BRE150	basalt	Qvb	15.39	900.0	8.19	37.60	0.703137(23)	0.512886(9)	+4.8
93BRE151	basalt	Qvb	14.45	874.1	6.59	30.79	0.702700(18)	0.512871(4)	+4.6
93BRE153	trachyte	xenolith	24.94	227.3	2.99	15.09	0.703182(11)	0.512950(8)	+6.1
93BRE190	trachyte (glass)	$Qvap_6$	82.72	1.21	23.06	109.8	0.703959 (36)	0.512921(7)	+5.5

[1] Bracketed values represent the 2σ analytical error.

APPENDIX A3

Error propogation and Affinity calculations

Appendix A3.1.

Least squares regression of the raw experimental data yields a slope (m) and an uncertainty on the slope (σ_m) that reflects how well the data fit a linear model. This uncertainty can be propagated through subsequent calculational procedures used to compute ν. For example, to convert the nominal dissolution rate (ν^*) and its associated uncertainty (σ_{n^*}) to the appropriate normalized dissolution rate (ν) and its associated uncertainty (σ_n) requires propagation of σ_{n^*} through the following equation:

$$\sigma_n = (d\nu / d\nu^*)^2 \sigma_{n^*}^2$$

For all rates reported in Tables 3 to 6 with values of R^2 greater than 0.9, the propagated errors are equal to or smaller than the symbol sizes in Figures 3.3, 3.4, and 3.6a.

Appendix A3.2.

By definition, the affinity (**A**) for a reaction is equal to

(a) $\mathbf{A} = -\Sigma\, \alpha_i\, \mu_i$

where α_i is the stoichiometric coefficient and μ_i is the chemical potential of each of the components involved in the reaction (Prigogine, 1967). Thus, the value of **A** for the reaction $SiO2_{(Qtz)} \Rightarrow SiO2_{(melt)}$ can be calculated using

(b) $\mathbf{A} = -\left(\alpha_{qtz} \left(\mu^{\circ}_{qtz} + RT \ln \mathbf{a}_{SiO2}\right) + \alpha_{SiO2,liq} \left(\mu^{\circ}_{SiO2,\,liq} + RT \ln \mathbf{a}_{SiO2,liq}\right)\right).$

where $\mathbf{a}_{SiO2}$ represents the activity of SiO_2 in quartz and the melt phase. The values of **A** for a given reaction can be calculated by using standard state thermodynamic properties for solids of Berman (1988), whereas the corresponding melt properties derive from Ghiorso and Sack (1995). Alternatively, the Melts software (available from http://msgmac.geology.washington.edu//MeltsWWW/ Melts.html) provides values of **A** for a limited set of mineral compositions at specified values of **T**, **P** and melt composition.